Structural aspects of modelling biopolymer networks

Daniel Luke Humphries

Magdalen College
University of Oxford

A thesis submitted for the degree of
Doctor of Philosophy

Michaelmas 2017

Abstract

Many biological systems involve intricate, hierarchical networks formed from cross-linked filaments, including the cytoskeleton of eukaryotic cells and the collagen scaffold of the extracellular matrix. Experiments performed on these biopolymer networks have identified exotic and desirable mechanical behaviours that cannot be easily understood without discussing the underlying microstructures and their properties. As such, the theoretical and computational modelling of filament assemblies has increasingly utilized discrete fibre network (DFN) models to investigate their complex local and global mechanical properties. This thesis investigates some of the many structural aspects of these networks, and how details of the network architecture can influence the mechanics of the system. We discuss how the geometry of a fibrous substrate can influence the long-ranged displacement fields generated by contractile resident biological cells, and the extent to which long-ranged mechanical communication between distant cells is plausible. A variety of architecture choices are discussed and compared. Motivated by improvements in electrospinning technologies and recent experiments, we develop a new fibre network model, where cross-link density is allowed to vary while geometry is controlled. The affine-nonaffine transition in this model is discussed and characterized, and theoretical predictions for the scaling of the network shear modulus are presented. As much of the DFN literature focusses on monotypic fibre networks, the mechanics of polymer assemblies formed from two or more filament types, which often arise in Nature, is poorly understood. We seek to address this by extending monotypic fibre network models to incorporate two distinct fibre types. In the low density regime we present extensive theoretical predictions and supporting numerical results for the network response as numerous parameters are varied. The importance of network architecture is discussed in the context of nonaffine fluctuations and their influence on the mechanical response. Finally, dense, random heterotypic networks are studied, in light of experiments and theoretical models that observe 'exceptional stiffening' in such systems. We propose a novel explanation for this phenomenon, and provide evidence for our interpretation over others given in the literature. The implications of the research presented here for higher dimensional systems and for finite strains are discussed. Together, this thesis constitutes an argument for the mechanical importance of the detailed structural properties possessed by biopolymer networks, in a variety of systems and at multiple scales.

Structural aspects of modelling biopolymer networks

Daniel Luke Humphries

Magdalen College

University of Oxford

A thesis submitted for the degree of

Doctor of Philosophy

Michaelmas 2017

For Amy

Wherever he dream, under mountain or stream,
The Spirit he loves remains.

Percy Bysshe Shelley,
The Cloud

Acknowledgements

The work presented in this thesis owes much to the generous and patient guidance offered by my supervisor Prof. Eamonn Gaffney. His sharp and perceptive mind, many creative suggestions and kind support over the past three years have been invaluable. I have particularly enjoyed our meetings, where discussions across a range of topics both mathematical and otherwise have always left me feeling reinvigorated and with renewed motivation. I shall miss Eamonn's company and consider myself extremely fortunate to have worked with him.

I wish to offer many thanks to Dr. James Grogan, who kindly became a second supervisor and enabled this thesis to grow in new directions. In particular, his expertise in Abaqus and considerable mechanics knowledge have been immeasurably useful, as were his contributions to discussions and his research advice. I owe James a great deal.

I consider myself privileged to have worked with several excellent supervisors throughout my time at Oxford, who encouraged and fostered an appreciation for research, in particular within the field of mathematical biology. Prof. Ruth Baker's undergraduate teaching first brought me towards this field, and I thank her for her kind and patient supervision during my Master's dissertation and during a short project rotation, co-supervised with similar care and attention by Prof. Christian Yates. Further thanks are offered to all the staff at the Systems Biology Doctoral Training Centre, in which I enjoyed an extremely fun first year under the dedicated mentorship of Prof. Elspeth Garman.

I have enjoyed my time as a graduate thanks, in no small part, to the extremely friendly and supportive working environment offered by the Wolfson Centre for Mathematical Biology. I thank all the current and past members I've had the pleasure of meeting for contributing towards a research space that is singularly welcoming. In particular, I thank Prof. Philip Maini for his perpetual joviality which leads by example in creating this working environment. I have gained a lot from my long-serving officemates Jonathan Harrison and Eddie Rolls. Whether due to their mathematical and computational insight, their conversation and a little stern debate, or their ability to brighten some of the less palatable research periods, my time has been considerably enriched by their company.

My time in the office might not have been quite so readily enjoyed had I not been so lucky as to have formed some excellent and lasting friendships outside of

the mathematical world. To my good friends Russ and Andrew, I thank you for the many discussions and debates across a remarkable breadth of topics, as well as your ever-appreciated company. I have learned far more from your company than I could have expected. I wish to thank Ryan for his continued close friendship, which remains as entertaining as ever. His cantankerous contemplations provide a welcome break from the Oxford bubble. I also wish to thank those long-standing friends who I met many years ago, and who have remained important throughout my life. I look forward in particular to reuniting with James, Luke and Joe, who have always been very welcome, if too infrequent, divertissements from the Oxford scene.

I wish to thank those teachers earlier in my education who proved so important to my mathematical upbringing. In particular Lois Nichol and Trevor Williams, who were instrumental in encouraging my application to this University, and from whose enthusiasm and intelligence my love for mathematics grew.

The support, love and care offered, without hesitation and at all times, by my parents is something for which I am always grateful. I consider myself very fortunate to have benefited from their sensitive encouragement throughout my education. I am thankful for all they have given me. The friendship and support of my brothers Dominic and James is always appreciated, as is the joy of seeing Kelly, Evan and Tahlia.

Finally, I must acknowledge my closest friend and partner, Amy. We began our time together at the onset of my graduate endeavours, and I would have struggled to reach this stage without you. I thank you for all the support and kindness you've given me from the very start until this day. As this chapter of our life draws to a close, I look forward keenly to what comes next.

Abstract

Many biological systems involve intricate, hierarchical networks formed from cross-linked filaments, including the cytoskeleton of eukaryotic cells and the collagen scaffold of the extracellular matrix. Experiments performed on these biopolymer networks have identified exotic and desirable mechanical behaviours that cannot be easily understood without discussing the underlying microstructures and their properties. As such, the theoretical and computational modelling of filament assemblies has increasingly utilized discrete fibre network (DFN) models to investigate their complex local and global mechanical properties. This thesis investigates some of the many structural aspects of these networks, and how details of the network architecture can influence the mechanics of the system. We discuss how the geometry of a fibrous substrate can influence the long-ranged displacement fields generated by contractile resident biological cells, and the extent to which long-ranged mechanical communication between distant cells is plausible. A variety of architecture choices are discussed and compared. Motivated by improvements in electrospinning technologies and recent experiments, we develop a new fibre network model, where cross-link density is allowed to vary while geometry is controlled. The affine-nonaffine transition in this model is discussed and characterized, and theoretical predictions for the scaling of the network shear modulus are presented. As much of the DFN literature focusses on monotypic fibre networks, the mechanics of polymer assemblies formed from two or more filament types, which often arise in Nature, is poorly understood. We seek to address this by extending monotypic fibre network models to incorporate two distinct fibre types. In the low density regime we present extensive theoretical predictions and supporting numerical results for the network response as numerous parameters are varied. The importance of network architecture is discussed in the context of nonaffine fluctuations and their influence on the mechanical response. Finally, dense, random heterotypic networks are studied, in light of experiments and theoretical models that observe 'exceptional stiffening' in such systems. We propose a novel explanation for this phenomenon, and provide evidence for our interpretation over others given in the literature. The implications of the research presented here for higher dimensional systems and for finite strains are discussed. Together, this thesis constitutes an argument for the mechanical importance of the detailed structural properties possessed by biopolymer networks, in a variety of systems and at multiple scales.

Contents

List of Figures viii

List of abbreviations and notation xxvii

1 Introduction 1
- 1.1 Context . . . 1
  - 1.1.1 Biopolymers and their networks . . . 8
  - 1.1.2 Interactions between cells and matrix . . . 13
  - 1.1.3 Theoretical modelling of biopolymer networks . . . 17
- 1.2 Network generation . . . 27
  - 1.2.1 Spanning connected components . . . 31
  - 1.2.2 Removal of short lengths . . . 32
- 1.3 Thesis contributions . . . 34
- 1.4 Thesis structure . . . 35
  - 1.4.1 Publications and submissions . . . 36

2 The importance of network architecture to mechanical cell-cell communication 37
- 2.1 Introduction . . . 38
- 2.2 Methods . . . 42
  - 2.2.1 Model fibre choices . . . 42
  - 2.2.2 Network geometry . . . 45
- 2.3 Results . . . 48
  - 2.3.1 Network stiffness under uniaxial extension is dependent on network choice . . . 48
  - 2.3.2 Displacement fields arising from single contractile cells exhibit qualitative differences with choice of initial network geometry 52
  - 2.3.3 Network choice strongly influences stress transmission and membrane reaction force . . . 53
  - 2.3.4 Fibre reorganisation far from the cell membrane depends on geometry choice, and correlates with fibre strain . . . 58
  - 2.3.5 The dependence of mechanical response upon network geometry persists at higher densities . . . 60

2.3.6 Pairwise contractile cells can mechanically signal through transmitted stress in certain architectures 62
2.4 Conclusions 66

3 The mechanics of phantom Mikado networks 71
3.1 The Finite Element Method for beam networks 72
3.2 Implementation of a DFN model on the Abaqus FE platform 80
3.3 The mechanics of a phantom Mikado model 87
3.4 Model 91
3.5 Results 93
3.5.1 Behaviour in the nonaffine regime 93
3.5.2 Transition between affine and nonaffine deformation 98
3.6 Discussion 107

4 Mechanics of low density heterotypic fibre networks 112
4.1 Introduction 113
4.2 Model 118
4.3 Results 122
4.4 Discussion 139
4.5 Conclusions 142

5 Stiffening in heterotypic fibre networks 144
5.1 Introduction 144
5.2 Model 149
5.3 Results 151
5.4 Discussion 170
5.5 Conclusions 174

6 Discussion and future directions 175
6.1 Thesis contributions and conclusions 176
6.2 Future directions 179
6.3 Closing remarks 182

Appendices

A Statistical properties of Mikado networks 184

B Affine deformations and discrete fibre network models 187

References 191

List of Figures

1.1 Microscopy images displaying some examples of biopolymer networks found in Nature. **(a)** Three-dimensional confocal microscopy image of a collagen type-I network, reproduced with permission from Beroz et al. [20]. **(b)** The intracellular F-actin network (red) in bovine pulmonary artery endothelial cells is displayed through fluorescence microscopy. Microtubules are shown in green, spanning the cell from the nucleus (blue) to the cell periphery. Image taken from ImageJ under public domain, at http://rsb.info.nih.gov/ij/images/. **(c)** Electron microscopy of actin filaments in keratocyte lamellipodia, showing the branching 'brush-like' region towards the cell leading edge (top right) and the smooth fibre network towards the lamellipodium centre (bottom right). Reproduced with permission from Svitkina et al. [21]. 6

1.2 A schematic of the hierarchical structure of tendon, illustrating the organisation of biopolymers and their networks at a range of length scales. Individual collagen molecules cross-link in a triple helix structure. These collagen molecules are themselves cross-linked into collagen fibrils, where there are periodic gap regions, of approximately 67nm. At larger length scales, the collagen fibrils are structured within a flexible proteoglycan matrix in the fascicle, where cells, such as tenocytes, may be present. The bundling together of several fascicles produces the tendon fibre. As such, structure exists from the nanometre to the hundreds of micrometres scales. 11

1.3 Some examples of cell-matrix interactions in different biopolymer systems. **(a)** Scanning electron microscope images of rat neural stem/progenitor cells, anchored to electrospun polymer scaffolds. Many cells adopt a stretched morphology when interacting with the nanofibres. Reproduced with permission from Christopherson, Song, and Mao [130]. **(b)** Scanning electron images of osteoblasts within a fibre network, showing cell spreading, integration and elongation in the direction of fibre alignment. Arrows indicate cell locations. Reproduced with permission from Stachewicz et al. [131]. **(c)** Matrix fibres between two tumour spheroids, separated by 3mm, imaged using reflectance microscopy. Fibre alignment and localized cells are observed between the spheroids. Reproduced with permission from Sander [132]. 15

1.4 Illustrations of some commonly used discrete fibre network architectures, including **(Left)** Mikado networks, formed from the intersections of randomly placed monodisperse rods, **(Centre)** Voronoi-type networks, given from the edges of a 2D Voronoi partition of the domain, and **(Right)** Diluted triangular lattice, where edge deletion is employed so as to introduce disorder into the network. 27

1.5 A flow chart depiction of the computational algorithm employed to generate Mikado network architectures in this thesis. The inputs for generating Mikado networks are number of fibres N, the fibre length L, and the computational square domain size W. The code outputs the quantities needed to describe a Mikado geometry, namely a list of nodes (cross-links), edges (segments connecting pairs of nodes), boundary points (those nodes that will be subjected to displacements or loads), periodic elements (connections used to fix degrees of freedom between nodes on periodic boundaries) and a fibre list (labelling the fibre to which a node belongs). 29

1.6 Schematics for the generation of a Mikado network. **(Left)** The deposition of fibres with midpoints (red circles) within a domain of area W^2, at orientations θ_i with the x-axis, and with length L. **(Right)** An illustration of the geometric periodicity of the fibres. Fibres exiting the domain on one boundary reappear on the opposite face. On upper and lower boundaries, the locations of fibre-boundary crossings are stored as boundary nodes. When filaments cross left and right boundaries, nodes are placed at these points and a periodic edge is introduced between them, shown in green dash. 30

1.7 An illustration of network generation for the basic Mikado geometry. **(Left)** Fibres are placed in the domain, and geometric periodicity is enforced, such that fibres leaving the domain along one boundary reappear on the opposite edge. **(Centre)** Fibre-fibre and fibre-boundary crossings are identified as nodes, and edges are introduced along fibres, connecting the nodes. Boundary points are introduced where fibres cross upper and lower boundaries (white squares). Periodic edges are introduced between nodes formed where fibres leave the domain on the left and right boundaries (dash lines). Dangling ends, that is the ends of fibres not connected to the greater network structure, are removed naturally at this point. The connected components are identified and labelled (shown in red, blue and green). **(Right)** Only *spanning* connected components, that is connected components that span the domain from top to bottom, contribute to the static elastic moduli of the DFN. Non-spanning components are discarded. 31

1.8 An illustration of the identification and resolution of a pathologically short edge that arises in network generation. Edges that fall below a prescribed minimum length $l_{\text{crit.}}$ are located. The two nodes connected by the short edge are merged into a new node located at the midpoint of the original edge. The short length is removed, whence the algorithm continues to check for short edges. 33

2.1 A visualisation of the local structure and geometry for each model architecture. Details for network generation are given in section 2.2.2. Dual and Voronoi networks share similar topologies, while the network structure of Perturbed architectures is identical to those of Growth networks. 43

2.2 Model domains for computational tests. Displaced boundary nodes are highlighted in red. **(a)** Uniaxial extension of a dual type network. Boundary nodes are displaced horizontally, as indicated by arrows. **(b)** Single cell contraction within a Voronoi network. An interior circle is removed from the domain, and inner boundary nodes are displaced in the radial direction towards the cell centre, with outer boundary nodes fixed. **(c)** Pairwise mechanical cell communication within a dual network. Two interior circles are removed from a network within a rectangular domain. Both cells contract as in the single cell case. The separation distance between pairwise cells is defined to be the shortest membrane-membrane distance. Triangular markers signify zero displacement boundary edges. 49

2.3 Mechanical response of networks under uniaxial extension. **(a)** Engineering stress-strain curves show that Voronoi networks are relatively stiff, while growth cases exhibit the most compliant response. The inset shows the uniaxial test performed. **(b)** The tangent modulus K with strain is plotted for each network architecture. All networks exhibit strain-stiffening, though the onset of strain-stiffening occurs later in dual and growth architectures. Voronoi and perturbed networks display qualitatively similar nonlinear behaviour. **(c)** The orientation parameter Ω_{xx}, defined in the text, increases with strain for all networks, as constituent fibres reorient with the direction of extension. **(d)** Cumulative fibre stretch (λ) distributions within different network geometries at 50% strain underline micromechanical differences, with far fewer strained, and more buckled, fibres present in growth networks than in Voronoi geometries. Bars give 1 s.d. about the mean value. 50

2.4 Displacement fields $|\boldsymbol{U}|$ (µm) due to a contractile cell show clear qualitative differences as network architecture is varied. In particular, largely symmetric fields are observed in Voronoi geometries, while a highly heterogeneous field, involving symmetry breaking, arises in growth networks. Black arrows give displacement vectors for fibre midpoints. Continuous plots here and throughout are generated through natural neighbour interpolation in MATLAB. 54

2.5 Comparison of displacement fields induced by a contracting cell in different architectures. **(a)** Mean displacement $|\boldsymbol{U}|$ is plotted with distance from the cell membrane; long-range effects are observed for all cases considered, though growth networks extend considerably less far. In Voronoi, dual and perturbed networks, mean substrate displacement above 1 µm is observed more than 3 (final) cell diameters distant. Dashed line shows equivalent displacement decay in a homogeneous elastic continuum. **(b)** Asymmetry in cell-derived displacement fields, showing the highly asymmetric fields in growth geometries, and the more symmetric fields induced within Voronoi networks. **(c)** Mean transverse displacement $|U_\theta|$ as distance from the cell membrane increases. Significant transverse motion is present in growth networks, while displacement is largely radial in Voronoi cases. Bars give 1 s.d. about the mean value. 55

2.6 Visualisations of transverse displacement fields $|U_\theta|$ (µm) due to a single contractile cell in each network. Considerable transverse displacements, above 1 µm, are observed in growth networks a large distance from the cell membrane, while displacement fields observed in Voronoi architectures act almost entirely in the radial direction. . 56

2.7 Strain energy density (SED) fields derived from single cells contracting in each network. Highly heterogeneous, shorter ranged fields are observed in growth geometries, while long-range stress transmission to the distant boundary is observed in Voronoi and perturbed networks. In growth networks, clear stress paths extend from the cell membrane to the outer boundary, suggesting that the majority of strained fibres exist within these isolated paths. Note the order of magnitude differences between architectures, as illustrated by log scale colour bars. 58

2.8 The transmission of stress in fibre networks. **(a)** Mean fibre strain energy density (SED) is plotted for maximum cell contraction, showing far greater range of stress transmission in Voronoi and perturbed geometries than in growth or dual networks, with considerable strain energy more than 5 cell diameters distant. **(b)** Cells contracting in Voronoi and perturbed networks experience a far stiffer response than those in growth and dual networks. **(c)** Stress reaches the distant outer boundary in perturbed and Voronoi geometries, even at low cell contraction while in growth networks the distant boundary experiences very little stress. **(d)** Cell contraction leads to the buckling of $\approx 20\%$ of growth network fibres. The more shallow sigmoid found in Voronoi and perturbed geometries suggests that fibre strain is more equally distributed in these networks. Bars give 1 s.d. about the mean value. 59

2.9 Alignment and reorganisation of non-buckled fibres. **(a)** Orientation of fibre families with increasing stretch ratio is plotted, showing a strong correlation between increasing fibre stretch and radial alignment in all networks. The strain distribution in Voronoi and perturbed geometries allows for families of fibres under considerable strain $(1 - 2\%)$ to remain misaligned with the direction of radial stretch. **(b)** Mean rotation (radians) of constituent fibres within a network is plotted. Considerable fibre rotation is observed in growth networks, and far from the cell boundary in dual networks. The geometry of Voronoi and perturbed networks restricts rotation of fibres far from the cell membrane, and encourages stretching of individual network fibres. Bars give 1 s.d. about the mean value. . 61

2.10 Important architecture-dependent differences in network response persist for a range of densities. **(a)** Mean displacement $|U|$ is plotted with distance from the cell membrane, for three cross-link densities. A slight variation, within 1 s.d., is found upon increasing fibre density. **(b)** Cumulative frequency plots for fibre stretch ratio is shown. The distributions remain almost identical under a two-fold increase in cross-link density. As such, the results presented here are sensitive to architecture and appear insensitive to network cross-link density. Bars represent 1 s.d. about the mean value. 62

2.11 Visualisations of fibre strain energy density for pairwise contracting cells at a separation distance of 50 µm = 5 final cell diameters in **(a)** dual, **(b)** Voronoi, **(c)** growth, and **(d)** perturbed networks. Increased strain energy density in the intercellular region is clear in all networks, as evidence by the bright band in between cells. Note the log scale colour bars, underlining order of magnitude differences in strain energy fields. **(b) (inset)** To highlight the presence of SED banding between cells in the Voronoi case, a rescaled plot is included. Logarithmic colour scaling gives one order of magnitude difference. 63

2.12 Visualisations of fibre strain energy density for cells contracting at maximum separation distance 70 µm = 7 (final) cell diameters. **(a)** Increased strain energy between cells is observed for cells contracting in Voronoi networks at a higher separation distance of 7 cell diameters. Inset is a rescaled plot to highlight SED banding between cells. Logarithmic colour scaling gives one order of magnitude difference in this case. **(b)** No such increase is found in growth networks, suggesting that cells cannot robustly communicate mechanically over such distances in this architecture. 64

2.13 Mechanical communication via stress transmission through different network architectures. **(a)** The stress signal at the cell membranes as cell contraction increases is plotted for separation distance of 50 µm = 5 final cell diameters. A robust, stronger signal is observed in Voronoi networks, with weaker, variable signal in growth geometries. Large standard deviation in perturbed cases underlines high network-to-network variability in signal propagation. **(b)** The stress signal at maximal contraction (5 µm) for increasing cell separation is plotted. Voronoi networks produce the largest mechanical signals at all separation distances. Robust stress transmission beyond 5 cell diameters of separation appears to fail in growth networks, as evidenced by the large standard deviation. Bars give 1 s.d. about the mean value. 65

3.1 Schematic of the FEM treatment for a fibre segment, which involves a truss element for fibre extension, and a beam element for fibre bending. 74

3.2 Illustrations of a zoomed-in region of a fibre network under simple shear in the nonaffine (left, large λ_1) and affine (right, small λ_1) regimes. Nonaffine networks (low bending length scale l_b) are bending dominated, with most fibres storing the majority of internal strain energy in bending deformations. In contrast, most fibres in affine networks store energy in stretching modes. Log-scaled colour displays the ratio of stretching energy $\mathcal{H}_{\text{stretch}}$ to the total energy $\mathcal{H}_{\text{fibre}}$ in each fibre segment, while the log-scaled line width displays the ratio of fibre energy to total network energy. More than 99.99% of energy in the nonaffine network is stored in bending modes, while more than 99% of energy is contained in stretching in the highly affine network. 83

3.3 The shear modulus of 2D Mikado networks, normalized by the affine prediction, are shown under two choices of the length scale for affinity λ_i. In both cases the transition between a nonaffine and affine regime are clear. **(Left)** Data collapse for L/λ_1, where $\lambda_1 = (l_c^4/l_b)^{1/3}$, showing excellent collapse for low to high densities, but small deviations for the very highest densities considered. **(Right)** A data collapse is sought under a theoretical prediction for the affine length scale $\lambda_2 = (l_c^7/l_b^2)^{1/5}$. Small deviations from a data collapse are consistently observed across different choices for L/l_c. Reproduced with permission from Head, Levine, and MacKintosh [170]. 84

3.4 The main results of Head, Levine, and MacKintosh [170] are reproduced within our model for both values of the affine length scale λ_i. We reproduce the collapse of data onto a common curve in both cases. However, we note that the deviations from the master curve observed in the original research are not present here for λ_2. The transition between affine and nonaffine occurs at the same point for these affinity lengths, suggesting that our model accurately matches others found in the literature, both qualitatively and quantitatively. 86

3.5 An illustration of the network energy partition as the length scales for affinity λ_i are varied. In particular, we reproduce the result that networks within the nonaffine regime are bending dominated and transition under the length-scale for affinity to stretching dominated. In both cases, the majority of total network energy is stored in either bending or stretching deformations, such that fibre shear contributions are minimal. White markers represent bending energy, while solid black markers illustrate stretching. 87

3.6 Probability density functions for the network fibre segment strain energy densities $\hat{\mathcal{H}}_{\text{fibre}}$. The energy content within nonaffine networks is dominated by a very small family of deformed fibres, while energy is shared far more equally between many fibres in stretching dominated cases. 88

3.7 **(a)** A sample Mikado network, with domain size W. Nodes attached to the bottom boundary are fixed in all degrees of freedom, while those on the top boundary are shifted horizontally to give a small bulk simple shear of γ. **(b)** A closer look at the microstructure of the fully cross-linked Mikado model, showing model cross-links in red, fibres in black and the segment lengths l^0, where 0 denotes quantities in the original network. The mean cross-link spacing is given by $l_c^0 := \langle l^0 \rangle$. **(c)** A partially cross-linked Mikado network is shown for the same sample as in **(b)**. In particular, the proportion of remaining cross-links is given by $p := n/n_0$, for number of cross-links n. Longer fibre segment lengths l are observed than in the fully cross-linked case for equivalent polymer density, leading to a larger value of mean cross-link spacing $l_c :=< l >$. 92

3.8 **(a)** The bulk shear modulus $\mathcal{G}$, non-dimensionalized with fibre stretching stiffness μ and polymer length L, is plotted against cross-link proportion parameter p for varying bending length scale $l_b = (\kappa/\mu)^{1/2}$. Significant reductions in $\mathcal{G}$ are observed for lower cross-link densities (decreasing p) in the higher density case $\rho = 44.9$. In particular, the reduction in shear modulus accelerates as cross-link density decreases. **(b)** The bulk shear modulus is normalized to the value for maximally cross-linked networks, showing similar scaling behaviour as l_b is varied for both low density network types. **(Inset)** Scaling of the shear modulus for high density networks shows the insensitivity of network mechanics to cross-link density except at very low values of p. Colour bar displays l_b. 95

3.9 The scaling of the shear modulus $\mathcal{G}$, normalized by the corresponding fully cross-linked value $\mathcal{G}_0$ is plotted against cross-link proportion parameter. For moderate values of p, we find that the theoretical scaling prediction $\mathcal{G} \sim p^6$ is a reasonable fit, suggesting that our treatment captures the general behaviour of the system well. However, for large $p \approx 1$ or small $p \ll 1$, the scaling diverges. 98

3.10 **(a)** Scaling behaviour of the bulk shear modulus $\mathcal{G}$, normalized by the corresponding affine value, in terms of L/λ_1, where $\lambda_1 = l_c(\frac{l_c}{l_b})^{1/3}$. Unlike in the maximally cross-linked case, there is no data collapse under the length scale λ_1. **(b)-(e)** Density-dependent data collapses are shown for four polymer densities under the proposed length scale λ_c. Colour bar displays cross-link proportion parameter p. 100

3.11 **(a)-(b)** The ratio of bend and shear to stretching energy in networks of two densities is plotted against length scale λ_c, showing a clear transition from bending to stretching dominated deformations. Deviations for those most affine networks (highest L/λ_c) are due to fibre shear energy. **(c)-(d)** The total energy content $\mathcal{H} = \mathcal{H}_{\text{total}}$ of each network is partitioned into the three deformation modes, stretch, shear and bending. In all cases, shear energy forms only a small part of total energy, suggesting that the mechanical network response is largely independent of fibre shearing in this study. Densities and the colour bar are inherited from **(a)-(b)**. Colour bar displays cross-link proportion parameter p. 101

3.12 **(a)-(c)** Cumulative fibre segment strain energy density is plotted, with comparison to the analytic affine prediction (dash line) given in Eq. 3.48. **(a)** Example results are displayed for affine (yellow) and highly nonaffine (blue) networks in the standard Mikado case, $p = 1$. Affine networks more closely follow the theoretical prediction, while nonaffine networks are characterized by the presence of a small family of energetic fibre segments. The same result is plotted for **(b)** affine and **(c)** nonaffine networks as cross-links are removed. In affine networks, the strain energy density distribution is almost constant as cross-links are deleted, until the lowest values are reached, at which point a sudden move to the nonaffine profile is observed. The strain energy density distribution in nonaffine networks appears similarly insensitive to cross-link parameter p, though surprisingly a modest move towards the affine energy distribution is observed for the most sparsely cross-linked nonaffine networks. **(d)-(f)** Cumulative fibre energy content is plotted against proportion of fibres, with parameters inherited from **(a)-(c)**, showing that similar results hold for fibre energy content as for segment energy density. Inset shows the energy fraction of the top 10% of fibres by energy content, highlighting the fact that a small family of fibres contributes a majority of total network energy. Markers are included to distinguish near identical data arising from networks within a given regime. 103

3.13 Displacement measure D, scaled by domain size W and strain γ is plotted against L/λ_c for varying cross-link and polymer density and varying bending length scale l_b, as incorporated in λ_c. The transition between affine and nonaffine deformation is clear from the move between two constant values. This transition occurs at similar values of λ_c as seen for equivalent energy measures of affinity, suggesting that changes in the displacement and energy based measures of affinity are governed by the same underlying physics. As cross-links are removed, we observe larger nonaffine fluctuations in the nonaffine regime for all polymer densities considered. Colour displays cross-link proportion parameter p. 106

4.1 Illustrations of single inclusion composites used in this work. Networks are constructed within square domains of area W^2. Nodes attached to the lower boundary are fixed in all degrees of freedom, while those affixed to the upper boundary are shifted to produce a bulk shear of γ. Periodic boundary conditions exist on left and right boundaries. **(Left)** A Voronoi base network in which an inclusion of length L_i is placed at an orientation of θ_i with the horizontal (x) axis. **(Right)** A Mikado single inclusion composite. The lengths of fibre extents between network cross-links, l, take a mean value of l_c. Wherever fibres from the base network cross an inclusion, a new 'welded' cross-link is formed. The length of Mikado base fibres is denoted by L. 117

4.2 A visualization of the base fibre energy content $\mathcal{H}$, normalized by total network energy $\mathcal{H}_{\text{total}}$, in the vicinity of a single stiff inclusion. The inclusion is oriented at an angle $\theta_i = \pi/4$, and has length $L_i/l_c \approx 180$. When inclusions are neglected, both base networks are located within the nonaffine, bending-dominated regime, with **(Left)** Voronoi networks having $l_b/l_c \approx 10^{-3}$, and **(Right)** Mikado networks having $L/l_c = 43.5$ and $l_b/l_c \approx 10^{-4}$. We take the inclusion to be far stiffer in both stretching and bending, such that the inclusion does not experience significant deformations, with $l_b^i/l_b = 10^4$ in Voronoi cases and $l_b^i/l_b = 10^5$ in Mikado networks. In both cases, the stretching modulus for the inclusion is larger than the base modulus, $\mu_i/\mu_b = 10^3$. Results are averaged over 20 different realisations of the base network. In Voronoi networks, the effect is similar to that expected in a continuum, with base network energy reaching its largest values near the fibre end points, and an absence of energy near the centre of the fibre. Qualitatively similar but less pronounced effects are observed within Mikado composites. 119

4.3 The angular measure of affinity $\langle \delta\theta(r)^2 \rangle$, which quantifies the difference between the rotation of a line formed between two sample locations a distance r apart, and the affine prediction, is plotted for Voronoi and Mikado base networks. **(Left)** In Voronoi base networks the nonaffinity measure remains relatively small, even for networks that are classified as highly nonaffine in terms of bending-dominated energy content. **(Right)** The same quantity is measured in Mikado composites, where we observe that for nonaffine networks (triangle and square markers) the degree of nonaffinity is more than two orders of magnitude larger than the corresponding Voronoi cases. In particular, even at larger probing distances $r/L \approx 1$, the nonaffinity measure is larger than in the Voronoi case at the scale of the fibre segment $r/L \approx 0.06$. As such, the discussion of nonaffinity in terms of both displacement and rotation must be addressed independently of energetic definitions, as the two characterizations decouple for different network architectures. 121

4.4 An illustration of the spatial deviations from the affine displacement field for network cross-links in the base network, $|U - U_{\text{affine}}|/\gamma W$, for stiff inclusions placed at different orientations within Voronoi networks. Inclusion and base network properties are identical to those used in Fig. 4.2. Results are averaged over 20 realisations of the base network. Nonaffine deviations are observed to be largest for inclusion orientations approaching $\theta_i = \pi/4$, and are localized to areas close to the inclusion end points. The locations of largest displacement nonaffinity correspond with regions of greater energy content, as displayed in Fig. 4.2. 123

4.5 The spatial partition of energy in Mikado composite networks is illustrated for the same networks as in Fig. 4.2, displaying the stretching and bending contributions to the total fibre energy in base network segments. No notable increase in stretching contributions **(Left)** along the inclusion body is observed, though base networks do experience a marked decrease in bending energy **(Right)** adjacent to the inclusion. As such, we expect that the observed increase in bend-to-stretch ratio noted elsewhere is instead the consequence of a decrease in bending energy, rather than an increase in base fibre stretching. 124

4.6 The percentage increase in total network energy $\delta\mathcal{H}/\mathcal{H}_0$, where $\mathcal{H}_0$ refers to the total energy content in the base network in the absence of the inclusion, is shown for varying inclusion orientation θ_i. The elastic moduli for the inclusion are taken such that the inclusion is stiff in extension and bending. When Voronoi base networks (stars) are considered, the data closely fit a curve proportional to $\sin^2 2\theta_i$, corresponding to a correction to the affine strain field in the axial direction of the fibre. In Mikado composites (circles), the increase in network energy is asymmetric, with a larger increase observed for vertical ($\theta_i = \pi/2$) than for horizontal ($\theta_i = 0$) fibres. Introducing a term proportional to $\sin^4 \theta_i$, accounting for the affine rotation angle, allows for a good agreement with the observed data. In Mikado simulations, there is a notably greater increase in network energy in the presence of a stiff inclusion, even for horizontal fibres, where rotational and axial contributions predicted in scaling theories vanish, owing to the suppression of larger nonaffine fluctuations. 127

4.7 The scaling of the change in total network energy $\delta\mathcal{H}/\mathcal{H}_0$ with inclusion length L_i is plotted, for both Voronoi **(Left)** and Mikado **(Right)** base networks within the nonaffine regime. The change in energy for non-fibrous, Voronoi base cases scales according to L_i^2, as expected for an axial correction to the affine displacement field by the stiff inclusion. A weaker dependence is noted for Mikado base networks. In particular, for longer inclusions $L_i/l_c > 150$, the scaling with L_i is approximately equal to $L_i^{1.57}$. For shorter inclusions in Mikado networks, this scaling reduces to close to unity. 131

4.8 The percentage increase in total network energy for Voronoi composites is investigated as the inclusion stretching modulus μ_i varies. **(Left)** The increase for four different parameter choices for the base network density and bending stiffness as well as for the inclusion length are considered for varying μ_i, normalized by the base fibre rigidity μ_b. We note the existence of a transition, where above a critical value μ_c of the inclusion stretching stiffness, further increases do not lead to likewise rises in total network energy. **(Right)** The same results are rescaled under the theoretical prediction for the critical value μ_c, with the increase in network energy normalized by the square of the inclusion length. We observe an excellent data collapse under this critical value, suggesting that the scaling arguments discussed capture the physics of this transition. In all cases, the bending rigidity of the inclusion is taken to be sufficiently large to avoid any significant deflections. 132

4.9 The percentage increase in total network energy for Mikado composites is investigated as the inclusion stretching modulus μ_i varies. **(Left)** Similar transitions under varying μ_i are observed in Mikado composites as in Voronoi cases, shown for four different parameter choices for the base network density and bending stiffness as well as for the inclusion length, normalized by the base fibre rigidity μ_b. **(Right)** The results are rescaled under the corrected prediction for the critical value μ_c in Mikado composites. By considering a corrected critical stiffness μ_c in the presence of additional contributions from Mikado base fibre length, we achieve a data collapse such that the transition for all composites considered occurs under the same values of μ_i/μ_c. We note that for equivalent base fibre bending stiffness this transition occurs at larger values of μ_i than in Voronoi composites. . 135

4.10 The scaling of the total network energy increase with increasing inclusion bending stiffness κ_i is investigated for Mikado composites under three sets of parameter choices within the nonaffine regime. Similar to the results for varying the inclusion stretching modulus, we again observe a transition to a plateau region, in which further increases to the bending rigidity do not lead to likewise energy increases in the total network energy. The percentage energy increase is scaled according to this plateau value $\delta\mathcal{H}_{\kappa s}$, while the fibre bending stiffness is scaled according to the critical value κ_c predicted from scaling arguments. A good data collapse is observed across the three parameter sets, with the network energy increase scaling close to the $\kappa_i^{1/3}$ predicted. **(Inset)** The same transition is considered for Voronoi composites. Here, the change in percentage network energy increase is small (below 1%) over 12 orders of magnitude in the inclusion stiffness, such that the inclusion bending rigidity is not likely to be a dominant factor in determining the energy increase in Voronoi composites. 136

5.1 Examples of composite networks used in this work. Fibre networks are generated within square domains of area W^2. Nodes on the upper boundary are shifted to produce a bulk small shear strain γ, while nodes on the lower boundary are fixed in all degrees of freedom (d.o.f). Periodic boundary conditions apply on left and right boundaries. **(a)** A Voronoi base network to which a low density ρ_i of rigid inclusions, length L_i, have been added. **(b)** A Mikado composite with high inclusion density. The base network is comprised of Mikado fibres of length L, where $L_i/L = 2$. A closer look at the microstructure is shown, displaying segment length l; throughout $l_c := \langle l \rangle$. Where inclusions and base fibres intersect, a permanent cross-link is formed, but no direct connections between inclusions exists, that is inclusions are not cross-linked with each other. 150

5.2 The scaling of the bulk shear modulus $\mathcal{G}$ with the ratio of bending length scale l_b and mean segment length l_c in Voronoi (star) and Mikado (circle) composite networks, normalized by the affine prediction $\mathcal{G}_a$ (indicated by dash line). While both network types undergo a bend-stretch transition, coinciding with a move towards more affine displacements, this transition occurs at smaller values of l_b/l_c in Mikado networks, due to the presence of the additional length scale L of the fibres. Within the nonaffine regime, both networks scale linearly with bending stiffness κ. The slight increase in shear modulus within the affine regime is due to fully welded, rather than rotating, cross-links being employed, whence exact affine deformations are precluded. 152

5.3 The scaling of the shear modulus of composite networks with the bending length scale l_b, normalized by mean segment length l_c, is plotted for composite networks of both types, as the density of stiff inclusions ρ_i is increased, normalized by the affine shear modulus of the base network. As inclusion density increases, Mikado architectures **(Left)** rapidly lose their linear dependence on κ, with even a small density of inclusions leading to a greatly reduced sensitivity to fibre bending rigidity. While networks without inclusions experience an increase in stiffness of approximately 5 orders of magnitude over the bending rigidities considered here, this is reduced to a below 100 fold increase for composites with inclusion density $\rho_i \approx 4$. In contrast, despite a jump in the stiffness of Voronoi composites **(Right)** as inclusions are introduced, a close to linear dependence on κ persists until the number of inclusions becomes far greater. Even for the highest inclusion densities considered, a greater than 100 fold increase in stiffness is observed in nonfibrous, Voronoi cases as the bending length scale l_b increases. These observed architectural differences disappear within the affine regime, with both composite types behaving similarly, as expected. These results suggest that outside of the affine regime, the bending length-scale of the base network is insufficient to determine the scaling behaviour of the shear modulus. Colour bar gives inclusion density ρ_i. 155

5.4 The scaling of the composite shear modulus $\mathcal{G}$ with base network affinity $\mathcal{G}_0/\mathcal{G}_a$ is plotted. Clear differences in the scaling behaviour of the shear modulus are observed for curves of equivalent inclusion density, and for equivalent affinity in the base networks. In combination with Fig. 5.3 this suggests that neither the mechanical properties of the constituent biopolymers, nor the bulk network affinity are sufficient to explain the mechanical differences observed between composites formed from different network architectures. 157

5.5 A visualisation of the ratio between total stretch and bending energy content in composite networks comprised of different inclusion densities, and for increasing l_b/l_c. Even at low inclusion densities, Mikado networks with nonaffinely deforming bases become stretch dominated. In contrast, Voronoi composites do not become stretch dominated, even at the highest inclusion densities considered, but remain marginally bend dominated until the base network enters the affine regime. Colour bar displayed inclusion density ρ_i. **(Inset)** The ratio of stretch energy in the composite base network to that in the zero density case, $\Theta\mathcal{H} := \mathcal{H}_{\text{stretch}}/\mathcal{H}^0_{\text{stretch}}$, showing many order of magnitude increases in the stretching contributions for nonaffine Mikado base networks. Parameters for square, triangle, side-triangle, diamond, dot and circular markers in the inset plot are for $l_b/l_c \approx 9.4\times10^{-6},\ 2.5\times10^{-5},\ 6.8\times10^{-5},\ 1.8\times10^{-4},\ 4.9\times10^{-4}$, and 9.4 respectively. 158

5.6 The total energy content of the stiff inclusions $\mathcal{H}_i$, normalised by the affine energy prediction for the whole network $\mathcal{H}_a$, is shown for increasing l_b/l_c, showing many order of magnitude differences between the two architectures. Inclusions within Mikado composites appear to contain significant energy, suggesting that the base Mikado network is able to deform the rod-like inclusions. In contrast, far less energy is stored in the stiff inclusions in nonfibrous cases, even at the highest inclusion densities ρ_i. **(Inset)** The ratio of inclusion energy in Mikado ($\mathcal{H}_m$) and Voronoi ($\mathcal{H}_v$) composites for equivalent ρ_i and l_b/l_c is shown, clarifying the marked differences between the energetics of the inclusions in the different architectures, despite identical inclusion geometry and constitutive choices being used. . . 159

5.7 Visualisations of the spatial energy partitions in Voronoi and Mikado composite networks. Here $\mathcal{H}_{\text{bend}}$ and $\mathcal{H}_{\text{stretch}}$ are defined through Eq. 3.38, while $\mathcal{H}_{\text{fibre}}$ refers to the sum of all energetic contributions in a fibre, and $\mathcal{H}_{\text{total}}$ is defined through Eq. 3.39. The base networks in the absence of inclusions are nonaffine and bending-dominated. In Voronoi networks, bending remains the predominant mode of energy storage, with energy concentrated towards the ends of inclusions. In contrast, large regions of Mikado composites become stretch-dominated in the presence of the stiff inclusions. Regions displaying low inclusion density experience no such rise in stretch energy, while regions with adjacent inclusions experience the largest increases. We hypothesize that the geometric fibre persistence, that is the additional length scale L present in Mikado networks, allows for individual base fibres to 'cross-link' the stiff inclusions, explaining the rapid transition at low inclusion densities from bend- to stretch-dominated Mikado composites. 162

5.8 The dependence of the composite shear modulus $\mathcal{G}$ on the base stretching stiffness μ in Mikado composites of density $\rho_i \approx 6$ is investigated, for base networks within the nonaffine regime. The bulk stiffness is observed to scale as $\mu^{0.86}$. This is in contrast to the monotypic base cases, where no such dependence is expected. **(Inset)** The analogous scaling with bending rigidity κ is also investigated, displaying a striking insensitivity to this parameter. 163

5.9 An investigation of the percolation threshold for double-fibre Mikado networks, where each fibre can only cross to those of the opposite type. **(Left)** The probability of observing a network which percolates across the domain from lower to upper boundaries is shown, calculated by averaging over 500 simulations for each inclusion density, and each base fibre length L. Base polymer density $\hat{\rho}$ is held constant. As base fibre length decreases, percolation occurs at higher inclusion densities. This is accompanied by a broadening in the transition region. **(Right)** The total length of the percolating cluster $\sum l_{\text{perc.}}$ is investigated for the same parameters as used for the left-hand plot, nondimensionalized by constant domain size W. In all cases we observed that the growth of the cluster becomes linear following an initially rapid increase. The cluster grows more slowly for shorter base fibres. Dotted lines display the extrapolated linear growth for inclusion densities beyond those simulated, assuming a constant linear growth. 165

5.10 The ratio of composite to base network stiffness $\mathcal{G}/\mathcal{G}_0$ is shown with increasing inclusion density ρ_i. Results are shown for varying values of l_b/l_c, highlighting that exceptional stiffening is most pronounced in nonaffine cases. In both networks, the increase in network stiffness with inclusion density is large. The most rapid increase in stiffness occurs at different inclusion densities in each of the base architectures considered. In Mikado composites, this stiffening occurs at very low inclusion densities, while there is a pronounced increase in the shear modulus of Voronoi composites near to the percolation threshold of the inclusions. Taken alongside Fig. 5.9, the exceptional stiffening effect coincides with double-fibre network percolation. Within the affine regime (small circles), the stiffening effect is modest in both composite types, as expected for networks that are already stretch-dominated. 166

5.11 Probability density functions for the occurrence of fibre segments containing given energy densities in Voronoi and Mikado composites. Results are displayed both for the zero-inclusion base case $\rho_i = 0$, and higher density $\rho_i = 6$ as used for the spatial energy partition in Fig. 5.7. We observe a slight shift towards higher energy densities in Voronoi networks as inclusion density increases, along with a broadening of the energy density profile. A similar broadening in the energy density profile is noted in Mikado composites. However, an additional peak in higher energy densities arises, which we attribute to the sub-family of base fibres which stretch when 'cross-linked' to the inclusions. 167

5.12 The percolation phenomenon is investigated for networks in which inclusions are placed at a constant orientation $\theta_i = \pi/4$. **(Left)** Longer fibres still exhibit relatively sharp transition regimes, moving from percolated to non-percolated over a small increase in inclusion density. However, for short fibres, the transition region becomes large, and knowledge of the fibre network parameters are insufficient to infer whether the network is percolating or not. **(Right)** The total polymer length in the connected spanning component is measured. In all cases the clusters grow more slowly than in the random cases, again approaching a linear regime for inclusion densities above the percolation threshold. 168

5.13 The stiffening effect with inclusion density is quantified for aligned inclusions $\theta_i = \pi/4$ in Voronoi and Mikado networks. Networks are categorized according to whether a percolating cluster of base-inclusion fibres spans the domain, with solid black markers representing nonpercolating networks, and white indicating percolating cases. In Voronoi networks, the exceptional stiffening observed for random inclusions is now absent, leading to a ≈ 30 fold increase in the shear modulus, in comparison to the far greater factor 10^4 increase previously observed in random Voronoi composites. In fibrous, Mikado composite examples, a jump in network stiffness is observed at the percolation threshold, leading to far greater stiffness increases for equivalent inclusion densities. Background gradient displays the probability of percolation, from Fig. 5.12. 170

List of abbreviations and notation

Provided below is a summary of many of the variables and acronyms used within this thesis

1D, 2D, 3D	One, two, or three-dimensional, referring in this thesis to spatial dimensions.
DFN	Discrete fibre network, referring to models in which a fibre network structure is explicitly realised.
ECM, ICM	Extracellular or Intracellular matrix, referring to the collection of molecules inside and outside cells.
FE/ FEM	Finite element/ finite element method.
$\mu,\ \kappa$	The stretching and bending stiffnesses for a filament.
$E,\ G_f$	Young's, shear moduli for a filament
$A,\ I$	The area and second moment of area for a filament.
$\mathcal{G}$	Network shear modulus.
L	(Initial) fibre length.
$l,\ l_c$	Distance between two cross-links, and the mean of this value.
W	The width and height of a square computational domain.
$\mathcal{H}$	The energy content within a fibre or the whole fibre network.
$\rho,\ \hat{\rho}$	Network density measures.
$\lambda_1,\ \lambda_2$	Affine length scales.
l_p	Thermal persistence length.
l_b	Bending length scale.
$z,\ \langle z \rangle$	Node coordination number and the mean of this value.
$\mathbf{X}, \mathbf{x}$	Spatial coordinates.
$\epsilon,\ \gamma$	Extensional and shear strains.

1 Introduction

1.1 Context

The development of mathematics that can accurately describe the deformations, forces and flows arising in the physical world has afforded a profound understanding of, and control over, our environment. Indeed, in the centuries following Robert Hooke's pioneering proposition that *Ut tensio, sic vis*, as the extension, so the force, the ability of the mathematician and physicist to model the responses of solids and fluids to external stimuli has expanded greatly. The mathematics developed to capture the behaviour of solids under deformation has allowed for an understanding of rubber elasticity and finite deformations, while theoretical contributions in polymer physics and thermodynamics has provided physical explanations for experimentally observed behaviours. An understanding of materials subjected to large strains has been accompanied by novel research into the irreversible deformation of materials through plasticity theory, and the modelling of fracture mechanics has granted a better understanding of material failure. While progress has accelerated in the field of solid mechanics, the mathematical treatment of fluid dynamics has equally contributed a remarkable understanding of the many compressible and incompressible flows observed in liquids and gases. Here again, complimentary research from physicists and in the statistical mechanics world has enabled a more

comprehensive understanding of observed physical phenomena. These advances have altered the human experience to a remarkable extent, allowing for constructions of increasing complexity, novel materials with curious and desirable properties, and even new forms of transportation.

Despite their great success at scales visible to the human eye, continuum descriptions of the physical world do not offer a complete understanding of the mechanical behaviours exhibited by many solids and fluids central to life. A further quotation from Hooke emphasises that the triumphs of these continuum descriptions should not preclude more detailed models of living matter, the complexity of which we now understand extends to length scales far below those visible to the naked eye.

> '*... by the help of microscopes, there is nothing so small, as to escape our inquiry; hence there is a new visible World discovered to the understanding*' [1].

This visible, yet hitherto *invisible* world has proven not only to be fascinating, where structures at the nano- and microscales display exquisite complexity, but is also enlightening, with new physics and mathematical modelling required to understand its foreign behaviours. In this thesis it is the microscale world whose mechanics we shall concern ourselves with. In particular, we aim to investigate the micromechanics of one particularly complex and intricate example, namely biological fibre networks. Here, assemblies of filaments form fascinating structures and architectures across many scales and in a diverse range of animal and plant species. Of course, capturing the inherent complexity encountered here precludes quite such elegant rules as those presented in the 17$^{\text{th}}$century, but we are instead rewarded with a rich and exotic range of behaviours. We aim to embrace this complexity, through detailed models for these *biopolymer networks*. The desideratum in such efforts is to gain insights into the mechanics of the living world at the micro- and nanoscales, and (where advantageous) to replicate these mechanics in novel material designs.

A surprising number of materials, both synthetic and organic, mundane and exotic, exhibit complex fibrous structures at their smallest length scales. The fibrillar building-blocks of these assemblies are *biopolymers*, naturally occurring

polymers of which well-known examples are DNA, filamentous actin (F-actin) that grants cells much of their mechanical stability and motions [2], and various types of collagen, found in cartilage, bone and extracellular spaces [3]. The utility of the behaviours exhibited by these fibre networks has attracted the attention of researchers who are keen to reproduce their characteristic mechanics for use in new materials, or in understanding how their properties contribute to some of the fascinating behaviours observed in biological systems *in vivo*. Synthetic examples of fibre networks are found in battery electrodes and various types of paper [4, 5]. Fibrous assemblies are observed with particular frequency in Nature, with common examples including wool, chitin, wood, bone, cartilage and spider silk [6]. That fibrous microstructures arise so frequently in biology is itself of interest, suggesting that advantages are conferred to materials formed in this way.

Research into micro- and nanoscale networks has illuminated new physics that explain their behaviours, where the length scales involved require characterisations that are not relevant to larger scale network structures [7]. Improvements in microscopy have allowed for the generation of remarkable and revealing images for these geometrically detailed and often multiscale networks, from structures at the nanoscale, such as those found within epoxy resins, to microscale biological examples such as the collagen scaffold around cells and tissue [8]. With rapidly improving 3D printing techniques, polymer electrospinning devices, and advances in the understanding of the cross-linking agents that allow fibres to associate into larger structures, we are increasingly able to generate a multitude of biological microsystems within laboratory environments [9]. Here, the material properties, molecular constituents, the microstructure, and any fluid phases can all be controlled to assess their contribution to the local and bulk mechanical properties of the biopolymer network [10]. To accompany these exciting advances in experimental platforms, we require increasingly detailed theoretical and computational models, which can facilitate a more thorough understanding of the physical system, and aid in the design of synthetic tissues and substrates.

As mentioned above, it is prudent to ask why it should be that fibrous networks and their related systems arise so frequently in Nature. The answer in part might be given through their material properties, which can often seem counterintuitive in the context of our macroscopic world. For example, biological networks can often offer an attractive compromise between stiffness and toughness, able to balance both desirable properties through their microstructure [11]. Similarly, they might be stiff for their light weight, as observed in spider silk [12]. This allows for a form of mechanical 'bet hedging', where materials can provide a compromise between for example the protective accommodation of damage and the failure of constituent fibres or cross-links, and the preservation of mechanical integrity and stiffness. Biopolymer networks confer further desirable properties in their adaptability. Indeed, these fibre assemblies, like their host systems, are rarely static objects that retain a given structure over long time scales. Instead, they are better viewed as dynamic and active systems that allow for significant remodelling according to both local and bulk requirements. This is observed in the realignment of fibres with a load direction, leading to increased stiffness along that axis, or in the sequestering of fibres by mechanically active cells embedded within a substrate [9, 13]. It is also observed in the binding and unbinding of cross-links, leading to fibre networks that can quickly transition between solid and liquid phases, and in networks that involve the dynamic bundling and unbundling of fibres, as observed in the formation of stress fibres within cells [14]. This ability to adapt to fluctuating surroundings is vital to the proper functioning of many biological systems.

The network systems that have motivated this thesis are often intrinsically multiscale, a property that can frustrate the modelling of their mechanics, geometry and function. By way of an example, consider a chondrocyte cell embedded within articular cartilage. The intracellular matrix (ICM) of the chondrocyte comprises nanoscale biopolymers, such as actin, vimentin and tubulin, which allow for the mechanical stability of the cell in an environment that experiences varying stresses [15]. This cell is embedded and integrated within cartilage, formed from collagens and other molecular constituents. Locally, different matrices with varying functions,

such as territorial or pericellular matrix, regulate the loads experienced by the chondrocyte, with important consequences for cell viability [16]. At larger length scales, organised structures that have important consequences for the mechanical functioning of the tissue are observed. Famous examples of this ordering are found in the Beninghoff arcades, where elastic fibre alignment varies according to the depth within the cartilage tissue, leading to organisation across scales that are orders of magnitude greater than those associated with the networks within the resident cell [17]. While remaining mindful of the different length scales of the constituent structures, we must also consider *heterotypic* networks, where several polymer types interact, and multiple time scales, which may contribute further towards the complexity of the system under investigation. Unfortunately, it cannot always be assumed that these different scales may be trivially separated and studied independently. Many systems involve processes that span many scales, such as the long-range mechanical sensitivity of certain cell types, the remodelling of networks experiencing active forces, or the presence of long range correlations in networks formed from long fibres [18, 19]. When viewed holistically, this complexity can prove a formidable challenge to overcome in modelling. However, there is always an important and critical place for models that can isolate, characterize and investigate potentially relevant mechanics and physics, all the while maintaining a cautious view of how the constituent parts of such systems combine to generate different behaviours.

In the systems discussed above, it is increasingly clear that topology and geometry are important regulators of a network's biological function. Consider for example a fibre network placed under extension. It has been observed that constituent fibres will rotate and realign with the direction of loading, such that a network that is initially isotropic and random in fibre orientation might become anisotropic and structured. In this example, it is the discrete geometry of a network that facilitates a desirable adaptivity in the biological system. Further, the topology of a filament network can result in dramatically different stiffness properties through the regulation of its connectivity, where the removal or introduction of cross-links can

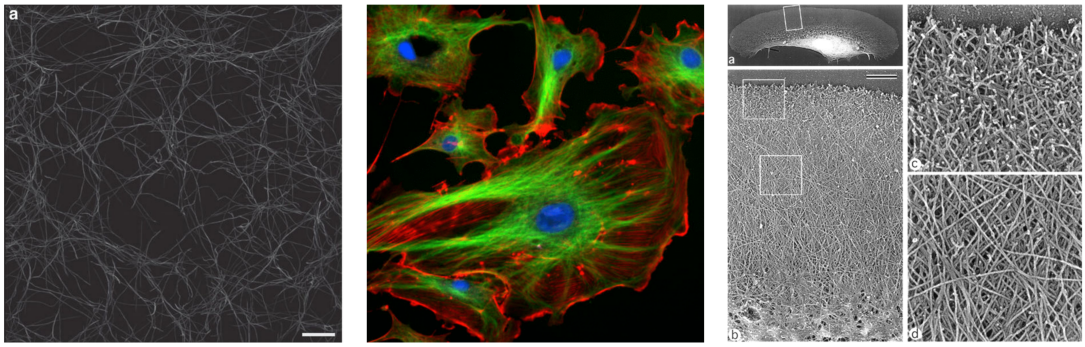

(a) (b) (c)

Figure 1.1: Microscopy images displaying some examples of biopolymer networks found in Nature. **(a)** Three-dimensional confocal microscopy image of a collagen type-I network, reproduced with permission from Beroz et al. [20]. **(b)** The intracellular F-actin network (red) in bovine pulmonary artery endothelial cells is displayed through fluorescence microscopy. Microtubules are shown in green, spanning the cell from the nucleus (blue) to the cell periphery. Image taken from ImageJ under public domain, at http://rsb.info.nih.gov/ij/images/. **(c)** Electron microscopy of actin filaments in keratocyte lamellipodia, showing the branching 'brush-like' region towards the cell leading edge (top right) and the smooth fibre network towards the lamellipodium centre (bottom right). Reproduced with permission from Svitkina et al. [21].

locally fix or release local fibre strains. Indeed, the observation that cells respond to the local stiffness of their substrate, and that fibrous substrates can adapt so as to regulate their stiffness through functional geometries, is a fascinating example of the relevance and utility of network structures in Nature [15, 22]. The geometric and topological features in filament networks should be discussed in light of the aforementioned multiscale nature of biopolymer systems, where networks that might appear locally random may be structured at larger probing scales, and vice versa. How structural properties, such as network geometry and topology, can lead to variations in the mechanics of fibrous systems will be the central theme of this thesis.

Given the size and scope of the field of biopolymers and their networks, with its diverse applications and wealth of distinct biological examples to draw upon, it is perhaps unsurprising that it has attracted an impressive literature of modelling efforts, including experimental, theoretical and computational research. While *in vitro* work has highlighted many remarkable properties of polymer networks, theoretical investigations have sought to provide predictive tools with which to

classify the responses of fibrous architectures within common frameworks. Within these frameworks, one can then explicitly vary the constitutive choices for the polymers considered, the network architecture and topology, potential cross-link agents and their behaviours, and the spatial dimensionality of the problem. The results of this theoretical and computational work have lead to influential predictions and discoveries that have impacted the experimental view of these systems. There is, of course, no single correct approach, and the modelling paradigm employed must always be selected for its suitability in addressing the question under investigation, as well as the tractability of the problem.

We have discussed the ubiquity, complexity, function and desirable mechanics present in many biopolymer network systems; this thesis is motivated by the need to approach these attributes with suitable models and theory. In particular, we shall focus on the structural properties of the fibre networks, and how varying structural parameters, including cross-linking, architecture, and constitutive properties affects the local and bulk mechanics of the biopolymer system. While we largely draw motivation from examples found within biological systems, we intend the scope to remain general enough such that much of the work presented here may also be relevant to researchers from other fields. Given the previously discussed geometric and topological intricacies of the relevant biological systems, we aim to produce models that are able to probe the effects of geometric variability. In particular, we aim to gain as much geometric resolution as possible, within the computational limits afforded by the problem. Thus the goals of this thesis are two-fold. Firstly, we intend to illuminate where geometric features are functional to the biopolymer system, and to elucidate the physics of the system in the context of this geometry. Secondly, we hope that much of the work here will serve as a foundation and motivation for future models, either continuum or discrete; only once the effects of the microstructure are better understood can they be correctly incorporated (or safely neglected) in other models.

1.1.1 Biopolymers and their networks

Biopolymers refer to polymers, that is long strands of molecules formed from repeating subunits, that occur in Nature, as opposed to well-known synthetic polymers such as polystyrene or nylon. Within this thesis we shall primarily be interested in biopolymers whose filaments assemble into larger structures, such as bundles or networks. Such networks may be entangled [23–26], where interweaving fibres grant the network viscoelastic properties, or cross-linked, either covalently through cross-linking agents such as filamin [27] or fascin [28, 29], by motor proteins such as myosin [30, 31], or through other means, such as ionic bonding [9, 32]. We concern ourselves only with permanently cross-linked structures, such that we neglect some of the behaviours observed in certain biopolymer networks with transient cross-linking [33]. Cross-linked networks have been subject to growing interest in recent years due to their interesting and novel physics. A prominent, and now famous, example of these remarkable properties is the observed 'negative Poynting effect' exhibited by many fibre networks under simple shear [13, 34, 35]. This result, where the shear plates move together, is the opposite of what is observed and predicted for many materials; in continuum modelling, pure and simple shears applied to hyperelastic materials lead to expansions between the shear plates, provided that certain inequalities hold [36]. This suggests that exotic mechanical responses can emerge in biopolymer network systems, either from the mechanical properties of the biopolymer filaments themselves, or from the network structure in which they have been arranged. Further interesting and well-characterized behaviours include pronounced strain-stiffening [37–39]; remodelling, rearrangement and alignment of the constituent fibres under loading [40, 41]; and softening under compression [42–44].

Biopolymers exist across many scales, from nanoscale instances, such as RNA and DNA, up to those examples visible to the human eye, such as a spider's web. Before we discuss specific biopolymer examples in further detail, we first discuss a broad classification of polymers, which frames these differences in scale in terms of a quantity known as the thermal persistence length ℓ_p [45]. This quantity measures

the length over which tangent-tangent correlations decay as e^{-l/ℓ_p}, where l denotes some distance along a polymer chain, and ℓ_p is given in terms of the temperature T, the bending stiffness of the polymer κ and Boltzmann constant k_B as $\ell_p := \kappa/k_BT$. Consider a polymer segment of length l_c, either between entanglements and network cross-links, or free and unconstrained. Those polymers for which $\ell_p \gg l_c$ are termed 'stiff'; they appear straight and thermal forces do not feature significantly in the mechanics of the polymer. Under certain network conditions and temperatures, collagen fibres can be modelled as lying in this regime, as can microtubules [46–48]. In contrast for 'flexible' polymers, for which $\ell_p \ll l_c$, entropic forces dominate, encouraging the collapse of the polymer chain into a random coil. In particular, if one is considering a flexible polymer network, tangent correlations do not persist through network cross-links. Well-known examples include DNA, molecular collagen, and polyacrylamide [3, 49, 50]. In between these regimes are 'semiflexible' polymers, $l_c \approx \ell_p$ [51]. Here, the backbone stiffness of the polymer just out-competes the tendency of the filament to collapse into a random coil, resulting in straight polymers that experience thermal undulations. Many interesting behaviours arise from this regime, to which many well-known biopolymers and their networks belong, including F-actin, keratin, vimentin and many other intermediate filaments [2, 52–54]. While the above descriptions are often used in reference to the polymer chains and fibres in which we are interested, it is important that when describing a biopolymer network, we consider the system holistically. Here, temperature differences [55], fluid phases [56], and cross-linking agents [33, 57, 58] can all affect the structure and properties of the material architecture, such that the classification of a network may be nontrivial.

One important and well-studied example of a semiflexible fibre assembly is provided in the cytoskeletal networks within cells. This intracellular matrix is comprised of an F-actin network, which may be entangled [59], or may include other elements such as filamin [27] and myosin [60], to produce a mechanically stable network structure. Actin filaments are considered microfilaments, and exist within the semiflexible regime, with experimental measurements giving persistence lengths 17μm, contour length ≈ 20μm and diameter ≈ 7nm [51]. Actin networks can be

active, capable of dynamic remodelling, and are observed to align in the direction of stress and strain [61, 62]. The ability for F-actin to form large bundles, known as stress fibres, which can span the cytoskeleton and provide tensional homeostasis, is vital for cell rigidity and mechanical action [14, 15]. In motile cells, these stiffer actin bundles allow for cell migration, and enable cells to respond sensitively to mechanical cues in their local environment [63]. Stress fibres interact with the wider actin network within the cell, such that the ablation of some stress fibres leads to complex relaxation and remodelling effects [64]. A microscopy image displaying the intracellular F-actin network of endothelial cells is shown in Fig. 1.1 **(b)**. The actin networks within cells are also responsible for cellular protrusions, such as filopodia [65, 66], where an actin treadmill from the ICM can lead to protrusions extending over many cell diameters [67], and lamellipodia, where a planar actin network extends from the leading edge of the cell, allowing for rapid cell motility [68, 69]. An example of the complex, branching morphology of the actin network in a lamellipodium protrusion is shown in Fig. 1.1 **(c)**.

Another biopolymer vital to human physiology is fibrin, which plays a key role in blood clotting. This biopolymer forms when fibrinogen in the blood stream is exposed to thrombin [70, 71]. The resulting filaments have notably large failure strains, and exhibit strong strain-stiffening, as well as being far more compliant to bending deformations than might be predicted from their diameter [72, 73]. These filaments can form the network structures in which the fibrin network interacts with other cellular and blood materials to occlude flow [74, 75]. Indeed, given their *in vivo* function in forming clots to prevent the flow of blood, fibrin networks possess a toughness not readily found in classical materials [72, 76, 77]. This desirable toughness must then be overcome when it is necessary to induce lysis of the clots after their physiological purpose has been fulfilled, else the host risks thromboses [78, 79]. In recent years, fibrin has proven to be a useful and important substrate for experimental platforms [80–82], while fibrin scaffolds, that is engineered biopolymer networks formed from fibrin, have been used to treat cardiac [83] and liver [84]

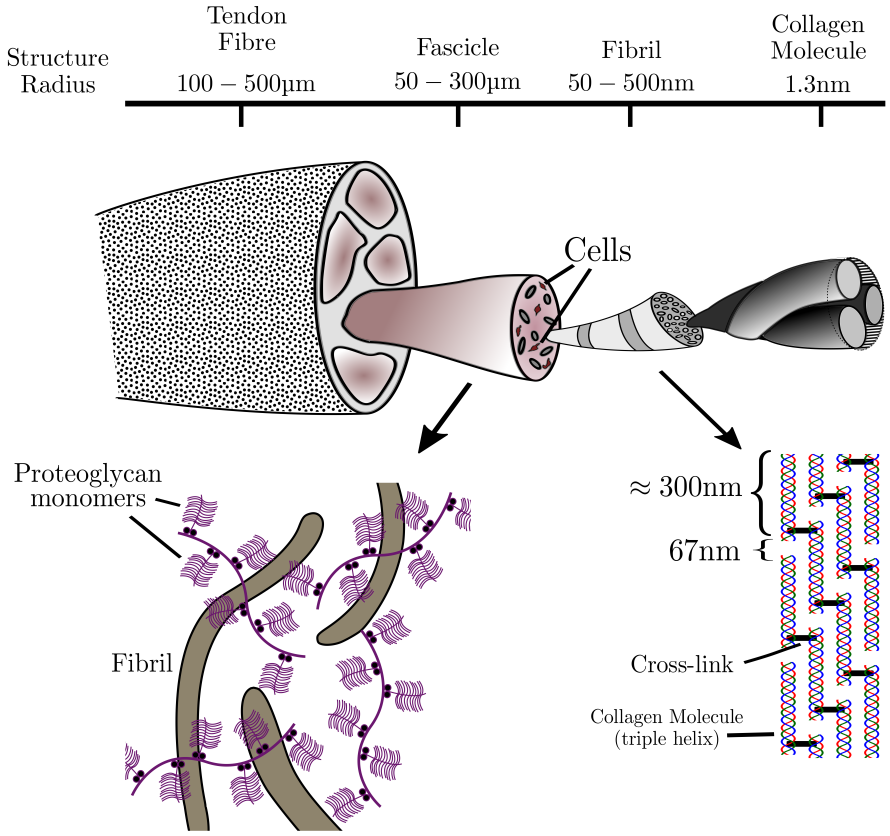

Figure 1.2: A schematic of the hierarchical structure of tendon, illustrating the organisation of biopolymers and their networks at a range of length scales. Individual collagen molecules cross-link in a triple helix structure. These collagen molecules are themselves cross-linked into collagen fibrils, where there are periodic gap regions, of approximately 67nm. At larger length scales, the collagen fibrils are structured within a flexible proteoglycan matrix in the fascicle, where cells, such as tenocytes, may be present. The bundling together of several fascicles produces the tendon fibre. As such, structure exists from the nanometre to the hundreds of micrometres scales.

injuries. Similar to observations from actin networks, fibrin gel microstructure can influence both the bulk mechanics and the local micromechanics [73, 85].

The most abundant protein in the human body by mass is collagen, with humans estimated to possess approximately 10^{21} collagen I monomers [86]. In total, 28 types of collagen have been identified, of which five are fibrillar [3]. The fibres that form have a hierarchical structure that can span many length scales. In particular, collagen chains combine to form a triple helical tropocollagen molecule. These in turn combine to form fibrils. For example, in tendons, the grouping together of fibrils, along with proteoglycans and cells, generates fascicles, several of which

can bundle together to produce a tendon fibre [3, 87]. This multiscale structure is illustrated in Fig. 1.2. Networks of collagen fibrils or fibres are found in many locations throughout the body. In particular, a collagen network forms the primary structural, load-bearing component of extracellular matrix (ECM), a complex and hierarchical material that forms the non-cellular component of tissue [8, 88, 89]. Collagen network mechanics vary drastically depending on their function and architecture [90, 91]. In ECM, initially random fibres are often observed to align with mechanically active cells, and densify at their periphery [9, 92, 93]. Similar alignment to that observed in other biopolymer networks is observed when collagen gels are subjected to strain [40]. In cartilage, of which the primary component is collagen, the fibre network must be robust to repeated loading and unloading, and possesses a particular structure to accommodate this task, as seen in the Beninghoff arcades [94, 95]. Likewise, the organic component of bone and teeth consists of collagen matrix, where architecture and structure again influence the network function [96, 97]. The importance of network organisation in collagen matrices is highlighted in pathologies that stem from their disordering, as seen in cartilage [98], fibroses [99] and scar tissue [100]. An example collagen network is displayed in Fig. 1.1 **(a)**.

The biological examples discussed above illustrate the spectrum of biopolymers, and the diverse systems within which they arise. In particular, they serve to highlight the important physiological functions they perform within the human body, and how frequently biopolymer networks are observed to be critical for the correct mechanical behaviour of a system. We have not discussed in detail those non-human biopolymers, or their important functional properties, as observed in chitin or spider silk [101, 102]. The biopolymer assemblies discussed are intended to highlight the multiscale nature of fibre networks within the body, as well as their ubiquity. We also note that we have largely discussed monotypic biopolymer networks, that is those formed from a single biopolymer type; many *in vivo* examples occur instead as complex composites, where fibres formed from distinct proteins act together to generate even richer behaviours [103, 104]. How these networks interact across different scales,

and how heterotypic examples behave differently from single polymer networks, is a question of even greater complexity in an already intricate and involved field.

1.1.2 Interactions between cells and matrix

The fascinating interplay between the bulk and microscale mechanics of biopolymer networks, and between networks at different scales, is perhaps best illustrated through the interactions between cells and their substrates. Given that certain cells have been known to be mechanically sensitive for over a decade [105, 106], it might be prudent to ask whether such cells respond to the stiffness of their substrate and if so, whether it is the stiffness of the polymer fibres or of the fibre network that the cell senses. In this sense, it is not clear whether cells respond more to local or global mechanical properties of their substrate. We note that these cells can themselves be viewed as an additional component of the complex network structure, either as active units generating local forces, or as a constituent in a composite assembly, affecting architecture and stiffness.

The interactions between cells and their substrates have increasingly been studied and debated over the past 20 years [15, 107], with various behaviours observed in different cell types and for contrasting substrates. Within the scope of this thesis, it is particularly interesting to discuss those cells for which the mechanical cell-matrix coupling is strong, as observed for fibroblasts, for example [15, 108]. One of the clearest examples of cell-matrix interactions is found in cell migration, where cells must either crawl along the surface of a two-dimensional (2D) substrate, or navigate through a three-dimensional (3D) fibrous environment [89]. Adherent cells can deform the surrounding matrix [109], through the use of extensions such as filopodia or lamellipodia, and through degradation of various regions of the matrix [110–113]. Cell mobility has been observed, studied, and characterized in many *in vivo* systems, including cancer cell invasion [114, 115], neural crest cell migration [116, 117], and morphogenesis [118, 119]. Interestingly, and still somewhat controversially, some cell types are observed to migrate towards stiffer locations in the matrix, a process termed ‘durotaxis’ [15, 120]. In fact, not only

the migration direction, but also speed appears dependent on matrix stiffness, with cells appearing to crawl fastest on gels possessing 'goldilocks' stiffnesses, neither too compliant nor too stiff [121]. It has been argued that durotaxis can robustly emerge from the collective cell behaviour, even when individual cells do not exhibit this phenomenon [107]. Increased polymer density can also lead to greater motility speeds, even when bulk stiffness is held constant [113]. While many historic studies have involved cells seeded on nonfibrous, and linearly elastic, polyacrylamide gel [122], it is increasingly clear that cell migration within biopolymeric substrates, such as matrigel, electrospun scaffolds, or native fibrous matrices, is distinct [89, 123]. For example, cells migrating within fibrous substrates respond to the constituent filament diameter [124] and the polymer density [113]. The discrete, fibrous nature of a substrate can be of vital importance where colonies of cells are migrating collectively, or peripheral to a tumour stroma, where the constituent network fibres may align with the cells [114, 125, 126]. The importance of this alignment is observed in cancers, where prognosis directly correlates with matrix alignment [127], and invasive behaviours can be controlled through the matrix architecture [128, 129]. Fig. 1.3 **(c)** shows the matrix fibre alignment that can occur between tumour spheroids, along with an increased density of cells within this region.

Many of the interesting behaviours described above involve a transmission of traction forces, generated from within the cell, to the ECM. The manner in which this mechanical interplay between cell and substrate occurs is still hotly debated. One leading theory for the interaction between mechanically active cells and matrix is that of 'dynamic reciprocity' [15, 133]. Here, it is proposed that adherent contractile cells draw matrix fibres to their periphery, generating local strains in the matrix and aligning filaments with the direction of contraction [22, 134]. This remodelling of the matrix leads to material anisotropy on the scale of the cell, with the peripheral matrix becoming stiffer in the direction of alignment, which is coincident with the direction of contraction. Responding to this increased stiffness, the mechanically sensitive cell proceeds to generate further contractions in this direction, resulting in a positive feedback loop [15, 135]. This cyclical behaviour can

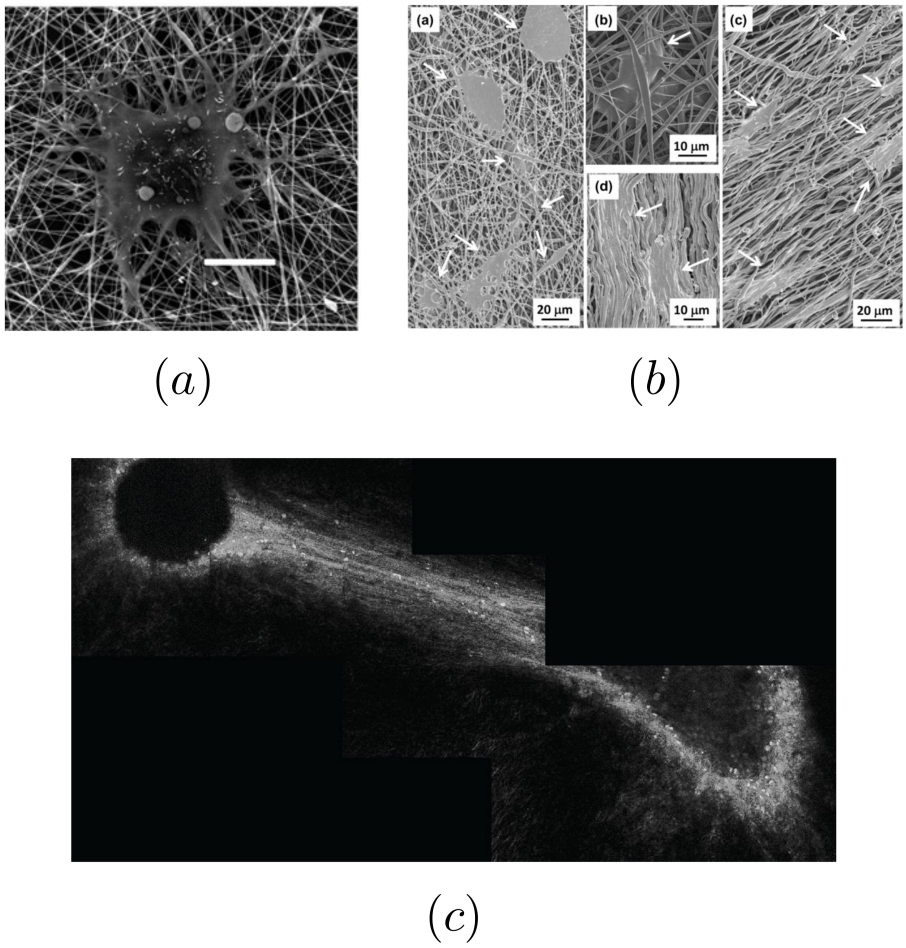

Figure 1.3: Some examples of cell-matrix interactions in different biopolymer systems. **(a)** Scanning electron microscope images of rat neural stem/progenitor cells, anchored to electrospun polymer scaffolds. Many cells adopt a stretched morphology when interacting with the nanofibres. Reproduced with permission from Christopherson, Song, and Mao [130]. **(b)** Scanning electron images of osteoblasts within a fibre network, showing cell spreading, integration and elongation in the direction of fibre alignment. Arrows indicate cell locations. Reproduced with permission from Stachewicz et al. [131]. **(c)** Matrix fibres between two tumour spheroids, separated by 3mm, imaged using reflectance microscopy. Fibre alignment and localized cells are observed between the spheroids. Reproduced with permission from Sander [132].

result in remarkable cell aspect ratios, where cells become increasingly long and thin [136–138], and significant substrate strains [139]. Various microscopy techniques have detected significant displacements as a result of cell contraction in both 2D and 3D matrices, which occur dynamically and involve contraction and relaxation

phases [140, 141]. This mechanical activity can be utilized by cells in a variety of situations. For example, cells can detect distant boundaries that are many cell diameters distant [142]. Likewise, it was found that cells were able to mechanically sense substrate depth [143], as well as distant matrix disturbances [144]. Cellular mechanical sensitivity is implicated in collective migration, where long-range force transmission through the substrate allowed cell clusters to exhibit durotaxis, even when isolated cells did not [107]. In addition to the ability to mechanically detect faraway boundaries, there is also evidence for mechanical communication between distant cells [145, 146], including correlated migration [147–149], alignment [126, 150, 151], and cooperative force generation [152, 153]. Further evidence for the importance of matrix mechanics and architecture to cell behaviour is provided by the differences observed in cell spreading area and morphology. For example, cells seeded on linear gels tend to adopt a round morphology, and are less mechanically active than those on fibrous, nonlinear substrates, which exhibit far larger spread areas [108, 145] and extend a greater number of protrusions [9, 154]. This cell spreading can be dependent on the mechanics of matrix fibres, as well as aspects of the network structure, such as cross-link density [9, 155]. Example cell morphologies as they interact with fibrous substrates are shown in Fig. 1.3 **(a)** - **(b)**.

The range of behaviours exhibited by cells seeded on fibrous substrates, and in particular how the mechanics and geometry of the fibre network at the scale of the cell is central to their mechanical regulation, necessitates a move away from simple classical representations of substrates, and towards a structural view, where the network mechanics is viewed as the sum of contributions from individual fibres. In particular, we note that the mechanical properties that a cell senses locally could be largely independent from the bulk material, and that there may be significant variation between different substrates with similar parameters, or at various positions within the same biopolymer network. Further, it is possible that the local properties might vary dynamically under the action of contractile cells, all while the bulk stiffness and density remain constant. These considerations

provide further motivation to examine both the local and global properties of fibrous structures, and be mindful of where separations between the two might occur.

1.1.3 Theoretical modelling of biopolymer networks

Given their interesting and often counterintuitive behaviours, there have been extensive efforts to model individual fibres (either free or in confinement), polymer bundles, such as those observed in stress fibres, and whole fibre assemblies. Naturally, the scale and resolution of the model must vary, depending on the level of detail required to capture the physics relevant to the investigation, and the analytic or computational feasibility of the study. Within the continuum literature, there exist many efforts aimed at capturing the nonlinear bulk behaviour of the biopolymer material, and its response to local deformations [19, 145, 156, 157]. This work has been successful in capturing many aspects of biopolymer mechanics. However, in order to fully understand how the microscale informs the bulk material properties, it is often necessary to first implement models that explicitly account for the complex architecture. These investigations can inform future continuum models, where microstructural effects can be correctly accounted for [19, 137]. In this thesis we shall focus on modelling networks in which the microstructure is represented explicitly, such that we do not discuss the continuum literature further here. Similarly, there exist increasingly detailed and parametrized models, employing Brownian or Stokesian dynamics to simulate the network structure, dynamics and mechanics [158, 159]. While these models contain impressive detail, simulation constraints do not allow for the same flexibility in investigating biopolymer networks across a large range of relevant parameter values, whence they sacrifice generality. As a compromise, we instead focus on an intermediate regime, where the network may be explicitly represented, yet the detail in the biopolymers themselves is limited. We shall refer to such models throughout as discrete fibre network (DFN) models. These models allow for thorough investigations into microstructural changes, parameter sweeps and constitutive flexibility. We are clear that this modelling paradigm should not be seen as competing with, or superior to, continuum approaches, or those more

detailed efforts. Instead, it acts to complement other research, where the knowledge gained on the importance of various structural aspects of biopolymer networks can be utilized to aid the development of continuum models, and may locate interesting regions in parameter space where greater resolution may be most useful. Below, we briefly review some relevant theory and some of the many modelling efforts from the DFN literature, as they relate to this thesis.

Wormlike chain model and thermal persistence length

Before we discuss the modelling of biopolymers when assembled into a network structure, it is natural to ask how one should model individual biopolymers. When considering semiflexible filaments on small length scales, one can model an undulated polymer as inextensible, and supporting bending deformations. This model is often referred to as the 'wormlike chain' (WLC) model for biopolymers, the energy for which may be written as:

$$\mathcal{H}_{\text{bend}} := \frac{\kappa}{2} \int_L \left(\frac{d\psi(s)}{ds} \right)^2 \mathrm{d}s \ , \tag{1.1}$$

where ψ gives the rotation of the plane normal to the polymer backbone at arc-length position s, and κ gives the *bending rigidity*, with units of length times energy and relates to classical beam theory as $\kappa \sim EI$, where E is the filament elastic modulus, and I is the second moment of area for the cross-section. The integral runs along the polymer backbone of length L [51, 160]. Consider regular points along the fibre axis, ordered by suffix i and separated by N small, constant distances $\delta s = s_i - s_{i-1}$. Defining the difference between tangent orientations ψ at those points to be $\delta\psi_i = \psi_i - \psi_{i-1}$, the discretized version of Eq. 1.1 may be written as:

$$\mathcal{H}_{\text{bend}} \approx \frac{\kappa}{2} \sum_i^N \left(\frac{\delta\psi_i}{\delta s} \right)^2 \delta s \ . \tag{1.2}$$

Assuming that the N angles $\delta\psi_i$ are independent, then it follows from the equipartition theorem that:

$$\frac{\kappa}{2\delta s} \sum_i \langle \delta\psi_i^2 \rangle = \frac{\kappa}{2} \langle \sum_i \delta\psi_i^2 / \delta s \rangle = \langle \mathcal{H}_{\text{bend}} \rangle = \frac{N}{2} k_b T \ , \tag{1.3}$$

for Boltzmann constant k_b and temperature T, so that:

$$\langle \delta\psi_i^2 \rangle = \frac{k_b T \delta s}{\kappa} \ . \tag{1.4}$$

Earlier we discussed the thermal persistence length, which we described as measuring the decay of correlations between tangents along the fibre axis. We are now in a position to derive this quantity mathematically. Consider the unit tangent vectors formed from the first three links in the discretized chain, $\boldsymbol{t}_0$, $\boldsymbol{t}_1$, and $\boldsymbol{t}_2$. Then we have:

$$\langle \boldsymbol{t}_0 \cdot \boldsymbol{t}_1 \rangle = \langle \cos(\delta\psi_1) \rangle \tag{1.5}$$

$$\langle \boldsymbol{t}_0 \cdot \boldsymbol{t}_2 \rangle = \langle \cos(\delta\psi_2 + \delta\psi_1) \rangle = \langle \cos(\delta\psi_2)\cos(\delta\psi_1) \rangle = \langle \cos(\delta\psi) \rangle^2 \ , \tag{1.6}$$

where we have used the independence of the $\delta\psi_i$ to drop the subscript i, and the fact that the expected value of $\sin(\delta\psi)$ is zero. By induction, we can continue this process. If we consider unit tangent vectors $\boldsymbol{t}_m, \boldsymbol{t}_n$ at discrete points, s_m, s_n along the polymer, and assume that the changes in orientation $\delta\psi$ are small for semiflexible filaments, we may write:

$$\langle \boldsymbol{t}_m \cdot \boldsymbol{t}_n \rangle = \langle \cos(\psi_m - \psi_n) \rangle = \langle \cos(\delta\psi) \rangle^{|m-n|} \approx \left\langle 1 - \frac{\delta\psi^2}{2} \right\rangle^{|m-n|} \ . \tag{1.7}$$

For the separation distance of the two points, we have the expression $|s - s'| = \delta s|m - n|$. Using the expression for $\langle \delta\psi^2 \rangle$ from Eq. 1.4, and the assumption that $\delta\psi$ is small for semiflexible fibres, we have:

$$\left(1 - \frac{\langle \delta\psi^2 \rangle}{2}\right)^{|m-n|} = \left(1 - \frac{k_b T \delta s}{2\kappa}\right)^{|s-s'|/\delta s} \to e^{-k_b T |s-s'|/2\kappa} \ \text{ as } \delta s \to 0. \tag{1.8}$$

As such, the decay of tangent-tangent correlations can be written as:

$$\langle \boldsymbol{t}(s) \cdot \boldsymbol{t}(s') \rangle = e^{-|s-s'|/\ell_p}, \tag{1.9}$$

introducing the persistence length $\ell_p = 2\kappa/k_b T$. The above treatment was for planar filaments; accounting for both transverse polarizations in 3D recovers the quantity mentioned earlier in the text $\ell_p = \kappa/k_b T$. In this manner, the influence of the bending stiffness κ on the *thermal* persistence length is made clear, with filaments possessing larger bending rigidities remaining straight over longer distances.

An affine model for network elasticity

One of the more important historical models for semiflexible biopolymer networks has been the affine model described by MacKintosh, Käs, and Janmey [7]. We begin by considering individual semiflexible filaments under extension in 3D, governed by an effective Hamiltonian expressed via the wormlike chain model as:

$$\mathcal{H} = \frac{1}{2}\kappa u''(z) + \frac{1}{2}\tau u'(z) \ , \tag{1.10}$$

Here, $u(z)$ denotes the transverse deviation from the z-axis, κ is the filament bending stiffness, and τ is an extension force, which limits the conformations the semiflexible biopolymer can take. If we consider the fully stretched length of the filament to be L_∞, we can write:

$$L_\infty = \int_0^L \mathrm{d}l = \int_0^L (1+u'^2)^{1/2}\,\mathrm{d}z \approx L + \frac{1}{2}\int_0^L u'^2\,\mathrm{d}z \ . \tag{1.11}$$

As such, we may write the contraction as $L_\infty - L = \delta L = \frac{1}{2}\int_0^L u'^2\,\mathrm{d}z$, where L is the equilibrium length in the absence of extension force τ. Now, consider a Fourier series representation of a filament $u(z) = \sum_{n=1}^{\infty} A_n \sin(n\pi z/L)$, where we have assumed fixed ends. The energy content of the fibre may then be written as:

$$\mathcal{H}_{\text{fibre}} = \int_0^L \sum_{n,m=1}^{\infty} A_n A_m \frac{\kappa}{2}\left(\frac{n\pi}{L}\right)^2\left(\frac{m\pi}{L}\right)^2 \sin(n\pi z/L)\sin(m\pi z/L) \tag{1.12}$$

$$+ A_n A_m \frac{\tau}{2}\left(\frac{n\pi}{L}\right)\left(\frac{m\pi}{L}\right)\cos(n\pi z/L)\cos(m\pi z/L)\,\mathrm{d}z \tag{1.13}$$

$$= \frac{L}{4}\sum_{n=1}^{\infty}\left(\frac{\kappa n^4\pi^4}{L^4} + \frac{\tau n^2\pi^2}{L^2}\right)A_n^2 \tag{1.14}$$

The partition function here is:

$$\mathcal{Z} = \int_{-\infty}^{\infty}\prod_{i=1}^{n^*}\mathrm{d}A_i\ e^{-\frac{L}{4k_bT}\sum_{n=1}^{n^*}\left(\kappa n^4\pi^4/L^4 + \tau n^2\pi^2/L^2\right)A_n^2} \ , \tag{1.15}$$

$$= \prod_{n=1}^{n^*}\int_{-\infty}^{\infty}\mathrm{d}A_n\ e^{-\frac{L}{4k_bT}\left(\kappa n^4\pi^4/L^4 + \tau n^2\pi^2/L^2\right)A_n^2} \ , \tag{1.16}$$

where we have introduced a large finite cut-off n^* for the low energy modes, else the large n Fourier modes vary at sub-molecular scales, violating the continuum

approximation. By the properties of the Gaussian integral:

$$\langle A_n^2 \rangle = \frac{2k_bT}{L\left(\frac{\kappa n^4\pi^4}{L^4} + \frac{\tau n^2\pi^2}{L^2}\right)} \tag{1.17}$$

Returning to the pulling out of the filament, we can now calculate the expected extension $\langle \delta L \rangle$ as:

$$\langle \delta L \rangle = \frac{1}{2}\int_0^L \langle u'^2 \rangle \, \mathrm{d}z \approx \frac{L}{4}\sum_{n=1}^{n^*} \frac{n^2\pi^2}{L^2}\langle A_n^2 \rangle \tag{1.18}$$

Substituting the expression for $\langle A_n^2 \rangle$ into the above form, and multiplying by 2 to account for both x and y polarizations,

$$\langle \delta L \rangle = 2 \times \frac{L}{4}\sum_{n=1}^{n^*} \frac{2k_bTn^2\pi^2/L^2}{L\left(\kappa n^4\pi^4/L^4 + \tau n^2\pi^2/L^2\right)} \approx k_bT\sum_{n=1}^{\infty}\frac{1}{\kappa\frac{n^2\pi^2}{L^2} + \tau} \ . \tag{1.19}$$

Expanding the sum, and assuming the tension is small so that we can neglect quadratic and higher order terms in τ,

$$\sum_{n=1}^{\infty}\left(\tau + \kappa\frac{n^2\pi^2}{L^2}\right)^{-1} \approx \sum_{n=1}^{\infty}\frac{1}{n^2}\left(\frac{L^2}{\kappa\pi^2}\right) - \tau\frac{1}{n^4}\left(\frac{L^4}{\kappa^2\pi^4}\right) = \frac{L^2}{6\kappa} - \tau\frac{L^4}{90\kappa^2} \ . \tag{1.20}$$

The first term represents the equilibrium contraction of the polymer, while the response of a filament to an applied tension is given by the second. Recalling our definition of the thermal persistence length, we may write this in the form of a thermal spring constant:

$$\tau \sim \frac{\kappa\ell_p}{L^4}\delta L \ . \tag{1.21}$$

With this expression for the thermal spring constant, we may derive expressions for the network stiffness by assuming that all points in the sample deform *affinely*. In particular, consider a semiflexible polymer network subjected to a simple shear; we can find an expression for the network shear modulus as follows. Assuming that all points in the sample deform according to an applied simple shear γ, such that constituent polymer segments of length L_e experience an extension $\delta L \sim \gamma L_e$, and assuming there are $\sim 1/\xi^2$ filaments per unit area for mesh size ξ, the stress can be written as:

$$\sigma \sim \frac{\tau}{\xi^2} \sim \gamma L_e\frac{\kappa\ell_p}{L_e^4\xi^2} \ , \tag{1.22}$$

whence the shear modulus scales as:

$$\mathcal{G} \sim \frac{\kappa \ell_p}{L_e^3 \xi^2} \ , \tag{1.23}$$

For densely cross-linked networks, the mesh spacing is similar to the cross-link separations, $L_e \sim \xi$, so that the shear modulus takes the form:

$$\mathcal{G} \sim \kappa \ell_p \xi^{-5}. \tag{1.24}$$

Further details for specific biopolymers and their network structures can allow for further predictions in terms of polymer concentration and monomer size [7]. We present a detailed discussion of the above affine model as part of this literature due to its perhaps surprising accuracy in a number of experimental studies on semiflexible polymer networks, including actin [38] and intermediate filament [161] networks. As such, this affine model has proved to be an influential model, and remains an important comparison point when discussing models for biopolymer network elasticity.

Discrete fibre network models: beyond the affine assumption

Affine models, such as the one discussed above, have been influential in several areas of elasticity, dating back to studies in rubber elasticity [51, 162]. The assumption that at all scales in the model the local deformation field matches that of the bulk can greatly simplify calculations for the network elasticity. Indeed, one can provide an estimate for the shear modulus based only on macroscopic properties such as total polymer density, and the polymer constitutive properties such as persistence length or stretching modulus μ [7, 163]. However, we should not expect any network to exhibit perfectly affine deformations, and there will exist length scales under which significant nonaffine displacements can be observed [104, 164]. Furthermore, it has been suggested that in networks where the lengths of polymer segments vary significantly, the affine limit might not be stable, given the dependence of a thermal stretching modulus on the segment length [165]. These nonaffine phenomena are expected to be of particular importance to the microscale elasticity, where nonaffine

fluctuations in the strain field may be experienced by, for example, resident cells, and could have profound implications for networks with defects and in the behaviours of composite networks [137, 166]. Within this thesis, we seek to investigate DFN models in which these deviations from affinity may be explicitly probed and characterized. Below, we discuss and review some of the important literature in the DFN field, which provides the technical context for our research.

Any DFN representation for a biopolymer network must involve a choice of network topology and geometry. In the absence of a specific network structure or organisation, networks are often considered to be statistically random, with fibre orientation, cross-link and polymer density taken to be uniformly random in space. Perhaps the most well known and best studied example of a random DFN is the Mikado-type architecture and related structures [163, 167–169]. In this simple case, model fibres are taken to be lines of monodisperse length L, placed within some computational domain. Wherever two fibres cross, the point of intersection is regarded as a cross-link, and as the polymer density increases, so a network structure of fibres and cross-links emerges. By considering constituent fibres as beams, early modelling efforts identified a central feature of DFN models; as the bending stiffness of a filament increases, the relative contributions to the total network energy from fibre bending deformation modes decreases, and the network becomes dominated instead by fibre stretching deformations [163, 170]. Crucially, this move to fibre stretching coincides with a nonaffine-affine transition, where the measured bulk shear modulus approaches that predicted by subjecting each fibre to an affine deformation under the bulk shear, and nonaffine fluctuations become smaller [18, 170, 171]. Throughout this thesis we shall refer to affine-nonaffine and bend-stretch transitions; unless explicitly otherwise stated, these terms refer to the same phenomenon. Length scales for this transition have been proposed, either as empirical relations [170, 172] or through scaling arguments and effective medium theories [170, 173]. The response of networks to local perturbations can be characterized under the same length scales for affinity [174]. While the above studies were concerned with small deformations, the bend-stretch crossover is also

observed to occur in the context of large deformations, where an initially nonaffine network becomes stretch-dominated at some critical strain [160, 175]. Interestingly, certain networks could remain bend-dominated even at large strains, depending on the bending stiffness and density of the polymer. It was also found that introducing small fibre crimps did not significantly alter this behaviour at larger strains, with the undulations being straightened out as strain increases. The finite strain mechanics of these networks are essentially governed by this 'pulling out' of fibre undulations, and a percolation of axially stressed fibres that cross the domain [176]. It would seem that affine-nonaffine transitions are a generic property of fibre networks, having been observed in anisotropic, nematically aligned networks [177], in networks of polydisperse length [178], as well as when the deformation is incurred by the contractile activity of model cells [137]. The above research into Mikado networks has been developed further, with extensions including variations in the cross-link density of Mikado networks [179, 180], and the constituent fibre elastic moduli [181]. While studies have largely focussed on 2D networks, several extensions to 3D have used similar geometries, where Mikado fibres are connected through finite length cross-links [169, 182] or where each fibre is segmented into beads and springs, connections forming between proximal beads on different fibres [183].

Many of the interesting properties of Mikado networks stem from the complex relation between fibre length, fibre density and the resulting network structure. Indeed, for low fibre densities, placing fibres according to a Mikado geometry would not yield a network at all, with insufficient fibre intersections leading to many isolated fibres and clusters [184]. As fibre density rises, and the number of intersections (whence cross-links) increases, clusters of connected fibres grow and a solid network structure starts to form. Following a critical value in network density, these clusters percolate a domain of arbitrary size, whence a Mikado network is formed [168, 170, 184]. How the network elastic modulus scales around this percolation threshold, where fibres are present in very low densities, was characterized by Head, MacKintosh, and Levine [185]. The statistical properties of the Mikado network can also be characterized in terms of fibre density. Consider Mikado networks

generated within a square domain of area W^2, with fibre length L, and fibre number N. Then the cross-link spacing, that is the length l of segments formed between two model cross-links, is exponentially distributed as $P(l) = e^{-l/l_c}/l_c$, where $l_c := \langle l \rangle$ denotes the mean segment length [185, 186]. A result dating back to Kallmes and Corte [4] relates the fibre density to the mean segment length as $l_c \approx \pi/2\hat{\rho}$, for sufficiently high fibre density $\hat{\rho} = NL/W^2$. Understanding the statistics of Mikado networks allows for a better theoretical understanding of their mechanics, as shall be discussed throughout this thesis. Further details for the statistical properties of Mikado networks are provided in Appendix A.

While Mikado models have proven to be highly influential, many other DFN geometries have been employed. Networks based upon both Voronoi and Delaunay geometries have been used [172, 186–189], and can be particularly useful in 3D modelling, where guaranteeing network connectivity becomes non-trivial in Mikado architectures [181, 188]. Another large class of models uses network structures derived from regular lattices. These include Hexagonal, Kagome, face-centered cubic, triangular and square [165, 190–193]. In order to introduce randomness and disorder into these regular structures, network edges are often diluted, such that a given proportion of fibre segments are removed [55, 194]. Alternatively, small spatial perturbations may be introduced to model cross-links, generating a small degree of disorder [187]. The use of these disordering effects allow such architectures to combine the advantages of easy-to-understand geometry and topology with the need to generate irregular or random DFNs. The bend-stretch transition has been observed to occur in lattice models, as in the random Mikado cases. Interestingly, it has been argued that the linear regime could be vanishing for long fibre lengths or very flexible filaments within certain 3D lattice models [192]. Using diluted and undiluted triangular lattices to represent a substrate, Ronceray, Broedersz, and Lenz [195] studied force transmission within fibre networks, as generated from the contractile action of a model cell. The network microstructure was implicated in amplifying the stress signal predicted from linear elasticity. How important the lattice microstructure is to local active units, such as resident cells, and how

different geometries impact the many mechanical cell behaviours we discussed earlier remains an intriguing question. Three example network geometries commonly used within the DFN literature are displayed in Fig. 1.4.

Alongside a choice of network architecture, DFN models also require a constitutive model for the network fibres. Once again, this choice should depend on the system and research question under investigation. Model fibres have often been modelled as springs or trusses, which can be linear [168, 183], asymmetric in tension and compression [196], and strain-stiffening [72]. However, most network architectures considered reside within the 'subisostatic' regime, where networks are mechanically unstable and do not possess a classical static linear elastic modulus in the presence of only central forces. The identification of this subisostatic regime dates back to a counting argument given by Maxwell [197]. In particular, for average node coordination $\langle z \rangle$ and number of nodes n, we have a total number of constraints owing to central forces given by $n\langle z \rangle/2$, and degrees of freedom nd, where d denotes the spatial dimension. As such, linear mechanical stability in central force networks occurs for $\langle z \rangle = 4$ in 2D, or $\langle z \rangle = 6$ in 3D. Voronoi, Mikado and many diluted lattice networks fall below this threshold. Therefore, the use of spring modelling in these networks would be most suitable for finite strain studies [72], dynamic models [168], for fibre networks in the presence of thermal forces [198], or for geometries where the node coordination is above the threshold, such as triangular lattices or Delaunay networks [194]. As many real fibre assemblies involve networks formed from the crossings of fibres, whence the network can only approach the isostatic threshold from below, we expect many physical networks to reside in the subisostatic regime. In order to investigate the linear regime of these DFNs, models frequently often take fibres to support both bending moments and axial forces, thus stabilizing the system. These choices include Euler-Bernoulli or shear flexible beams, or similar discretized versions of the worm-like chain model, after Eq. 1.1, often with additional terms to allow for fibre extension [199]. Further constitutive choices must be made for the model cross-links, where the constraints imposed by crossing fibres can vary. This can involve freely-jointed cross-links, where only translational

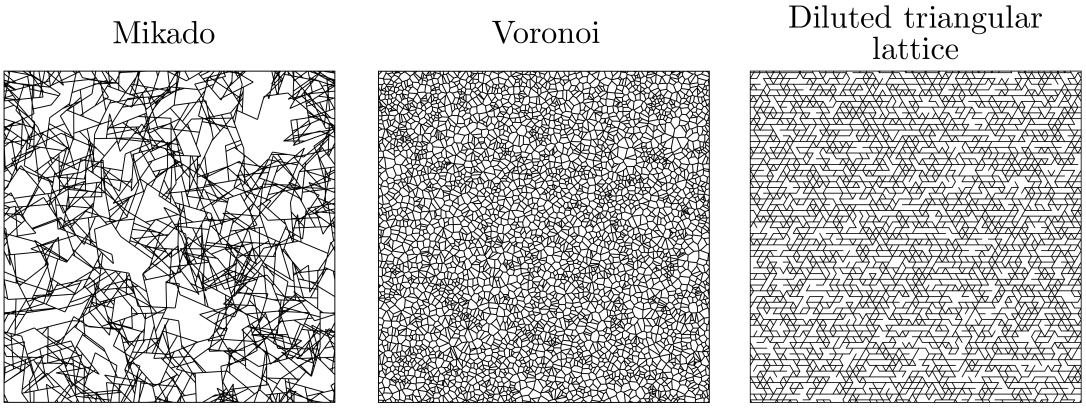

Figure 1.4: Illustrations of some commonly used discrete fibre network architectures, including **(Left)** Mikado networks, formed from the intersections of randomly placed monodisperse rods, **(Centre)** Voronoi-type networks, given from the edges of a 2D Voronoi partition of the domain, and **(Right)** Diluted triangular lattice, where edge deletion is employed so as to introduce disorder into the network.

degrees of freedom are enforced at network nodes [72, 198], fully 'welded' cross-links, where all rotational and translational degrees of freedom are fixed, and 'hinged' or 'freely-rotating' where two crossing fibres are free to rotate around the cross-link, but the translation of another fibre will incur bending deformations in the other [172]. Further extensions can include the introduction of torsional springs at cross-links [200]. Referring back to the earlier discussion on network percolation, we note that when fully welded cross-links are employed, the geometric percolation threshold coincides with the rigidity threshold, whereas stability occurs at slightly higher values for freely-rotating cross-links, which do not add as many constraints [185]. In 3D studies, finite length cross-links are frequently employed, where a short beam or spring connects proximal fibres, whence additional choices for the stretching, bending and compressive behaviour of the cross-links are required [169, 183].

1.2 Network generation

Throughout this thesis, we shall investigate various DFNs that undergo deformations under a variety of loading conditions, and in which the constitutive properties of the fibres vary. However, common to all chapters is the existence of a spatial fibre network, where nodes (cross-links) are connected by edges (fibres). We outline here

the basic algorithm that we employ to generate networks of a Mikado architecture. While many other network types are examined in this thesis, including extensions to the basic Mikado geometry, many of the details of their generation are often similar to, or can be inferred from, the detailed treatment we give here for the Mikado case. As such, the presentation here is intended to be detailed enough to apply to other networks throughout. The code for the generation of networks presented in this thesis is written both in MATLAB [201] and Python [202], and a flow chart describing the algorithm for their generation is shown in Fig. 1.5. We expand on the specifics and technical details of the main steps below.

Fibre-domain and fibre-fibre intersections

In order to find the intersection of line segments representing fibres, we first check whether an intersection has taken place, before calculating its location. In particular, consider two planar fibres, denoted $\boldsymbol{f_i} = \boldsymbol{x_b^i} - \boldsymbol{x_a^i} = \begin{bmatrix} x_b^i \\ y_b^i \end{bmatrix} - \begin{bmatrix} x_a^i \\ y_a^i \end{bmatrix}$, $i = 1, 2$, which represent segments of the lines $y = m_i x + c_i,\ i = 1, 2$. Then, an efficient criterion for checking whether two lines intersect is given by:

$$\operatorname{sgn}(y_a^1 - m_2 x_a^1 - c_2) \neq \operatorname{sgn}(y_b^1 - m_2 x_b^1 - c_2) \tag{1.25}$$

$$\texttt{and} \quad \operatorname{sgn}(y_a^2 - m_1 x_a^2 - c_1) \neq \operatorname{sgn}(y_b^2 - m_1 x_b^2 - c_1)\ , \tag{1.26}$$

which returns `True` when an intersect occurs. In words, this criterion is equivalent to requiring that the two points defining each line segment lie in different half spaces in the real plane, as bisected by the line in which the other segment resides. If this criterion returns `True`, the intersect (x, y) is then given as the intersection of the two lines as defined above:

$$(x, y) = \left(\frac{c_2 - c_1}{m_1 - m_2}, \frac{m_1 c_2 - m_2 c_1}{m_1 - m_2} \right) \tag{1.27}$$

We note that as we generate the orientations and fibre midpoints uniformly at random, there is no concern at this stage that horizontal or vertical line segments appear, such that the above algorithm is robust for locating fibre-fibre intersections. The operations to find fibre-fibre intersects are carried out between every pair

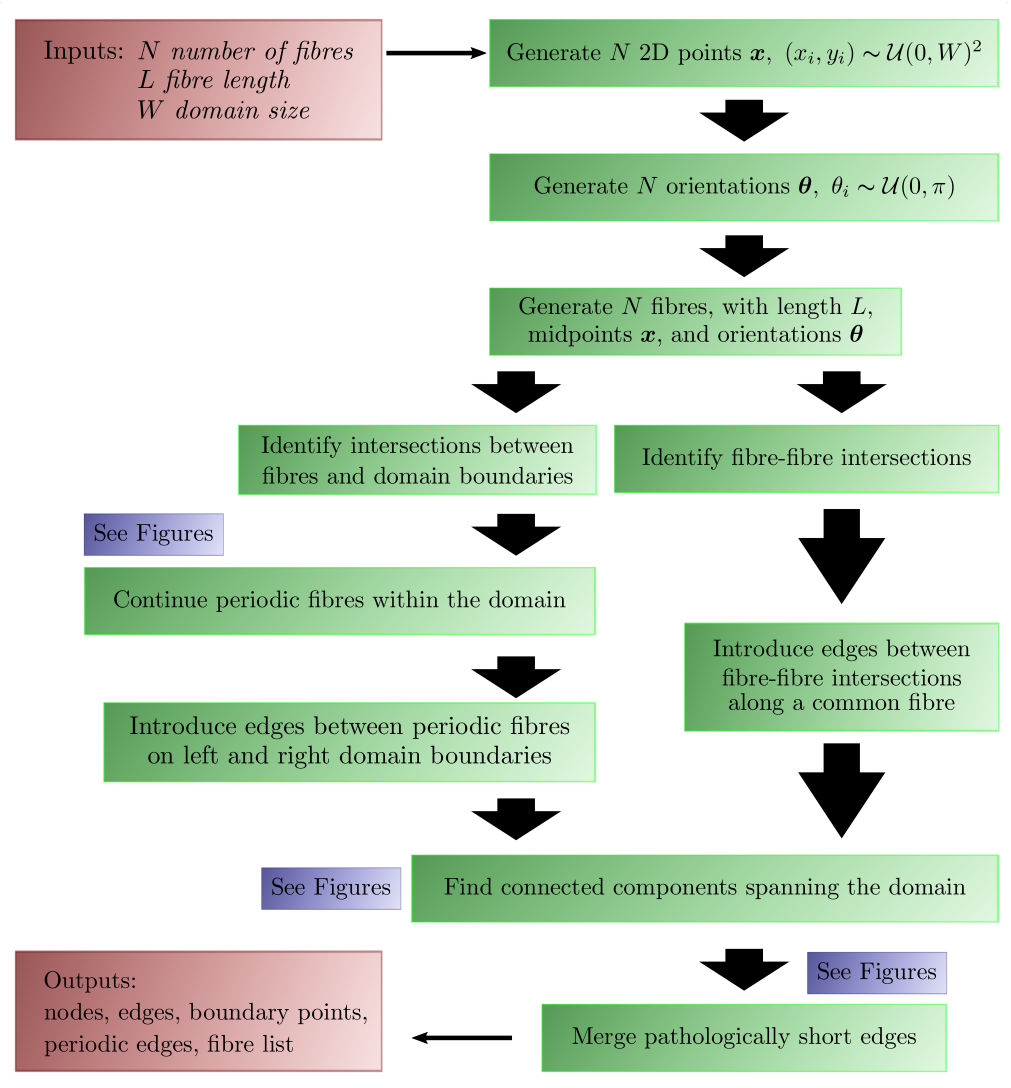

Figure 1.5: A flow chart depiction of the computational algorithm employed to generate Mikado network architectures in this thesis. The inputs for generating Mikado networks are number of fibres N, the fibre length L, and the computational square domain size W. The code outputs the quantities needed to describe a Mikado geometry, namely a list of nodes (cross-links), edges (segments connecting pairs of nodes), boundary points (those nodes that will be subjected to displacements or loads), periodic elements (connections used to fix degrees of freedom between nodes on periodic boundaries) and a fibre list (labelling the fibre to which a node belongs).

of fibres within the domain, that is $N(N-1)$ times. Having located all fibre intersections, we also wish to find those positions where fibres cross the domain boundaries. When considering domain-fibre intersections, the above algorithm is adapted so as to allow horizontal and vertical lines for the boundaries, and the domain 'fibre' given as an edge of the square domain.

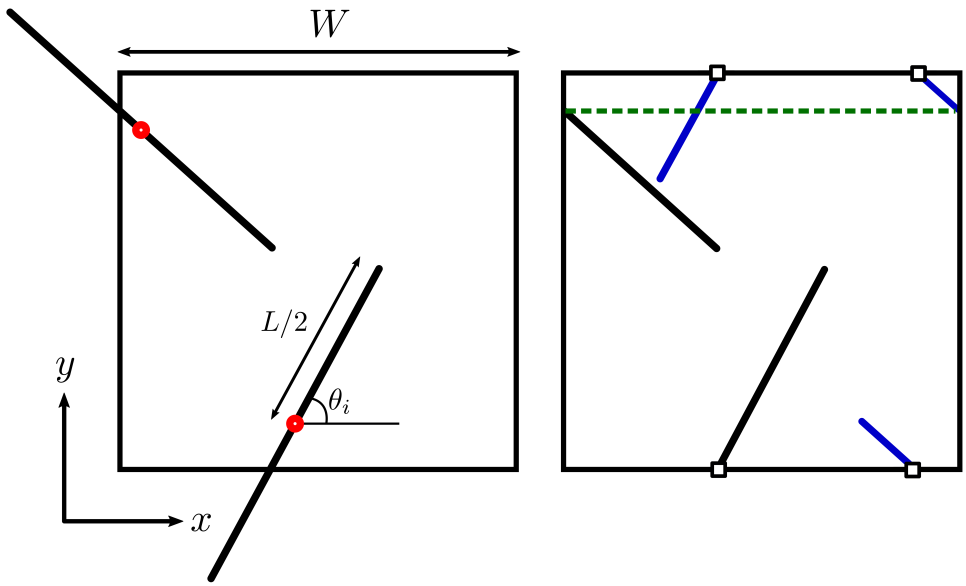

Figure 1.6: Schematics for the generation of a Mikado network. **(Left)** The deposition of fibres with midpoints (red circles) within a domain of area W^2, at orientations θ_i with the x-axis, and with length L. **(Right)** An illustration of the geometric periodicity of the fibres. Fibres exiting the domain on one boundary reappear on the opposite face. On upper and lower boundaries, the locations of fibre-boundary crossings are stored as boundary nodes. When filaments cross left and right boundaries, nodes are placed at these points and a periodic edge is introduced between them, shown in green dash.

Geometric periodicity

In some chapters we wish to construct fibre networks that are spatially periodic. In this case, fibres that exit the square domain at one boundary reappear at the opposite edge. We can capture this effect by either tracking the fibres explicitly, and ensuring that the correct fibre extent is reapplied to the domain, or by tiling the original computational domain into 9 squares, whence recovering the network in the central square provides the geometrically periodic network. The latter can be particularly useful when considering other types of network geometry, such as Voronoi architectures. In the standard Mikado model, networks are usually subjected to simple shears, for example with upper and lower boundaries shifted horizontally while periodic conditions exist on left and right domain edges. To enable the simulation of these boundary conditions, the intersections between fibres and top and bottom domain edges are stored as 'boundary' nodes. Where fibres cross

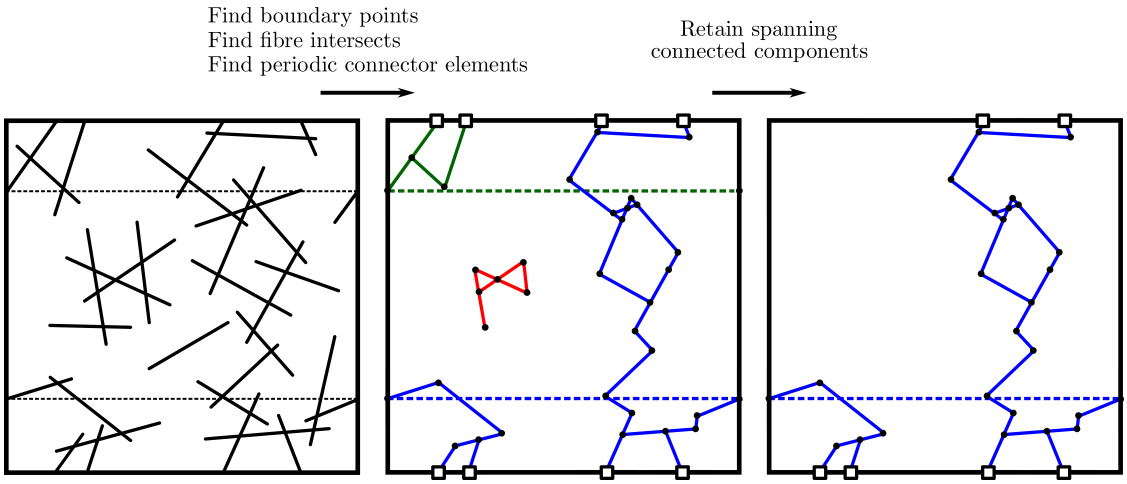

Figure 1.7: An illustration of network generation for the basic Mikado geometry. **(Left)** Fibres are placed in the domain, and geometric periodicity is enforced, such that fibres leaving the domain along one boundary reappear on the opposite edge. **(Centre)** Fibre-fibre and fibre-boundary crossings are identified as nodes, and edges are introduced along fibres, connecting the nodes. Boundary points are introduced where fibres cross upper and lower boundaries (white squares). Periodic edges are introduced between nodes formed where fibres leave the domain on the left and right boundaries (dash lines). Dangling ends, that is the ends of fibres not connected to the greater network structure, are removed naturally at this point. The connected components are identified and labelled (shown in red, blue and green). **(Right)** Only *spanning* connected components, that is connected components that span the domain from top to bottom, contribute to the static elastic moduli of the DFN. Non-spanning components are discarded.

the left and right boundaries, periodic nodes are introduced, which are connected by periodic elements. This procedure is illustrated and clarified in Fig. 1.6.

1.2.1 Spanning connected components

Some of the network geometries considered for DFN models involve architectures that only percolate the domain after a certain density is reached. As previously mentioned, for low density Mikado networks, the probability that two fibres intersect is low, whence the probability of edges spanning the domain from the upper to the lower boundary becomes small. Likewise, if bond dilution becomes too large in diluted triangular lattices, islands of disconnected edges and nodes can form, which will not contribute to the mechanics of the network when a background medium is not considered. In fact, only connected components that involve at least one upper and one lower boundary nodes can contribute to the elasticity of the

solid in these DFN models. As the simulation results presented in this thesis are not be affected by these regions, we wish to remove them from the simulation for the purpose of efficiency and accuracy. To locate the connected components, we can begin at a vertex and produce a list of all vertices that may be reached by travelling along any connected edges. Once all such vertices have been identified, the resulting set of nodes and edges is one such connected component. This list is then removed from the total set of network nodes and the algorithm is restarted with a new initial vertex. This process is repeated until all nodes are identified as a member of a unique connected component (noting that each node belongs to exactly one connected component, including the trivial case of isolated nodes). Connected components containing at least one node on the lower boundary and one node on the upper boundary are identified. All other connected components are discarded, resulting in a network consisting of nodes and elements from the identified *spanning* connected components. An illustration of the spanning connected components that are retained in network generation is given in Fig. 1.7.

1.2.2 Removal of short lengths

In many DFN models, in particular those that are generated with random geometries such as Mikado and Voronoi architectures, pathologically short fibre segment lengths can emerge. For example, in Mikado networks the distribution of segments lengths is exponential, whence at high fibre densities it is necessary to check for and resolve short lengths for computational efficiency and accuracy. In particular, as a large difference in segment lengths can arise, large local stiffness differences may occur, such that simulations involving the original network may become inaccurate or inefficient. To avoid these problems, we pre-process original networks by locating edges of length less than a prescribed minimum quantity $l_{\text{crit.}}$. At these locations, the nodes connected by the short edge are merged into a new node, located at the midpoint of the short line segment. The original edge is removed, resulting in a near identical network structure. The procedure for the removal of short fibre segments is illustrated in Fig. 1.8.

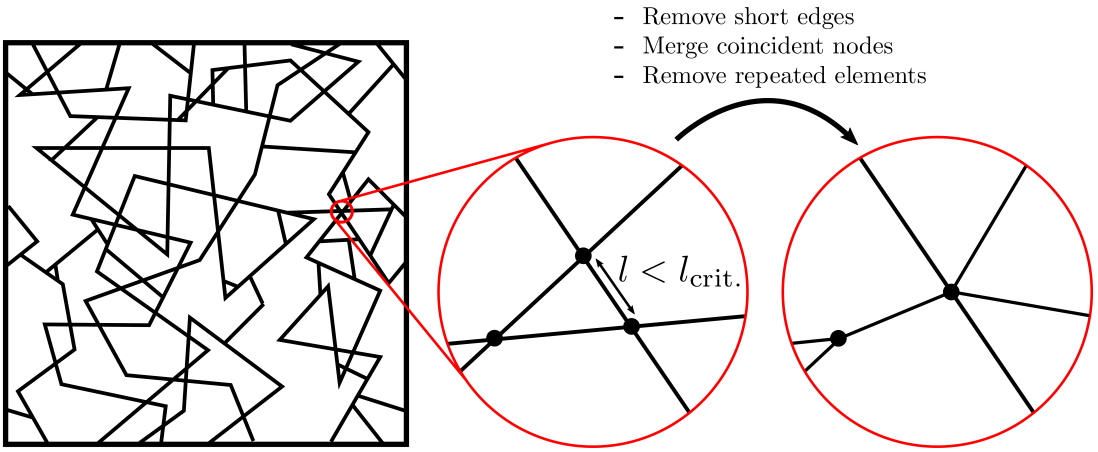

Figure 1.8: An illustration of the identification and resolution of a pathologically short edge that arises in network generation. Edges that fall below a prescribed minimum length $l_{\text{crit.}}$ are located. The two nodes connected by the short edge are merged into a new node located at the midpoint of the original edge. The short length is removed, whence the algorithm continues to check for short edges.

Network Outputs

The result of the network generation algorithm, in any of the architectures considered in this thesis, is a node array $[\boldsymbol{x}, \boldsymbol{y}]$ of size $(n, 2)$, containing the n spatial coordinates (x_i, y_i) of the network nodes, and an element array, $[\boldsymbol{i}, \boldsymbol{j}]$, of size $(e, 2)$, containing the e node-node connections, where (i, j) represents a network edge between the i^{th} and j^{th} nodes. Further, in the standard Mikado case the algorithm returns a boundary node vector, labelling each node as either 'inner' (not boundary), 'upper' or 'lower' (affixed to upper or lower boundary respectively), and a periodic element array, $[\boldsymbol{i}^p, \boldsymbol{j}^p]$, where superscript p indicates 'periodic', which represents the connector edges between nodes on opposite sides of the left and right boundaries (see Fig. 1.7). In some cases, in particular where rotating cross-links are employed, the fibre to which each node and edge belongs is important, whence the algorithm also returns a fibre list consisting of N sets of ordered nodes relating to the cross-links along each network fibre. To model the freely-rotating cross-links, additional connector elements are introduced between coincident nodes on different fibres, which are used to fix translational degrees of freedom while allowing differences in nodal rotation. This geometric output is then passed to the relevant numerical solver

for simulating the network deformation.

1.3 Thesis contributions

The objective of this thesis is to investigate the mechanics of DFN models, with an emphasis on their varying structural properties, and how they relate to the local and bulk mechanics of the material. Several different microstructures are investigated, including monotypic and composite architectures. The main thesis contributions may be summarized as follows.

- the development of a large code base in MATLAB and Python that allows for the generation and characterization of many different DFN geometries, including:
  - the generation of Mikado and Voronoi networks, under a variety of geometric boundary conditions and within different domains,
  - the development of further architectures arising from alterations, perturbations or extensions to existing DFN geometries,
- the development of a new simple model for investigating mechanical cell-cell communication as mediated by different DFN microstructures, allowing for a comparative investigation into the importance of network geometry to long range mechanical cell-cell communication,
- the development of a beam fibre network model, with further code to generate finite element meshes and input files for use in commercial finite element software. This model is validated against important and historic results from the DFN literature,
- the development of a novel Mikado-type model, used to characterize the influence of cross-link density on the bulk network mechanics,
- the development of a double-fibre network model used to represent composite or heterotypic biopolymer systems,

- the generation of novel theoretical and computational results for both low and high density double-fibre networks,

- the presentation of a new explanation for the 'exceptional stiffening' observed in double-fibre networks, supported by simulation results.

1.4 Thesis structure

Having discussed some of the relevant literature and background theory within this introduction, we proceed in Chapter 2 with an investigation into the varying responses of different network architectures under the contractile activity of resident cells. In particular, the mechanics of spring networks with different geometries is studied, and the ability for cells to produce and detect mechanical signals, mediated by different network geometries, is investigated. We begin Chapter 3 with a brief presentation of some relevant theory for the Finite Element Method (FEM) which is employed through the Abaqus commercial FE solver [203] in Chapters 3 - 5. Having discussed this theory, we present a DFN model developed for the Abaqus platform, and validate this model against some of the main historic results in the DFN literature. Following a background discussion of the Mikado model, we investigate a new model which characterizes the mechanics of Mikado networks where cross-link density is allowed to vary without changing the total polymer density or network geometry. Finally, in Chapters 4 - 5 we extend the monotypic DFN model to include double-fibre networks, where filaments can possess different lengths, stiffnesses, orientations and densities. In Chapter 4 we present an extensive theoretical treatment to explain the mechanical differences that arise when stiff inclusions are placed in networks of distinct geometries, focussing on fibrous Mikado, and foam-like Voronoi types. Theoretical predictions are supported with numerical simulations. In Chapter 5 the low density, single fibre inclusion systems studied in Chapter 4 are extended to include dense double-fibre networks. We discuss and characterize the mechanics of these systems in terms of fibre, network and

geometrical properties. Future research directions and a synthesis of the thesis findings are given in Chapter 6, together with a closing statement.

1.4.1 Publications and submissions

- Humphries, D. L., J. A. Grogan, and E. A. Gaffney. "Mechanical Cell–Cell Communication in Fibrous Networks: The Importance of Network Geometry." *Bulletin of Mathematical Biology* 79.3 (2017): 498-524.
- Humphries, D. L., J. A. Grogan, and E. A. Gaffney. "The mechanics of phantom Mikado networks." *under review, Journal of Physics Communications.*
- Humphries, D. L., J. A. Grogan, and E. A. Gaffney. "The mechanical influence of single fibre inclusions in discrete fibre networks." *Submitted to Physical Review E.*
- Humphries, D. L., J. A. Grogan and E. A. Gaffney. "Filament length governs exceptional stiffening in double-fibre networks." *In preparation.*

This chapter is extensively based on the paper "Mechanical Cell–Cell Communication in Fibrous Networks: The Importance of Network Geometry." Bulletin of mathematical biology 79.3 (2017): 498-524., Humphries, D. L., J. A. Grogan, and E. A. Gaffney. [204]

2

The importance of network architecture to mechanical cell-cell communication

Cells contracting in extracellular matrix (ECM) can transmit stress over long distances, communicating their position and orientation to cells many tens of micrometers away. Such phenomena are not observed when cells are seeded on substrates with linear elastic properties, such as polyacrylamide (PA) gel. The ability for fibrous substrates to support far reaching stress and strain fields has implications for many physiological processes, while the mechanical properties of ECM are central to several pathological processes, including tumour invasion and fibrosis. Theoretical models have investigated the properties of ECM in a variety of network geometries. However, the effects of network architecture on mechanical cell-cell communication has received little attention. In this chapter, we investigate the effects of geometry on network mechanics, and thus the ability for cells to communicate mechanically through different networks. In particular, we investigate the mechanics of two distinct DFN architectures, used elsewhere in the literature, under both bulk and local deformations. Two further architectures, with highly similar or identical topology but different geometry, are also studied. We aim to quantify the extent to which network choice is important to DFN modelling, in particular through a study of mechanical cell signalling, mediated

by the network architecture. This work therefore informs the construction of theoretical models for biopolymer network mechanics and experimental explorations of cell-cell communication in fibrous substrates.

2.1 Introduction

How cells interact with their substrate is of fundamental importance to many physiological processes, ranging from cell communication [108, 147], motility and migration [120], cell fate [205, 206] and morphology [9, 154]. While changes in ECM may be signatures of pathology, including tumour invasion [114] and fibrosis [207], it is increasingly clear that the passive mechanical properties of matrices are important for intrinsic cell function [15, 208]. The mechanical response of many soft tissues is moderated by a fibrous network that comprises collagen, elastin and other proteins, which exhibits a geometrically complex and hierarchical structure [8]. A clear understanding of this microenvironment is challenging, in part due to the nonaffine response of the substrate [18, 167], where the local deformations of the matrix differ from those at the bulk scale. Further complexity is introduced in cell-matrix interactions, which can occur in a feedback loop termed 'dynamic reciprocity'. Substrate reorganises under cell-generated tractions, leading to a strain-stiffening response that feeds back into an intracellular response. In particular, the realignment of network fibres under traction leads to fibre bundling along the load direction, contributing to a stiffer mechanical response. Stress fibres, that is actomyosin bundles important for cell contraction, are subsequently recruited to sites of high stiffness, leading to further cell contraction, whence the feedback loop continues [15]. Investigating how matrix alignment and stiffness are related is important for developing a better understanding of cell-matrix interactions.

Substrates derived from matrix proteins have diverse mechanical properties, contributing to their function. Perhaps most striking is the ability to support long-ranging, cell-generated strain fields. In a series of experiments, Winer, Oake, and Janmey [108] demonstrated that fibroblasts and human mesenchymal stem cells (hMSCs) could significantly deform substrate more than five cell diameters

away. This effect was notably absent in cells seeded on linear elastic substrates, such as polyacrylamide (PA) gels. Cell shape was acutely affected, with the round morphology displayed on linearly elastic substrates changing to larger spread area and greater elongation on strain-stiffening gels, similar to other investigations into cell morphology [154]. The morphological influence of a fibrous substrate is increasingly apparent, with cells responding sensitively to network density, as well as the constituent fibre stiffness [9].

There is now considerable evidence that cells respond to micromechanical cues within the substrate. Seminal experiments found that strong fibre alignment is induced between tissue explants seeded in collagen gels. These aligned fibres form tracts, which may function as topographic guides for cell migration [119]. This phenomenon, termed 'contact guidance', is observed in tumour cell invasion, where cells migrate along aligned regions within ECM, as seen in Fig. 1.3 [109, 209]. Similar behaviour on the scale of individual cells has been identified in the formation of tethers, dense regions of highly aligned matrix fibres, between pairs of fibroblasts seeded on fibrin substrates [196]. Cells have also been observed to migrate up stiffness gradients found within gels, a process known as 'durotaxis' [120, 210]. Reinhart-King's work, on cells seeded in compliant substrates [147], found that the motility of pairwise endothelial cells was dependent on both substrate stiffness and cell-cell interactions. Similar responses were absent on substrates that were either too soft, thus not supporting far reaching strain fields, or too stiff, in which cell tractions are unable to significantly deform the substrate. These studies provide evidence that mechanical cues, transmitted through the substrate, allow for pairwise cell interactions.

Various studies have also suggested that cells within matrix-derived gels can detect distant boundaries. While cells cultured upon PA gels can fail to sense substrate properties more than approximately 20 micrometers beyond the cell membrane, hMSCs seeded on collagen I gel appear to detect rigid boundaries further than 100 µm away [211]. Within a new model system, in which regular boundaries were introduced around cells on fibrous substrates, Mohammadi, Janmey, and

McCulloch [142] found that cell-induced displacements extended beyond 500 µm, but failed to reach boundaries 1700 µm distant [142]. Interestingly, when cells detected boundaries, they produced a greater number of protrusions, known as filopodia, and these cellular processes were longer on average, suggesting further physiological changes in cells introduced by the mechanical microenvironment.

Theoretical efforts have investigated phenomena such as nonlinear (strain-stiffening) matrix response and fibre realignment. More recently, many investigations have utilized DFN models to represent the fibre matrix, recognising the importance of local microstructure to both the bulk and local properties of biopolymer networks. Such models explicitly include fibres within a network structure, and break from affine assumptions found elsewhere in the literature [212]. As the *in vivo* geometry and topology of matrices is not well established, it is often necessary to use either segmented imaging data, or to adopt an artificial geometry. Confocal microscopy data for a collagen I network was used by Sander [22] to propose a critical radius within which alignment of network fibres, due to cell contraction, is localized. Modelling based upon imaging of 3D collagen networks lead Stein et al. [200] to suggest that geometric realignment, rather than mechanical nonlinearity of the filaments, lead to the network strain-stiffening response. In particular, the rotation and alignment of filaments contributed to a stiffer response at higher strains. Cell communication was investigated through segmented images of fibroblast-seeded collagen, demonstrating an increased range of stress transmission in fibrous substrates when compared with linear or strain-stiffening continua [146]. Models motivated by imaging data have the clear advantage that, in some sense, they represents the ground truth. However, in practice imaging artefacts are introduced, for example, through sample depth or misidentification of cross-links, entanglements or branching points. These inaccuracies limit the extent to which these networks may be taken as representative. Further, the difficulty of segmentation on the nano- and micro-scale limits the scope of using imaged networks. The desideratum for DFN models is therefore to generate synthetic networks whose statistical and

geometric properties are well characterized and that are representative of real biopolymer networks.

While many models have employed artificially generated networks, the choice of network geometry remains relatively free [172]. Mikado-type networks are commonly used, and are generated by placing fibres of uniform length and random orientation within a 2D domain, as described in Chapter 1 [163, 175, 185]. A cross-link is given by the intersection of two model fibres; as such each network node has coordination z between 2 and 4 once the free ends of fibres have been removed. In a similar construction, presented by Chandran and Barocas [167] and termed either 'micromesh' or 'growth' networks, uniformly seeded points are assigned a random orientation, from which fibres grow until meeting another, whence a cross-link is formed and growth halts. Nodes in such networks have coordination $z = 3$. Voronoi-type geometries, which also have node coordination 3 in the absence of symmetries, have been used to model fibre networks by viewing Voronoi edges as fibre segments and vertices as cross-links. If initial conditions are selected randomly, and a sufficiently large domain is chosen, these constructions all produce isotropic networks, that is they do not exhibit preferential directions.

The response of growth type networks was found to be nonaffine, with little correlation between initial and final fibre orientation [167]. The ability for such networks to reorganize reduced fibre strains, with the bulk deformation being accommodated by fibre rotations and translations. Growth geometries were used by Stylianopoulos and Barocas [213] to form a representative volume element (RVE). This RVE was used to motivate a macroscopic finite element model for collagen, finding good agreement with experiment. Investigations into polymer networks with a Mikado geometry have identified affine and nonaffine regimes, the transition between which was characterized [163, 185]. More recent work involving Mikado networks underlined the importance of cell aspect ratio in long range cell mechanical communication [137]. Voronoi networks have been used to represent a discrete collagen scaffold, embedded within a continuous, neo-Hookean solid [214]. This model resulted in good agreement with data from collagen gels, and

represented an holistic model, in which the fibrous network contributed to whole matrix mechanics. Other modelling approaches, alongside further details of those described above, are discussed in Chapter 1, as well as in the thorough review by Broedersz and MacKintosh [51].

The above modelling efforts have established DFN models as an important theoretical and computational modelling tool. However, the freedom of choice in network geometry raises questions on the generality of results derived from them. While it is known that prealigned geometries exhibit a far stiffer response at high strain [183], it is not clear how distinct isotropic architectures differ. We investigate the mechanical response of different isotropic networks that possess similar network topology. We aim to quantify the importance of network geometry, comparing different constructions in a range of systems. In particular, we investigate the effects of network choice on the deformation field around a contractile cell, the degree of fibre reorganisation and alignment within the matrix, and the heterogeneity in the mechanical response. We further investigate whether constituent fibre strain distributions are affected by geometry choice, and the plausibility of mechanical cell-cell communication within networks of different architectures. In summary, while controlling for material properties, together with network topology and cross-link density, we systematically investigate the relevance of geometry to the mechanical response of networks under uniaxial extension, local cell-derived tractions and cell-cell mechanical communication.

2.2 Methods

2.2.1 Model fibre choices

We present an athermal DFN model for a biopolymer matrix under deformation. In particular, fibre segments are modelled as elastic springs, which form a network structure through point cross-links that are freely jointed [172]. Fibres are assumed to have uniform diameter, so that the force-extension behaviour for each segment is equivalent. As such, our model takes the form of a subisostatic central force network, whence finite strains are employed, as discussed in Chapter 1.

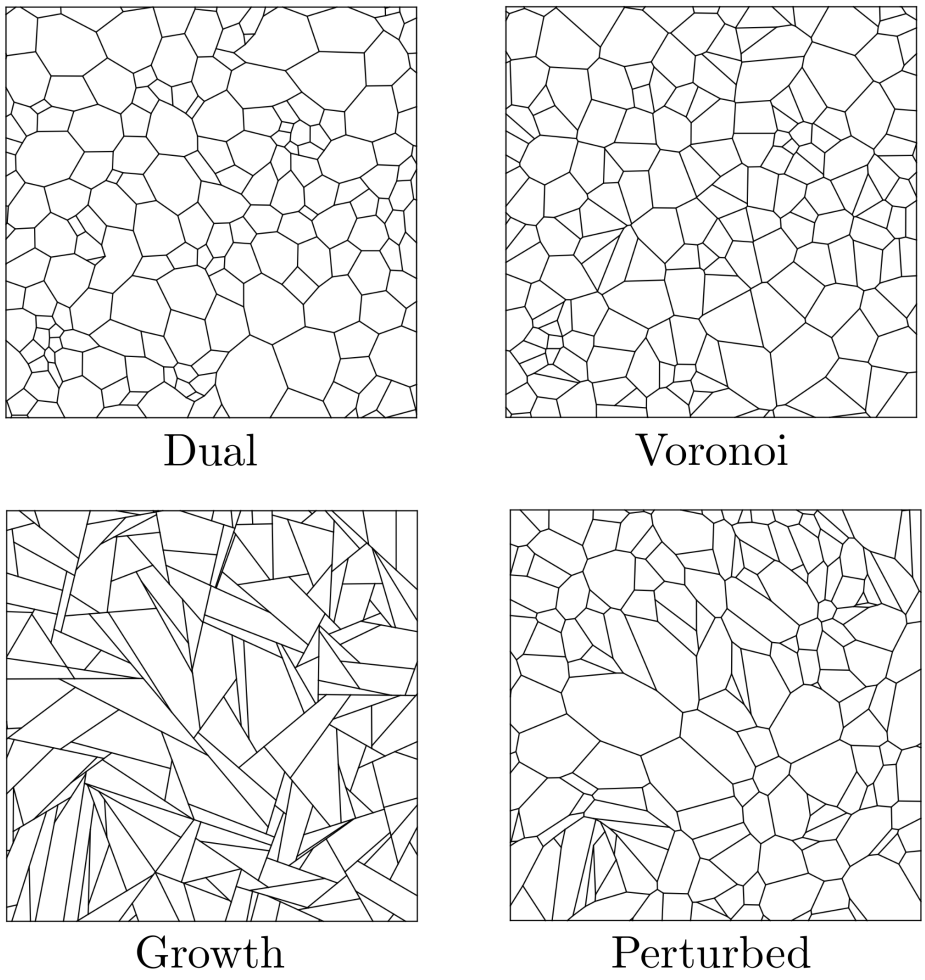

Figure 2.1: A visualisation of the local structure and geometry for each model architecture. Details for network generation are given in section 2.2.2. Dual and Voronoi networks share similar topologies, while the network structure of Perturbed architectures is identical to those of Growth networks.

As material nonlinearity in fibre networks arises primarily due to the geometric rearrangements of constituent filaments, we take model fibres to have a linear stress-strain relation [215]. We expect that slender matrix fibres should not support large compressions, as they would buckle instead. This is accounted for through a far softer fibre response in compression, similar to other studies [167, 196], giving a piecewise linear stress-strain relation. As stress is force per unit area, the fibre

extension or compression behaviour is given as:

$$F = \sigma A = EA\epsilon \ , \tag{2.1}$$

$$= \mu\epsilon \ , \tag{2.2}$$

where F is the force resulting from a fibre under extension or compression, A is filament cross-sectional area, E is the fibre elastic modulus, and $\sigma = E\epsilon$ is fibre stress, for strain ϵ. The fibre engineering strain ϵ is given by the ratio between the difference between initial and final fibre lengths and the initial length, that is:

$$\epsilon := \frac{\Delta L}{L} = \frac{L^{\epsilon} - L}{L} \ , \tag{2.3}$$

where L is the initial fibre length, and L^{ϵ} is the corresponding deformed length, with ΔL denoting the difference between the two quantities. The fibre stretching stiffness μ is related to the filament Young's modulus E, and cross-sectional area A as $\mu = EA$. A diameter of 200 nm was used as representative of a typical substrate fibre, and a Young's modulus $E_t = 1\,\text{MPa}$ was used for fibre extension. To represent the softer compressive or buckling response of fibres under compression, preliminary investigations were undertaken with Young's moduli between 0.1 - 100 kPa. It was found that the mechanical network response was insensitive to this choice, and for the results presented below a value of $E_c = 10\,\text{kPa}$ has been used for the Young's modulus of a fibre under compression. The above modelling choices are similar to several existing studies in the literature [72, 167, 183, 196].

Solutions are obtained through an over-damped, quasistatic scheme developed in the MATLAB environment [201]. In particular, small fixed displacements are iteratively enforced at domain boundaries and interior nodes relax to effective equilibrium. Explicitly, for the position vector $\boldsymbol{x}$ of a model cross-link, we have:

$$\frac{\mathrm{d}\boldsymbol{x}}{\mathrm{d}t} = \frac{1}{\nu}\sum_i \mu_i \epsilon_i \boldsymbol{t}_i \ ,$$

where summation is over fibres coincident to the cross-link, ϵ_i are the fibre strains, μ_i is the relevant fibre stiffness (either for extension of compression), $\boldsymbol{t}_i$ gives the fibre tangent direction, $|\boldsymbol{t}_i| = 1$, and ν is a damping term. For numerical solutions,

the above equation is non-dimensionalized with scales chosen such that there is unit damping. Boundary nodes are displaced and the overdamped system relaxes; the termination condition for this relaxation is given by the requirement that the maximum force on any network cross-link is six orders of magnitude smaller than the force scale associated with fibre extensions on the scale of the natural length, that is $\mu \times 10^{-6}$, ensuring effective force balance. This numerical method has been used by other studies investigating the large deformations of spring or truss networks [183]. While units are given as representative of substrate fibres, we emphasise that these values are taken so as to facilitate a comparative study into different network geometries rather than relate to experiment. As such, results are insensitive to these parameter choices within the overdamped limit.

2.2.2 Network geometry

Network architecture is defined through both a graph structure, that is the network topology or connectivity, and the network geometry, which is the spatial embedding of the mathematical graph. In order to investigate the impact of geometry on the network mechanical response, we select artificial networks of a given type. In 2D, it is possible to select networks used in existing models that have distinct geometric properties, but whose topology is similar. Furthermore, many of the interesting properties of fibre networks, including strain-stiffening, nonaffine response and fibre alignment are observed in both two and three dimensions [175, 216]. We therefore restrict ourselves to 2D networks, which may also be of greater relevance to the many planar studies published to date.

Throughout, network nodes are viewed as permanent cross-links between two fibre segments. We investigate networks with node coordination $z = 3$, which allows for comparisons between existing network types, and is similar to typical values for fibrin networks [196]. In particular, Voronoi- and 'growth'- type geometries are studied. Voronoi networks are generated by seeding M random points uniformly in a given domain as generators, from which a Voronoi diagram is formed. The resulting Voronoi edges are viewed as fibre segments, between either fibre branching

points or cross-links. For comparison, we also produce growth networks, as outlined by Chandran and Barocas [167]. These networks are generated by seeding N random points within the computational domain, and assigning each seed a random direction. These N fibres extend forwards and backwards in this direction until contacting either another fibre segment or a domain boundary, whence a cross-link is formed and the growth terminates.

Producing Voronoi networks from random seed points produces a random network with little local structure. In contrast, the fibre structure in growth networks results in interior nodes that support two parallel edges, so that an angle of π is present between two fibre segments at each node (see Fig. 2.1 **(c)**). As we wish to investigate the importance of geometry, we control for network topology by introducing two further network types, which can be viewed as geometric 'perturbations' of the primary architectures considered. Firstly, we use the same Delaunay triangulation corresponding to a given Voronoi network to produce a different dual graph. Here, nodes are introduced at each Delaunay triangle centre, whence connecting these cross-links through a shared triangle edge generates a network structure. The resulting architecture possesses a similar topology to the original Voronoi network. We refer to this geometry as 'dual'- type throughout. A geometric perturbation to growth networks is performed by introducing a small tension into each fibre segment, whence the system is allowed to relax to equilibrium. This equilibrium state is then taken as a strain-free network. In this way, the local structure observed at each node in growth networks, where each node shares two fibre segments separated by an angle of π, is removed. This perturbed network is thus a different spatial embedding of the same graph produced by growth networks, and differences in the mechanical response of these two network types derive purely from this geometric perturbation, rather than from the network topology. Throughout, these networks are referred to as 'perturbed'-type. The random procedures used to generate these geometries ensure that all architectures are isotropic at the network scale, and the Kolmogorov-Smirnov test [217] was used to confirm that networks exhibited no preferential fibre orientation. All networks are considered initially stress free, so

that initial and natural fibre lengths coincide. Visualisations of each architecture used in this chapter are shown in Fig. 2.1.

As cross-link and fibre density cannot be independently specified for each geometry in 2D, we control for cross-link density, which is known to strongly influence fibre network mechanics [169]. In particular, this ensures that the same number of constraints exists in each network type. Except where otherwise specified, networks of cross-link density $0.2\,/\mu m^2$ are used. This gives corresponding mean fibre densities of $0.63\,\mu m/\mu m^2$, $0.70\,\mu m/\mu m^2$, $0.8\,\mu m/\mu m^2$ and $0.67\,\mu m/\mu m^2$ for dual, Voronoi, growth and perturbed networks respectively. We note the slightly lower fibre density for dual geometries and slightly higher density for growth networks, which is a consequence of fixing cross-link density.

Three mechanical tests are employed to investigate the importance of network geometry at different scales. Firstly, networks are subjected to uniaxial extension, as shown in Fig. 2.2 **(a)**. Here, boundaries are defined so as to include boundary polygons, thus avoiding dangling ends, which do not contribute to the static mechanics of the network. A domain size of approximately $100\,\mu m$ is selected, which was sufficient to ensure an isotropic distribution in fibre orientation. Boundary nodes (marked in red, Fig. 2.2 **(a)**) are subjected to fixed horizontal displacement. Single cell contractions are modelled by removing a circular region from a network, as in Fig. 2.2 **(b)**. The inner circular region, representing a model cell, is allowed to contract radially, while nodes attached to the outer boundary remain fixed. Model cells have initial diameter of $20\,\mu m$ and final diameter of $10\,\mu m$, within a domain of diameter $120\,\mu m$. Mechanical cell-cell communication is investigated by introducing cells (final diameter $10\,\mu m$) into a larger rectangular domain such that boundaries are never closer than in the single cellular case, as shown in Fig. 2.2 **(c)**. A cell separation distance ranging between $50 - 70\,\mu m$, corresponding to separations of 5-7 final cell diameters, is used to investigate the ability for cells to communicate mechanically. Results are averaged across 20 network realisations to allow for an investigation of variability in network response.

In summary, we investigate the finite strain mechanics of four different network architectures. Each network is paired with another of similar or identical graph structure, to control for the effects of topology, and cross-links in all networks have node coordination $z = 3$, such that the number of constraints is equivalent. We control for density by fixing cross-linking density across all networks. Equivalent material parameters are used for all network choices. Mechanical tests are performed so as to investigate bulk and local responses of different network architectures. As such, this model is designed to isolate, so far as is possible, the importance of geometry to the mechanical response.

2.3 Results

2.3.1 Network stiffness under uniaxial extension is dependent on network choice

We first investigate the response of different networks under uniaxial extension, as shown schematically in Fig. 2.2 **(a)**. Many biopolymer assemblies exhibit a strain-stiffening response, with characteristic toe, heel and linear regions [3, chap. 17]. Networks of different architectures are strained up to 50% stretch, and stress is calculated by summing over the normal forces at boundary nodes, dividing by the total edge length. Engineering stress-strain curves for each network considered are given in Fig. 2.3 **(a)**. As strain increases to 50%, all networks exhibit a strain-stiffening response. Interestingly, a far stiffer response is present in Voronoi than growth networks, with stress at 50% strain in Voronoi geometries almost double that found in the growth case. To further investigate the nonlinear behaviour in each network architecture, we plot the tangent modulus K with strain in Fig. 2.3 **(b)**. Strain-stiffening occurs at low bulk strains $\epsilon < 3\%$ in both Voronoi and perturbed networks, such that the linear regime is small. The response of these two architectures is qualitatively similar across the range of strains considered, though Voronoi networks consistently exhibit a slightly stiffer response. The onset of strain-stiffening occurs later in dual networks, and later again in growth architectures, at approximately 7% bulk strain. The tangent modulus in

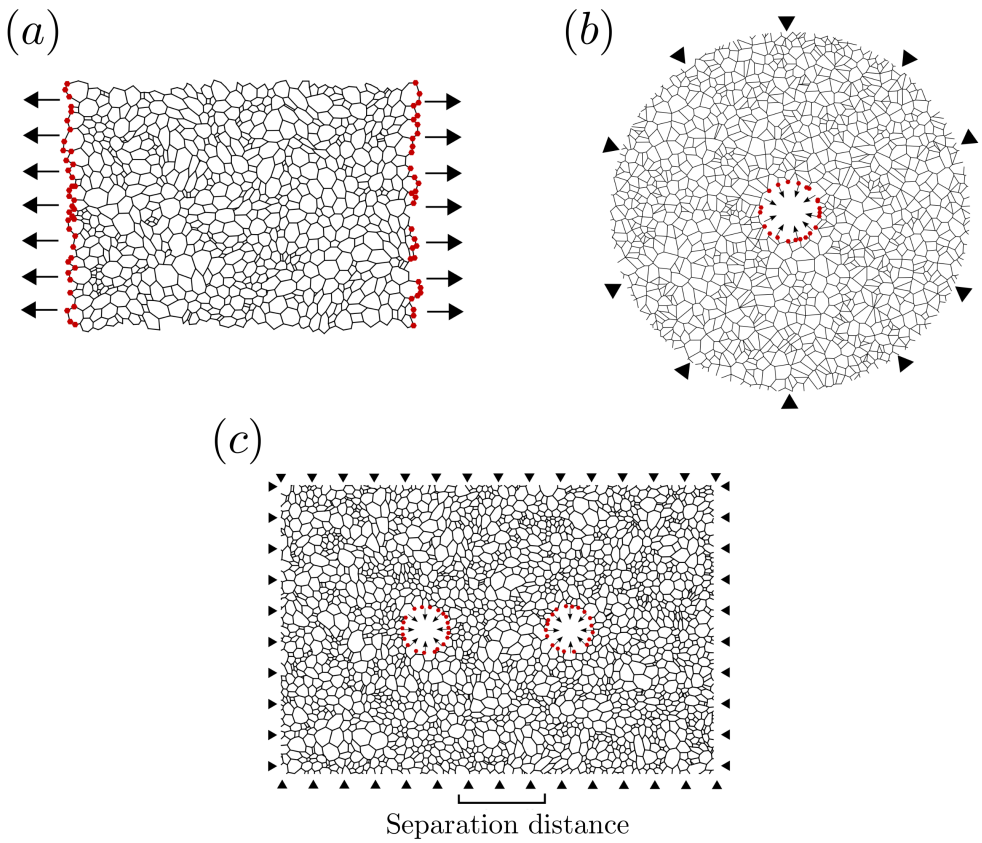

Figure 2.2: Model domains for computational tests. Displaced boundary nodes are highlighted in red. **(a)** Uniaxial extension of a dual type network. Boundary nodes are displaced horizontally, as indicated by arrows. **(b)** Single cell contraction within a Voronoi network. An interior circle is removed from the domain, and inner boundary nodes are displaced in the radial direction towards the cell centre, with outer boundary nodes fixed. **(c)** Pairwise mechanical cell communication within a dual network. Two interior circles are removed from a network within a rectangular domain. Both cells contract as in the single cell case. The separation distance between pairwise cells is defined to be the shortest membrane-membrane distance. Triangular markers signify zero displacement boundary edges.

growth networks is notably smaller than in other architectures across all strains considered. Given that model fibres have a piecewise linear response, the observed nonlinearity is purely geometric in origin, due to the reorganisation of network fibres. Notably, the perturbation to the growth type geometry has the effect of changing both the quantitative stiffness and the qualitative shape of the stress-strain curve under uniaxial extension, suggesting that geometry plays a key role in planar substrate network mechanics.

We investigate the cause of this increase in stiffness from a micromechanical

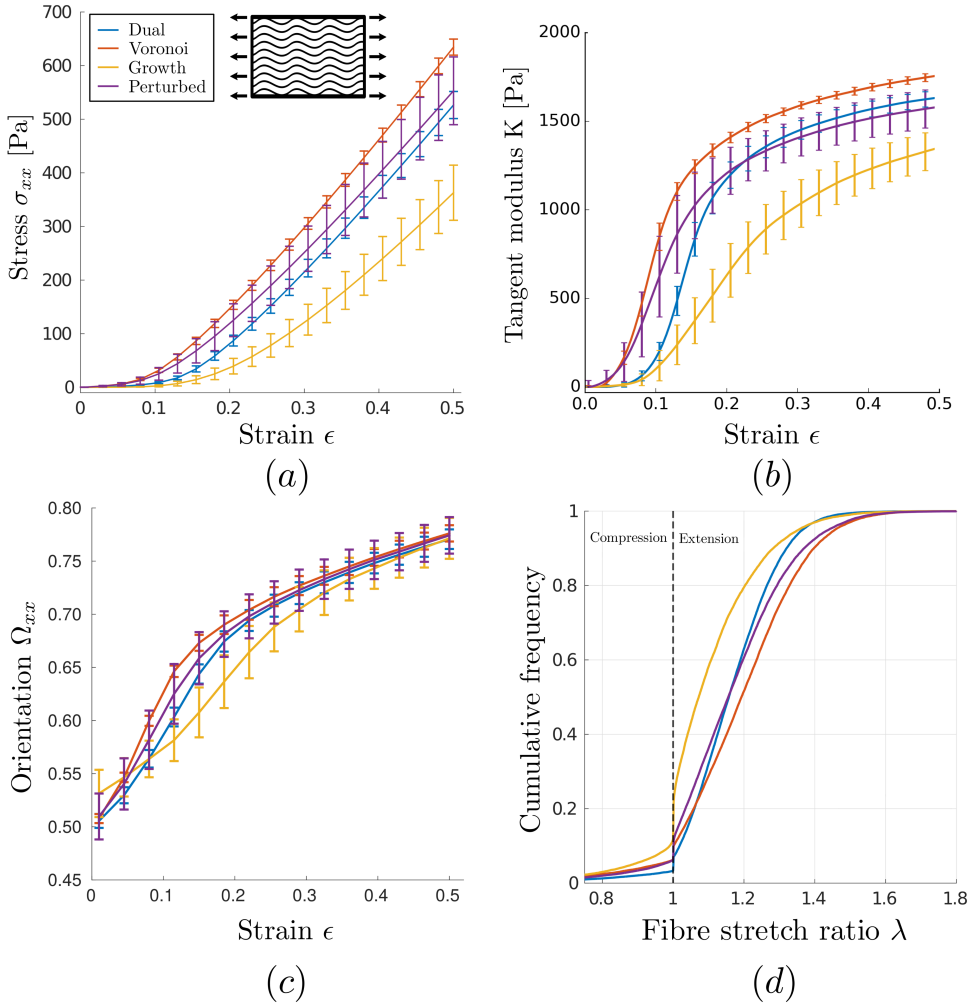

Figure 2.3: Mechanical response of networks under uniaxial extension. **(a)** Engineering stress-strain curves show that Voronoi networks are relatively stiff, while growth cases exhibit the most compliant response. The inset shows the uniaxial test performed. **(b)** The tangent modulus K with strain is plotted for each network architecture. All networks exhibit strain-stiffening, though the onset of strain-stiffening occurs later in dual and growth architectures. Voronoi and perturbed networks display qualitatively similar nonlinear behaviour. **(c)** The orientation parameter Ω_{xx}, defined in the text, increases with strain for all networks, as constituent fibres reorient with the direction of extension. **(d)** Cumulative fibre stretch (λ) distributions within different network geometries at 50% strain underline micromechanical differences, with far fewer strained, and more buckled, fibres present in growth networks than in Voronoi geometries. Bars give 1 s.d. about the mean value.

perspective, that is as quantified through single fibre properties. Firstly, we investigate network fibre alignment. We introduce the orientation tensor:

$$\Omega_{ij} := \frac{\sum\limits_k p_i^k p_j^k}{\sum\limits_k |\mathbf{p}^k|} \ , \tag{2.4}$$

as a measure of geometric alignment. Here, $\mathbf{p}$ are vectors describing a given family of k network fibres, while i, j are axis directions. Explicitly, we can represent a model fibre through the vector:

$$\boldsymbol{p} := \begin{bmatrix} p_x \\ p_y \end{bmatrix} = |\boldsymbol{p}| \begin{bmatrix} \cos\theta \\ \sin\theta \end{bmatrix} \ ,$$

where θ denotes the angle between the fibre and the positive (horizontal) x-axis. For alignment with the direction of extension, that is with the horizontal, the above expression and Eq. 2.4 yields:

$$\Omega_{xx} := \frac{\sum\limits_k p_x^k p_x^k}{\sum\limits_k |\mathbf{p}^k|} = \frac{\sum\limits_k |\mathbf{p}^k| \cos^2\theta^k}{\sum\limits_k |\mathbf{p}^k|} \ , \tag{2.5}$$

where θ^k is the angle between a fibre and the positive x-axis. A value of 0.5 represents nominal isotropy, while a value of 1 gives a perfectly aligned network. We do not expect orientation to be meaningful for buckled fibres, such that we neglect fibres with $\lambda < 1$, where stretch ratio $\lambda := L^\epsilon/L$ gives the ratio of deformed L^ϵ to initial L fibre length. The change in orientation parameter as strain increases is shown in Fig. 2.3 **(c)**, showing that fibres become progressively more aligned with the direction of displacement as strain increases. The orientation measure is similar across dual, perturbed and Voronoi cases, with minor differences observed in growth networks, as strain increases. Despite these differences, considerable reorientation of network fibres with the direction of loading is observed in all networks, with similar alignment from 30% strain.

We further quantify the fibre segment strains throughout each network under bulk uniaxial extension. Cumulative frequency distributions for fibre stretch are shown in Fig. 2.3 **(d)**. Interestingly, growth type networks contain considerably more buckled, and fewer strained fibres than other network geometries. As buckled fibres are not included in our consideration of alignment, this provides a partial explanation for the

different orientation response of growth networks. In contrast, Voronoi geometries favour a greater number of strained fibres, in agreement with their stiffer response.

Given the above differences in stiffness under a bulk mechanical test, we proceed to investigate whether geometry continues to be an important regulator of network mechanics for local perturbations, and consider the implications for cell function in different architectures.

2.3.2 Displacement fields arising from single contractile cells exhibit qualitative differences with choice of initial network geometry

Adherent cells contract and reorganise their substrates, leading to long-range displacement fields that extend for many cell diameters [108]. We wish to quantify the degree to which different network geometries support these far-reaching substrate disturbances. The magnitude of the cross-link displacement fields, as generated by a uniformly contracting cell adhered to the substrate, are visualised in Fig. 2.4 **(a)** - **(d)**. Interestingly, the choice of network geometry profoundly affects cell-derived displacement fields. All networks supported a long-ranged displacement field, with large substrate displacements (above 1 μm) between four and five cell diameters distant, similar to experimental results [108]. The average mean displacement decay over 20 networks of each type is quantified in Fig. 2.5 **(a)**, showing displacement fields reaching the outer boundary in dual, perturbed and Voronoi geometries. A similar mean displacement decay rate is observed in these three geometries, while growth networks supported a shorter-ranged mean field.

Inspection of the displacement fields arising in individual growth networks, as in Fig. 2.4 **(c)**, suggests that localized network regions display displacements of several micrometers many cell diameters away, while other regions are relatively unperturbed. As such, the displacement field in growth geometries is symmetry-breaking, which is also observed to a lesser extent in dual and perturbed networks. As a measure of asymmetry, each annular domain was binned into 12 angular segments. Mean displacement within each binned region was calculated, and normalized to the maximum value across all bins. The standard deviation in these

quantities provides a measure of angular variation in the displacement fields, and therefore symmetry-breaking, as shown in Fig. 2.5 **(b)**. We find that this quantity is lowest for Voronoi networks, suggesting that the displacement field here respects the symmetry of the deformation, but is considerably larger in other architectures. In particular, growth networks support the largest measure of asymmetry, agreeing with the visual discussion of Fig. 2.4.

Within a simple elastic medium, the motion of a material under radial contraction would not involve a transverse component. However, where fibres are free to rotate and translate, this property is lost, and we expect to see some displacements away from the radial direction. Visualisations of these transverse displacement fields $|U_\theta|$ are shown in Fig. 2.6 **(a)** - **(d)**, and quantified in Fig. 2.5 **(c)**. Despite the purely radial cell contraction, considerable transverse motion is observed in all networks, except for in Voronoi architectures, where it appears minimal. In particular, these transverse motions appear large in growth geometries. This result could have important implications for cells communicating through substrate displacements [147], as the signal mediated by the fibrous substrate might not robustly communicate the direction of displacement when large transverse displacements arise.

2.3.3 Network choice strongly influences stress transmission and membrane reaction force

Having discussed the displacements arising as cells contract in fibre networks, we now consider the nature of stress transmission through different network architectures. Experiments suggest that cells contracting within compliant substrates transmit stress over long distances, allowing for the detection of distant cells and boundaries [142, 211]. We investigate the constituent fibre strains induced through the contraction of a single cell. To investigate stress transmitted through the substrate, individual fibre strain energy densities (SED) were calculated, according to:

$$\hat{\mathcal{H}} = \frac{1}{2}\sigma\epsilon = \frac{\mu\epsilon^2}{2A} \,, \tag{2.6}$$

where $\hat{\mathcal{H}}$ is fibre SED, ϵ is fibre strain after Eq. 2.3, A is the cross-sectional area and μ is the relevant stiffness for extension or compression, as given in Eq. 2.2. The

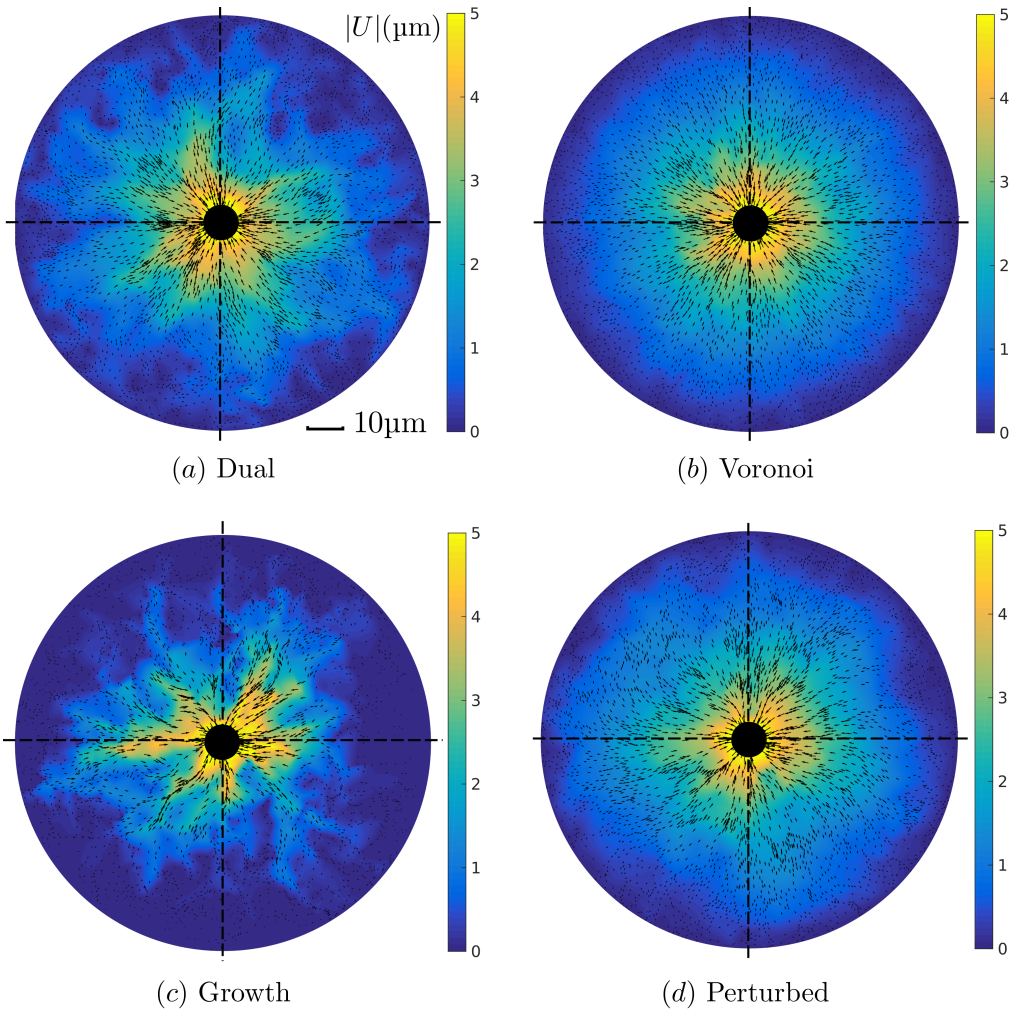

(a) Dual (b) Voronoi

(c) Growth (d) Perturbed

Figure 2.4: Displacement fields $|\boldsymbol{U}|$ (μm) due to a contractile cell show clear qualitative differences as network architecture is varied. In particular, largely symmetric fields are observed in Voronoi geometries, while a highly heterogeneous field, involving symmetry breaking, arises in growth networks. Black arrows give displacement vectors for fibre midpoints. Continuous plots here and throughout are generated through natural neighbour interpolation in MATLAB.

spatial SED resulting in each network geometry under cell contraction is visualized in Fig. 2.7, highlighting orders of magnitude architecture-dependent differences. In particular, a small family of fibres in growth geometries appear to form paths, reaching towards the outer boundary, while other constituent fibres experience very little stress. In contrast, Voronoi and perturbed networks support largely symmetric and far reaching fields. Stress transmission in dual networks is qualitatively similar to that in Voronoi and perturbed cases, though a greater degree of symmetry-breaking is observed, alongside a far lower SED. The decay of mean fibre SED with distance

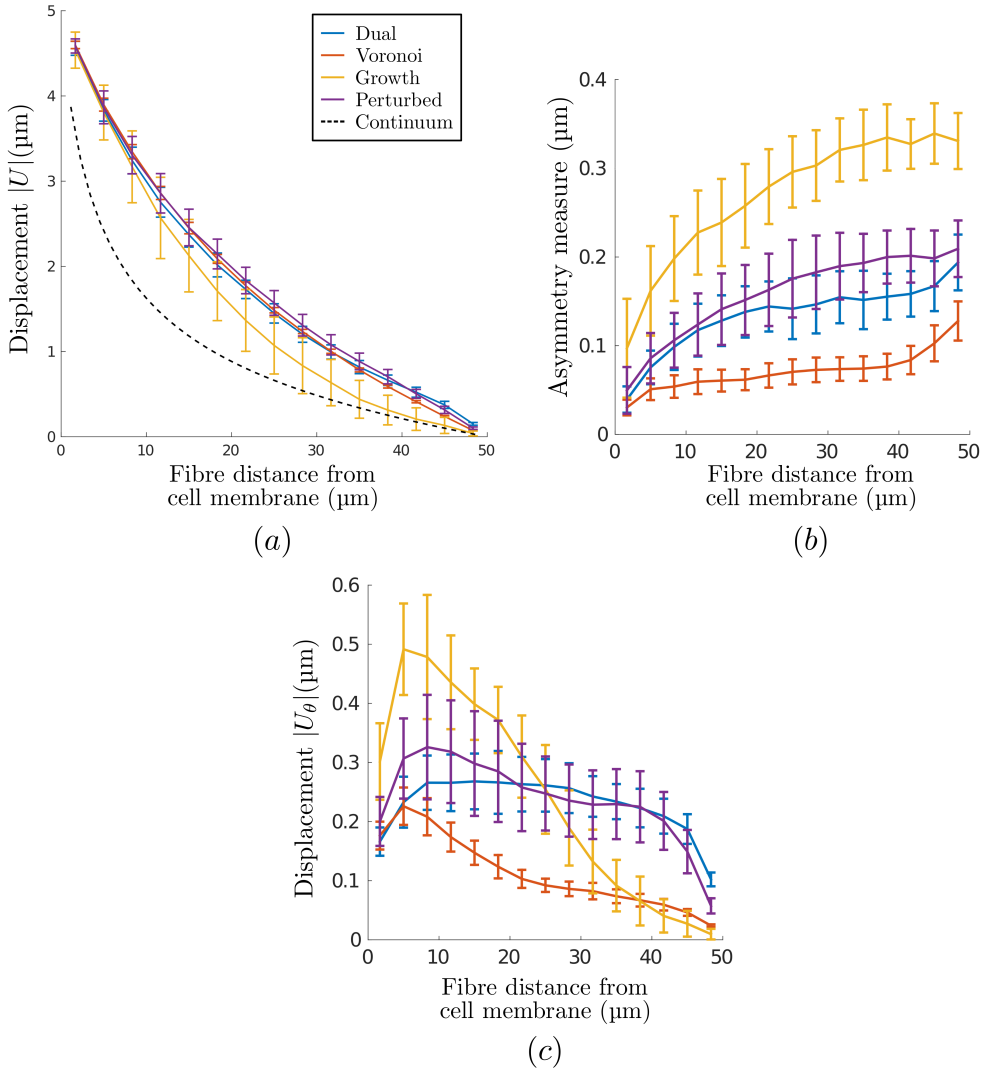

Figure 2.5: Comparison of displacement fields induced by a contracting cell in different architectures. **(a)** Mean displacement $|\boldsymbol{U}|$ is plotted with distance from the cell membrane; long-range effects are observed for all cases considered, though growth networks extend considerably less far. In Voronoi, dual and perturbed networks, mean substrate displacement above 1 µm is observed more than 3 (final) cell diameters distant. Dashed line shows equivalent displacement decay in a homogeneous elastic continuum. **(b)** Asymmetry in cell-derived displacement fields, showing the highly asymmetric fields in growth geometries, and the more symmetric fields induced within Voronoi networks. **(c)** Mean transverse displacement $|U_\theta|$ as distance from the cell membrane increases. Significant transverse motion is present in growth networks, while displacement is largely radial in Voronoi cases. Bars give 1 s.d. about the mean value.

from the cell membrane is quantified in Fig. 2.8 **(a)**. The decay of fibre SED in Voronoi and perturbed networks is notably similar, with SED decaying to a constant value far from the cell, evidencing the transmission of stress to the outer boundary.

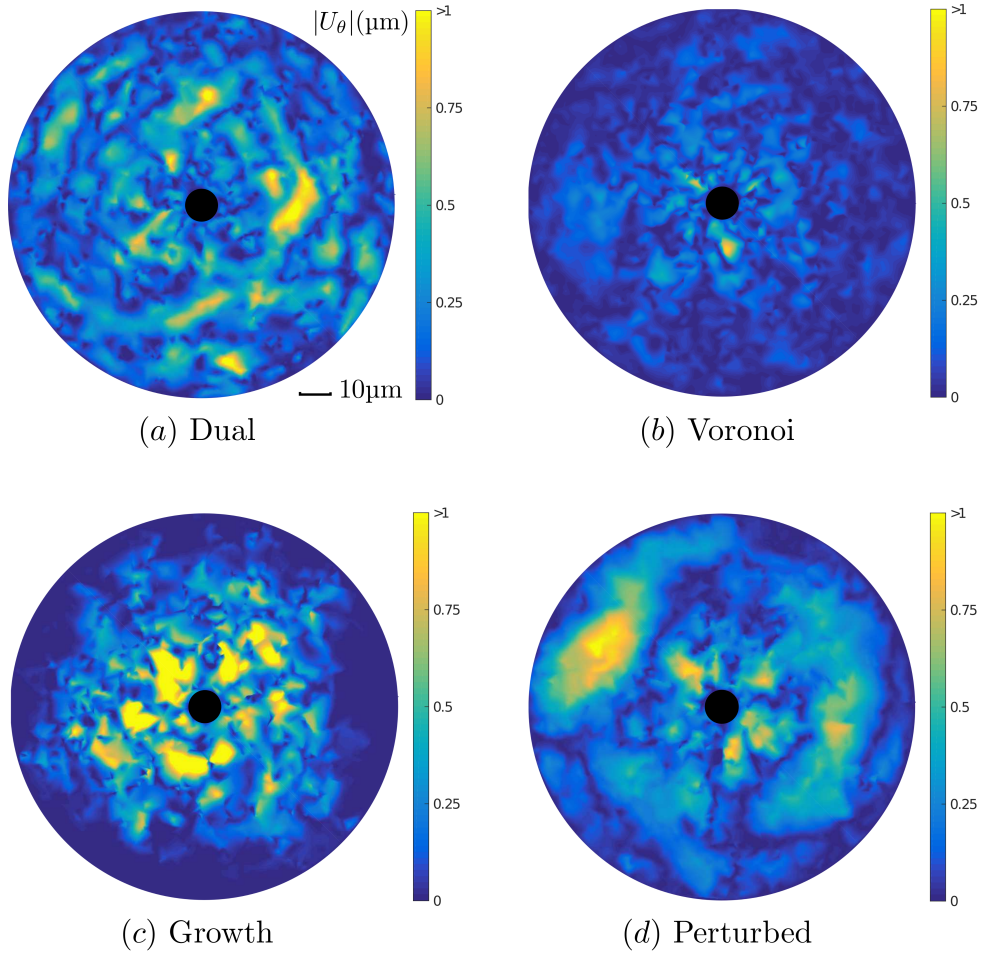

Figure 2.6: Visualisations of transverse displacement fields $|U_\theta|$ (µm) due to a single contractile cell in each network. Considerable transverse displacements, above 1 µm, are observed in growth networks a large distance from the cell membrane, while displacement fields observed in Voronoi architectures act almost entirely in the radial direction.

In contrast, relatively little strain is transmitted beyond roughly one cell diameter distant in growth and dual cases. We note that despite the similar displacement decay rate observed for dual, Voronoi and perturbed architectures (Fig. 2.5), marked differences arise in the ability to transmit stress through the network.

Cells respond sensitively to substrate stiffness, likely through a stress-limited mechanism [15, 108]. We quantify the stress at the cell membrane as a measure of how stiff a substrate appears to a contractile cell in Fig. 2.8 **(b)**. In particular, we calculate normal membrane stress as the sum, over fibres connected to the cell membrane, of the normal components of fibre reaction forces, divided by the

original cell membrane area. Despite equivalent cross-link density and material parameters, cells contracting in Voronoi and perturbed geometries experience a far stiffer response than those in growth or dual networks. Interestingly, cells in Voronoi and perturbed geometries experience resistance to contraction even at small strains. In reference to Fig. 2.7, we anticipate this is due to the rapid appearance of stress paths, where initially slack paths become constrained as the cell contracts. The absence of all but an isolated few such paths forming in growth networks, even at maximum cell contraction, explains the less stiff response experienced by cells in this geometry. The transmission of stress to the distant outer boundary is quantified in Fig. 2.8 **(c)**. Cell contraction induces a reaction force at the outer boundary in Voronoi and perturbed geometries, even for small cell contractions. Within dual type networks, a stress response at the outer boundary occurs once cell contraction reaches approximately 2.5 μm, leading to a clear stress signal at full contraction. In contrast, very little stress is transmitted to the boundary in growth networks, suggesting long range detection of boundaries might not be possible in this geometry. Again, this result can be viewed in terms of the stress paths, visually clear in Fig. 2.7.

We investigate the fibre scale origins of these notable differences in strain and stress transmission by plotting the cumulative fibre stretch distribution in Fig. 2.8 **(d)**, for each of the four architectures considered. Interestingly, approximately 20% of fibres in growth networks buckle or compress under cell contraction, with larger strains, above 1%, localized to just 10% of total fibre segments. Dual networks do not contain the same extent of buckled fibres, though filaments here are generally less stretched than in Voronoi or growth networks. The steep sigmoidal shape suggests that the dominant contributions to strain energy are from a relatively small family of fibres. In contrast, strain is distributed more evenly throughout perturbed and Voronoi geometries, with fewer buckled fibres, and $80-90\%$ of fibres above 1% strain. Similarities between strain distributions in perturbed and Voronoi cases suggest that the perturbation applied to growth networks encourages a geometry that favours long-range stress transmission.

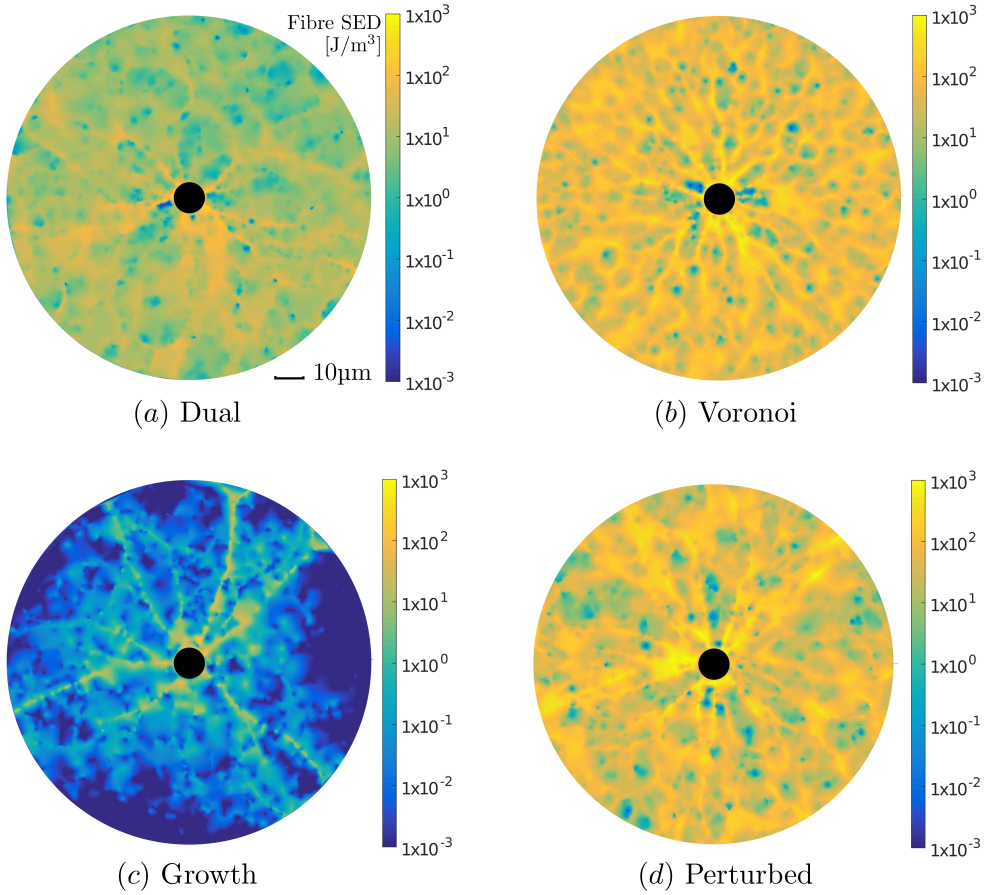

Figure 2.7: Strain energy density (SED) fields derived from single cells contracting in each network. Highly heterogeneous, shorter ranged fields are observed in growth geometries, while long-range stress transmission to the distant boundary is observed in Voronoi and perturbed networks. In growth networks, clear stress paths extend from the cell membrane to the outer boundary, suggesting that the majority of strained fibres exist within these isolated paths. Note the order of magnitude differences between architectures, as illustrated by log scale colour bars.

2.3.4 Fibre reorganisation far from the cell membrane depends on geometry choice, and correlates with fibre strain

We now seek an explanation for the qualitative differences identified in the displacement and SED fields for distinct network geometries. In particular, we investigate correlations between fibre stretch ratio and fibre alignment, and the rotation of constituent fibre segments with distance from the cell membrane.

The quantity Ω_{rr}, the radial analogue of Eq. 2.4, measures the radial alignment of fibres. Fig. 2.9 **(a)** shows the relation between this alignment parameter and fibre

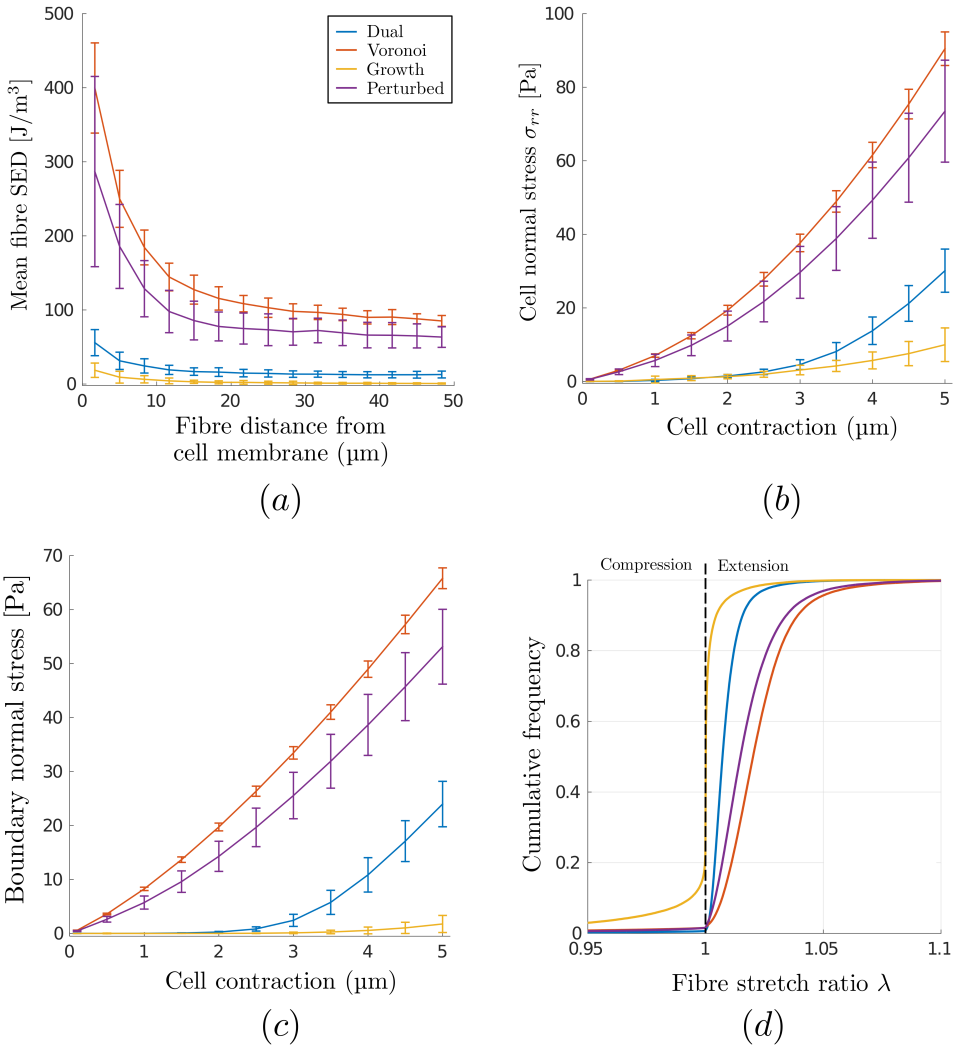

Figure 2.8: The transmission of stress in fibre networks. **(a)** Mean fibre strain energy density (SED) is plotted for maximum cell contraction, showing far greater range of stress transmission in Voronoi and perturbed geometries than in growth or dual networks, with considerable strain energy more than 5 cell diameters distant. **(b)** Cells contracting in Voronoi and perturbed networks experience a far stiffer response than those in growth and dual networks. **(c)** Stress reaches the distant outer boundary in perturbed and Voronoi geometries, even at low cell contraction while in growth networks the distant boundary experiences very little stress. **(d)** Cell contraction leads to the buckling of $\approx 20\%$ of growth network fibres. The more shallow sigmoid found in Voronoi and perturbed geometries suggests that fibre strain is more equally distributed in these networks. Bars give 1 s.d. about the mean value.

stretch. In all networks, increasing fibre stretch correlates with increased alignment. In growth networks, the most strained fibres are almost all highly aligned in the radial direction. This result is largely true in dual networks, though fibre strains

are larger in general. The lower alignment value for Ω_{rr} in perturbed and Voronoi cases suggests that strained fibres can exist in a variety of conformations, both aligned and unaligned. Interestingly, in both Voronoi and perturbed cases, we see that fibres up to 1% strain are more likely to exist in an unaligned configuration. As such, geometric differences in these networks allow for stretched fibres to exist in a greater range of configurations, allowing for enhanced stress transmission in comparison with growth and dual networks.

To investigate why fibres exhibit higher strains in certain geometries, thus propagating stress, we quantify fibre rotation, that is the angle through which constituent fibres rotate under the action of the contractile cell, with distance from the cell membrane in Fig. 2.9 **(b)**. Fibre segments in growth networks move through larger rotation arcs on average, implying that these network architectures allow for the reorganisation of fibres. The differences between the rotational behaviour of fibres in Voronoi and perturbed cases are small, with both displaying little rotation far from the cell boundary. Given that fibre SED extends far from the cell membrane, this implies that fibres are constrained to stretch rather than rotate, thus allowing for the greater extent of stress transmission, as seen in Fig. 2.7. Dual networks behave similarly to Voronoi and perturbed cases close to the cell membrane, though the higher degree of fibre rotation beyond 2 cell diameters away suggests that this geometry is not as constrained with regards to fibre reorganisation, accommodating the bulk strain though fibre rotations rather than filament extension. It is interesting to note that a purely geometric difference, between growth and perturbed networks, encourages or prevents rotation over fibre stretch. These results offer a micromechanical explanation as to how geometry can promote qualitative differences in network response to local perturbations.

2.3.5 The dependence of mechanical response upon network geometry persists at higher densities

Before exploring the ability for pairwise cells to mechanically communicate through networks of different geometries, we first investigate whether the architectural

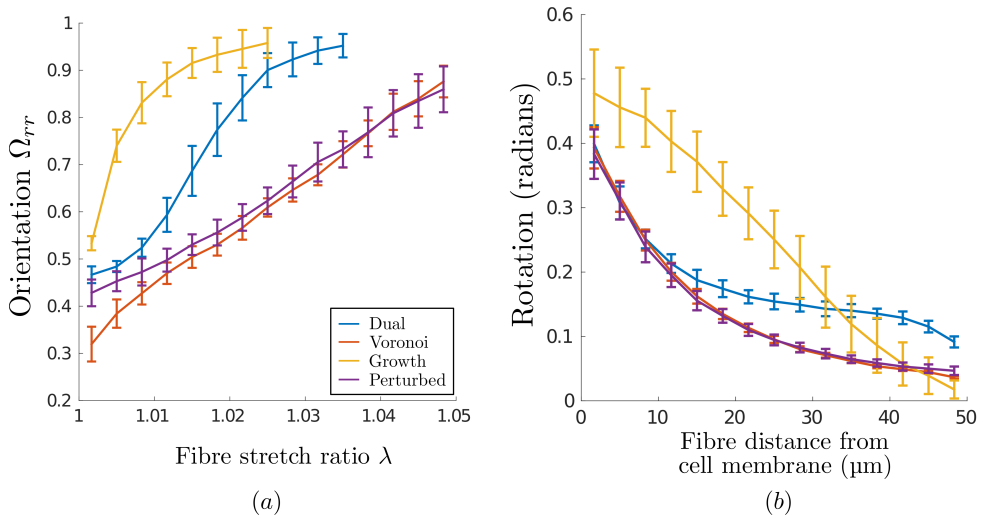

Figure 2.9: Alignment and reorganisation of non-buckled fibres. **(a)** Orientation of fibre families with increasing stretch ratio is plotted, showing a strong correlation between increasing fibre stretch and radial alignment in all networks. The strain distribution in Voronoi and perturbed geometries allows for families of fibres under considerable strain ($1 - 2\%$) to remain misaligned with the direction of radial stretch. **(b)** Mean rotation (radians) of constituent fibres within a network is plotted. Considerable fibre rotation is observed in growth networks, and far from the cell boundary in dual networks. The geometry of Voronoi and perturbed networks restricts rotation of fibres far from the cell membrane, and encourages stretching of individual network fibres. Bars give 1 s.d. about the mean value.

differences observed in stress transmission and displacement fields depend sensitively on network density. That is, we investigate whether the differences are robust to increases in density. As such, we compare displacement and fibre stretch results for networks of 1.5 and 2 times cross-link density, which corresponds to cross-link densities of $0.3\,/\mu m^2$ and $0.4\,/\mu m^2$ respectively. As network density increases, the mean segment length becomes small, and we might expect networks to become stiffer. Displacement with distance from the cell membrane for Voronoi and growth networks of the three densities considered are shown in Fig. 2.10 **(a)**. We find that the differences in our results as cross-link density is varied are small, and clearly within one standard deviation for individual networks of equal density, suggesting the extent of cell-derived displacement fields persists at a range of densities. Further, cumulative fibre stretch distributions show negligible differences as network density increases, as shown in Fig. 2.10 **(b)**. This insensitivity to a two-fold increase in

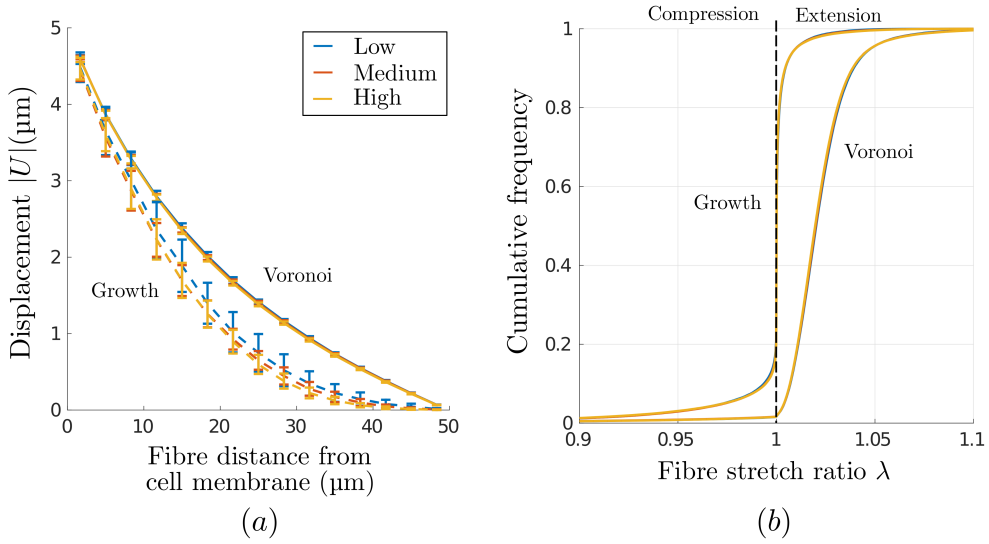

Figure 2.10: Important architecture-dependent differences in network response persist for a range of densities. **(a)** Mean displacement $|U|$ is plotted with distance from the cell membrane, for three cross-link densities. A slight variation, within 1 s.d., is found upon increasing fibre density. **(b)** Cumulative frequency plots for fibre stretch ratio is shown. The distributions remain almost identical under a two-fold increase in cross-link density. As such, the results presented here are sensitive to architecture and appear insensitive to network cross-link density. Bars represent 1 s.d. about the mean value.

cross-link density suggests that these results are features of the specific architectures, rather than the specific network parameters selected. We therefore continue to investigate pairwise cell interactions at a single density without loss of generality.

2.3.6 Pairwise contractile cells can mechanically signal through transmitted stress in certain architectures

Certain cells possess the ability to communicate mechanically through substrates, with pairwise cell motility influenced by substrate compliance [147], and alignment of both cells and substrate over long distances [108]. We investigate the ability for mechanical signals to be transmitted between pairs of cells through different network geometries, as shown schematically in Fig. 2.2 **(c)**. Fibre SED within networks containing pairs of cells at three distances, corresponding to separations of 5, 6 and 7 (final) cell diameters, is investigated. Single network visualisations are shown in Fig. 2.11 for cell separations of five cell diameters. In this case, where the separation distance is relatively small, bands of high strain energy are clearly

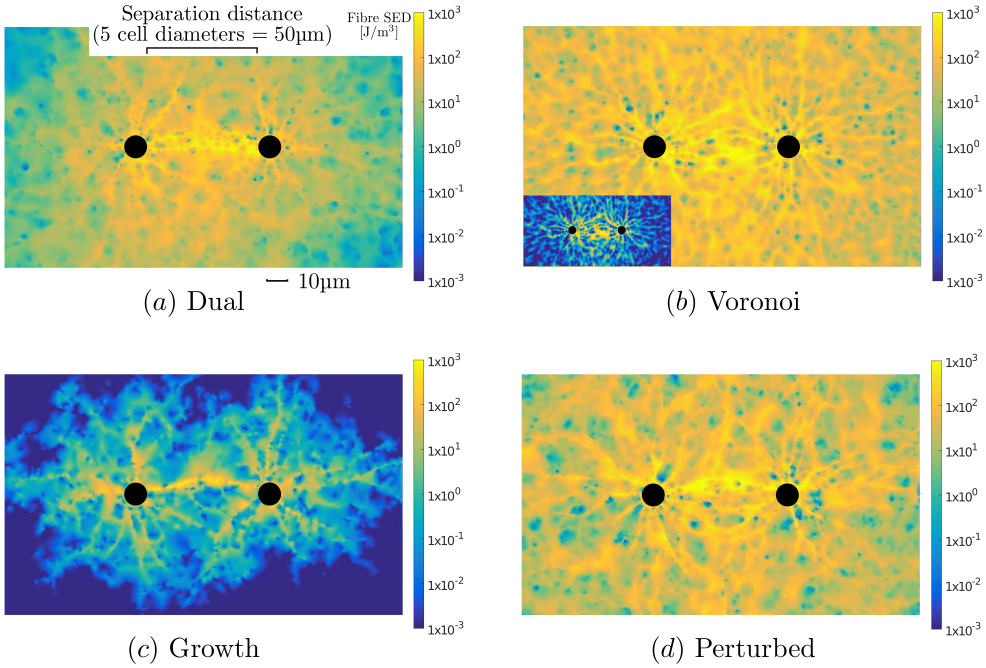

(a) Dual (b) Voronoi

(c) Growth (d) Perturbed

Figure 2.11: Visualisations of fibre strain energy density for pairwise contracting cells at a separation distance of 50 μm = 5 final cell diameters in **(a)** dual, **(b)** Voronoi, **(c)** growth, and **(d)** perturbed networks. Increased strain energy density in the intercellular region is clear in all networks, as evidence by the bright band in between cells. Note the log scale colour bars, underlining order of magnitude differences in strain energy fields. **(b) (inset)** To highlight the presence of SED banding between cells in the Voronoi case, a rescaled plot is included. Logarithmic colour scaling gives one order of magnitude difference.

visible between contracting cells. At greater separations, corresponding to 7 cell diameters, as shown in Fig. 2.12 **(a)** - **(b)**, increased SED between cells is still clear in Voronoi networks **(a)**, while this banding is minimal or absent in growth geometries **(b)**. We define a mechanical signal between two cells to be the difference in normal stress measured on the two halves of the cell, that is the halves facing towards and away from the other cell. In particular, if the cell membrane stress on the half facing towards a distant cell is greater than that on the other half, this signal is positive. We plot the mechanical signal with increasing cell contraction in Fig. 2.13, for a separation distance of 5 cell diameters. A stress signal at maximum radial contraction (5 μm) is observed in all geometries. However, the larger standard deviation in this signal for the growth network cases highlights the possibility that cells in these geometries cannot communicate mechanically. In contrast, the stronger

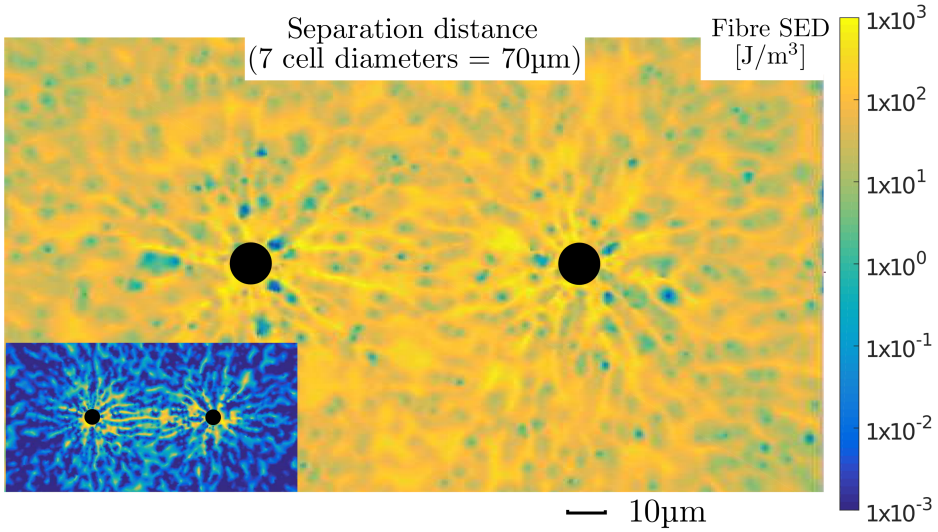

(*a*) Voronoi - high separation distance

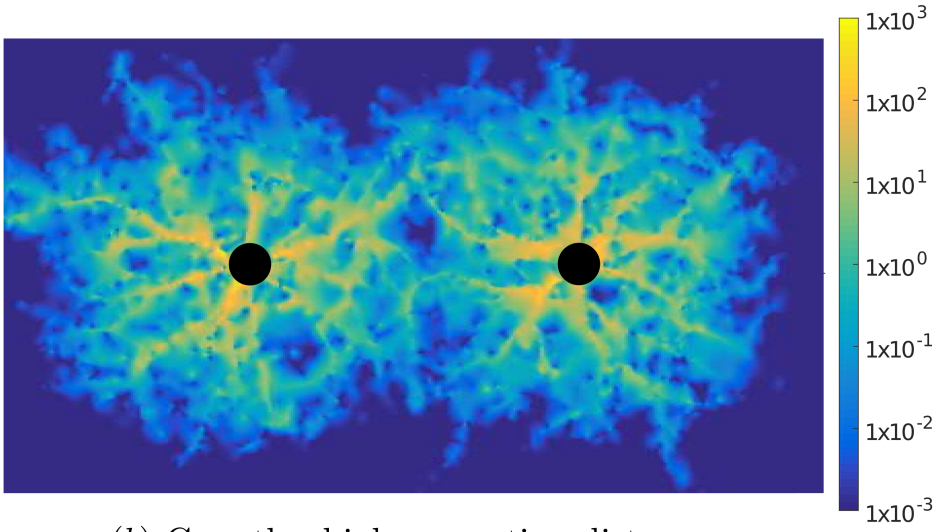

(*b*) Growth - high separation distance

Figure 2.12: Visualisations of fibre strain energy density for cells contracting at maximum separation distance $70\,\mu m = 7$ (final) cell diameters. **(a)** Increased strain energy between cells is observed for cells contracting in Voronoi networks at a higher separation distance of 7 cell diameters. Inset is a rescaled plot to highlight SED banding between cells. Logarithmic colour scaling gives one order of magnitude difference in this case. **(b)** No such increase is found in growth networks, suggesting that cells cannot robustly communicate mechanically over such distances in this architecture.

signal, and smaller standard deviation, in Voronoi networks implies that there exists a more robust transmission of stress signal between cells.

Fig. 2.13 **(b)** shows the signal parameter in each network geometry for maximum

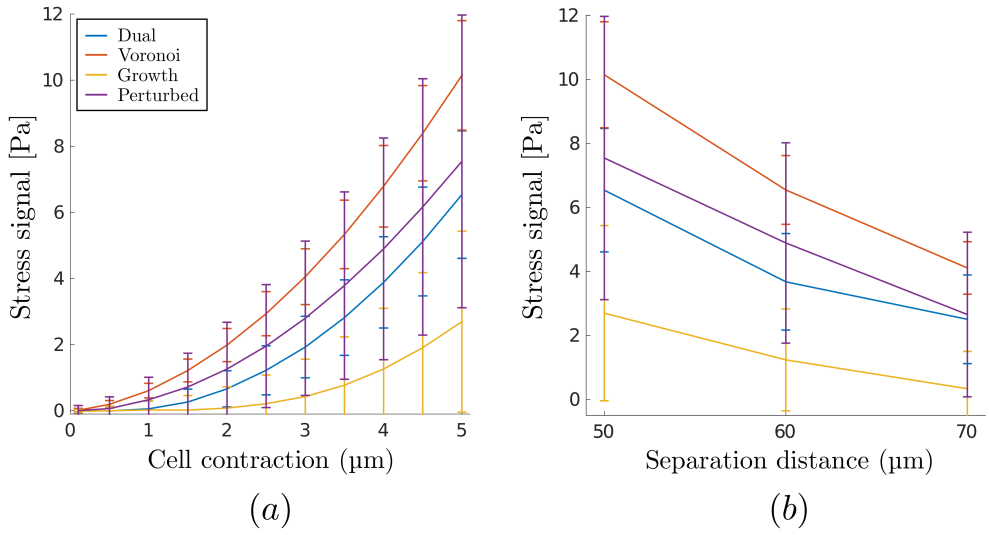

Figure 2.13: Mechanical communication via stress transmission through different network architectures. **(a)** The stress signal at the cell membranes as cell contraction increases is plotted for separation distance of 50 µm = 5 final cell diameters. A robust, stronger signal is observed in Voronoi networks, with weaker, variable signal in growth geometries. Large standard deviation in perturbed cases underlines high network-to-network variability in signal propagation. **(b)** The stress signal at maximal contraction (5 µm) for increasing cell separation is plotted. Voronoi networks produce the largest mechanical signals at all separation distances. Robust stress transmission beyond 5 cell diameters of separation appears to fail in growth networks, as evidenced by the large standard deviation. Bars give 1 s.d. about the mean value.

radial contraction (5 µm) as separation distance is increased. Robust signalling persists in Voronoi networks, even at a larger separation of 7 cell diameters. A smaller signal is observed in both dual and perturbed networks on average, and growth geometries produce the weakest signals for all separation distances. Further, the large standard deviations for growth cases at all separation distances underline the possible failure of cells to achieve a signal. In all cases, the most robust (smallest standard deviation) and largest mean signals derive from Voronoi network geometries. Interestingly, the change in geometry type, from growth to perturbed, yields two distinct architectures whose ability to support mechanical signalling, as defined above, is very different. Perturbed networks support signals of 4 times the amplitude found in growth cases at the shortest distance considered, and with a stronger signal at 7 cell diameter separation than found in growth networks at 5 cell diameter separation, emphasising that stress transmission can depend

sensitively on network geometry.

2.4 Conclusions

In this chapter we have presented a DFN model for biopolymer networks that employed four different geometries. These architectures were chosen to investigate the importance of geometry for network mechanical response in a variety of biologically relevant cases. The dominant effect of network geometry was investigated by controlling for topology, with each network paired with another of highly similar or identical topology. All networks considered were nominally isotropic at the whole network scale, offering no preferential directions. Through a simple model for constituent fibres and cross-links, we demonstrated that purely geometric differences can have a profound effect on network mechanics. These effects were investigated for networks under uniaxial extension, as well as for systems of one and two cells contracting within a network. Investigations into the influence of cross-link density (whence mean segment lengths) found that results were robust up to a two-fold increase; the striking similarity in micromechanical properties as cross-link density varied suggests that the results here are features of the individual architectures investigated. The primary conclusions from this work may be described as follows.

Qualitative differences in long-ranged displacement fields due to single contracting cells

All networks supported long-ranged displacement fields, with large substrate displacements measured beyond 4 cell diameters. However, growth type geometries had a considerably shorter mean displacement field, and substantial displacements were localized to branching paths originating from the cell membrane, as seen in Fig. 2.4. Displacement asymmetry was observed for growth geometries, and to a lesser extent for dual and perturbed networks, though Voronoi architectures supported largely symmetric displacement fields. Transverse network displacements that were greater than 1 μm in magnitude arose from uniform radial cell contraction

in growth networks, suggesting that directional displacement signalling may be precluded by this architecture. As such, we found that certain geometries supported heterogeneous, asymmetric displacement fields arising under uniform contraction in isotropic networks. Importantly, the geometric perturbation of growth networks substantially increased the extent of cell-derived mean displacement fields, and reduced the degree of asymmetry.

Stress transmission through fibrous networks is dependent on network choice

The degree to which stress could be transmitted through the model substrates was found to depend strongly on geometry. In Voronoi and perturbed geometries, cell-derived network deformations transmitted stress to boundaries more than 5 cell diameters distant, even when cell contractions were small. In these architectures, cells experienced greater membrane stress than those in dual or growth networks. In contrast, far less stress was transmitted to the outer boundary in growth or dual networks. Cells experienced these networks to be more compliant, and stress transmission appeared to be limited to relatively few stress paths, which formed at large cell contractions between the cell membrane and the outer boundary. As such, the perturbation performed to growth networks fundamentally changed the networks ability to support constituent fibre strains. Interestingly, fibre strain distributions showed that many more fibres buckled in growth networks, suggesting that the less stiff response may be due to a geometry that encourages fibre buckling.

Choice of geometry can favour or limit fibre reorganisation

High radial alignment of fibres was found in the region proximal to the cell membrane in all network choices. However, the extent of fibre reorganisation with increasing distance from the cell membrane was sensitive to network architecture. Voronoi and perturbed geometries appeared to limit the degree to which fibres far from the cell membrane could rotate. This resulted in families of stretched yet unaligned fibres, which amplified stress transmission. In contrast, distant fibres in growth and dual networks underwent greater rotations, such that the strains induced by cell contractions could be contained in fibre reorganisation rather than fibre

stretch. A positive correlation between fibre stretch and alignment was observed in all network architectures.

Mechanical communication between distant cells is supported by certain architectures

Pairs of model cells, separated by 5 (final) cell diameters, were able to transmit a mechanical signal through the fibre substrate, with regions of higher strain energy observed between cells. However, as separation distance increased, up to seven cell diameters, not all growth networks succeeded in transmitting a mechanical signal. At all separation distances investigated, larger and robust signalling was measured in Voronoi networks, underlining the possibility of long-range cell-cell mechanical communication in this architecture. Weaker signalling on average than in the Voronoi cases was observed in dual and perturbed networks, with the latter exhibiting larger standard deviations, suggesting a greater network-to-network variability in this architecture. In growth networks signal transmission was minimal or absent at $6-7$ cell diameter separation; in contrast their perturbed counterparts, possessing identical network topology, supported far stronger signals. As this study was comparative, we cannot talk about the magnitude of the signals in absolute terms. However, it is evident that the geometry of the network used to model substrate mechanics can have profound effects on the results of a study, and that geometry can act to regulate mechanical cell-cell communication.

Discussion

The above results provide an insight into the potential importance of network geometry to cell behaviour. Throughout, specific fibre material properties were not discussed, so as to facilitate a comparative study between different geometries. We might expect that certain filaments, such as semiflexible polymers characterized by long persistence lengths, would favour geometries in which correlations between fibre orientations persist through model cross-links. While this was the case in growth networks, such correlations are not present in the other architectures discussed, as seen in Fig. 2.1. We expect that when modelling stiffer filaments with large bending

stiffnesses, these correlations will be more important, especially in the small strain regime, before stress paths form [175]. Different experimental geometries can be generated in biopolymer networks by varying the gelation temperatures. Indeed, collagen gels formed at lower temperatures exhibit more fibrous architectures, compared with those polymerized at higher temperatures, which appear more homogeneous even after subsequent cooling [55]. Further, many biopolymers exhibit fibre branching, where filament bifurcations lead to network nodes with coordination 3 [179]. As such, the results presented within this work could be relevant to a wide range of biopolymer substrates. Further work could investigate how model geometries relate to specific *in vitro* networks.

In this chapter, the response of different network geometries to local, cell-derived deformations has been accounted for through a simple, symmetric displacement of nodes affixed to the model cell boundary. Importantly, this allowed for an investigation of network-derived asymmetry in the presence of perfectly symmetric displacement. However, the action of real cells involves tractions exerted upon the matrix, such that we do not expect to see such symmetric displacements arising *in vitro*. In particular, if a matrix is considerably more compliant, we expect to observe larger displacements, where the cell-derived force is more able to induce rearrangements in the fibre network, recruiting fibres more effectively. Furthermore, many mechanically sensitive cells polarize in response to the local matrix stiffness, leading to larger tractions in some directions than in others. Together, this implies that, in some situations, the geometry dependence noted in the above results could be reversed. For example, the stiff Voronoi networks might not permit significant substrate rearrangements, while the compliant growth architectures might allow for large displacements, including the rotation of peripheral fibres to align with the strain direction. Further work should investigate the consequences of employing local traction forces instead of imposed cell boundary displacements, whence the implications for real systems can be explored in greater detail.

We simulated fibre microbuckling through the use of an asymmetric force-extension law, and freely rotating cross-links. Recent work, using a similar modelling

paradigm, suggests that it is this anisotropy that allows for mechanosensing in extracellular matrices [196]. We note that the bending forces resulting from buckling often still act in the fibre axial direction, suggesting that the fibre buckling behaviour might be more important than filament bending in large strain studies [218]. As such, we expect that the asymmetric force-extension law used in this chapter captures the essential behaviour of the slender matrix fibres; that they are far stiffer under extension than compression. Future work could investigate how the network response differs as this parameter varies, in particular to identify whether there is a threshold value, above which mechanical cell-cell communication is prohibited, and how this depends on network geometry. The importance of an explicit filament bending behaviour is discussed later in this thesis, for DFN models under small strains. While this has not been addressed within this chapter, the differences identified under a range of mechanical tests suggest that network geometry is likely to play a key role in the mechanics of cellular activity within biological networks.

The research presented in this chapter is extensively based on the manuscript "The mechanics of phantom Mikado networks", under review, Journal of Physics Communications. Humphries, D. L., J. A. Grogan, and E. A. Gaffney.

3

The mechanics of phantom Mikado networks

The elasticity of networks comprised of semiflexible polymers plays a vital role in regulating the mechanics of both intra- and extracellular matrices. As discussed in Chapter 1, the behaviour of this polymer scaffold will depend on the nature and density of cross-linking between constituent fibres, as well as many other geometric and constitutive considerations. While previous modelling efforts have investigated the effects of cross-link density in biopolymer networks, this is often accompanied by changes in both the fibre density and the network structure. In this chapter, we address the importance of cross-link density in DFN models by investigating the elasticity of a quasi-2D architecture. In particular, we develop a network model in which cross-link density is allowed to vary while polymer density is held constant. Mikado architectures are selected for their relevance to numerous existing DFN studies. To investigate the effects of varying cross-link density within the Mikado model, we first develop a DFN model that is suitable for studying the deformation of networks within the small strain regime. Recalling that many fibre networks reside in the subisostatic regime, where truss or spring networks do not possess a classical static shear modulus, we here discuss a model in which constituent fibres support bending, in the form of a beam network model. Finite element modelling

is used to locate the static equilibrium of the fibre assemblies under simple shear deformations. We begin this chapter with a brief discussion of some theory relevant to the numerical scheme that we employ in the finite element software Abaqus. The model that we have developed is validated against major results from the DFN literature. Subsequently, we extend the standard Mikado model by allowing network fibres to cross one another without forming cross-links, while maintaining polymer density and network fibre geometry. In doing so, the competing contributions to the shear modulus from cross-link density, mesh size, geometry and polymer density can be decoupled. We find that previous scaling laws fail to capture the well-studied transition from bend- to stretch- dominated elasticity as cross-link density is varied. We identify a length scale that relates cross-link density to the transition between affine and nonaffine regimes, and that provides a collapse of data curves for varying cross-link densities. Various other model properties, including displacement nonaffinity and the energy partition in Mikado filaments, are also discussed.

3.1 The Finite Element Method for beam networks

Within the DFN literature, a lot of attention is given to the small displacement deformations of fibre networks [18, 170, 186]. Within this small strain regime, the dependency of the static elastic moduli on various network properties, such as fibre density, stiffness and geometry has been thoroughly examined. In particular, a considerable body of work has investigated the effects of varying filament stretching and bending behaviours, and the influence of these choices on the network elasticity. For a fibre along the horizontal x-axis, we can consider the energy content to be given by:

$$\mathcal{H}_{\mathbf{fibre}} = \frac{1}{2}\int_0^L \kappa \left(\frac{\partial^2 v}{\partial x^2}\right)^2 + \mu \left(\frac{\partial u}{\partial x}\right)^2 \mathrm{d}x \ , \tag{3.1}$$

for fibres of length L, displacement $\boldsymbol{u} = (u, v)$, stretching stiffness μ and bending rigidity κ. The mechanical parameters $\mu,\ \kappa$ are related to quantities from beam mechanics as $\mu \simeq EA,\ \kappa \simeq EI$, where E is the fibre or beam Young's modulus, A is the cross-sectional area, and I is the filament cross-section second moment of area. As such, μ has units of force, while κ has dimensions of force times length

squared. We note from Chapter 1 that the elasticity of biopolymer filaments can originate from a variety of physical phenomena, including thermal undulations, or interfibrillar cross-linking. It is therefore necessary to move away from restrictive definitions for the bending and stretching behaviours of the filaments that depend purely on the fibre cross-sectional shape and area. Throughout the remainder of this thesis, we refer to general stretching and bending stiffnesses μ and κ, which are not defined through the geometric quantities in classical beam theory.

The fibre networks whose behaviour we wish to model can be comprised of many thousands of cross-links and fibres. As such, we require a computational scheme to determine the network response to deformations and loads. In this thesis, we shall find solutions for the equilibrium configurations of beam networks through the finite element method (FEM). Many existing studies have adopted this approach [18, 19, 219], such that our choice is consistent with the literature, and facilitates direct comparison with other published research. We note that some other research groups have instead employed gradient descent methods to minimize the total network energy [170, 177], though results are expected to be highly similar.

Our finite element approach allows us to find an equilibrium configuration for a network of fibres under loads or displacements by discretizing each fibre segment, that is the fibre length between two model cross-links, into a number of *elements*, each connecting two finite element *nodes*. We can then formulate the problem in terms of variables specified at these locations in space. An approximate solution at all material points in the fibre network can then be recovered through interpolation. As discussed above, we include both bending and extensions of network filaments. We can accomplish this by considering three *nodal variables* for each cross-link, namely the displacement of nodes in the fibre axial direction u, transverse nodal displacements v, and nodal rotations θ. As such, each node within our 2D problem will possess three degrees of freedom; the contributions towards these variables are derived from incidental fibres, with energy defined according to Eq. 3.1. In this discussion, we consider beam stretching and bending independently; a linear truss element accounts for fibre extensibility, and a cubic

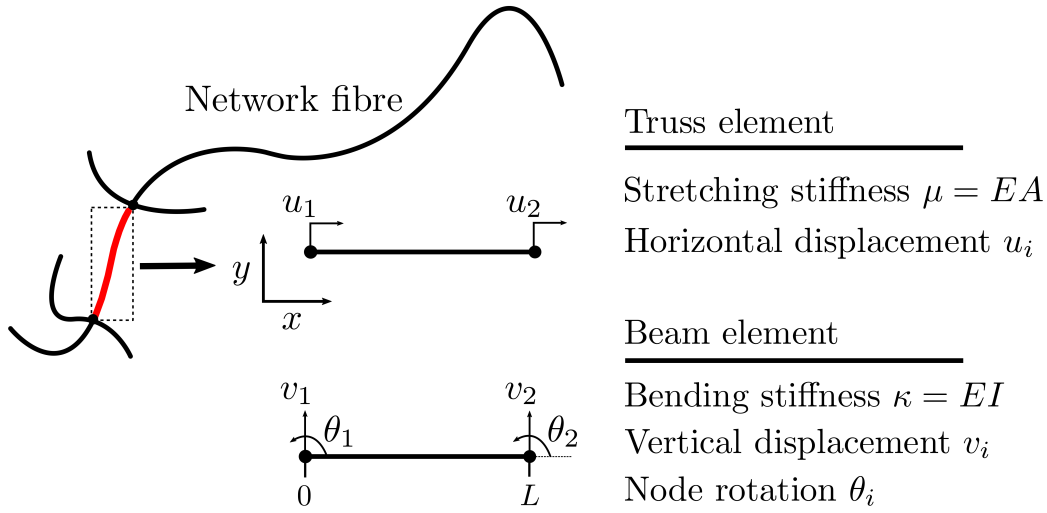

Figure 3.1: Schematic of the FEM treatment for a fibre segment, which involves a truss element for fibre extension, and a beam element for fibre bending.

beam element models fibre deflections. A schematic summarising these choices is displayed in Fig. 3.1. Throughout, we restrict our model to small strain elasticity. The following discussion is based upon the treatment presented by Dunne and Petrinic [220]. Before proceeding with theory for the implementation of an FEM scheme, we briefly discuss Hamilton's principle, which shall be used to obtain the equilibrium equations for the beam network.

Hamilton's principle

Consider the *Lagrangian* of a system, which is given in terms of the total external work W done by non-conservative forces, kinetic energy T, and internal energy U as:

$$\mathcal{L} = T - U + W \ . \tag{3.2}$$

Further, consider a corresponding functional, known as the $J-$integral, given by the integral of the Lagrangian over a given time period with prescribed initial and final conditions:

$$J = \int_{t_1}^{t_2} (T - U + W)\, \mathrm{d}t \ . \tag{3.3}$$

Hamilton's principle states that the first variation of the $J-$integral is zero, that is:

$$\delta J = \int_{t_1}^{t_2} \delta(T - U + W)\, \mathrm{d}t = 0 \ . \tag{3.4}$$

In words, this means that the average value of the Lagrangian relative to any compatible path is stationary at equilibrium. Consider the Lagrangian for an elastic medium within a region of space Ω, with kinetic energy, internal strain energy, and external work defined by:

$$T = \frac{1}{2}\int_\Omega \rho \dot{u}_i \dot{u}_i \,\mathrm{d}V \ , \qquad U = \frac{1}{2}\int_\Omega \sigma_{ij}\epsilon_{ij}\,\mathrm{d}V \ , \qquad W = \int_{\partial\Omega} t_i u_i \,\mathrm{d}A \ , \tag{3.5}$$

for material density ρ, displacement $\boldsymbol{u}$, stress $\boldsymbol{\sigma}$, strain $\boldsymbol{\epsilon}$, and traction force $\boldsymbol{t}$. The first variation of the relevant $J-$integral of this Lagrangian is:

$$\delta J = \delta \int_{t_1}^{t_2} \frac{1}{2}\int_\Omega \rho \dot{u}_i \dot{u}_i \,\mathrm{d}V - \frac{1}{2}\int_\Omega \sigma_{ij}\epsilon_{ij}\,\mathrm{d}V + \int_{\partial\Omega} t_i u_i \,\mathrm{d}A\,\mathrm{d}t \tag{3.6}$$

$$= \int_{t_1}^{t_2} \left(\int_\Omega \rho \dot{u}_i \delta\dot{u}_i \,\mathrm{d}V - \int_\Omega \sigma_{ij}\delta\epsilon_{ij}\,\mathrm{d}V + \int_\Omega \frac{\partial}{\partial x_i}\left(\sigma_{ij}\delta u_j\right)\mathrm{d}V \right)\mathrm{d}t \ , \tag{3.7}$$

where we have used Cauchy's stress theorem followed by the divergence theorem in the form:

$$\int_{\partial\Omega} t_i \delta u_i \,\mathrm{d}A = \int_{\partial\Omega} \sigma_{ij} n_i \delta u_i \,\mathrm{d}A = \int_\Omega \frac{\partial}{\partial x_i}\left(\sigma_{ij}\delta u_j\right)\mathrm{d}V \ . \tag{3.8}$$

Integrating by parts, this integral can be written as:

$$\delta J = \int_{t_1}^{t_2} \left(-\int_\Omega \rho \ddot{u}_i \delta u_i \,\mathrm{d}V - \int_\Omega \sigma_{ij}\delta\epsilon_{ij}\,\mathrm{d}V + \int_\Omega \left(\frac{\partial \sigma_{ij}}{\partial x_j}\delta u_i + \sigma_{ij}\delta\epsilon_{ij} \right)\mathrm{d}V \right)\mathrm{d}t \tag{3.9}$$

$$= \int_{t_1}^{t_2} \int_\Omega \left(-\rho\ddot{u}_i + \frac{\partial \sigma_{ij}}{\partial x_j} \right)\mathrm{d}V \delta u_i \,\mathrm{d}t \ , \tag{3.10}$$

where we have expanded the divergence using the chain rule and used the relationship between strain and displacement $\boldsymbol{\epsilon} := \nabla \boldsymbol{u}$. Requiring that the $J-$integral is stationary for all permissible variations δu_i leads us to the well-known equilibrium equations for an elastic material in the form:

$$-\rho\ddot{\boldsymbol{u}} + \nabla \cdot \boldsymbol{\sigma} = 0 \ . \tag{3.11}$$

Fibre bending using a beam element formulation

We shall now use the discussion of Hamilton's principle above in the derivation of relevant equilibrium equations relating to the deformation of a beam network. First, we consider the representation of fibre deflections using a beam element formulation.

Here, as illustrated in Fig. 3.1, we consider only the bending contribution to the fibre energy, that is:

$$\mathcal{H}_{\text{bend}} = \frac{1}{2}\int_0^L \kappa \left(\frac{\partial^2 v}{\partial x^2}\right)^2 \mathrm{d}x \ . \tag{3.12}$$

For a single beam element, connecting two nodes at either end of a fibre or fibre segment of length L, we have four degrees of freedom; rotation θ_i and transverse displacement v_i for each node. To simplify the discussion, we move to a local coordinate system for the 1D element, $r \in [0,1]$, which relates to the spatial coordinate x as $r = x/L$, so that $\mathrm{d}x = L\,\mathrm{d}r$. As discussed above, we require interpolation to represent the continuum variables in the fibre network in terms of the finite number of variables used in the discrete scheme. For this we introduce *shape* or *interpolation* functions. Here, we consider cubic shape functions of the form:

$$h = \sum_{i=0}^{3} a_i r^i \ . \tag{3.13}$$

though we note other forms of shape function can be used. Consider the following *nodal displacement* vector for the relevant degrees of freedom $\boldsymbol{v} = [v_1, \theta_1, v_2, \theta_2]$; we wish to use shape functions where h_i or its derivative is zero at the boundary except for the relevant unitary contribution. For the first degree of freedom, v_1, this prescribes the following conditions:

$$r = 0: \ h_1 = 1 \ , \ \frac{\mathrm{d}h_1}{\mathrm{d}r} = 0 \ , \tag{3.14}$$

$$r = 1: \ h_1 = 0 = \frac{\mathrm{d}h_1}{\mathrm{d}r} \ , \tag{3.15}$$

which yields a linear system in the coefficients a_i. Proceeding similarly for the remaining shape functions, and solving for the relevant coefficients, we find that the shape functions are given by the cubic Hermite splines:

$$h_1 = 1 - 3r^2 + 2r^3 \ , \qquad h_2 = r - 2r^2 + r^3 \ , \tag{3.16}$$

$$h_3 = 3r^2 - 2r^3 \ , \qquad h_4 = -r^2 + r^3 \ . \tag{3.17}$$

Writing the vector of these shape functions as $\boldsymbol{h}(r) = [h_1, h_2, h_3, h_4]$, the interpolated displacement v along the fibre can be written as:

$$v = v(r,t) \approx h_1(r)\, v|_{r=0} + h_2(r)\, \frac{\partial v}{\partial r}\bigg|_{r=0} + h_3(r)\, v|_{r=1} + h_4(r)\, \frac{\partial v}{\partial r}\bigg|_{r=1} , \tag{3.18}$$

$$= h_1(r)\, v|_{x=0} + Lh_2(r)\, \frac{\partial v}{\partial x}\bigg|_{x=0} + h_3(r)\, v|_{x=L} + Lh_4(r)\, \frac{\partial v}{\partial x}\bigg|_{x=L} , \tag{3.19}$$

$$= h_1(r)v_1(t) + Lh_2(r)\theta_1(t) + h_3(r)v_2(t) + Lh_4(r)\theta_2(t) , \tag{3.20}$$

which we write in the form:

$$v = \boldsymbol{h} \cdot \boldsymbol{v} = [h_1,\ Lh_2,\ h_3,\ Lh_4][v_1,\ \theta_1,\ v_2,\ \theta_2]^T . \tag{3.21}$$

Referring back to the energy $\mathcal{H}_{\text{bend}}$ in Eq. 3.12, the second derivative of the transverse displacement can be written as:

$$\frac{\partial^2 v(x,t)}{\partial x^2} = \frac{1}{L^2}\frac{\partial^2 v}{\partial r^2} = \frac{1}{L^2}\frac{\partial^2 \boldsymbol{h}}{\partial r^2} \cdot \boldsymbol{v} = \boldsymbol{B}\boldsymbol{v} , \tag{3.22}$$

where $\boldsymbol{B} := \frac{1}{L^2}\frac{\partial^2 \boldsymbol{h}}{\partial r^2}$. The internal strain energy then takes the form:

$$\mathcal{H}_{\text{bend}} = \frac{1}{2}\int_0^L \kappa \left(\frac{\partial^2 v}{\partial x^2}\right)^2 \mathrm{d}x = \frac{1}{2}\boldsymbol{v}^T \left(\int_0^L \kappa \boldsymbol{B}^T\boldsymbol{B}\, \mathrm{d}x\right)\boldsymbol{v} , \tag{3.23}$$

$$= \frac{1}{2}\boldsymbol{v}^T\boldsymbol{k}\boldsymbol{v} , \tag{3.24}$$

where we have introduced the *stiffness matrix* $\boldsymbol{k} := \int_0^L \kappa \boldsymbol{B}^T\boldsymbol{B}\, \mathrm{d}x$. In this thesis, we are only interested in the static equilibria of beam networks, such that we neglect inertia terms. Introducing the *force vector* $\boldsymbol{f}$, the Lagrangian here is therefore given as:

$$L = -U + W = -\frac{1}{2}\boldsymbol{v}^T\boldsymbol{k}\boldsymbol{v} + \boldsymbol{v}^T\boldsymbol{f} . \tag{3.25}$$

Taking the first variations of the corresponding $J-$integral and applying Hamilton's principle gives:

$$\delta\int_{t_1}^{t_2} L\, \mathrm{d}t = \int_{t_1}^{t_2} \left(-\boldsymbol{v}^T\boldsymbol{k}\delta\boldsymbol{v} + \boldsymbol{f}^T\delta\boldsymbol{v}\right)\mathrm{d}t = \int_{t_1}^{t_2} (-\boldsymbol{v}^T\boldsymbol{k} + \boldsymbol{f}^T)\cdot\delta\boldsymbol{v}\, \mathrm{d}t = 0 , \tag{3.26}$$

for all permissible variations $\delta\boldsymbol{v}$. We therefore arrive at the equilibrium equations for the deflection of a fibre:

$$\boldsymbol{k}\boldsymbol{v} = \boldsymbol{f} . \tag{3.27}$$

Solving this linear system provide the transverse displacements, rotations and forces for the FE nodes. Recalling the definition of the stiffness matrix $\boldsymbol{k}$, and matrix $\boldsymbol{B}$, we have:

$$\boldsymbol{k} := \int_0^L \kappa \boldsymbol{B}^T \boldsymbol{B}\, \mathrm{d}x = \frac{\kappa}{L^3} \begin{bmatrix} 12 & 6L & -12 & 6L \\ & 4L^2 & -6L & 2L^2 \\ & & 12 & -6L \\ \text{Sym.} & & & 4L^2 \end{bmatrix} , \tag{3.28}$$

so that the linear system to be solved is:

$$\frac{\kappa}{L^3} \begin{bmatrix} 12 & 6L & -12 & 6L \\ & 4L^2 & -6L & 2L^2 \\ & & 12 & -6L \\ \text{Sym.} & & & 4L^2 \end{bmatrix} \begin{bmatrix} v_1 \\ \theta_1 \\ v_2 \\ \theta_2 \end{bmatrix} = \begin{bmatrix} m_1 \\ t_1 \\ m_2 \\ t_2 \end{bmatrix} , \tag{3.29}$$

for nodal moments and torques $m_i,\ t_i$.

Filament extension with two beam elements

Above we considered the finite element formulation and the path to a solution for the deflection of a fibre. To demonstrate how multiple elements can be combined along a fibre, we now formulate the problem for fibre extension through the use of two linear truss elements, each described according to Fig. 3.1. Here, we consider only the stretching contribution to the internal strain energy:

$$\mathcal{H}_{\text{stretch}} = \frac{1}{2} \int_0^L \mu \left(\frac{\partial u}{\partial x} \right)^2 \mathrm{d}x \ . \tag{3.30}$$

For the purpose of demonstration, two truss elements of equal length are placed along the fibre or fibre segment, of length L. Similar to before, we introduce local variable $r = 2x/L$ along the first truss, and likewise for the second. As each truss element connects two nodes, and there is a common node to both elements. We can discuss the extension in terms of nodal displacements $\boldsymbol{u}^i$, where $\boldsymbol{u}^1 = [u_1, u_2]$, $\boldsymbol{u}^2 = [u_2, u_3]$. For this simple case, we use linear interpolation functions for each truss element, given by $\boldsymbol{N} = [N_1, N_2]$. For the first truss, this gives:

$$N_1(r) = 1 - r \ , \qquad N_2(r) = r \ . \tag{3.31}$$

In terms of this discretization, we can simply write the uniform displacement along the truss as:

$$u = N_1(r)u_1 + N_2(r)u_2 \ . \tag{3.32}$$

The strain energy takes the form:

$$\mathcal{H}_{\text{stretch}} = \frac{1}{2}\int_0^L \mu \left(\frac{\partial u}{\partial x}\right)^2 \mathrm{d}x = \frac{1}{2}\boldsymbol{u}^T \left(\int_0^L \mu \boldsymbol{B}^T \boldsymbol{B}\, \mathrm{d}x\right) \boldsymbol{u} \ , \tag{3.33}$$

where here:

$$\boldsymbol{B} := \left[\frac{\partial N_1}{\partial x},\ \frac{\partial N_2}{\partial x}\right] = \frac{2}{L}\left[\frac{\partial N_1}{\partial r},\ \frac{\partial N_2}{\partial r}\right] = \frac{2}{L}[-1,\ 1] \ . \tag{3.34}$$

Switching the integration variable to r, and noting the symmetry between the two truss elements, we can write the *element* stiffness matrices $\boldsymbol{k}_i$ for each truss element as:

$$\boldsymbol{k}_i = \frac{2\mu}{L}\begin{bmatrix} 1 & -1 \\ -1 & 1 \end{bmatrix} \ . \tag{3.35}$$

Combining these two element stiffness matrices, we can assemble the *global* stiffness matrix $\boldsymbol{K}$, given by:

$$\boldsymbol{K} = \begin{bmatrix} \boldsymbol{k}_1 & & 0 \\ & & 0 \\ 0 & 0 & 0 \end{bmatrix} + \begin{bmatrix} 0 & 0 & 0 \\ 0 & & \\ 0 & & \boldsymbol{k}_2 \end{bmatrix} = \frac{2\mu}{L}\begin{bmatrix} 1 & -1 & 0 \\ -1 & 2 & -1 \\ 0 & -1 & 1 \end{bmatrix} \ . \tag{3.36}$$

Then the solution for the three nodal variables u_i and forces f_i applied to those nodes is given as:

$$\boldsymbol{K}\boldsymbol{u} = \frac{2\mu}{L}\begin{bmatrix} 1 & -1 & 0 \\ -1 & 2 & -1 \\ 0 & -1 & 2 \end{bmatrix}\begin{bmatrix} u_1 \\ u_2 \\ u_3 \end{bmatrix} = \begin{bmatrix} f_1 \\ f_2 \\ f_3 \end{bmatrix} \ . \tag{3.37}$$

For the beam networks that we wish to model, comprised from thousands of fibre segments, we must assemble a global stiffness matrix and force vector for the whole problem. Throughout, we have assumed that fibre strains, displacements and rotations are small, such that reference and current configurations are taken to be equivalent. In large displacement analysis, the above treatment would be insufficient, and we would need to compute the Jacobian matrix to move between frames of reference.

3.2 Implementation of a DFN model on the Abaqus FE platform

In Chapter 2, we considered large displacements induced in fibre networks of different geometries, where fibres stretched, but filament bending was neglected. Here, and henceforth, we wish to extend the constitutive behaviour of the DFN to allow for fibre bending behaviours in subisostatic networks, while restricting ourselves to the small strain regime. Rather than develop a bespoke FEM assembler and solver, that is code to assemble the matrices described above and to solve the resulting linear system, we instead choose to use the commercial FE platform Abaqus [203]. This has many advantages, such as robust testing, having been used in many DFN studies to date [18, 19, 219], as well as allowing for efficient, optimised computations. To this end, we developed a FE preprocessor in Python, into which we input the computational network geometries (defined according to Chapter 1). This code defines the FE nodes, elements and connectivity, boundary and loading conditions, and fibre constitutive properties. The preprocessor generates an Abaqus input file that can be used to run the desired simulation using the Abaqus FE solver. More specifically, networks of a given architecture are generated in Python, whence each fibre segment is discretized by a given number of elements. The loading and boundary conditions, as well as additional constraints pertaining to periodic boundary conditions, are specified and a text input file is created and submitted to the Abaqus solver, whence the static equilibrium is found according to theory similar to that presented above. The assembly of the bulk stiffness matrix and load vector, and the inversion of the stiffness matrix are handled by the Abaqus software. Throughout the research presented in this thesis, approximately $100,000$ networks are considered, each constructed from $\mathcal{O}(10^5)$ elements and nodes. As such, computational efficiency is a concern. The most efficient beam elements for use in Abaqus are shear flexible linear beam elements ('B21' for planar cases), of which we use between 2 and 4 along each fibre segment. Here, an additional

shear term is introduced into the internal strain energy of the element, which is given in Abaqus for a general beam in space as:

$$\mathcal{H} = \frac{1}{2}\int_L \mathrm{ds}\ \underbrace{EI\ \left(\frac{d\psi(s)}{ds}\right)^2}_{\mathcal{H}_{\mathrm{bend}}} + \underbrace{EA\ \left(\frac{du(s)}{ds}\right)^2}_{\mathcal{H}_{\mathrm{stretch}}} + \underbrace{KG_fA\ \left(\frac{dv(s)}{ds} - \psi(s)\right)^2}_{\mathcal{H}_{\mathrm{shear}}} . \quad (3.38)$$

Here, E and G_f are the fibre elastic and shear moduli respectively, while A and I give the area and second moment of area. The axial and transverse displacements along a fibre are given by u and v, and s is the fibre arc length. The rotation of the plane normal to the beam axis is given by ψ, while $\frac{dv}{ds}$ gives the rotation of the fibre cross-section (equal to ψ for Euler-Bernoulli beams), and $\frac{du}{ds}$ gives the axial strain. Finally, K is a shear correction factor accounting for cross-section geometry, and the integral runs along the contour length of each fibre. The terms in the above energy equation can be partitioned as shown into bending, stretching and shearing modes, as indicated. As discussed at the beginning of this chapter, we wish to define fibre bending and stretching behaviours independently from the filament geometry. We therefore employ general beam sections to remove any dependence on filament radii, and the stiffnesses $\mu \simeq EA$ and $\kappa \simeq EI$ are only nominally related to the fibre geometry. We take the fibre shear modulus to be half the corresponding elastic modulus, and unit shear correction factor. This results in fibres with comparatively large shear stiffness, whence shear energy storage is small, as validated later in this chapter. Summing over all fibres in the composite, as denoted by $\sum_N$, the total network energy is given by:

$$\mathcal{H}_{\mathrm{total}} := \frac{1}{2}\sum_N \int \mathrm{ds}\ \kappa\left(\frac{d\psi(s)}{ds}\right)^2 + \mu\left(\frac{du(s)}{ds}\right)^2 + \frac{1}{2}\mu\left(\frac{dv(s)}{ds} - \psi(s)\right)^2 . \quad (3.39)$$

In our model as applied in Abaqus, the introduction of this additional shear correction term does not involve further nodal degrees of freedom. For slender beams, the results for shear flexible beams remain close to the theory discussed above. Indeed, comparative studies have investigated the effects of this additional term, and found that only small corrections are introduced by its inclusion, largely when considering polymers that involve very short segments [199]. We now seek

to validate our model choices, including the shear correction term and our mesh choices. In particular, we seek to reproduce the main results from a model presented by Head, Levine, and MacKintosh [170]. This study remains one of the key works in the field, and has been highly influential in subsequent research. The model involves a Mikado DFN subjected to a small simple shear strain. As discussed in Chapter 1, Head, Levine, and MacKintosh [170] found that fibre networks can reside in two distinct elastic regimes, classified according to the bending and stretching energetics of the network. Fibre cross-links are modelled as freely rotating, with rotations around cross-links incurring no energy cost, but the translation of one fibre able to incur bending deformations in the other [172]. We model this effect in our DFN model by introducing rigid connector elements that act on coincident nodes at cross-links, ensuring that the translational degrees of freedom on these nodes match, but allowing for different nodal rotations. Likewise, periodic boundary conditions on the left and right boundaries are modelled by matching all degrees of freedom, both translational and rotational, between nodes on opposite sides of the domain. Mikado geometries are generated according to the procedure presented in Chapter 1.

Each Mikado network is subjected to a small simple shear deformation as follows. Nodes on the top boundary are fixed both in rotation and vertical displacement, and shifted horizontally to give 0.05% bulk shear strain. Nodes on the lower boundary are fixed in all degrees of freedom. Periodic boundary conditions apply on all degrees of freedom for nodes on vertical (left and right) boundaries. Each fibre segment, that is the fibre extent between two model cross-links, is discretized with four beam elements. The resulting simulations are performed in Abaqus/Standard [203]. For total network energy $\mathcal{H}_{\text{total}}$, small strain γ, and domain edge size W, we can calculate the network shear modulus as $\mathcal{G} = 2\mathcal{H}_{\text{total}}/\gamma^2 W^2$.

The main results that we seek to replicate as evidence for the suitability of our model are that i) there exist distinct elastic regimes, affine and nonaffine, which are stretching and bending dominated respectively; and that ii) these regimes allow for the collapse of data relating to the shear modulus of the network onto a single curve, under the affine length scales λ_i defined in the original study [170]. The proposed

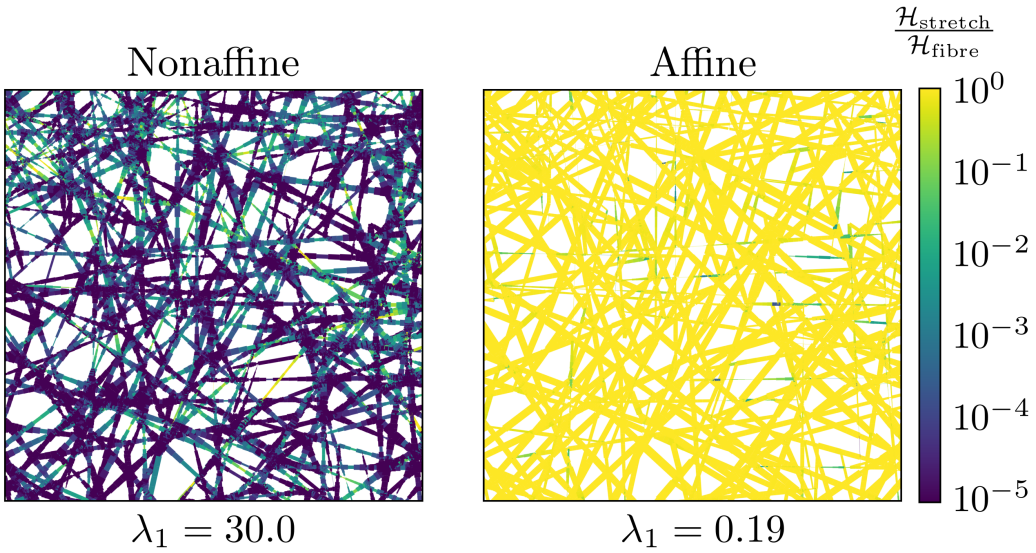

Figure 3.2: Illustrations of a zoomed-in region of a fibre network under simple shear in the nonaffine (left, large λ_1) and affine (right, small λ_1) regimes. Nonaffine networks (low bending length scale l_b) are bending dominated, with most fibres storing the majority of internal strain energy in bending deformations. In contrast, most fibres in affine networks store energy in stretching modes. Log-scaled colour displays the ratio of stretching energy $\mathcal{H}_{\text{stretch}}$ to the total energy $\mathcal{H}_{\text{fibre}}$ in each fibre segment, while the log-scaled line width displays the ratio of fibre energy to total network energy. More than 99.99% of energy in the nonaffine network is stored in bending modes, while more than 99% of energy is contained in stretching in the highly affine network.

affinity lengths are given by $\lambda_i = l_c(l_c/l_b)^{A_i}$ for $i = 1,\ 2$, where A_i is given as either $1/3$ or $2/5$ respectively, determined either empirically (λ_1) or through scaling arguments (λ_2). Here, we have introduced the *bending length scale* $l_b := (\kappa/\mu)^{1/2}$.

Illustrated in Fig. 3.2 are the constituent fibre energy contents resulting in our Mikado model, for two different fibre bending stiffnesses. In particular, we plot a small region from within the same network for two different values of the affine length scale $\lambda_1 \approx 30,\ 0.19$, relating to networks in each regime. Clearly, the nonaffine network ($\lambda_1 \approx 30$) is dominated by bending deformations, while fibres in the affine network ($\lambda_1 \approx 0.19$) are stretch-dominated.

In order to reproduce results from the literature, we require a prediction for the affine shear modulus $\mathcal{G}_{\text{affine}}$, that is the shear modulus resulting from a network in which every fibre undergoes a precisely affine deformation according to the bulk

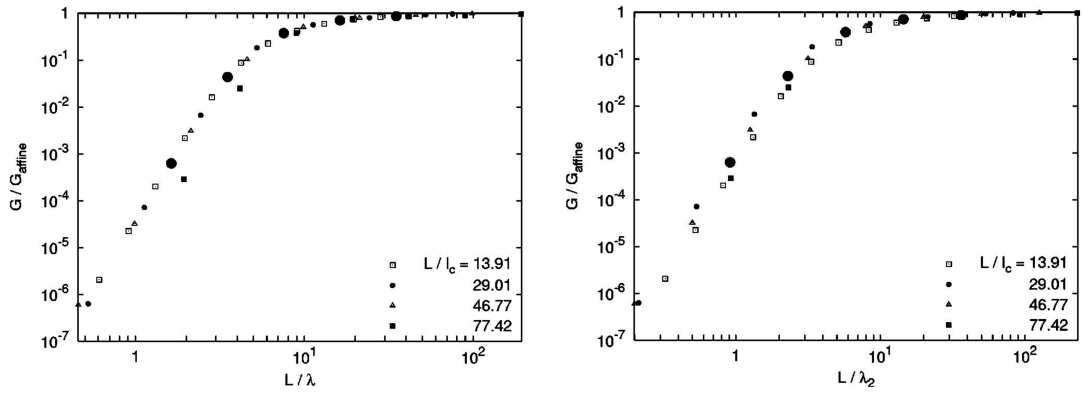

Figure 3.3: The shear modulus of 2D Mikado networks, normalized by the affine prediction, are shown under two choices of the length scale for affinity λ_i. In both cases the transition between a nonaffine and affine regime are clear. **(Left)** Data collapse for L/λ_1, where $\lambda_1 = (l_c^4/l_b)^{1/3}$, showing excellent collapse for low to high densities, but small deviations for the very highest densities considered. **(Right)** A data collapse is sought under a theoretical prediction for the affine length scale $\lambda_2 = (l_c^7/l_b^2)^{1/5}$. Small deviations from a data collapse are consistently observed across different choices for L/l_c. Reproduced with permission from Head, Levine, and MacKintosh [170].

simple shear. By summing over all constituent fibres, and averaging over the uniform fibre orientations θ, we arrive at the expression $\mathcal{G}_{\text{affine}} \approx \pi\mu/16l_c$. This quantity is discussed in detail in Appendix B. As the affine-nonaffine transition is characterized by a bend-stretch transition, we expect the network shear modulus in the affine regime to remain close to this prediction, while the nonaffine shear modulus should be orders of magnitude smaller. Shown in Fig. 3.3 are the results of normalizing the shear modulus by the affine prediction, $\mathcal{G}/\mathcal{G}_{\text{affine}}$, plotted under the two length scales for affinity λ_i defined above, reproduced from Head, Levine, and MacKintosh [170]. Within the nonaffine regime the shear modulus scales with bending stiffness κ, while the affine regime is evidenced by the plateau region, where the shear modulus approaches the affine prediction and scales with stretching stiffness μ. For λ_1, Head, Levine, and MacKintosh [170] found an excellent data collapse for most networks, except for the highest density networks $L/l_c > 70$, as shown in Fig. 3.3 **(Left)**. For λ_2, which was predicted from scaling arguments, the researchers found a less convincing summary of their data, as shown in Fig. 3.3 **(Right)**.

Equivalent results from our model, where the shear modulus normalized by the

affine prediction is plotted against the two length scales for affinity, is shown in Fig. 3.4, for networks of 4 densities similar to those used by Head, Levine, and MacKintosh [170]. Results are averaged over 20 simulations for each parameter choice, and shown for 12 values of the bending length scale l_b, over a 6 orders of magnitude variation. The results of our DFN model agree closely with those published in the literature, with a data collapse under both affine lengths λ_i, suggesting that our model captures the same essential physics. Interestingly, the deviations from a master curve observed for λ_2 in Fig. 3.3 are largely absent in our results. This might be due to improvements in computational power over the past decade, which allow us to perform more simulations, each with a larger number of beam elements per fibre. Indeed, the original study considered fibre bending to be represented only through the deflection of fibre segment midpoints, which might lead to inaccuracies for the densest networks considered.

As further validation of our model, we also seek to confirm that networks are bend-dominated for lower values of l_b, and transition to become stretch-dominated as κ increases, under the same length scales λ_i. In particular, we seek confirmation here that shear contributions remain small. Fig. 3.5 displays the network energy partition for both choices of λ_i, clearly demonstrating that the move towards the affine regime coincides with a bend-stretch transition. Importantly, within either regime, the energy content is clearly dominated by either bending or stretching terms, and shear contributions do not affect the results. This confirms that the DFN model we have developed is suitable for modelling fibres with bending and stretching contributions. That the inclusion of fibre shearing results only in small corrections is confirmed elsewhere in the literature, such that the efficiency gains from using such elements in Abaqus do not sacrifice accuracy [199].

Before proceeding to investigate an extended Mikado model, we draw attention to an often neglected feature of these networks that could have potentially important consequences *in vitro* and *in vivo*. In particular, we wish to explore how the network energy content is shared between the constituent fibres. Indeed, in Chapter 2 we found that a relatively small family of fibres can contain a large amount of total

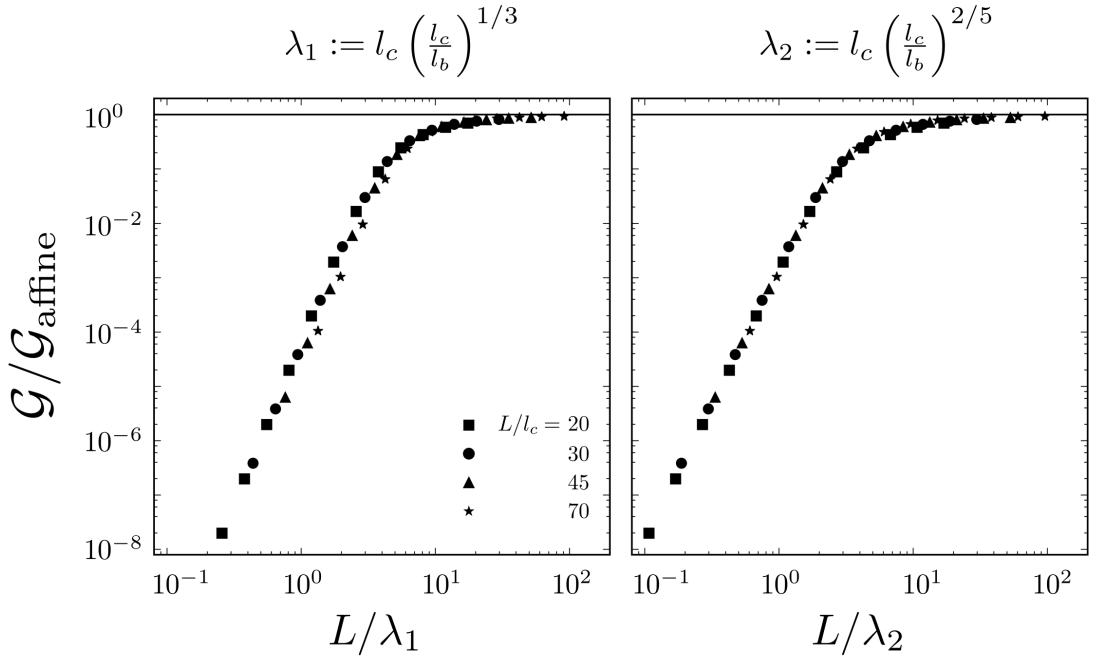

Figure 3.4: The main results of Head, Levine, and MacKintosh [170] are reproduced within our model for both values of the affine length scale λ_i. We reproduce the collapse of data onto a common curve in both cases. However, we note that the deviations from the master curve observed in the original research are not present here for λ_2. The transition between affine and nonaffine occurs at the same point for these affinity lengths, suggesting that our model accurately matches others found in the literature, both qualitatively and quantitatively.

network energy. Fig. 3.6 displays the probability density function (pdf) for the log-scaled energy density of fibre segments for each of the four network densities considered. For nonaffine networks (blue curves), a very small family of fibres contains the majority of network energy, as evidenced by the broader peaks and log-scaled x-axis. For affine networks, many fibres share in the total energy content, with the width of the peak narrowing. While this might not be of particular interest to the bulk behaviour here, it could have important consequences when considering material damage, as well as for the local micromechanics, as discussed in Chapter 2.

Having validated our DFN model as implemented in Abaqus, and having discussed the essential features of, and results from, the standard Mikado model, we now present an extended Mikado model, developed so as to investigate the

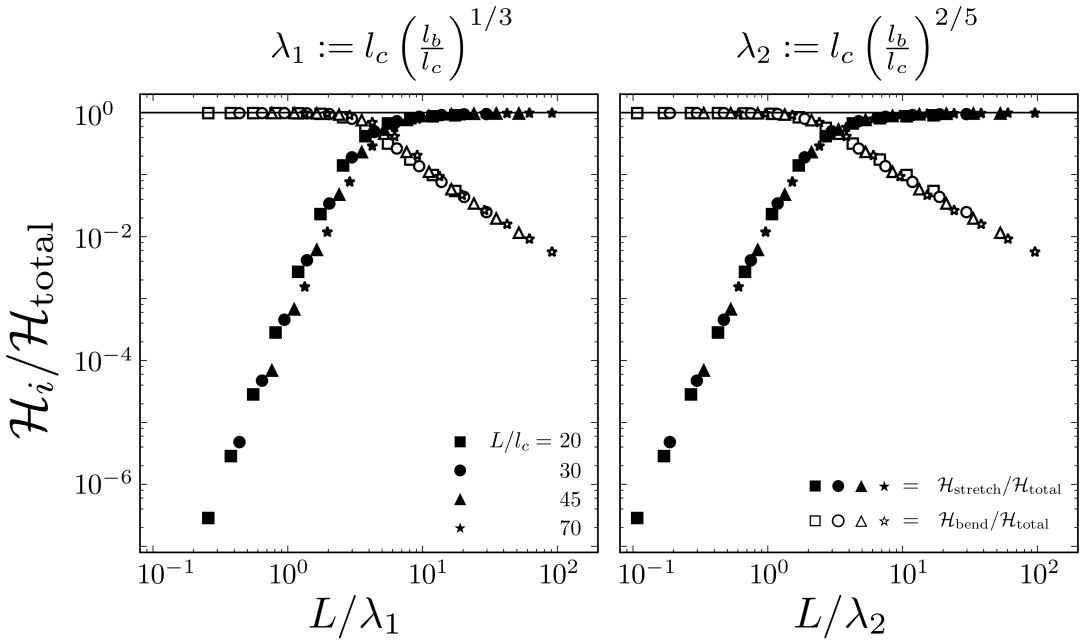

Figure 3.5: An illustration of the network energy partition as the length scales for affinity λ_i are varied. In particular, we reproduce the result that networks within the nonaffine regime are bending dominated and transition under the length-scale for affinity to stretching dominated. In both cases, the majority of total network energy is stored in either bending or stretching deformations, such that fibre shear contributions are minimal. White markers represent bending energy, while solid black markers illustrate stretching.

mechanics of Mikado networks where cross-link density is varied while total polymer density is held constant.

3.3 The mechanics of a phantom Mikado model

As discussed in Chapter 1, biopolymer networks are ubiquitous in living matter, from the collagen-dominant extracellular matrix (ECM) to the actin cortex of eukaryotic cells. The mechanics of such networks are vital to the proper functioning of many processes, including cellular motility [120, 147], mechanical cell-cell communication [108, 137] and stress management in articular cartilage [221]. In Chapter 2 we discussed how the choice of DFN geometry can influence the extent to which stress signals can be transmitted through the fibre network by varying the network geometry while holding cross-link density constant. Indeed, it has been established

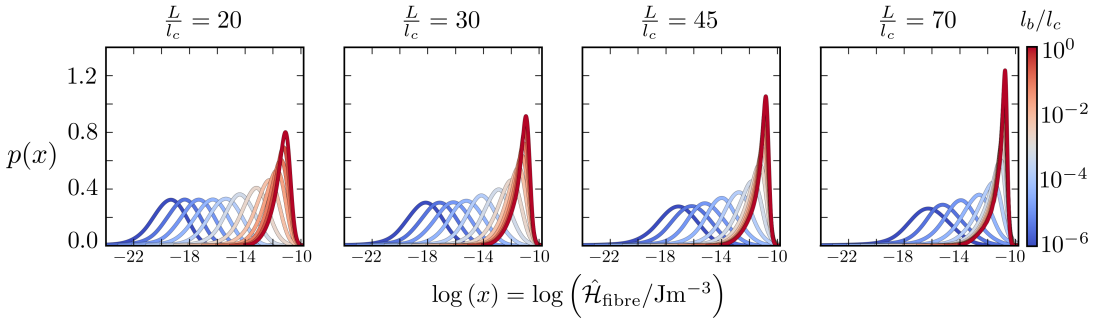

Figure 3.6: Probability density functions for the network fibre segment strain energy densities $\hat{\mathcal{H}}_{\text{fibre}}$. The energy content within nonaffine networks is dominated by a very small family of deformed fibres, while energy is shared far more equally between many fibres in stretching dominated cases.

that cross-link density can be a critical parameter in the mechanics of fibre networks [169]. As such, the importance of cross-linking to the mechanical response of fibre assemblies has been receiving increasing attention, both in theoretical and *in vitro* studies. Using an image-based model of elastic rods, Stein et al. [200] found that tuning the torsional stiffness of cross-links could result in good agreement between simulation and experimental network moduli. Other studies have shown a sensitive dependence of the bulk elastic moduli on cross-link density in 3D [169]. Simulations have suggested that network toughness increases with cross-link density, indicating an important function for cross-linking in semiflexible networks [179]. Cross-links found in biological networks can be transient, in which case their binding and unbinding dynamics can affect stress relaxation and transmission in cytoskeletal networks [33, 222]. 3D models in which cross-links of varying length form between simulation fibres, showed that it was possible to vary cross-link density such that the simulation mechanics followed those of 3D collagen gels [183]. Excitingly, improvements in electrospinning technology have granted far better experimental control of network cross-links, allowing for the development of novel substrates with tunable cross-linking [9]. Here, cells resident within a biopolymer scaffold responded sensitively to network cross-link density, with cells displaying different morphologies as cross-link density varied. Taken as a whole, this evidence supports the view

that the nature of cross-linking within a fibrous assembly can have important consequences for the bulk and local mechanics.

As evidenced by the standard Mikado model [18, 163], the elastic regime in which a network resides can be determined by both network and material properties. Experimental evidence for elastic regimes in biopolymer networks has accumulated over the past two decades, with many example assemblies seemingly governed by an affine description of the network deformation field [38, 161]. While direct experimental evidence for nonaffine deformation modes remains somewhat elusive, some studies have found evidence for its existence in collagen gels [104, 223] and double-fibre networks [103]. Clearly, microscale investigations into constituent fibre energetics when embedded within a network are often experimentally intractable. It has thus been of great value to use theoretical and computational models to investigate the existence and behaviour of these regimes, and to discuss the origins of the distinct behaviours.

According to the standard Mikado model, the geometry for which is described in Chapter 1, wherever two fibres overlap, a permanent cross-link is formed. Despite the utility and success of this model, the distribution of inter-cross-link distances that arises may not match those of real biopolymer networks. Indeed, the exponentially-distributed segment lengths observed in the Mikado model (as discussed in Appendix A and elsewhere [4, 181]) do not necessarily agree with those measured in collagen I filament networks [224], which are three-dimensional and may possess heterogeneous cross-link density. Furthermore, even for quasi-2D networks, where fibres form a largely planar network, it should not be expected that all fibre crossings are associated with cross-links. Indeed, the substrates developed by Baker et al. [9] had tunable cross-linking, where fibres that crossed could be welded together or left disassociated. In order to model these real-world effects, it is prudent to investigate how the mechanics of the Mikado model varies as the assumption of forced cross-linking for over-lapping fibres is relaxed. We expect that allowing more general cross-linking will also provide insight into the physics

of biopolymer networks more generally, and how their deformation depends on the various structural parameters involved.

Alongside Mikado networks, lattice models have also provided insight into stress propagation and network mechanics in biopolymer systems. Here, regular periodic geometries are used to represent the fibre assembly, with lattice edges diluted so as to generate networks of a given polymer or cross-link density, or average coordination number [55, 190]. One step towards describing 3D network mechanics has been provided through the use of *phantom* face-centred cubic lattices [192, 225]. In such models, while many fibres might pass through a lattice node, not all are considered cross-linked. Instead, only certain fibres form connections, such that the network structure and cross-link density can be somewhat decoupled. In reference to these lattice models, we term the model presented in this chapter the "phantom Mikado" model, in which cross-link and line density can be independently specified. This is achieved by relaxing the constraint that all fibre crossings represent cross-links. Instead, a proportion of cross-links with node coordination 4 from a standard Mikado model are removed, without otherwise adjusting the fibre constitutive properties. Note that dangling ends, that is the free segments at the ends of model fibres, are removed during network construction as detailed in Chapter 1. As such, networks possess many cross-links of coordination either 2 or 3; these will not be removed within the phantom model, as to do so would remove polymer lengths from the network.

Our objective is to study and characterize the mechanics and deformation of biopolymer networks in which cross-link and line density are decoupled. In particular, we aim to characterize the transition between the affine and nonaffine regimes for phantom Mikado networks. We investigate the length scales that inform where this transition occurs, and clarify how these may differ from the standard Mikado model. We further aim to investigate whether displacement measures for affinity capture the bend-stretch transition in this model.

3.4 Model

As per the procedure described in detail in Chapter 1 and earlier in this chapter, we consider Mikado networks formed by placing N monodisperse fibres of length L at uniformly distributed orientations within a square domain of area W^2. We refer throughout to nondimensional polymer density $\rho = NL^2/W^2$, used elsewhere in the literature and discussed in greater detail in Appendix A [185]. Briefly, it provides a description of the number of cross-links along a single fibre as $\rho \simeq L/l_c$. On sufficiently large length-scales W, networks appear isotropic and homogeneous, such that this domain length scale does not affect results. In this study, domains of size $W/L = 2.5 - 15$ are employed, which ensured fluctuation errors remained small. While networks are being generated, we assign a permanent cross-link to the crossing of two rods. Once the Mikado network has been formed, all dangling ends are removed, as these will not affect the static shear modulus of the network; in all the networks considered, the average coordination number was observed to be between 3 and 4, formed from nodes of coordination 2, 3 or 4. To investigate the effects of cross-link density on network mechanics, further networks are produced from an initial Mikado geometry by removing a given proportion of cross-links. The resulting networks are described by a parameter p, which measures the ratio of initial to final cross-links in the sample as $p := n/n_0$, for cross-link number n, and subscript 0 denoting quantities in the standard Mikado case. So as not to disrupt the fibre geometry, and to keep polymer density constant under the cross-link removals, only nodes of coordination 4 are removed; if those with coordination 2 or 3 are removed, additional 'dangling ends' are introduced, so that the effective network density has been lowered. Now, as there exist NL/l_c cross-links in a Mikado network, and approximately $2N$ nodes of coordination 2 or 3, we can relate the proportion of coordination 4 cross-links remaining q, to the total proportion p as:

$$p \simeq \frac{q\,(NL/l_c - 2N) + 2N}{NL/l_c}\ , \tag{3.40}$$

$$\simeq \frac{q\,(\rho - 2) + 2}{\rho}\ . \tag{3.41}$$

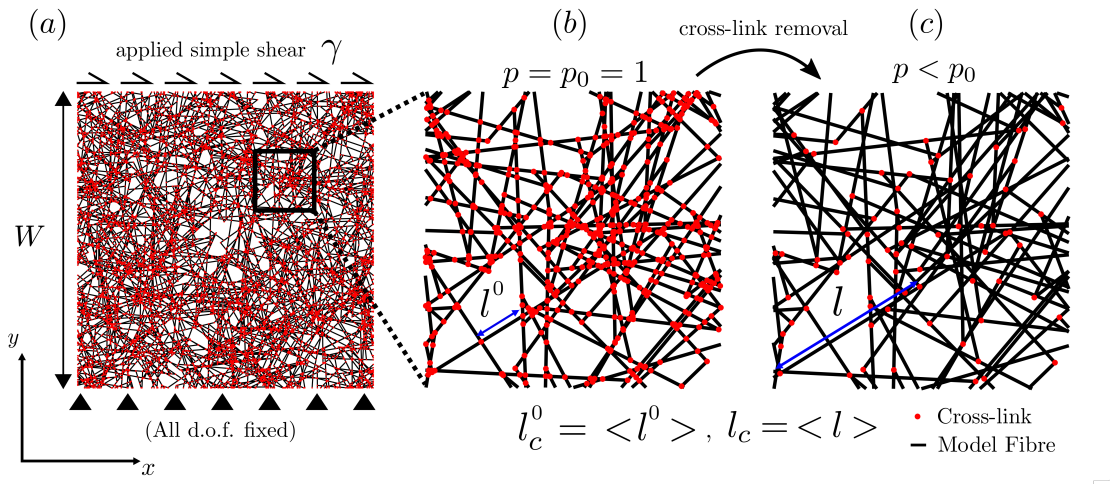

Figure 3.7: (a) A sample Mikado network, with domain size W. Nodes attached to the bottom boundary are fixed in all degrees of freedom, while those on the top boundary are shifted horizontally to give a small bulk simple shear of γ. **(b)** A closer look at the microstructure of the fully cross-linked Mikado model, showing model cross-links in red, fibres in black and the segment lengths l^0, where 0 denotes quantities in the original network. The mean cross-link spacing is given by $l_c^0 := \langle l^0 \rangle$. **(c)** A partially cross-linked Mikado network is shown for the same sample as in **(b)**. In particular, the proportion of remaining cross-links is given by $p := n/n_0$, for number of cross-links n. Longer fibre segment lengths l are observed than in the fully cross-linked case for equivalent polymer density, leading to a larger value of mean cross-link spacing $l_c :=< l >$.

Nodes of coordination 4 are removed uniformly at random according to the above quantities. Following the removal of these cross-links, the crossings of two fibres is no longer necessarily identified with a cross-link, and many overlapping filaments do not constrain one another. In other models, the removal of cross-links usually corresponds to reductions in the overall network density and changes in the network geometry [179, 180]. Mechanical stability can become an issue in these models, and it is often not feasible to remove more than fifty percent of model cross-links before network percolation is disrupted [180]. An illustration of cross-link deletion, with cross-links highlighted in red, is shown in Fig. 3.7, demonstrating that polymer density is held constant as cross-link density varies. We note that networks of lower polymer density will have proportionally fewer nodes of coordination number 4, and thus proportionally fewer cross-links can be removed under our modelling assumptions.

Having generated networks with varying polymer and cross-link densities, we simulate small simple shear deformations in the same manner as Section 3.2. For reference, the relevant model parameters that determine the deformation of model networks are as follows. Alongside fibre number N, rod length L, and polymer density $\rho = NL^2/W^2$, we also have mean segment length $l_c = \langle l \rangle$, bending length scale $l_b = (\kappa/\mu)^{1/2}$, and cross-link proportion parameter $p = n/n_0$.

3.5 Results

We now proceed to investigate results pertaining to the deformations of phantom Mikado networks. We begin by investigating the mechanics that arise within the bending-dominated, nonaffine regime, before investigating the affine-nonaffine transition.

3.5.1 Behaviour in the nonaffine regime

As Mikado rods are placed within the domain, and the line density increases, a solution of rods becomes cross-linked into a network that acquires a static shear modulus, ceasing to be a liquid. This mechanical stability occurs with geometric network percolation when welded cross-links are employed, and at slightly higher fibre densities when freely-rotating links are used, as in this work. Owing to the small bending length scales $l_b = (\kappa/\mu)^{1/2}$ observed for semiflexible polymers, filaments in this regime are often far more compliant in bending than extension. Following this percolation, the mean cross-link spacing l_c decreases with increasing polymer density (as discussed in greater detail in Appendix A). As l_c becomes small, the rods become more difficult to bend, instead storing energy in stretching modes. Now, if cross-link density is lowered for networks of high polymer density, through the random removal of model cross-links, mean cross-link spacing increases (though the network never becomes a solution through the procedure described for this model). We expect that stretching modes will become unfavourable, and energy will be contained in the more compliant bending modes, whence the network returns to the nonaffine regime. As the above transition is predicted to occur for constant network

geometry and constitutive choices, we predict that knowledge of the fibre elastic moduli and network fibre density will not be sufficient to determine the elastic regime in which a fibre network resides in the presence of variable cross-linking.

The nonaffine regime in fibre networks has been discussed previously [163, 167], and is often characterized in Mikado networks through either a low polymer density, small bending length scale $l_b := (\kappa/\mu)^{1/2}$ or a combination of the two. For the standard Mikado model investigated earlier in this chapter, it is characterized by large values of the affine length scales λ_i. We expect that, due to the dependence of fibre bending response on mean segment length, cross-linking should be important to the network response in this regime. As the affine response of a fibre network, as discussed in Appendix B, is independent of fibre segment length, we do not expect a similar sensitivity to the cross-link density for networks within the affine regime. We investigate nonaffine network behaviour by plotting the shear moduli for networks of two (lower) densities as cross-link density is reduced, in Fig. 3.8 **(a)**.

We find that decreasing cross-link density corresponds with a rapid reduction in the network shear modulus, as predicted. This effect becomes increasingly pronounced as the number of cross-links continues to decrease, such that the difference in shear modulus as p varies from $p \approx 0.25$ to $p \approx 0.15$ is far more pronounced than for $p = 1$ to $p \approx 0.9$. In the former case, we find that for networks of polymer density $\rho \approx 44.9$ there is a reduction in the shear modulus of almost two orders of magnitude as cross-link parameter p changes by just 0.1. As such, relatively small changes to cross-link density can drastically alter the macroscopic mechanics of nonaffine samples, suggesting an important mechanism by which biopolymer network mechanics might be regulated. The changes for networks with almost maximal cross-linking are far slighter, so that such assemblies are relatively robust to small variations in cross-link density. For the lowest density networks considered ($\rho \approx 12.8$) differences in the shear modulus remain slight except for those networks with the lowest extent of cross-linking, where again small changes in the nature of network cross-linking can dramatically alter the bulk shear modulus, as illustrated by Fig. 3.8 **(a)**, starred markers.

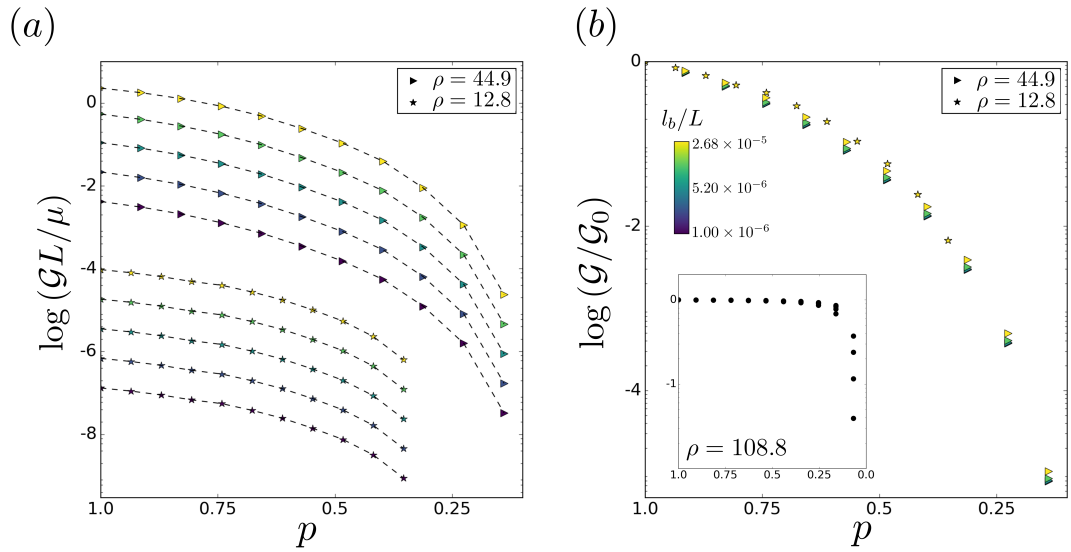

Figure 3.8: (a) The bulk shear modulus $\mathcal{G}$, non-dimensionalized with fibre stretching stiffness μ and polymer length L, is plotted against cross-link proportion parameter p for varying bending length scale $l_b = (\kappa/\mu)^{1/2}$. Significant reductions in $\mathcal{G}$ are observed for lower cross-link densities (decreasing p) in the higher density case $\rho = 44.9$. In particular, the reduction in shear modulus accelerates as cross-link density decreases. **(b)** The bulk shear modulus is normalized to the value for maximally cross-linked networks, showing similar scaling behaviour as l_b is varied for both low density network types. **(Inset)** Scaling of the shear modulus for high density networks shows the insensitivity of network mechanics to cross-link density except at very low values of p. Colour bar displays l_b.

In Fig. 3.8 **(b)** we normalize the shear modulus $\mathcal{G}$ by that found for maximal cross-linking, that is the shear modulus corresponding to the standard Mikado model $\mathcal{G}_0$. In the lowest density case, $\rho \approx 12.8$, scaling with increasing cross-link removal is almost identical across an order of magnitude variation in the bending length l_b. Small deviations are observed for the higher density network, with polymer density $\rho \approx 44.9$, though the scaling across both densities and all bending lengths considered remains similar, suggesting that this behaviour is conserved throughout the nonaffine regime. We also briefly compare to the behaviour in the affine regime, with large polymer density $\rho \approx 109$, in Fig. 3.8 **(b) (Inset)**. As predicted for stretch-dominated fibre networks, reductions in the cross-link density lead only to a small decrease in the shear moduli of these networks, as the network continues to deform affinely. However, at the very lowest values of p, there is a sudden transition into the nonaffine regime, leading to a sudden, sharp reduction in network stiffness.

In order to compare our model with the standard Mikado model, we investigate a scaling argument, discussed by Head, Levine, and MacKintosh [170] and later Heussinger and Frey [173] for 'floppy' fibres within the nonaffine regime. In particular, we can consider networks of fibres with zero bending rigidity $\kappa = 0$. As the DFNs are subisostatic, a geometric rearrangement of fibres can accommodate the imposed boundary shear without requiring the stretching of any fibres [51]. Now, introducing a small but non-zero fibre bending rigidity $\kappa > 0$, networks acquire a non-vanishing static shear modulus $\mathcal{G}$ that can, by assumption, only depend on bending stiffness κ.

The bending behaviour of fibre segments of length l can be described by introducing an effective transverse spring constant, given by $k_\perp \sim \kappa/l^3$, by considering beam moments. Following an argument from Heussinger and Frey [173], we consider the filament deflections, of characteristic magnitude d, that arise when a single constituent fibre is translated. These fibre translations occur on the scale of a whole fibre, such that we do not expect that their magnitude has a dependence on l_c. As such, the only remaining geometric length (for floppy fibres) is L, whence the expected energy in a floppy fibre with deflections of characteristic magnitude $d \sim L$ can be written:

$$\langle \mathcal{H}_{\text{fibre}} \rangle \simeq \frac{L}{l_c} \int_{l_{\min}}^{\infty} \kappa P(l) \frac{d^2}{l^3} \, \mathrm{d}l \simeq \frac{L}{l_c} \int_{l_{\min}}^{\infty} \kappa P(l) \frac{L^2}{l^3} \, \mathrm{d}l \ , \tag{3.42}$$

where L/l_c gives the number of cross-links per fibre, $l_{\min}$ is a minimum length, under which the fibre becomes too stiff to bend, and $P(l)$ is the fibre segment length distribution. Now, as the number of cross-links n within the phantom Mikado network can be written $n \simeq NL/l_c$, compared with the initial number $n_0 \simeq NL/l_c^0$, and given that the cross-link proportion parameter p gives $n = pn_0$, we have the relation $l_c \simeq l_c^0/p$. As discussed in Appendix A, the segment lengths in standard Mikado networks are exponentially distributed $P(l) \sim e^{-l/l_c^0}/l_c^0$. Cross-link removal is random, such that we expect the distribution of segment lengths to remain exponential. Combined, we can rewrite Eq. 3.42, using standard asymptotic

techniques for small $l_{\min} \ll l_c^0$, as:

$$\langle \mathcal{H}_{\text{fibre}} \rangle \simeq \kappa \frac{p^2 L^3}{\left(l_c^0\right)^2} \frac{1}{l_{\min}^2} \ . \tag{3.43}$$

We can self-consistently determine the minimum length $l_{\min}$ by considering the energy balance between a short fibre segment of this characteristic length under deflection, and the translation of an entire secondary filament, whose energy contribution is derived from the activation of the floppy modes there. In particular,

$$\frac{\kappa L^2}{l_{\min}^3} \simeq \kappa \frac{p^2 L^3}{\left(l_c^0\right)^2} \frac{1}{l_{\min}^2} \ , \tag{3.44}$$

such that:

$$l_{\min} \simeq \frac{\left(l_c^0\right)^2}{p^2 L} \ . \tag{3.45}$$

Substituting this minimum length expression back into Eq. 3.43, we arrive at the expected energy per fibre, as:

$$\langle \mathcal{H}_{\text{fibre}} \rangle \simeq \kappa \frac{p^6 L^5}{\left(l_c^0\right)^6} \ . \tag{3.46}$$

Multiplying the above expression by the fibre number N produces the expected total network energy. In particular, we predict that the shear modulus should scale as:

$$\mathcal{G} \simeq \kappa p^6 \frac{N}{W^2} \frac{L^5}{\left(l_c^0\right)^6} \simeq \kappa p^6 \frac{L^4}{\left(l_c^0\right)^7} \ , \tag{3.47}$$

where we have neglected to include strain γ, and used the relationship $NL/W^2 \sim 1/l_c^0$. We therefore expect that the shear modulus within the nonaffine regime should scale as p^6. A comparison of the scaling of the shear modulus in the nonaffine regime with this prediction is shown on double logarithmic axes in Fig. 3.9. For values of p neither too close to unity nor the lower limit, we find that the shear modulus to scale close to our prediction p^6. For the highest and lowest values of p, different scaling behaviour is observed. This is perhaps not surprising, as our arguments presented above do not necessarily hold for the extreme values of p. In particular, the requirement that only cross-links of coordination 4 can be removed is likely to change the probability distribution for l in the lower limit. For higher

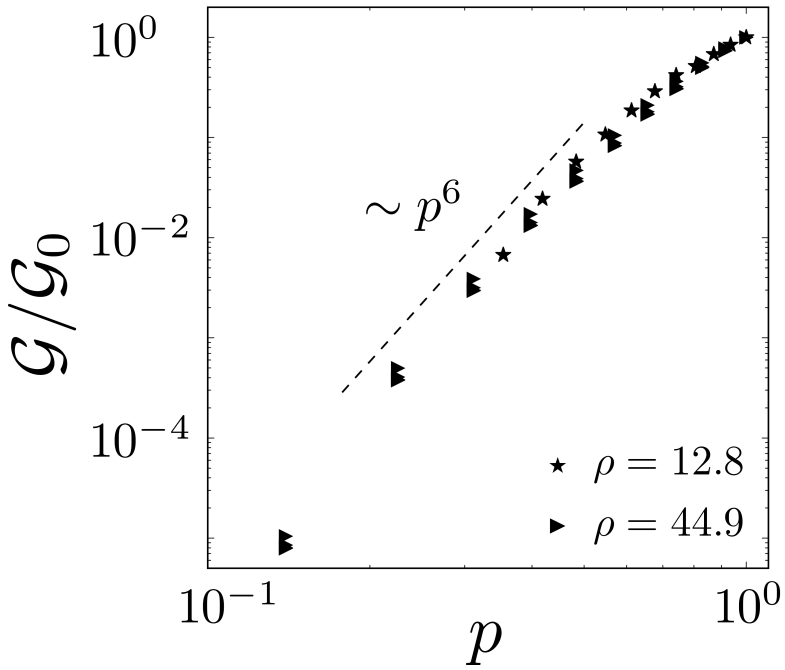

Figure 3.9: The scaling of the shear modulus $\mathcal{G}$, normalized by the corresponding fully cross-linked value $\mathcal{G}_0$ is plotted against cross-link proportion parameter. For moderate values of p, we find that the theoretical scaling prediction $\mathcal{G} \sim p^6$ is a reasonable fit, suggesting that our treatment captures the general behaviour of the system well. However, for large $p \approx 1$ or small $p \ll 1$, the scaling diverges.

values, where proportionally very few cross-links have been removed, the mechanics is likely still dominated by those fibres from which no cross-links have yet been removed. Nevertheless, the good agreement within the intermediate regime suggests a strong scaling with p, as predicted by our above theory.

3.5.2 Transition between affine and nonaffine deformation

As rigidity and density increase, bending deformations of network fibres become increasingly unfavourable and progressively more energy is stored in stretching modes. As such, a fibre network will move from the bending-dominated regime towards an affine, stretch-dominated one, as discussed earlier in this chapter. We briefly recap the scaling within this affine regime, as discussed in Appendix B, before investigating whether previous characterizations of the transition continue to describe the scaling of the network shear modulus in the presence of varying

cross-link density. When subjected to an affine deformation, a constituent fibre initially forming an angle θ with the x-axis will rotate and stretch according to a (shear) strain γ to incur an energy cost:

$$\delta\mathcal{H} = \frac{1}{2}\mu L\gamma^2 \sin^2\theta\cos^2\theta$$

for stretching stiffness μ. Averaging across all (uniformly distributed) angles θ, and summing over all network fibres gives the scaling of the shear modulus for high polymer-density networks within the affine regime stated previously:

$$\mathcal{G}_{\text{affine}} \sim \frac{\pi}{16}\frac{\mu}{l_c} \ .$$

Noting that cross-link constraints do not affect this affine prediction, the result holds independent of p. Further details on this result are presented in Appendix B. Earlier in this chapter, the transition between affine and nonaffine elastic regimes was investigated by Head, Levine, and MacKintosh [163], where the transition was governed by the length scale $\lambda_1 := l_c \left(\frac{l_c}{l_b}\right)^{A_1}$ for scaling exponent $A_1 = 1/3$. Using this length scale, the ratios of shear moduli with the corresponding affine prediction $\mathcal{G}/\mathcal{G}_{\text{affine}}$ collapse onto a common master curve across varying bending rigidities and polymer densities, as seen in Fig. 3.3. We wish to investigate whether this length scale still governs the transition in the presence of varying cross-link density. The attempted summary of our data using this length scale, for varying κ, p and ρ, and $A_1 = 1/3$ here and for the rest of this chapter, is shown in Fig. 3.10 **(a)**. As cross-link density varies, the data no longer collapse onto a single curve. Instead, considerable deviations of several orders of magnitude arise between networks possessing different bending length scales and densities for $p < 1$. Given the dependence of the shear modulus in the nonaffine regime after Eq. 3.47, we seek a collapse by including an addition term into the length scale, dependent on cross-link proportion parameter $p = n/n_0$.

Fig. 3.10 **(b)** - **(e)** shows the attempted collapse for networks of each of the polymer densities considered here under a corrected length scale $\lambda_c = \lambda_1 p^{\frac{1}{2}-\alpha}$, where alpha is a density dependent parameter $\alpha = 8/\rho$. We find that plotting the

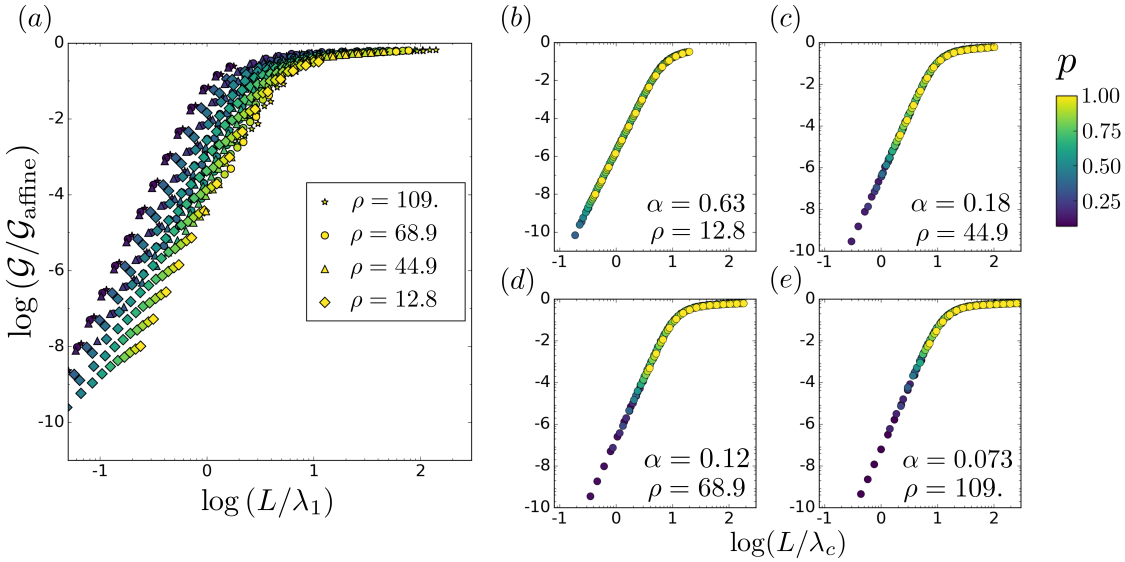

Figure 3.10: (a) Scaling behaviour of the bulk shear modulus $\mathcal{G}$, normalized by the corresponding affine value, in terms of L/λ_1, where $\lambda_1 = l_c(\frac{l_c}{l_b})^{1/3}$. Unlike in the maximally cross-linked case, there is no data collapse under the length scale λ_1. **(b)-(e)** Density-dependent data collapses are shown for four polymer densities under the proposed length scale λ_c. Colour bar displays cross-link proportion parameter p.

shear modulus normalized by the affine prediction against L/λ_c gives an excellent data collapse within networks of a given polymer density, for varying κ and cross-link density. For large density $\rho \gg 1$, this length scale approaches the form $\lambda_c \simeq \lambda_1 p^{\frac{1}{2}}$, though for small densities, large differences can arise. There is no concern of a singularity in this exponent, as the the networks cease to exist below the percolation threshold, that is for low density ρ. Noting that this relation returns to the original length scale proposed in the limit $p \to 1$, we may view the previously reported length scale λ_1 under which the transition occurs as a particular case of this more general result.

We now proceed to investigate the origins of the affine-nonaffine transition as cross-link and polymer density, along with bending stiffness, are varied. The length scale λ_1, discussed earlier for the fully cross-linked Mikado model, partitions networks into those in which the energetics are governed by bending deformations, and those in which stretching dominates. We wish to see whether the new length scale λ_c given above still describes the transition between bending and stretching being the dominant modes of energy storage. The ratio of total bending to stretching

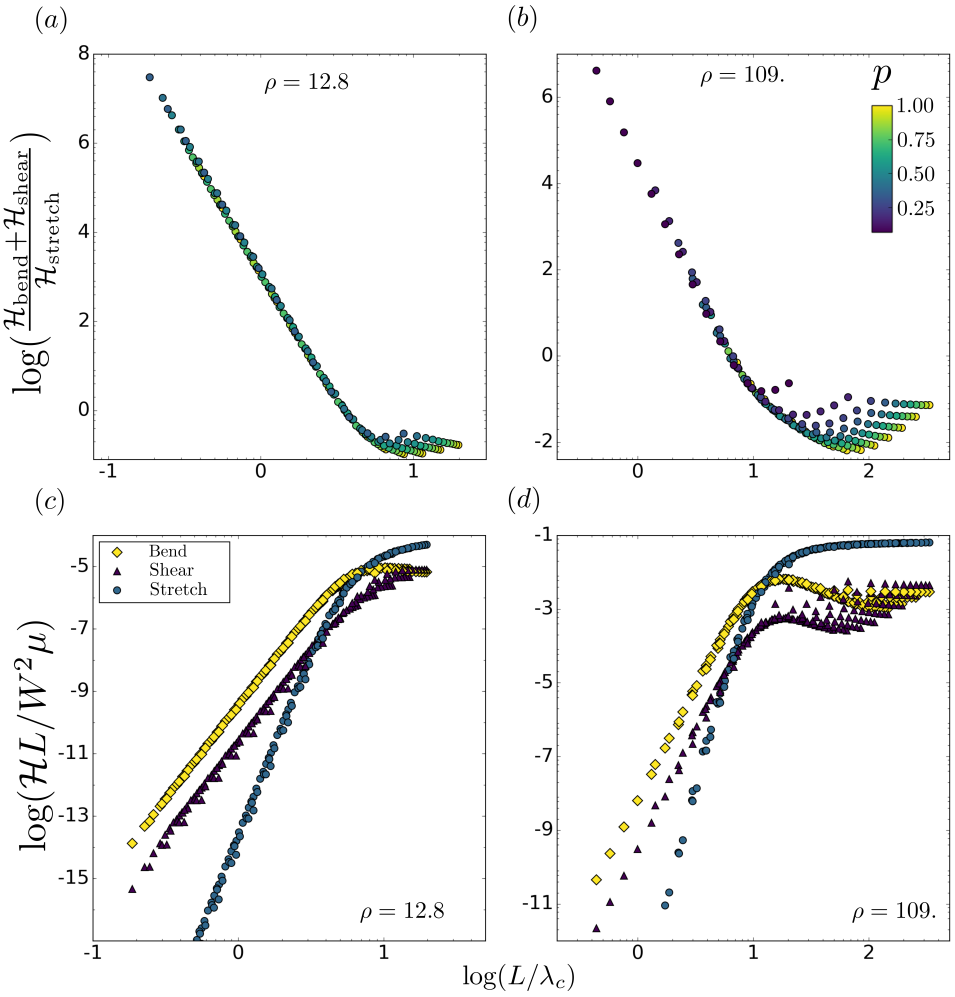

Figure 3.11: (a)-(b) The ratio of bend and shear to stretching energy in networks of two densities is plotted against length scale λ_c, showing a clear transition from bending to stretching dominated deformations. Deviations for those most affine networks (highest L/λ_c) are due to fibre shear energy. **(c)-(d)** The total energy content $\mathcal{H} = \mathcal{H}_{\text{total}}$ of each network is partitioned into the three deformation modes, stretch, shear and bending. In all cases, shear energy forms only a small part of total energy, suggesting that the mechanical network response is largely independent of fibre shearing in this study. Densities and the colour bar are inherited from **(a)-(b)**. Colour bar displays cross-link proportion parameter p.

energy contained within a network is plotted against L/λ_c in Fig. 3.11 **(a)** - **(b)**. We find that, under the new length scale, dominant energy storage switches at the transition from bending to stretching, so that the shear modulus will scale with μ in the affine regime and κ in the bending dominated regime. This confirms that the new length scale describes the same physics as in the fully cross-linked

case. As expected from the validation of our model, beam shear energy does not change results dramatically, though leads to small-order corrections for the highest polymer density networks considered, as predicted. This can be seen in the deviation in bend to stretch ratio for high density networks, in Fig. 3.11 **(b)**, where for stretch-dominated networks, shear and bending energy contributions can become comparable. Further confirmation that the transition is governed by a switch between energy storage modes is given in Fig. 3.11 **(c)** - **(d)**, where the energy stored in shear, stretch and bending deformations of fibres is plotted independently. Here, the small perturbations due to shear, reported in other studies [199], are made explicit, and we can see that while there is some variation in beam shear and bending energies for networks in the affine regime, the sum of these energies remains small in comparison to that stored in fibre stretching. Interestingly, the changes in cross-link density considered here appear sufficient to induce the transition between regimes. Given that many physical biopolymer networks exist with parameters near the transition regime, this suggests a mechanism through which the stiffness of networks with constant polymer density can be extensively regulated to accommodate their biological function, while raising the possibility that pathological changes in cross-link density could have important mechanical implications for *in vivo* systems.

Having discussed the affine-nonaffine transition, and the dominant energy storage modes within the phantom Mikado networks, we now investigate the microscale distribution of fibre energies. In particular, we wish to understand how the network energy is partitioned between the many constituent fibres. We begin by investigating the strain energy densities of filament segments. In this case, we can produce an analytic affine prediction for the cummulative strain energy density with the proportion of fibre segments. Consider an affine network deformation, producing strain energy densities $\hat{\mathcal{H}}$ per fibre segment of:

$$\hat{\mathcal{H}} = \frac{1}{2}\mu\gamma^2 \sin^2\theta \cos^2\theta \ , \tag{3.48}$$

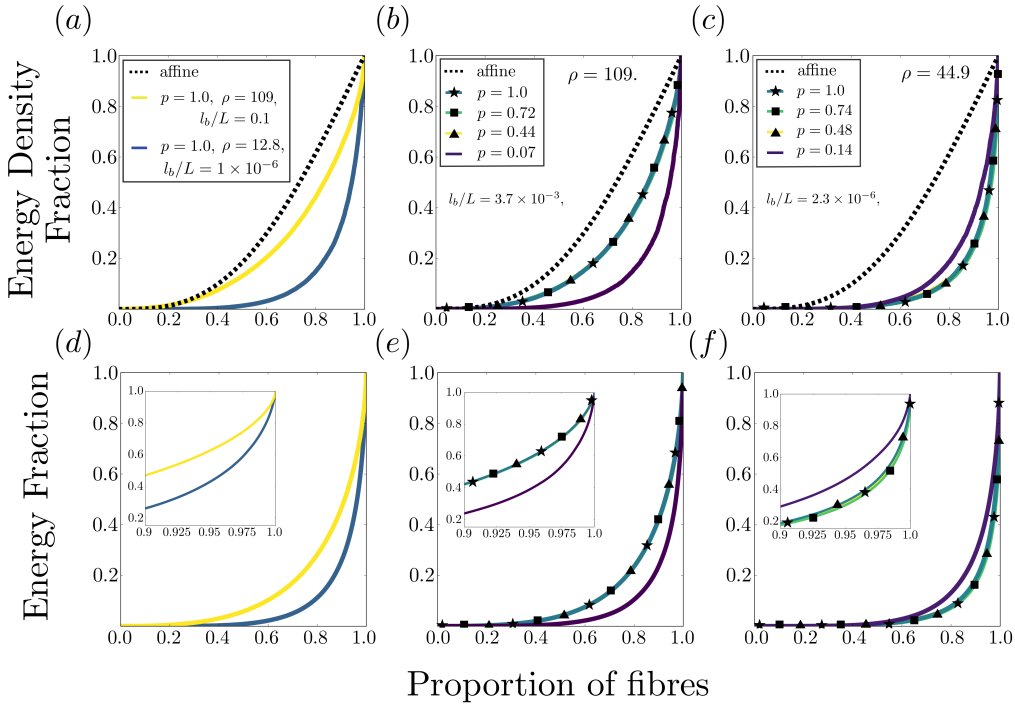

Figure 3.12: **(a)-(c)** Cumulative fibre segment strain energy density is plotted, with comparison to the analytic affine prediction (dash line) given in Eq. 3.48. **(a)** Example results are displayed for affine (yellow) and highly nonaffine (blue) networks in the standard Mikado case, $p = 1$. Affine networks more closely follow the theoretical prediction, while nonaffine networks are characterized by the presence of a small family of energetic fibre segments. The same result is plotted for **(b)** affine and **(c)** nonaffine networks as cross-links are removed. In affine networks, the strain energy density distribution is almost constant as cross-links are deleted, until the lowest values are reached, at which point a sudden move to the nonaffine profile is observed. The strain energy density distribution in nonaffine networks appears similarly insensitive to cross-link parameter p, though surprisingly a modest move towards the affine energy distribution is observed for the most sparsely cross-linked nonaffine networks. **(d)-(f)** Cumulative fibre energy content is plotted against proportion of fibres, with parameters inherited from **(a)-(c)**, showing that similar results hold for fibre energy content as for segment energy density. Inset shows the energy fraction of the top 10% of fibres by energy content, highlighting the fact that a small family of fibres contributes a majority of total network energy. Markers are included to distinguish near identical data arising from networks within a given regime.

for initial fibre orientation θ with the horizontal x-axis. From this expression, fibres parallel to the x- or $y-$axis store no energy under bulk simple shear to leading order in small strain γ, energy content is symmetric in $\theta = \pi/4$. Further, energy density increases until fibres are oriented at an angle $\theta = \pi/4$. The cumulative

strain energy density with fibre orientation $F(\theta)$ should take the shape of:

$$F(\theta) \sim \int \sin^2\theta \cos^2\theta \mathrm{d}\theta \sim \theta - \frac{\sin 4\theta}{4} \ .$$

As networks are isotropic, such that all orientations are equally likely, this expression, plotted between $\theta = 0 - \pi/4$, and normalized to the maximum value $F(\theta = \frac{\pi}{4})$, is equivalent to plotting the cumulative strain energy density against the proportion of fibres with those values. We compare this expression with the equivalent data from phantom Mikado networks in Fig. 3.12 **(a)** - **(c)**. We plot $F(\theta)$ in dash in Fig. 3.12 **(a)** - **(c)**. For the most affine networks considered (yellow in Fig. 3.12 **(a)**), the data are close to the prediction, though in general energy is less equally distributed in the simulated networks than in the affine prediction. As the cross-link density is allowed to vary, we observe very little difference between the cumulative energy density curves in affine networks (Fig. 3.12 **(b)**, markers) until p becomes very small, at which point a sudden switch to a nonaffine profile occurs. In nonaffine networks, a similar insensitivity is observed (Fig. 3.12 **(c)**, markers), until almost all eligible cross-links are removed, whence there is a slight move towards a more affine profile. Taken together with our results for the network shear moduli, this suggests that the distribution of strains throughout the sample do not significantly change, even though the bulk stiffness can change by orders of magnitude. We expect that the change in profile for the initially affine networks as cross-link density becomes small is due to a cross-link-induced affine-nonaffine transition, akin to that observed in Fig. 3.8 **(b)** **(Inset)**.

While we have quantified the fibre segment strain energy density distributions, it is not clear how the actual energy content in the constituent network fibres is distributed. In Fig. 3.12 **(d)** - **(f)** we plot the cumulative fibre energy against the proportion of fibres, for the same network parameters used for the strain energy density distributions. That is, we order network fibres according to their energy content, and use this information to produce the cumulative energy, highlighting the energy share of different fibre families. We find that a hallmark of nonaffine networks is the presence of an increasingly small family of fibres containing the majority

of network total energy, while those networks that deform affinely, according to the length scale λ_c discussed above, distribute energy across a greater number of fibres. Inset gives a closer look at the energy fraction of the top 10% of fibres by energy content, highlighting that the majority of network energy is contained in relatively few fibres. For initially affine networks (Fig. 3.12 **(e)**), over half the total network energy is stored in less than 7.5% of fibres, which is not changed by large reductions in network cross-links until the cross-link parameter becomes small, $p = 0.07$, whence 50% of total energy is contained in just $\approx 2.5\%$ of fibres. The small move back towards a more affine profile as cross-link density becomes low in nonaffine networks is repeated here in Fig. 3.12 **(f)**. While approximately 1% of fibres contain the majority of network energy, the removal of over 80% of cross-links more equally distributed fibre energy throughout the network.

In the above discussions, network deformations have been characterized through energy criteria. However, it is often more natural to characterize affinity in terms of the displacement and rotation of constituent fibres and cross-links. Such results may be harder to verify experimentally, requiring the analysis of tracer beads displaced within the biopolymer network in comparison to measurements of the material shear modulus. However, it is useful to have such a description where microscale displacements are important, for example when investigating displacement fields derived from cell tractions. It is also important to question whether affinity, as characterized by displacement, coincides with energy-based measures such as those discussed above. Here, we investigate the displacement field in phantom Mikado networks by comparing the mean deviation of cross-link displacement from the corresponding affine predictions. In particular:

$$D := \frac{\sum ||\mathbf{x}_i - \mathbf{x}_i^{\mathbf{affine}}||}{n} = \frac{\sum ||\mathbf{u}_i - \mathbf{u}_i^{\mathbf{affine}}||}{n}$$

where summation is over the number of cross-links n, $\mathbf{x}$ is the deformed position of a model cross-link, and $\mathbf{u}_i := \mathbf{x}_i - \mathbf{X}_i$ is the displacement of the i^{th} cross-link, at initial position $\mathbf{X}_i$. We plot this measure, scaled by domain size W and strain γ, against the length scale for (energetic) affinity λ_c in Fig. 3.13. While we do not

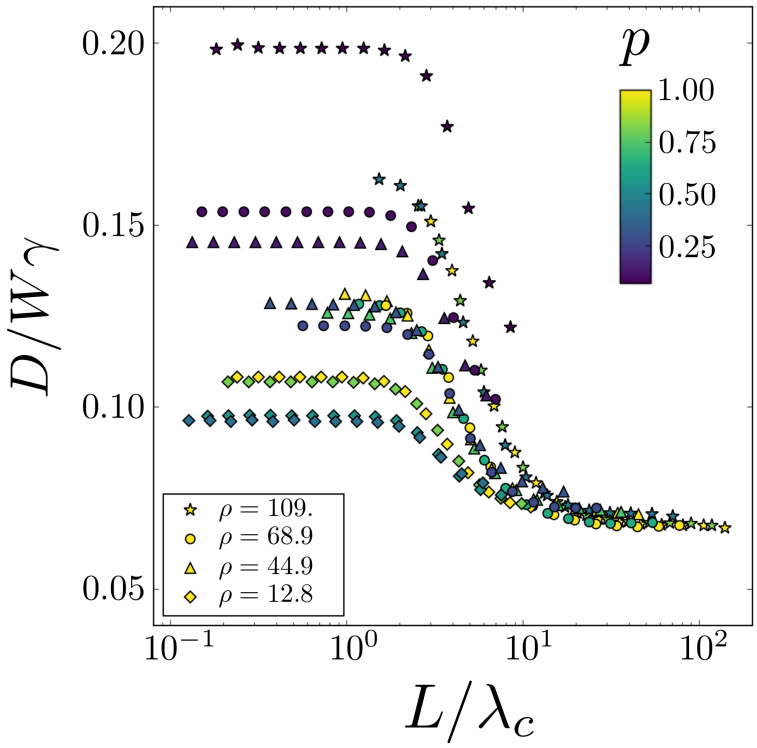

Figure 3.13: Displacement measure D, scaled by domain size W and strain γ is plotted against L/λ_c for varying cross-link and polymer density and varying bending length scale l_b, as incorporated in λ_c. The transition between affine and nonaffine deformation is clear from the move between two constant values. This transition occurs at similar values of λ_c as seen for equivalent energy measures of affinity, suggesting that changes in the displacement and energy based measures of affinity are governed by the same underlying physics. As cross-links are removed, we observe larger nonaffine fluctuations in the nonaffine regime for all polymer densities considered. Colour displays cross-link proportion parameter p.

find a data collapse for this measure, similar to other researchers [170], it is clear that a displacement-based affine-nonaffine transition does occur. This transition is evidenced by the move between two plateau values for displacement measure D, large for nonaffine networks and small for affine cases. At a similar value of λ_c observed for the energetic affine-nonaffine transition, there is a rapid switch between these plateau values. The removal of cross-links (lower values of p, indicated by colour) leads to larger nonaffine displacements throughout the sample, in all of the densities considered. We expect this to be relevant when considering the displacements

experienced by cells resident in substrates with variable cross-linking [9].

3.6 Discussion

The mechanics of fibre networks has been studied under a variety of modelling assumptions, from lattice and disordered fibre network simulations, to mean-field theories. The Mikado model, on which this work is based, has provided key insights into the mechanics of biopolymer networks, where the bending stiffness of the polymer species leads to non-trivial elastic regimes. However, within this model all crossing fibres are automatically bound together at a permanent cross-link. Given recent improvements in electrospinning and photocross-linking technologies, *in vitro* platforms now have far more control over the nature and extent of the biopolymer network structure and topology. Furthermore, many planar biopolymer networks might involve fibres that overlap yet do not rigidly cross-link. To address the need for a more flexible approach to cross-linking, while recognising the importance and influence of the Mikado model within the DFN field, we extended the standard model to incorporate situations in which not all fibre crossings result in the formation of a permanent cross-link.

We have shown in Fig. 3.8 that the scaling of the shear modulus with cross-link removal within the nonaffine regime, away from the affine transition, is qualitatively similar across different densities and bending stiffnesses. In particular, we found that the shear modulus of nonaffine, sparsely cross-linked phantom Mikado networks responded sensitively to the addition or removal of relatively few cross-links. For affine networks, we predicted and confirmed that, owing to the insensitivity of the affine model to the detailed nature or density of cross-links, the shear modulus should be unchanged as cross-links are removed. At the very lowest cross-link densities considered, even initially highly affine networks entered into the nonaffine regime, whence the shear modulus reduced sharply. We further produced a theoretical prediction, based upon DFN floppy mode theory [173], that the shear modulus should scale as $\mathcal{G} \sim p^6$, as all other network properties are held fixed. This scaling found good agreement with simulation data for moderate values of p, yet diverged for

the lowest and highest values considered. We expect that the cross-link coordination criterion, that is only cross-links of coordination 4 may be removed, leads to different fibre segment length distributions at the smallest values of p considered here. The differences observed for p close to unity likely arise due to a break down of the theoretical argument. In particular, when very few cross-links have been removed, we do not expect each network fibre to experience a similar reduction of cross-links, such that the averaging argument employed no longer holds. We note that the strong sensitivity to p within the nonaffine regime is likely to have implications for 3D biopolymer networks, where the ratio of polymer to cross-link density is far higher than in planar networks.

It was not clear whether the bend-stretch transition in Mikado networks with varying cross-link density occurs under the same length scale as for the maximally cross-linked cases, namely $\lambda_1 = l_c \left(\frac{l_c}{l_b}\right)^{1/3}$. However, we found that this length scale did not produce a data collapse for the shear moduli of phantom Mikado networks, as shown in Fig. 3.10. By considering an additional term dependent on the cross-link parameter p, we identified a corrected affine length scale $\lambda_c = \lambda_1 p^{\frac{1}{2}-\alpha}$, through which we found a data collapse to within a polymer density, as shown in Fig. 3.10 **(b)** - **(e)**. Within the simulations considered here, α depended inversely on density, $\alpha = 8/\rho$. For dense networks this length scale becomes independent of ρ, though for low density assemblies, we expect to observe sensitive differences according to polymer density. Furthermore, for fully cross-linked fibres, this length scale reduces to the original quantity λ_1.

To ensure that the data collapse for phantom Mikado networks was still due to the dominant storage of energy within fibres transitioning from bending to stretching modes, we further investigated the energy partitions in network fibres. Under the new length scale, networks clearly displayed a similar transition as with the maximally cross-linked cases, where fibres became progressively less compliant in bending, and stored energy in stretching instead, as seen in Fig. 3.11. The ratio of shear energy to the dominant energy mode in all cases remained small. We continued the investigation into the constituent fibre behaviours by quantifying

the cumulative segment strain energy density and fibre energy content in Fig. 3.12, compared with a theoretical affine prediction. In fully cross-linked Mikado cases, both segment energy density and fibre energy content were more equally distributed throughout the population than in nonaffine cases, where a small number of fibres contained the majority of total network energy. Generally, we found that the distributions investigated were robust to changes in cross-link density, despite the large changes in network stiffness that we observed when cross-links were removed from, for example, nonaffine networks. The largest changes observed occurred when large numbers of cross-links were deleted in initially affine Mikado networks, inducing the aforementioned affine-nonaffine transition, and leading to a likewise change in fibre energy distributions. The fact that such a large proportion of the total network energy is stored in so few fibres in nonaffine cases suggests that such assemblies might be sensitive to damage, with the scission of a small family of fibres potentially altering the macroscale response. However, we note that there is the potential for network redundancy in these situations, and that damage to energetic fibres could lead to the recruitment of nearby fibres to deform and store energy instead, though further work would be required to confirm this. The fibre energy distribution could also be important when investigating the mechanical response of cells embedded in fibrous matrices, as in Chapter 1, as the presence of relatively few energetic fibres could dictate different local responses from mechanically sensitive cells. Increasing the cross-link density could potentially protect against this effect, by more equally distributing energy among a larger group of fibres, suggesting another utility for varying cross-link density.

By measuring the mean deviations of network cross-links from the predicted affine displacement in Fig. 3.13, we investigated another measure for affinity that did not require any knowledge of fibre energetics. Measures for affinity deriving from displacement appear less well characterized in the literature than those derived from energy-based criteria. However, our results for mean deviations from the affine deformation field suggest that affinity as measured using displacement occurs on the same length scale λ_c. In particular, there still exists a sharp transition between

two regimes, where nonaffine displacement fluctuations are larger in energetically nonaffine networks. While we do not assign a definite quantitative interpretation to the values we observed, we do note that considerable differences in the displacement measure are observed as cross-link density varies, especially in those networks with high polymer densities. Here, far larger nonaffine fluctuations arise as cross-links are removed, suggesting that displacement nonaffinity is sensitive to cross-link density.

We have not reported on results for welded networks, where cross-links prevent the rotation of incident fibres, as preliminary simulations suggested that only minor differences arise. In particular, while networks are consistently slightly stiffer owing to the increased number of constraints, the transition between regimes occurred under the same length scale, and the qualitative behaviour was similar. Quantitative studies investigating the relevance of cross-link type and cross-link density compared with experimental data are topics for future work.

The results presented here have considered only planar simulations, and 3D networks have not been discussed. However, our predictions from nonaffine phantom Mikado networks, namely that in this regime biopolymer assemblies become sensitive to small changes in cross-link density, are likely to be relevant for 3D network mechanics. Indeed, the networks discussed in this chapter have far a greater ratio of polymer to cross-link density, which might better represent 3D systems than the maximally cross-linked standard Mikado case. The strict coupling of cross-link number with decreasing mesh size and increasing polymer density does not allow for an investigation into the different effects of distinct network parameters in most two-dimensional systems. As 3D assemblies are considerably less constrained than planar cases, we also expect that many such networks are likely to reside closer to the nonaffine regime, such that cross-link density could play a vital role in regulating the macroscopic network response.

The Mikado model has been crucial in expanding our theoretical understanding of fibre assemblies, in part due to the natural representation of the model network. However, this work demonstrates that the condition of maximal cross-linking does not give a complete understanding of the network behaviour. The extent to which

other network geometries are sensitive to cross-link density is an open question, though our predictions suggest that it is important to investigate, especially within the nonaffine regime. Our results provide further evidence that the mechanical response of fibrous networks are not insensitive to their detailed structure, even where isotropy is maintained, and suggest an important experimental target for photocross-linked electrospun polymer networks. How variations in structure and cross-link density can regulate the response of biopolymer networks *in vivo* remains a fascinating and important question.

In summary, we have investigated the mechanics of random networks of elastic rods in which cross-link density is varied. We observed that the scaling of the network shear modulus with cross-link removal in the nonaffine, bending dominated regime was the same across a range of bending rigidities and polymer densities, and provided theoretical predictions for the scaling of the shear modulus in this regime. We investigated previously characterized length scales for affinity in Mikado networks and demonstrated that they are not suitable for summarizing data from phantom Mikado architectures. Therefore, we provided a corrected length scale that characterizes the affine-nonaffine transition for a given polymer density as the extent of cross-linking is varied. On the scale of individual fibres, we confirmed that this transition occurred due to a bend-stretch change in energy storage, such that the corrected length scale described the same physics as in the maximally cross-linked cases. We also highlighted that in affinely deforming networks, a larger proportion of constituent fibres contribute to the total network energy, and that the distribution of fibre energies was largely robust to variations in network cross-linking. Finally, we confirmed that the affine-nonaffine transition occurred under the same length scale when characterized through cross-link displacements, with the magnitude of nonaffine fluctuations exhibiting a drastic increase as cross-link density was reduced.

This chapter is extensively based on the manuscript "The mechanical influence of single fibre inclusions in discrete fibre networks", submitted to Physical Review E. Humphries, D. L., J. A. Grogan, and E. A. Gaffney.

4

Mechanics of low density heterotypic fibre networks

The semiflexible biopolymer networks commonly found in biological systems, whether in the cytoskeleton of the cell or the extracellular matrix, often naturally occur as composites. Here, various components interact to generate rich mechanical behaviours, beyond the already complex and exotic responses that monotypic biopolymer networks exhibit. Given the frequency with which they occur in biological systems, it is both interesting and important to extend theoretical and computational models of DFNs to encompass this additional complication. This task is highly nontrivial, where filaments with different lengths, radii, mechanical properties, cross-linking behaviour and densities can interact; the resulting problem can be daunting in its complexity. In this chapter, we develop a DFN model for studying the mechanics of single fibre inclusions placed within two different architectures. Namely, we aim to investigate how the mechanics of Voronoi and Mikado networks varies in the presence of a single filament adhered to the matrix. Theory is presented for the scaling of the bulk stiffness as filament orientation, length and elastic properties vary, and computer simulations are compared with these analytic results. The model presented can be viewed as an investigation into

the mechanics of low density inclusion systems, where one fibre type is present in far lower densities than the other.

4.1 Introduction

The mechanics of fibre assemblies has been subject to growing interest in recent decades. Materials constructed from interwoven, entangled or cross-linked fibres include synthetic examples such as paper and textiles, as well as important biological systems, such as both extra- and intracellular matrices. Common to these materials is the importance of a discrete microstructure, in which filaments organise into a complex architecture, granting the bulk material remarkable properties [34, 72, 76, 187]. Within this thesis, we are primarily interested in biological examples, including the cytoskeleton of living cells, an active and dynamic fibre network which grants cells their mechanical rigidity [60, 226], and the complex, hierarchical fibre matrices surrounding living tissue and interacting with many cell types [9, 55, 137]. In both of these examples, it is not sufficient to describe the system according to properties relating to the individual biopolymers, nor bulk quantities such as density. Instead, the detailed assembly of the fibres into a specific network geometry must be considered, as well as a wealth of other factors, such as cross-linking agents, motor proteins, glycosaminoglycans and liquid phases [198, 227, 228]. Many biopolymer systems are formed from semiflexible fibres, where the backbone stiffness of the fibres contributes to longer thermal persistence lengths, yet where the filaments remain far more compliant in bending than in stretching [51, 160]. Composite networks formed from distinct types of semiflexible polymers often interact to grant the overall system diverse properties. For example, within cells, stiff microtubules interact with actomyosin, with important implications for the stiffness and strength of the fibre assembly [229, 230]. In ECM, collagen filaments exist across a large range of radii and organisations, from random and disordered to aligned and stiff, and interact with elastin and other polymers [3, 17, 231]. Furthermore, biopolymer networks seeded with mechanically active cells form a composite system in which the stiffness of the material is determined by the biopolymer scaffold, the reorganisation

of the network geometry by the resident cells, as well as the alignment and force generation of those cells [190, 204]. Given the remarkable properties observed in these polydisperse systems, there is considerable interest in gaining a better understanding of their physics and mechanics.

Considerable insights into the behaviour of composite materials have been granted from continuum studies [188, 232]. However, it is important to determine how the microstructure of the system affects the resulting mechanics. Consider for example an individual stiff rod fixed within a simple elastic solid [233]. In the absence of the inclusion, the displacement field is precisely affine, such that the inclusion can only act to disrupt the affine deformation. In discrete fibre composites, the displacement field of the matrix will depend sensitively on the detailed properties of the fibre network, including its geometry and mechanical attributes [170, 173]. It is not clear *a priori* whether the motions of the inclusion will induce bending or stretching deformations in this microstructure, nor how additional constraints placed upon a nonaffine matrix by such an inclusion will alter the network mechanics. By adopting a discrete approach, the energy partition in individual matrix fibres, the deformation modes that are most favourable, and the local displacements of network cross-links can all be investigated to provide an understanding of the bulk mechanics of the material from a micromechanical perspective, readily allowing for extensions, parameter variations and potentially motivating continuum approximations for composite systems.

Recent work within the context of theoretical studies into discrete fibre composites have highlighted some of the complexity inherent to these systems. Van Doorn et al. [194] investigated composites detailed around a triangular lattice architecture, suggesting that a rich range of mechanical behaviours was possible, depending on the details of the network structure and the mechanical moduli of the polymers. Inclusions could act to dramatically stiffen the bulk network, up to a hundred fold, while for other parameter regimes the mechanical response was dominated by the flexible background matrix. Composites formed from two distinct polymer types have also been investigated in three-dimensions [234]. In between regimes

characterized through either a fully percolated inclusion network or isolated stiff inclusions, distinct nonlinear behaviour was identified, dependent on the ratio of stiff to compliant fibres, as well as the fibre persistence lengths. Exceptional stiffening observed in composite networks *in vitro* has been discussed in the context of simulated Mikado networks, in which the rise in the composite's shear modulus was attributed to a percolation of 'interphases' [219]. Here, elliptical regions surrounding a stiff inclusion were found to be stretch dominated. As the length or density of the inclusions increases, the interactions of these elliptical interphases lead to a drastic increase in bulk stiffness. In parallel with experiments investigating the increase in network stiffness for microtubule-actin composites, Bai et al. [166] studied the mechanics of Mikado networks containing long, stiff inclusions and found an almost immediate rise in the stretching energy in these networks, despite the fact that the inclusions were prohibited from forming stress-bearing networks in the absence of the more compliant matrix fibres. Given that stiff filament density and geometric nonaffinity were strongly negatively correlated, the authors argued that the inclusions acted to locally suppress nonaffine fluctuations, redistributing these instead to regions of the network possessing lower densities of the stiff fibres. Related work into composites where assumptions such as monodispersity, simple cross-links and identical moduli are relaxed have also revealed a range of interesting behaviours [178, 181, 227]. While these investigations have highlighted the inherent complexity in fibre composites, little attention has been given to fibre networks containing lower densities of inclusions, in which the dominant changes to matrix mechanics arises from the detailed interactions between matrix and inclusion.

In order to discuss the mechanics of discrete fibre composites, it is necessary to consider the deformations of semiflexible polymer networks and how they relate to the network geometry and fibre elasticity. As discussed both in Chapters 1 and 3, many theoretical studies discuss DFN models through the characterization of distinct elastic regimes [18, 163]. In particular, analysis has often focussed on the transition between a bending-dominated regime, in which the network stiffness scales with the biopolymer's bending rigidity κ, and one in which fibre stretching,

governed by stiffness μ, constitutes the main deformation mode [170, 172, 173]. Within the bending-dominated regime, the local motions of cross-links are observed to decouple from the imposed bulk displacement, such that the deformation is nonaffine [171]. This places such systems in contrast to simple continua, in which the motion of all points within the sample locally follows that of the whole. As the ratio of bending rigidity to the average distance between cross-links l_c increases, the system transitions to a stretch-dominated regime, accompanied by a marked decrease in nonaffine displacement fluctuations. In Chapter 3 we discussed two length scales under which this affine transition occurs in Mikado networks, though various forms for the affine length scale have been proposed in the literature, where knowledge of the network architecture, fibre persistence length or fibre length L, polymer and cross-link density, spatial dimensions, and the bending and stretching moduli of the polymer all combine to place the system in one regime or the other [170, 186, 225, 235].

One can choose to characterize affinity in two different, yet related, ways. Firstly, the affine regime can be defined energetically, through the ratio of the measured bulk elastic moduli to those predicted from the energy present in fibres undergoing affine motions. Those networks for which this ratio is close to unity are deemed to be deforming affinely, while those in the nonaffine, bending-dominated regime display elastic moduli many orders of magnitude below this theoretical upper limit [163]. Alternatively, one can view the affine regime in terms of the displacement field, and its deviation from affinity [171, 223]. For example, the motion of cross-links in affine networks remains close to the theoretical prediction, while nonaffine networks may involve subregions experiencing local rigid-body motions, accommodated by the bending of fibres connecting these regions [166]. Approaching affinity from this view is perhaps more nuanced in the following sense. As one probes different length scales within the sample, one will find locally nonaffine rotations, though these become small at length scales approaching that of the bulk sample [170, 236]. As such, the discussion of affinity should be mindful of additional length scales present in a problem; even rubber-like materials will display small nonaffine deformations

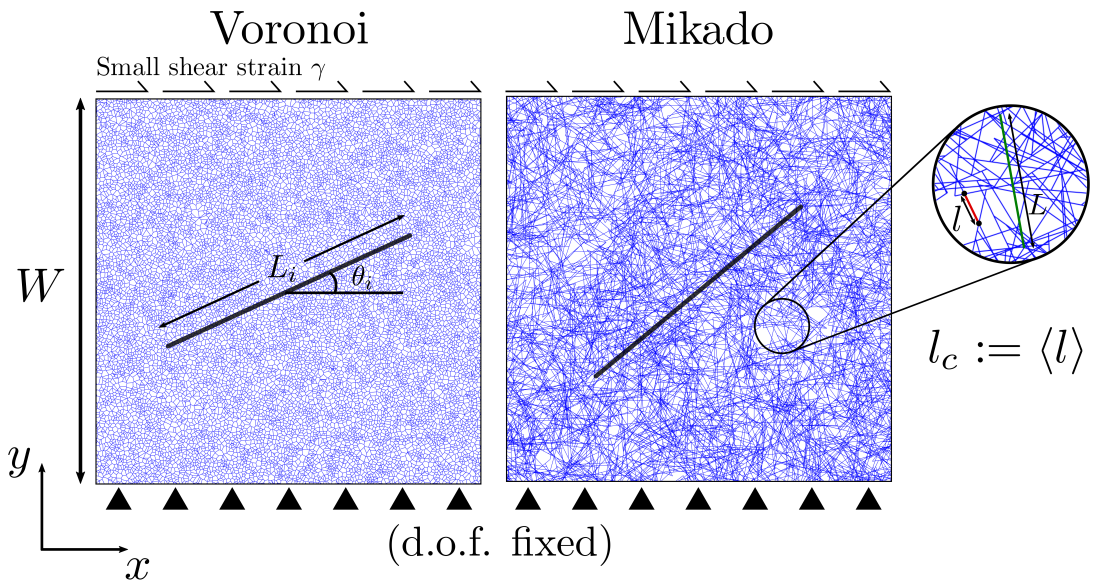

Figure 4.1: Illustrations of single inclusion composites used in this work. Networks are constructed within square domains of area W^2. Nodes attached to the lower boundary are fixed in all degrees of freedom, while those affixed to the upper boundary are shifted to produce a bulk shear of γ. Periodic boundary conditions exist on left and right boundaries. **(Left)** A Voronoi base network in which an inclusion of length L_i is placed at an orientation of θ_i with the horizontal (x) axis. **(Right)** A Mikado single inclusion composite. The lengths of fibre extents between network cross-links, l, take a mean value of l_c. Wherever fibres from the base network cross an inclusion, a new 'welded' cross-link is formed. The length of Mikado base fibres is denoted by L.

below a certain probing length scale [223, 237]. We expect this to be of particular importance in heterotypic networks, where additional length scales are present from multiple polymer types. In particular, one might consider the fluctuations at the length scale of one polymer to be large, yet these could be small at the scale of another, different polymer, whence the displacement field is considered approximately affine there. Furthermore, the relation between different definitions of affinity are likely to be architecture-dependent. If one considers two networks, both of which are considered equally nonaffine in energetic terms, it is not clear *a priori* that motions in the network will be similarly nonaffine in displacement and rotation. Indeed, while the bend–stretch transition is a generic property of subisostatic fibre networks, governed by varying the network density and bending stiffness, it is nontrivial to predict the displacement behaviour of general fibre networks.

We aim to investigate how properties of different network architectures can

contribute to the mechanical response of composite networks. Here, we investigate how the notion of geometric fibre persistence can lead to different network mechanics for low density fibre composites. In particular, we investigate the mechanics of composites formed when single fibre inclusions are placed within fibrous (Mikado) and nonfibrous (Voronoi) architectures within the nonaffine regime, where we expect the largest deviations from continuum modelling. Different modes of deformation are identified, which depend sensitively on network architecture, and theory is developed for the scaling of network energy with inclusion length and orientation. The wide range of mechanical behaviours in these systems is also discussed, and two different transitions are identified, which are determined by the stretching and bending stiffness of the inclusion. Theoretical predictions are presented that consider the different network behaviours, and which agree well with simulation data. These results are used to generate predictions for physical composite networks.

4.2 Model

As discussed above, we shall consider composites in which a single fibre inclusion is introduced into discrete fibre networks based upon two different network architectures. Namely, we shall investigate fibre assemblies constructed from Mikado [163, 168] and Voronoi [186, 187] geometries, which we shall refer to throughout as 'fibrous' and 'nonfibrous' network types respectively. These geometries are considered as two extremes, with Voronoi networks yielding no trivial interpretation of geometric fibre persistence beyond the fibre segment, while Mikado geometries contain perfectly straight fibres continuing through many cross-links. Both architectures considered in this work are planar, constructed within 2D square domains of side length W. Mikado networks are generated according to the procedures discussed in greater depth in Chapter 1. Voronoi-type, nonfibrous matrices are generated by first seeding M points within the domain, uniformly at random. This domain, complete with seeds, is then tiled into a 3×3 grid. A Voronoi partition is applied to the points in this extended, repeating domain in Python, using the qhull library [238]. A geometrically periodic Voronoi diagram may then be recovered by restricting the region of interest

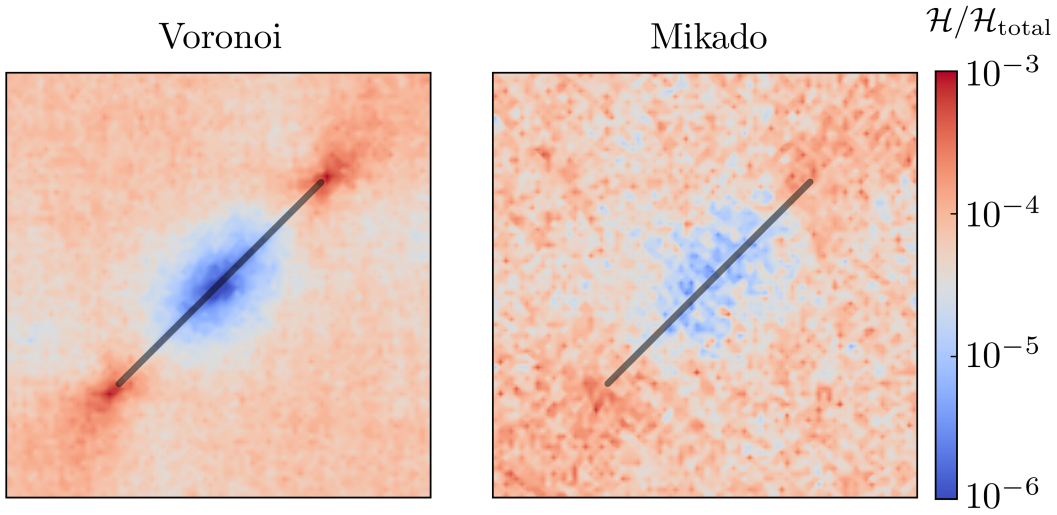

Figure 4.2: A visualization of the base fibre energy content $\mathcal{H}$, normalized by total network energy $\mathcal{H}_{\text{total}}$, in the vicinity of a single stiff inclusion. The inclusion is oriented at an angle $\theta_i = \pi/4$, and has length $L_i/l_c \approx 180$. When inclusions are neglected, both base networks are located within the nonaffine, bending-dominated regime, with **(Left)** Voronoi networks having $l_b/l_c \approx 10^{-3}$, and **(Right)** Mikado networks having $L/l_c = 43.5$ and $l_b/l_c \approx 10^{-4}$. We take the inclusion to be far stiffer in both stretching and bending, such that the inclusion does not experience significant deformations, with $l_b^i/l_b = 10^4$ in Voronoi cases and $l_b^i/l_b = 10^5$ in Mikado networks. In both cases, the stretching modulus for the inclusion is larger than the base modulus, $\mu_i/\mu_b = 10^3$. Results are averaged over 20 different realisations of the base network. In Voronoi networks, the effect is similar to that expected in a continuum, with base network energy reaching its largest values near the fibre end points, and an absence of energy near the centre of the fibre. Qualitatively similar but less pronounced effects are observed within Mikado composites.

to the original square domain. Voronoi nodes, that is the vertices of the Voronoi diagram, when generated from random seeds, have node coordination 3 in the absence of perfect symmetries. These nodes are taken to represent permanent network cross-links, and the edges of the Voronoi diagram are associated with polymer segments. As with Mikado networks, when considered at sufficiently large length scales these Voronoi networks are statistically isotropic in density and orientation.

The above procedures generate the networks that will represent compliant, nonaffine matrices, which we term 'base' networks, into which inclusions are introduced. Composites are formed by placing a straight fibre, of length L_i, into a base network of a given type, where subscript i refers to inclusion parameters. In these cases, the fibre midpoint is always placed to be halfway between upper and

lower boundaries. The orientation of this inclusion, θ_i is measured as a positive rotation from the x-axis, which is taken to be horizontal. Where this inclusion crosses base fibres, permanent network nodes are created; these are to be considered as welded cross-links, as motivated further below. Once all inclusion-base intersections have been identified, any remaining dangling ends are removed. Example networks of both types are displayed in Fig. 4.1, with Voronoi **(Left)** and Mikado types **(Right)**.

We model constituent network fibres of both types, that is base and inclusion, as shear-flexible beams in the small strain regime. In particular, beams are modelled in the same manner as those in Chapter 3, with the internal strain energy for a generic model fibre given by Eq. 3.38. The mechanical properties of base fibres are determined by stretching stiffness μ_b and bending rigidity κ_b. These same quantities, subscripted by i, refer to the inclusion, that is μ_i, κ_i. By considering beam moments, we can view fibres, or fibre segments, as possessing a transverse spring constant, given as $k_\perp = 3\kappa_b/l^3$ for bending rigidity κ_b and segment length l.

In Chapter 1, we briefly discussed different cross-link modelling choices, including freely jointed (as in Chapter 2), freely rotating (as for the standard Mikado model, modelled in Chapter 3), and welded. In Voronoi networks there is no natural notion of geometric fibre persistence through a cross-link, given the general order 3 node coordination. To ensure mechanical stability, cross-links are therefore modelled as fully welded in these architectures, where both the translation and rotation of fibre segments at cross-links are constrained. In order to avoid constitutive differences between the networks, we also employ welded cross-links in the Mikado networks considered, as well as for those cross-links existing between inclusions and base fibres, though the differences between welded and rotating cross-links are expected to be small [199].

The computational results for this chapter are obtained by producing small bulk simple shear deformations in Abaqus, as described in Chapter 3. The relevant geometric and mechanical parameters for this study are as follows. Inclusions are governed by two geometric lengths; L_i, the total length of the straight fibre inclusion, and l_c^i, the mean segment length along the fibre. Mikado base networks

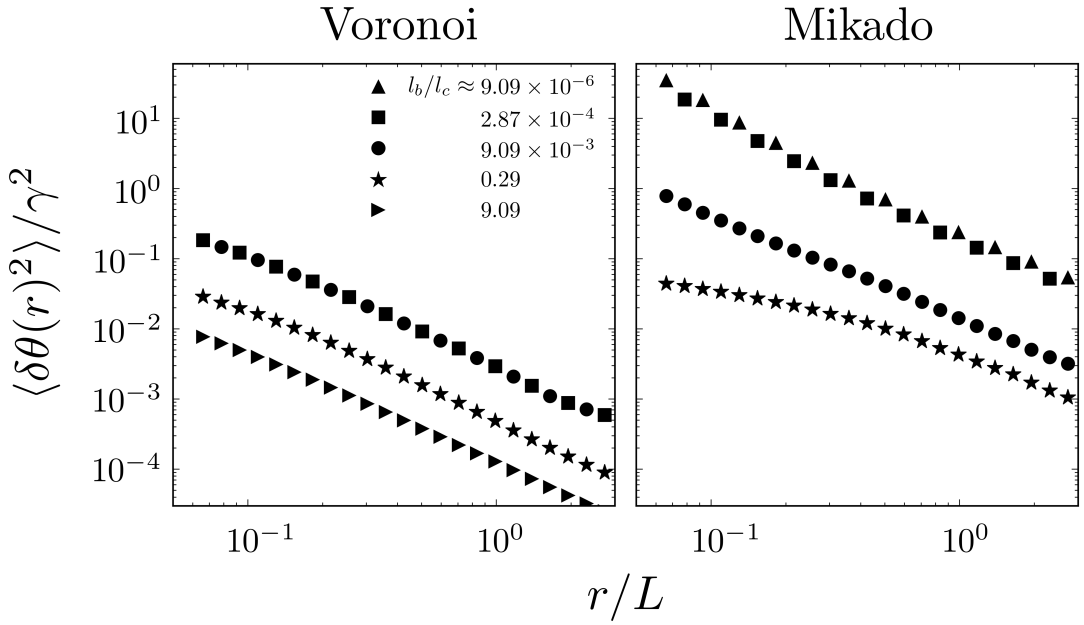

Figure 4.3: The angular measure of affinity $\langle \delta\theta(r)^2 \rangle$, which quantifies the difference between the rotation of a line formed between two sample locations a distance r apart, and the affine prediction, is plotted for Voronoi and Mikado base networks. **(Left)** In Voronoi base networks the nonaffinity measure remains relatively small, even for networks that are classified as highly nonaffine in terms of bending-dominated energy content. **(Right)** The same quantity is measured in Mikado composites, where we observe that for nonaffine networks (triangle and square markers) the degree of nonaffinity is more than two orders of magnitude larger than the corresponding Voronoi cases. In particular, even at larger probing distances $r/L \approx 1$, the nonaffinity measure is larger than in the Voronoi case at the scale of the fibre segment $r/L \approx 0.06$. As such, the discussion of nonaffinity in terms of both displacement and rotation must be addressed independently of energetic definitions, as the two characterizations decouple for different network architectures.

contain the same two geometric lengths, L and l_c, corresponding to the base Mikado fibres, with segment lengths in such networks being exponentially distributed, with probability density function $P(l) = e^{-l/l_c}/l_c$ [186]. More details on the statistics of Mikado networks can be found within Appendix A. In nonfibrous networks, there is only one geometric length, the mean segment length l_c, to consider, owing to the lack of a geometric fibre persistence length. This mean segment length scales as the inverse of total network line density $\hat{\rho} \propto l_c^{-1}$. Finally, there is the domain length W, which is always taken to be sufficiently large that size effects do not affect the results presented here [239]. The relevant constitutive properties are as follows. Base fibres possess a bending length-scale provided by the ratio of

bending and stretching stiffnesses as $l_b := (\kappa_b/\mu_b)^{1/2}$; this parameter, along with the geometric quantities discussed above determine the mechanical regime in which a base network resides. With the addition of inclusions, we also have the ratio of the stretching and bending stiffnesses for base and inclusion fibres, μ_i/μ_b and κ_i/κ_b. Computational results have been averaged over between 20 and 80 simulations, to ensure that fluctuation errors remain small.

4.3 Results

The mechanics of fibre composites are inherently more complex than those of simple continua or of monodisperse discrete fibre networks. In particular, it is less easy to predict which of the competing deformation modes, including fibre bending, stretching, translations and rotations, are dominant when additional moduli and length scales are introduced into the system. However, if we were to consider affine base networks, where the bending stiffness of the base polymer is such that stretching deformations are more favourable, and the local strain field matches that of the bulk material, we expect to observe a picture similar to that in continuum materials. Indeed, we expect the richest behaviour to emerge within the nonaffine regime, where the base fibres exhibit large deviations from the bulk displacement field, and the networks are bending dominated. Throughout this work, it is the interplay between nonaffine base network mechanics and the additional constraints of an inclusion that we investigate.

To gain intuition into the behaviour of single fibre composites, we begin this investigation by quantifying the spatial energy profile of the base network in the presence of an inclusion. Fig. 4.2 displays the energy contained within fibres, normalized by the total network energy, for base networks within the nonaffine regime. The inclusion, oriented at an angle $\theta_i = \pi/4$ with the x-axis and possessing moduli such that it is far stiffer in both extension and bending than the base network fibres, has a pronounced effect on the spatial distribution of energy in the base network. In nonfibrous (Voronoi) matrices, despite their discrete nature, the measured result is qualitatively similar to that expected in continuum models,

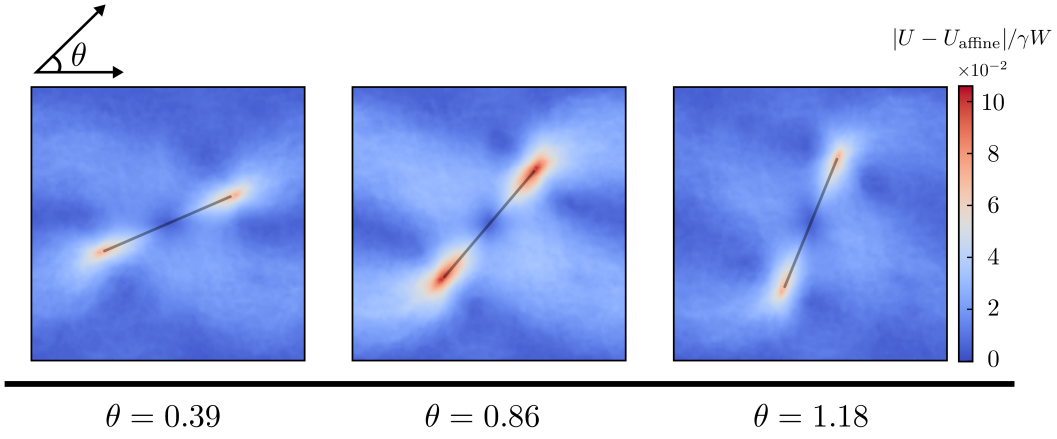

Figure 4.4: An illustration of the spatial deviations from the affine displacement field for network cross-links in the base network, $|U - U_{\text{affine}}|/\gamma W$, for stiff inclusions placed at different orientations within Voronoi networks. Inclusion and base network properties are identical to those used in Fig. 4.2. Results are averaged over 20 realisations of the base network. Nonaffine deviations are observed to be largest for inclusion orientations approaching $\theta_i = \pi/4$, and are localized to areas close to the inclusion end points. The locations of largest displacement nonaffinity correspond with regions of greater energy content, as displayed in Fig. 4.2.

in which the inclusion acts to incur significant energy increases at its termination points. Base fibres along the length of the inclusion, away from the end points, experience smaller deformations than elsewhere in the matrix, resulting in a large reduction in energy in this region. In fibrous (Mikado) architectures, the comparison with the continuum system is less clear. While qualitatively similar behaviours are observed, with a slight increase in network energy located at the inclusion ends, and a reduction in fibre energy in the vicinity of the inclusion midpoint, the effect is less pronounced than in nonfibrous base networks.

We interpret this result in terms of the nonaffine displacement field. In particular, we can consider nonaffine fluctuations in terms of the translations, of magnitude d, of floppy fibres [173]. This translation, whence the magnitude, is defined at the whole fibre scale, length L, such that we expect no dependence on segment length l_c, and we are left to conclude that $d \sim L$. In nonfibrous matrices, such as the Voronoi architecture considered here, nonaffine deformations are expected be at the scale of the mean segment length l_c instead, owing to the lack of an additional

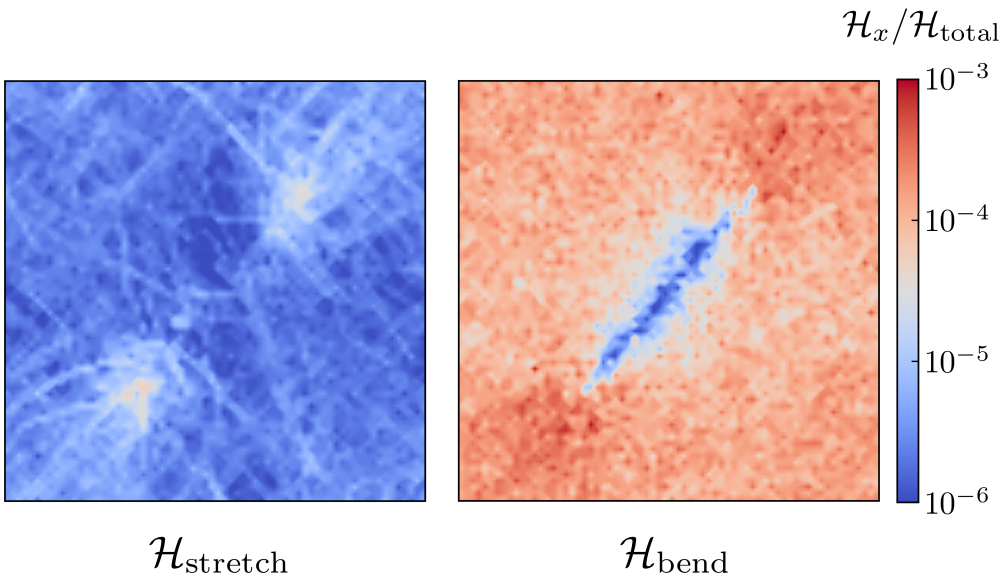

Figure 4.5: The spatial partition of energy in Mikado composite networks is illustrated for the same networks as in Fig. 4.2, displaying the stretching and bending contributions to the total fibre energy in base network segments. No notable increase in stretching contributions **(Left)** along the inclusion body is observed, though base networks do experience a marked decrease in bending energy **(Right)** adjacent to the inclusion. As such, we expect that the observed increase in bend-to-stretch ratio noted elsewhere is instead the consequence of a decrease in bending energy, rather than an increase in base fibre stretching.

fibre length, which is naturally smaller than the Mikado fibre length. As such, we expect the inclusion to experience smaller nonaffine displacement fluctuations in nonfibrous architectures than in Mikado composites, even when both networks display a similar nonaffinity as quantified energetically. This prediction shall be investigated later in this work, where we explicitly examine the consequences of different nonaffine fluctuations. We hypothesize that the inclusion acts as a probing length for the size of the nonaffine deformation field. While the deviation from affine displacements in the nonfibrous cases is small at the length of the inclusion, we expect it to be larger for Mikado cases, leading to a disruption of the spatial energy profile expected in continuum composites [233].

One can quantify deviations in the displacement field by considering the affinity measure $\langle \delta\theta(r)^2 \rangle = \langle (\theta - \theta_{\text{affine}})^2 \rangle$, where θ is the observed rotation, θ_{affine} is the corresponding angle change in a precisely affine deformation, and r is the distance

between two material points. This measure has been used to discuss a broad categorization of the displacement affinity of fibre networks [170]. In particular, we consider lines drawn between any model cross-links separated by a distance r, whence $\langle \delta\theta(r)^2 \rangle$ measures the deviation from the affine rotation angle. The nonaffinity in the displacement field for bending dominated base networks is plotted in Fig. 4.3, for varying degrees of energetic nonaffinity in the base architecture, that is for varying ratio bending length scale to mean fibre segment length l_b/l_c. Even for the most heavily bending-dominated Voronoi networks (left, squares), $\langle \delta\theta(r)^2 \rangle$ is still smaller for equivalent probing distances r than for networks approaching the bend-stretch transition in Mikado cases (right, circles). In particular, for networks of different architectures that possessed similar energetic nonaffinity, the deviations in rotation angles from the affine prediction are far larger in Mikado networks than in Voronoi cases. If this is related to an inclusion twice the length of a base Mikado fibre, $r/L = L_i/L = 2$, this leads to a 100 fold larger measure of displacement nonaffinity in fibrous base networks. As such, even at large probing distances, composites with Mikado architectures exhibit significant nonaffine displacements and rotations when compared with their nonfibrous counterparts.

In order to relate nonaffinity in the displacement field with the spatial energy profiles observed in Fig. 4.2 we wish to visualise a spatial measure of nonaffinity in the presence of a stiff inclusion. In Fig. 4.4, we plot the magnitude of the difference between the displacement field U and the affine prediction U_{affine} for base network cross-links, $|U - U_{\text{affine}}|$, as measured for nonaffine, nonfibrous base networks and inclusions placed at three different orientations θ_i. We observe that this quantity is largest at angles approaching $\pi/4$, and reduces as the angle approaches $\theta_i = 0, \pi/2$. These nonaffine deviations occur at the same locations as the large increase in spatial energy observed in Fig. 4.2. As such, it is clear that the mechanics of such networks can be understood through considering the affine strain field, and how both the base network and the additional constraints placed upon it by the inclusion lead to departures from this prediction.

Before proceeding with scaling arguments for the energy increase when inclusions are introduced to nonaffine networks of different geometries, it is prudent to briefly discuss observations made elsewhere in the literature. In particular, similar composite networks have been investigated in other work [219]. Here it was suggested that an inclusion, oriented at an angle $\theta_i = \pi/4$ with the horizontal, acted to locally increase the stretching energy in base fibres adjacent to the inclusion body. This increase in peripheral stretching energy could then explain a stiffening effect in networks containing many stiff inclusions, where these 'interphases' percolate at a density dictated by shape of the ellipses containing the stretching-dominated region. In order to compare with this theory, we investigate the spatial energy partitions in nonaffine Mikado single fibre composites in Fig. 4.5. The spatial energy partition for base fibres is displayed, normalized by the total network energy, and visualized with log-scale colours, emphasizing the large variations in energy content. While there is a modest increase in the stretching contributions in base fibres close to the inclusion ends, similar to that observed in Fig. 4.2, there is a drastic *reduction* in base fibre bending energy along the fibre inclusion body, where the inclusion acts to prevent significant fibre deformations. As such, we posit that the stretch-dominated region observed elsewhere is due to a reduction in the bending energy, rather than significant increases in the stretching energy. We now instead proceed with a discussion of the displacement affinity in the base network and how this relates to the observed increase in network energies.

We have observed that network energy contributions are largest towards the periphery of fibre inclusions in both Mikado and Voronoi composites. We interpret this observation as follows. Consider an affine displacement applied to all sample points $[X, Y]$ induced by a small shear γ, that is:

$$\begin{bmatrix} x \\ y \end{bmatrix} = \begin{bmatrix} 1 & \gamma \\ 0 & 1 \end{bmatrix} \begin{bmatrix} X \\ Y \end{bmatrix} \ . \tag{4.1}$$

We expect that at the length of the inclusion, the base fibre displacement field is close to the affine prediction, especially in the nonfibrous base architectures. This affine displacement can be applied to an inclusion described by the vector

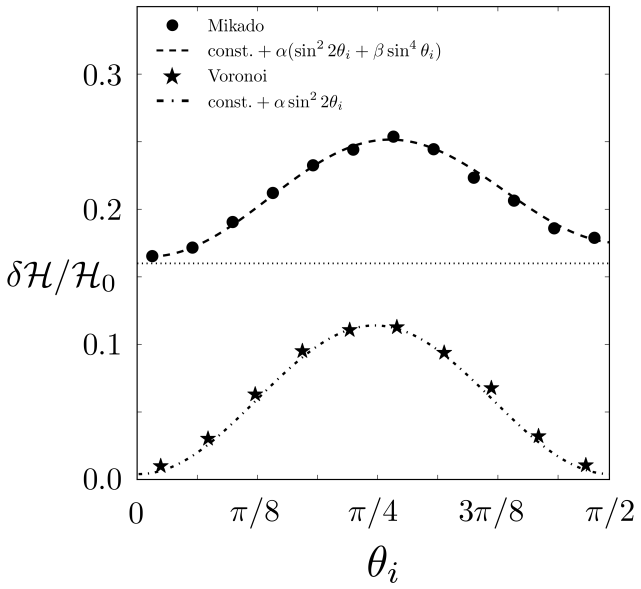

Figure 4.6: The percentage increase in total network energy $\delta\mathcal{H}/\mathcal{H}_0$, where $\mathcal{H}_0$ refers to the total energy content in the base network in the absence of the inclusion, is shown for varying inclusion orientation θ_i. The elastic moduli for the inclusion are taken such that the inclusion is stiff in extension and bending. When Voronoi base networks (stars) are considered, the data closely fit a curve proportional to $\sin^2 2\theta_i$, corresponding to a correction to the affine strain field in the axial direction of the fibre. In Mikado composites (circles), the increase in network energy is asymmetric, with a larger increase observed for vertical ($\theta_i = \pi/2$) than for horizontal ($\theta_i = 0$) fibres. Introducing a term proportional to $\sin^4 \theta_i$, accounting for the affine rotation angle, allows for a good agreement with the observed data. In Mikado simulations, there is a notably greater increase in network energy in the presence of a stiff inclusion, even for horizontal fibres, where rotational and axial contributions predicted in scaling theories vanish, owing to the suppression of larger nonaffine fluctuations.

$[x, y] = L_i[\cos\theta_i, \sin\theta_i]$, where θ_i determines the orientation of the inclusion with the horizontal. Accordingly, the stiff inclusion would experience an axial strain equal to $\frac{1}{2}\gamma \sin 2\theta_i$, to first order in the small strain γ. A discussion of this calculation is given in Appendix B. This would in turn lead to a considerable energy contribution, proportional to $\mu_i L_i \sin^2 2\theta_i$. For sufficiently stiff inclusions, this contribution is expected to be large, such that it is more energetically favourable to relax this inclusion strain at the expense of deformations in the background, compliant matrix. This involves a displacement in the base matrix in the inclusion axial direction proportional to $\gamma L_i \sin 2\theta_i$. From Fig. 4.2 and Fig. 4.4, we expect the displacements and the majority of the energy contribution to be limited towards the ends of the

rods, with a region close to the inclusion centre undergoing a rigid body rotation. Therefore the scaling of the increase in network energy $\delta\mathcal{H}$ should follow as:

$$\langle \delta\mathcal{H} \rangle \sim d^2 \sim \gamma^2 L_i^2 \sin^2 2\theta_i, \tag{4.2}$$

An important aspect of this prediction is that inclusions placed perpendicular or parallel with the shearing direction should lead only to negligible increases in the network energy, as the affine strain of the inclusion vanishes to first order. The energy increase for varying fibre orientation θ_i between $\theta_i = 0, \pi/2$ is quantified in Fig. 4.6. We find that the scaling prediction captures the behaviour of the nonfibrous Voronoi base networks well, with a large percentage increase in network energy for fibres oriented around $\theta_i = \pi/4$, decaying to almost no increase for horizontal or vertical fibres. While the data for Mikado networks initially appear to follow this theory, we observe that the data curve is asymmetric in this case, and ceases to follow the $\sin^2 2\theta_i$ prediction for vertical fibres, that is $\theta_i = \pi/2$. This deviation and asymmetry can be explained by considering displacements transverse to the fibre inclusion axis. In particular, we return to the observation that there exists a very low energy region towards the midpoint of the inclusion; we expect that this reduction in energy occurs due to incidental base fibres undergoing rigid body rotations with the stiff fibre, as all other deformation modes would lead to an increase in fibre energy. At some distance away from the inclusion fibre, fibres that extend from this rigid body domain must interact with the nonaffine background matrix, in a transition region. In terms of our chosen parameters θ_i, L_i, γ, the affine rotation angle for the inclusion can be derived from the cosine rule as follows. Let the deformed inclusion length be given by L_i^ϵ, then the affine rotation angle ϕ follows from:

$$\gamma^2 L_i^2 \sin^2\theta_i = L_i^2 + (L_i^\epsilon)^2 - 2L_i L_i^\epsilon \cos\phi \ , \tag{4.3}$$

so that for small γ, ϕ,

$$\phi \approx \gamma \sin^2\theta_i \ . \tag{4.4}$$

More details on this calculation are given in Appendix B. Consider a base fibre, length L, which crosses the transition between the rigid body region and the background

matrix. This fibre rotates according to the affine rotation ϕ of the inclusion, inducing (or incurring) additional displacements of order $L\phi \sim L\sin^2\theta_i$. As the number of such fibres scales as L_i/l_c, and the number of base fibres coincident to a given transition fibre scales as L/l_c, we expect the corresponding energy induced by these displacements to scale as:

$$\langle \delta\mathcal{H}_\phi \rangle \sim \frac{L_i}{l_c}\frac{L}{l_c}\left\langle \frac{\kappa_b (L\phi)^2}{l^3} \right\rangle \ , \tag{4.5}$$

$$\sim \frac{L_i L}{l_c^2}\left\langle \frac{\kappa_b (L\gamma \sin^2\theta_i)^2}{l^3} \right\rangle \tag{4.6}$$

$$\sim f(L, l_c)\kappa_b \gamma^2 L_i \sin^4\theta_i \ , \tag{4.7}$$

where averaging takes place over base fibre segment lengths l. We return to the scaling function f later in this chapter, though the scaling with $\sin^4\theta_i$ is sufficient for the discussion here. If we consider an additional contribution to the energy change in Mikado composites, of the form $\sin^2 2\theta_i + \beta \sin^4\theta_i$, as shown in Fig. 4.6, dashed, we find that we can explain the asymmetry in θ_i for data from Mikado–single inclusion networks and achieve a good agreement between data and theory. In both single inclusion composite types the amplitude of the data curve is similar, as expected for the axial nonaffine displacements induced by the inclusion. We note that we do not expect to find significant asymmetry in Voronoi cases, as there is an absence of long-range correlations, enforced by long base fibres that can span both regions. Interestingly, while almost no increase in total network energy is incurred for horizontal and vertical inclusions in Voronoi base networks, a small increase is observed for Mikado composites, even for horizontal fibres, where both of the energy contributions discussed in the above theory vanish. This may be understood by considering the larger nonaffine fluctuations in Mikado base architectures. Those fibres crossing the stiff inclusion are prevented from undergoing the nonaffine displacements that minimize energy in the base network. As such, constraints on these fibres induce deflections in other coincident base fibres, leading to a larger increase in energy, with approximately a 25% increase observed for $\theta_i = \pi/4$ in Mikado composites compared with $\approx 11\%$ in nonfibrous architectures.

In Voronoi cases, the additional constraints only lead to small corrections owing to the far smaller nonaffine displacements in this architecture, as evidenced by Fig. 4.3.

As discussed above, the correction to the affine displacement field in the tangent direction of the inclusion is expected to scale with the square of the length L_i, assuming a correction to the affine strain of the inclusion towards the fibre end points. We investigate this prediction in Fig. 4.7. When Voronoi base cases are considered **(Left)**, we find close agreement with this prediction, with network energy increase scaling as $(L_i/l_c)^{1.97}$ for constant l_c. However, the energy increase in Mikado networks deviates from this theoretical argument in Fig. 4.7 **(Right)**. In particular, for smaller stiff inclusions, similar to the length of the base fibres, a far weaker scaling with L_i was observed, where $\delta\mathcal{H} \sim L_i^{1.07}$. When far longer inclusions were considered, the dependence on L_i became more prominent, as $\delta\mathcal{H} \sim L_i^{1.57}$. We interpret this as a consequence of the scaling of nonaffine displacements in the base networks, as well as the various competing modes through which energy increases in fibrous composites. Indeed, the theory presented above breaks down if the surrounding matrix does not deform according to an affine displacement field. This is the case for short inclusions, which rotate and translate according to a locally nonaffine displacement field, and the increase in energy is largely due to the suppression of nonaffine base fibre deformations. We expect that to recover the theoretical scaling with L_i^2, the quantity L_i/L in Mikado composites must be of similar size to L_i/l_c in Voronoi cases. However, as this would involve fibre network systems larger than we are able to investigate in this work, we do not discuss this further.

We have thus far considered fibre inclusions which are far stiffer with respect to both extension and bending than the base network. We now proceed to relax these assumptions and investigate how the change in network energy scales as μ_i and κ_i increase from compliant to stiff.

We first consider the increase in energy from a fibre with varying stretching modulus μ_i in Voronoi architectures. We treat inclusions as stiff in bending, so that fibre deflections are minimal. If this fibre is compliant in extension, so that under

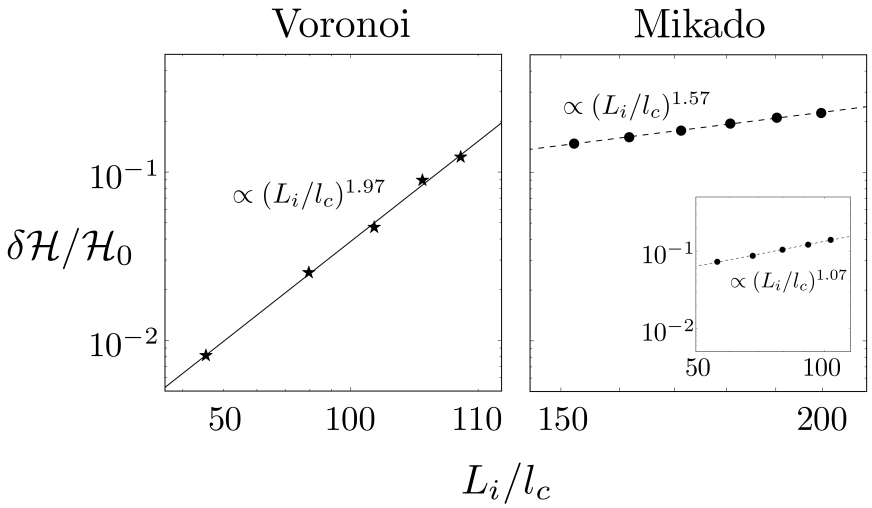

Figure 4.7: The scaling of the change in total network energy $\delta\mathcal{H}/\mathcal{H}_0$ with inclusion length L_i is plotted, for both Voronoi **(Left)** and Mikado **(Right)** base networks within the nonaffine regime. The change in energy for non-fibrous, Voronoi base cases scales according to L_i^2, as expected for an axial correction to the affine displacement field by the stiff inclusion. A weaker dependence is noted for Mikado base networks. In particular, for longer inclusions $L_i/l_c > 150$, the scaling with L_i is approximately equal to $L_i^{1.57}$. For shorter inclusions in Mikado networks, this scaling reduces to close to unity.

the motion of the base network the majority of the change in energy is stored in inclusion stretching, we expect the energy increase to scale as:

$$\delta\mathcal{H} \sim \frac{1}{2}\mu_i\epsilon_i^2 L_i \ , \tag{4.8}$$

$$\sim \mu_i\gamma^2 \sin^2 2\theta_i L_i \ , \tag{4.9}$$

where $\epsilon_i \sim \frac{\gamma}{2}\sin 2\theta_i$ denotes the affine strain in the inclusion. Now, recall that the transverse spring constant for the fibres is given by $3\kappa/l^3$, for segment length l. For random Voronoi networks neighbouring segments are expected to be independent, such that correlations between nearby edges are absent. Then, we make the assumption, similar to elsewhere in the literature [186], that we can discuss the system in terms of a single transverse spring constant $k_\perp \simeq \kappa/l_c^3$. If we consider the network energy increase from a stiff fibre (large μ_i), inducing displacements in the L_i/l_c crossing fibres according to a corrected strain field in the axial direction

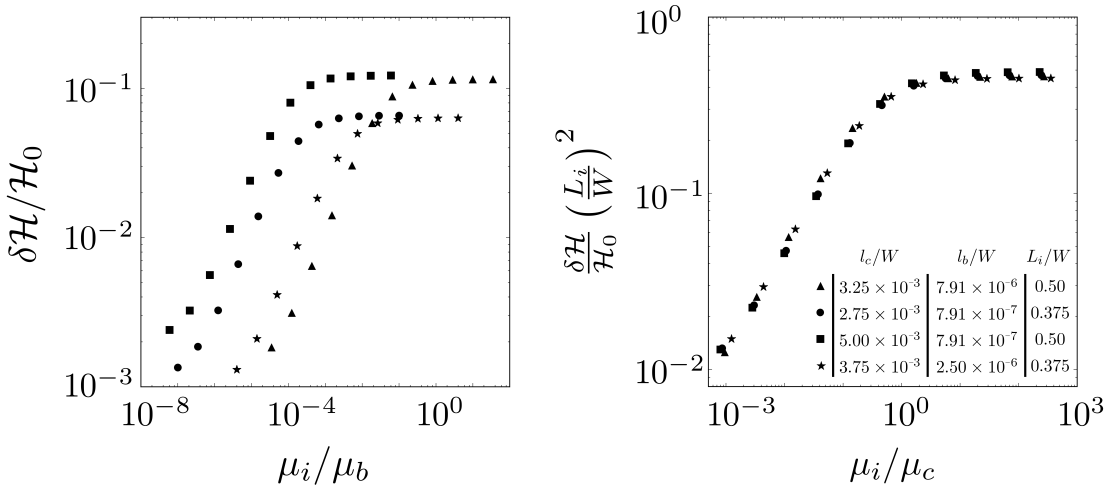

Figure 4.8: The percentage increase in total network energy for Voronoi composites is investigated as the inclusion stretching modulus μ_i varies. **(Left)** The increase for four different parameter choices for the base network density and bending stiffness as well as for the inclusion length are considered for varying μ_i, normalized by the base fibre rigidity μ_b. We note the existence of a transition, where above a critical value μ_c of the inclusion stretching stiffness, further increases do not lead to likewise rises in total network energy. **(Right)** The same results are rescaled under the theoretical prediction for the critical value μ_c, with the increase in network energy normalized by the square of the inclusion length. We observe an excellent data collapse under this critical value, suggesting that the scaling arguments discussed capture the physics of this transition. In all cases, the bending rigidity of the inclusion is taken to be sufficiently large to avoid any significant deflections.

of the fibre, we have:

$$\langle \delta\mathcal{H} \rangle \sim \frac{L_i}{l_c}\frac{\kappa_b}{l_c^3}\frac{1}{L_i}\int_0^{L_i/2}(z\sin 2\theta_i\gamma)^2\,\mathrm{d}z\ , \tag{4.10}$$

$$\sim \frac{\kappa_b\gamma^2\sin^2 2\theta_i L_i^3}{l_c^4}\ , \tag{4.11}$$

where we average over z, which measures the distance along the inclusion fibre from the midpoint. We predict that there exists a transition between these two regimes as μ_i increases. In this case, the two competing energy contributions must balance at the transition, such that for the critical value μ_c of the stretching stiffness, we have:

$$\mu_c\gamma^2\sin^2 2\theta_i L_i \simeq \frac{\kappa_b\gamma^2\sin^2 2\theta_i L_i^3}{l_c^4}\ , \tag{4.12}$$

so that:

$$\mu_c \approx \kappa_b\frac{L_i^2}{l_c^4}\ . \tag{4.13}$$

To investigate this prediction for the critical inclusion stiffness μ_c, we quantify the energy change in Voronoi networks for a variety of simulation parameters in Fig. 4.8. The left hand plot shows the results for 4 different parameter choices, as μ_i is varied across many orders of magnitude, normalized by the stretching stiffness of the base polymer μ_b. The predicted transition is clear, with an increase in total network energy with μ_i of over 2 orders of magnitude, until a plateau region is reached, where further increases in the inclusion axial stiffness do not lead to additional increases in total network energy. The result of scaling the inclusion stretching stiffness μ_i with the predicted critical modulus μ_c derived above is shown in the right hand figure, where the change in energy is scaled by the square of the inclusion length, as suggested by Fig. 4.7 and Eq. 4.2. We observe an excellent data collapse across all parameter choices under this critical value for the stretching modulus, evidencing that the transition does occur according to the change in deformation modes discussed above. Interestingly, we note that this critical μ_c can be small for nonaffine networks. Indeed we can rewrite the expression for the critical value as:

$$\frac{\mu_c}{\mu_b} \simeq \left(\frac{l_b}{l_c}\right)^2 \left(\frac{L_i}{l_c}\right)^2 \ , \tag{4.14}$$

where again the bending length-scale is given in terms of the bending and stretching base rigidities as $l_b = (\kappa_b/\mu_b)^{1/2}$. For nonaffine networks, the ratio of this quantity to the mean segment length l_c is typically small, such that the critical value for μ_c can be orders of magnitude smaller than that of the base network.

When considering Mikado networks, the assumption utilized in Voronoi architectures, namely that fibre segments are independent and act as springs in series, breaks down due to long base fibre length L, and we must consider the spring constant in more detail. In particular, we follow a similar approach to Heussinger and Frey [173], in the context of floppy modes in fibre networks. Consider again the average energy increase from base fibre deflections induced by the stiff inclusion correcting the affine displacement field. If we average over the base fibre segment

length distribution $P(l) \sim e^{-l/l_c}/l_c$, we have:

$$\langle \delta \mathcal{H} \rangle \sim \frac{L_i}{l_c} \int_{l_{\min}}^{\infty} \frac{2}{L_i} \int_0^{L_i/2} \kappa_b P(l) \frac{z^2 \sin^2 2\theta \gamma^2}{l^3} \, \mathrm{d}l \, \mathrm{d}z \ , \tag{4.15}$$

$$\sim \frac{\kappa_b \gamma^2 \sin^2 2\theta_i L_i^3}{l_c^2} \frac{1}{l_{\min}^2} \ , \tag{4.16}$$

where $l_{\min}$ is a regularizing length, under which the deflection of the fibre segment becomes too energetically expensive, and the bending energy of this segment is instead relaxed through the translation of an entire secondary base fibre, exciting the floppy modes there instead. If we consider the characteristic magnitude of these deflections to be given by d, this minimum length may be determined by balancing the energy content in a deflected short segment with that in an entire secondary fibre, as:

$$\frac{\kappa_b d^2}{l_{\min}^3} \simeq \frac{L}{l_c} \int_{l_{\min}}^{\infty} \kappa_b P(l) \frac{d^2}{l^3} \, \mathrm{d}l \ , \tag{4.17}$$

which suggests a minimum length of $l_{\min} \simeq l_c^2/L$, and therefore a corrected scaling in Mikado composites of:

$$\langle \delta \mathcal{H} \rangle \sim \frac{\kappa_b \gamma^2 \sin^2 2\theta_i L_i^3 L^2}{l_c^6} \ . \tag{4.18}$$

Balancing this expression with that for the energy in an affinely stretched fibre produces the expression for the critical stiffness μ_c in Mikado base networks:

$$\mu_c \simeq \kappa_b \frac{L_i^2 L^2}{l_c^6} \ . \tag{4.19}$$

Results for Mikado networks across a variety of parameter choices as μ_i is varied are shown in Fig. 4.9. The left hand figure displays the unscaled results, where we again note that a similar transition occurs in Mikado architectures as in Voronoi cases. However, the increase in energy is somewhat diminished, to approximately a 10 times increase in energy, rather than the 100 fold increase measured in Voronoi composites. The same data are displayed under the scaled μ_i in Fig. 4.9 **(Right)** where we have again rescaled the change in energy with L_i according to Fig. 4.7. We find that this corrected critical value again produces a good collapse for the simulation data, evidencing that the corrected value for the

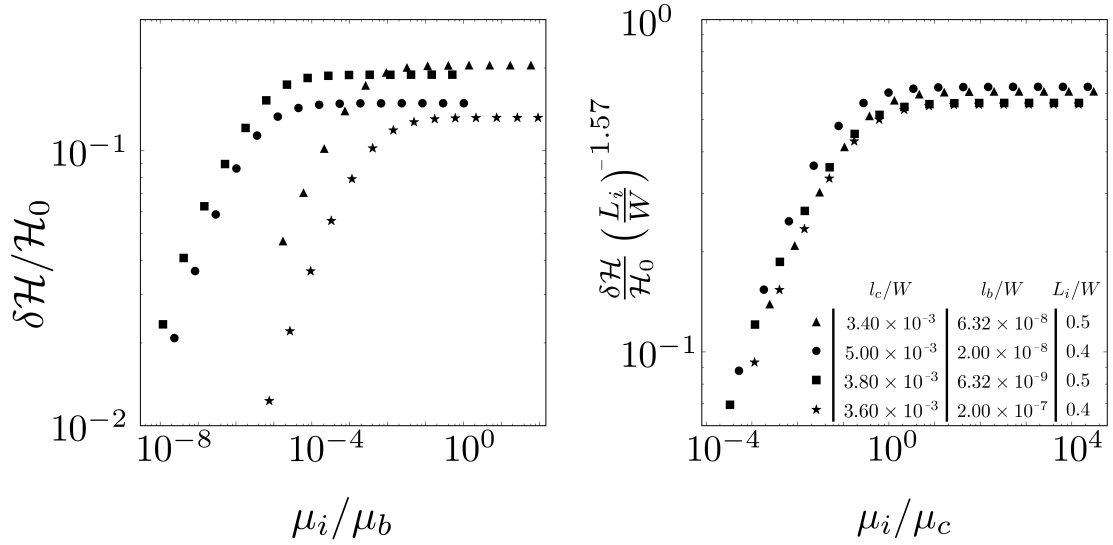

Figure 4.9: The percentage increase in total network energy for Mikado composites is investigated as the inclusion stretching modulus μ_i varies. **(Left)** Similar transitions under varying μ_i are observed in Mikado composites as in Voronoi cases, shown for four different parameter choices for the base network density and bending stiffness as well as for the inclusion length, normalized by the base fibre rigidity μ_b. **(Right)** The results are rescaled under the corrected prediction for the critical value μ_c in Mikado composites. By considering a corrected critical stiffness μ_c in the presence of additional contributions from Mikado base fibre length, we achieve a data collapse such that the transition for all composites considered occurs under the same values of μ_i/μ_c. We note that for equivalent base fibre bending stiffness this transition occurs at larger values of μ_i than in Voronoi composites.

critical stiffness captures the network behaviour at the transition. We note that the expression for this critical stretching stiffness is far larger than for Voronoi base networks, which is a consequence of the long fibre length L.

Having investigated the transition that occurs as the stretching stiffness of the inclusion increases from compliant to stiff, for high bending rigidity, we now wish to investigate how the network increase in energy varies with the inclusion bending stiffness. Given our discussion of Voronoi base networks, in which displacement nonaffinity is small, we do not expect large deflections in the inclusion, such that varying κ_i is not expected to produce significant variations in total network energy. However, the bending stiffness of the inclusion is expected to have important consequences for Mikado base networks, where significant fluctuations in the base network are likely to induce large bending deformations in the inclusion. Consider

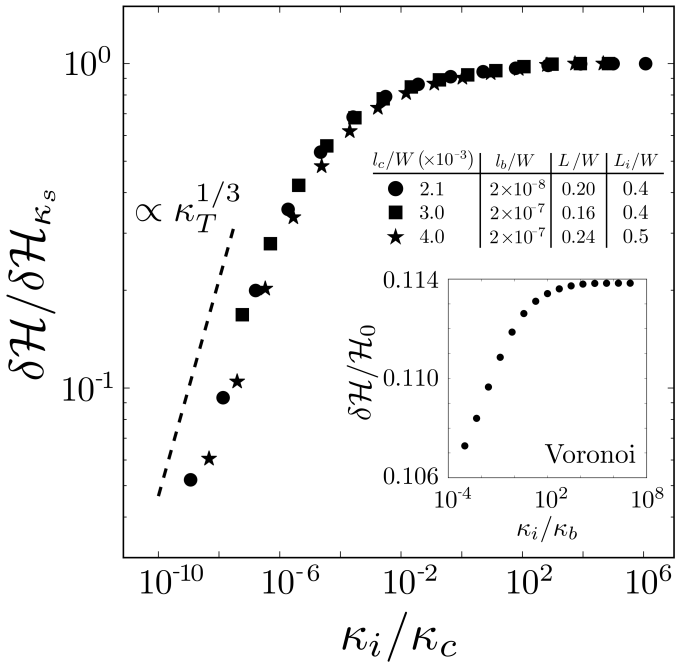

Figure 4.10: The scaling of the total network energy increase with increasing inclusion bending stiffness κ_i is investigated for Mikado composites under three sets of parameter choices within the nonaffine regime. Similar to the results for varying the inclusion stretching modulus, we again observe a transition to a plateau region, in which further increases to the bending rigidity do not lead to likewise energy increases in the total network energy. The percentage energy increase is scaled according to this plateau value $\delta\mathcal{H}_{\kappa s}$, while the fibre bending stiffness is scaled according to the critical value κ_c predicted from scaling arguments. A good data collapse is observed across the three parameter sets, with the network energy increase scaling close to the $\kappa_i^{1/3}$ predicted. **(Inset)** The same transition is considered for Voronoi composites. Here, the change in percentage network energy increase is small (below 1%) over 12 orders of magnitude in the inclusion stiffness, such that the inclusion bending rigidity is not likely to be a dominant factor in determining the energy increase in Voronoi composites.

first a 'floppy' inclusion, which deforms according to the background nonaffine Mikado network. The deflections incurred due to the base network are proportional to the size of the nonaffine displacements, scaling as L [173]. Then, as the bending stiffness κ_i increases from zero, we expect to see an increase in energy according to this fibres deflections. In particular, we can write this energy in the form:

$$\langle \delta\mathcal{H} \rangle \sim \frac{L_i}{l_c} \int_{l^i_{\min}}^{\infty} \kappa_i P(L_s) \frac{L^2}{L_s^3} \, \mathrm{d}L_s \ , \tag{4.20}$$

$$\sim \kappa_i \frac{L_i L^2}{l_c^2} \left(\frac{1}{l^i_{\min}} \right)^2 \ , \tag{4.21}$$

where $l^i_{\min}$ is the minimum length for a segment along the inclusion fibre to bend, rather than inducing displacements of crossing fibres, and L_s denotes fibre segment lengths between cross-links along the inclusion. We can determine this length self consistently as follows. For fibre segments possessing this minimum length, energy balance must exist between the deflection of the single segment (of characteristic magnitude d) and the energy in an entire secondary translated base fibre, which, utilizing the expression for $l_{\min}$ from above can be expressed as:

$$\kappa_i d^2 \left(\frac{1}{l^i_{\min}}\right)^3 \sim \frac{L}{l_c}\int_{l_{\min}}^{\infty} \kappa_b \frac{d^2}{l^3} P(l)\,\mathrm{d}l \ , \tag{4.22}$$

$$\sim \frac{\kappa_b L d^2}{l_c^2}\left(\frac{1}{l_{\min}}\right)^2 \ , \tag{4.23}$$

$$\sim \frac{\kappa_b d^2 L^3}{l_c^6} \ , \tag{4.24}$$

so that:

$$l^i_{\min} \sim \left(\frac{\kappa_i}{\kappa_b}\right)^{1/3} \frac{l_c^2}{L}, \tag{4.25}$$

and the corresponding increase in energy from Eq. 4.21 is given as:

$$\langle \delta \mathcal{H} \rangle \sim \frac{L_i L^4}{l_c^6} \kappa_i^{1/3} \kappa_b^{2/3} \ . \tag{4.26}$$

As such, we expect that the change in energy should scale as $\kappa_i^{1/3}$ in this regime for Mikado composites. Now, as κ_i increases, we expect to observe the formation of the low-energy, rigid-body region towards the centre of the inclusion, as deflections in the inclusion become energetically unfavourable. As discussed previously, we anticipate that this leads to additional energy contributions where filaments within the rigid body region interact with distant fibres in the base network, resulting in additional fibre deflections. As the number of fibres crossing the stiff inclusion scales as L_i/l_c, and the cross-links along a base fibre as L/l_c, we expect that the energy increase here should scale as:

$$\langle \delta \mathcal{H} \rangle \sim \frac{L_i L}{l_c^2}\int_{l_{\min}}^{\infty} \kappa_b P(l) \frac{L^2}{l^3}\,\mathrm{d}l \ , \tag{4.27}$$

$$\sim \kappa_b \frac{L_i L^5}{l_c^7} \ . \tag{4.28}$$

Seeking a balance of the two energy contributions, from the deflections in the inclusion and from the rigid body rotation, leads to a critical value of the inclusion bending rigidity κ_c given by:

$$\kappa_c \simeq \kappa_b \left(\frac{L}{l_c}\right)^3 . \tag{4.29}$$

We investigate these hypotheses for inclusions of different bending rigidities by simulating Mikado composites in which inclusions possess high stretching rigidity μ_i (above the previously identified critical value) and varying κ_i over many orders of magnitude. In Fig. 4.10 we illustrate the result of scaling the inclusion bending stiffness by the critical value discussed above for three different parameter choices. The change in energy $\delta\mathcal{H}$ is scaled by the plateau value, denoted $\delta\mathcal{H}_{\kappa_s}$, that is the equivalent quantity for very large κ_i, after which further increases do not change the result. Under scaling by κ_c, we observe a good collapse of data across different simulations with various parameters, suggesting that the theory captures the essential physics of the system. In particular, the scaling of the energy change before the plateau region is close to the predicted $\kappa_i^{1/3}$. Inset in Fig. 4.10 is an example analogous transition in Voronoi composites. However, we do not discuss this transition further, as the associated change in energy is small enough to be trivial compared to the increase in energy induced by the axial constraints produced by the inclusion. In fact, the variation of κ_i over 12 orders of magnitude only leads to a less than 1% variation in total network energy increase. This agrees with our prediction that the smaller nonaffine fluctuations in Voronoi architectures prevent large deflections in the inclusions. These results, for varying inclusions stiffnesses μ_i and κ_i detail an important difference between composites in different architectures. In particular, where filament composites possess long base fibres, we expect that the increase in network energy will depend sensitively on both inclusion stretching and bending rigidities, as in the Mikado composites studied here. However, where the length scales of the base fibres are far smaller than those of the inclusion, and the number of cross-links along each base fibre is low, we expect to see large increases in energy even when the inclusion is compliant in both

stretching and bending, as observed in the low critical stretching value μ_i, and insensitivity to bending stiffness κ_i, in Voronoi examples here.

4.4 Discussion

In order gain a better understanding of the mechanics of semiflexible biopolymer assemblies, including cytoskeletal and extracellular matrices, it is necessary to extend the scope of discrete fibre network models to composite materials. DFN modelling efforts have begun to move away from simple choices, in which networks are comprised of filaments with identical lengths and mechanical properties. This approach has been successful in reproducing and explaining experimental results [103], as well as improving the understanding of theoretical models and the relevant physics [194, 234]. However, the architectures utilized in such modelling should aim to reflect the diverse possibilities in real composite assemblies, including the topology and geometry of those matrices. In order to investigate the extent to which composite mechanics depend upon the details of the base network architecture and geometry, we investigated two choices for the base, nonaffine matrix. In particular, we investigated Voronoi networks, in which there is no notion of fibre persistence through a network cross-link, and Mikado networks, in which fibres are assumed to be perfectly straight along their backbone. Naturally, real biopolymer networks will possess geometries somewhere in between these extremes, depending on the thermal and mechanical properties of the fibre matrix under investigation.

The single fibre composites investigated here displayed many differences in their mechanics, owing to the choice of base network architecture. The most considerable variations occurred due to dissimilarities between their displacement and rotation nonaffinity. While mechanical regimes are often discussed in terms of the relative energy content in different deformation modes, namely bending and stretching of constituent fibres, we here found that the more relevant definition for affinity was given in terms of deviations in the displacement field from the affine prediction. That is to say, for equivalent energetic definitions of affinity, measured through the ratio of total network energy to the corresponding affine prediction, Voronoi networks exhibit

far smaller nonaffine displacement fluctuations than their Mikado counterparts, and it was these fluctuations that lead to distinct responses in the presence of a stiff inclusion. For nonfibrous, Voronoi composites, these departures from affinity were small at the scale of the inclusion, such that the inclusion rotated and translated according to a background affine displacement field. In contrast, the additional length scale L in Mikado composites distorted this picture for the inclusions of considered here, with nonaffine fluctuations persisting even at long inclusion lengths.

By considering a bulk affine strain, we were able to explain the localisation of energy at the terminations of the inclusion in terms of a correction to a background strain field that was largely affine in the absence of the inclusion. In particular, when a sufficiently stiff inclusion was placed into a base network, rather than stretching according to the base displacements of the compliant network, nonaffine corrections were introduced which deformed the base network in the axial direction of the inclusion. As such, spatially nonaffine regions in the network corresponded to regions of higher energy. We also observed a low energy region towards the centre of the inclusion body, where coincident base fibres underwent rigid body rotations with the inclusion.

We produced a theoretical prediction for the scaling of the increase in network energy with inclusion orientation θ_i and length L_i by considering corrections to the affine strain field in the inclusion axial direction, so as to prevent inclusion stretching. It was found that, in both cases, the theory agreed well with data from simulations for nonfibrous composites. However, additional energy contributions were observed in Mikado networks, leading to asymmetry in inclusion angle θ_i. In particular, we predicted that the occurrence of the rigid body region lead to additional deformations where fibres coincident to the inclusion antagonized distant base fibres. This interpretation lead to a correction to the scaling of energy increases in Mikado composites, with the introduction of an additional term proportional to $\sin^4\theta_i$ producing good agreement with synthetic data. It was observed that the scaling with L_i became nontrivial in Mikado cases, where competing contributions from the suppression of nonaffine deformation, rigid body rotations and axial

displacement corrections contributed to a lessened dependence on L_i within the range considered here. We predict that for a large enough ratio L_i/L the expected scaling of L_i^2 could be recovered as the nonaffine rotations in the base network become relatively insignificant.

While we initially considered inclusions that were far stiffer in both bending and stretching than base fibres, we observed transitions as both of these parameters were varied from low to high values. By considering balances between the energy content of a deformed inclusion and the displacement induced in the compliant base network by stiff inclusions, the locations of these transitions were identified for μ_i and κ_i in each network geometry. Interestingly, the critical value for μ_i in nonfibrous composites occurs at perhaps surprisingly low values, smaller than the corresponding quantity in the base network for many examples considered. The critical value in Mikado composites was greater due to the persistence of fibres through network cross-links, leading to long-rang correlations. The transition for inclusion bending rigidity κ_i was more complex. For networks deforming approximately affinely at the scale of the inclusion, such as the Voronoi networks considered in this work, the bending rigidity was largely unimportant, leading to only small increases in network energy across many orders of magnitude when compared with the other energy contributions. In contrast, large values of bending rigidity κ_i were required in Mikado composites to out-compete the nonaffine displacements occurring in the base network. This provides an important prediction for real fibre network systems, where even quite compliant inclusions placed within homogeneous matrices could lead to large changes in stiffness, while far longer, stiffer inclusions might be required to induce similar stiffness increases in matrices possessing long, straight polymer lengths. For both Voronoi and Mikado composite types, the collapse of data from computer simulations under our predictions evidenced the validity of our theory, such that the mechanics of low density double-fibre networks can be understood across a broad range of parameters throughout the nonaffine regime.

While the results presented in this chapter discuss a range of situations for both the base polymer system and the inclusion, we note that real world networks

have additional complexities that cannot be addressed within this planar model. In particular, when extended to 3D, additional deformation modes are available to the compliant base network; it is not clear how the addition of local twisting and torsional effects will alter the results presented within this work. However, as fibres in 3D environments might be considerably less affine, owing to a larger isostatic threshold and additional bending degrees of freedom, it could suggest that the behaviours observed here in 2D are present even in stiffer polymers in three dimensions. In contrast, it could also be the case that increased nonaffinity allows the base matrix to accommodate the constraints of the stiff inclusion in local nonaffine rotations, similar to the Mikado composites discussed in this work for small inclusion lengths L_i.

We have not discussed cellularized biopolymer networks in this chapter, which can be viewed as composite materials, and which possess rich mechanical behaviours when active cells are present. In particular polarized, contractile cells that are able to substantially deform the surrounding matrix might produce similar mechanical phenomena to those discussed here. Such cells, which can respond to the stiffness of the substrate, are likely to experience similar substrate displacements to the stiff inclusions modelled here. In mechanically active cells, we expect to observe contractile activity along the cell long axis, whence the theory discussed here for stiff inclusions can be applied. This approach could allow for predictions in cellularized fibre network systems, where other relevant phenomena include cell reorientation and alignment with induced strain direction, and sensitivity to substrate fibre bending stiffness.

4.5 Conclusions

We have investigated the mechanics of composites formed when a single inclusion is placed within fibre networks constructed from two different architectures by subjecting such composites to small shear deformations. To investigate how the mechanics of these systems can deviate from that observed in continua, fibre networks within the bending-dominated regime were used throughout. By investigating a

measure for displacement nonaffinity, we found that even when networks are located within a similarly bend-dominated regime, measures for nonaffine displacement can differ by orders of magnitude. By considering spatial measures of displacement nonaffinity in relation to the energy content in the compliant matrix, we observed that nonaffine displacements correlate with higher base fibre energy content. We interpreted the stiff inclusion as imposing a correction to the affine displacement prediction in the axial direction of the inclusion, and produced theoretical predictions for the scaling of the network energy. In nonfibrous, Voronoi examples, simulation data agreed closely with theory for both inclusion orientation and length. However, additional deformations were induced in Mikado composites, due to the additional length scale of the fibre. By considering further contributions to network energy owing to the existence of a rigid body region adjacent to the inclusion body, we recovered a good agreement between data and theory for inclusion orientation in such composites. We developed further theory to predict the existence and location of transitions for the network deformations as the inclusion stretching and bending stiffnesses increased, which produced a convincing data collapse across multiple parameter choices. In turn, this enables a simple, evidence-based understanding of the mechanics of networks with a single fibre inclusion, valid across a large region of parameter space. We observed that bending stiffness was largely unimportant in nonfibrous Voronoi composites, yet relatively low inclusion stretching stiffnesses could result in large increases in the total network energy. In Mikado composites, the critical values for the moduli were found to be greater than in the nonfibrous examples, as the additional nonaffinity in the matrix lead to more complex deformation behaviours.

The main findings of this chapter are presented in the manuscript "Filament length governs exceptional stiffening in double-fibre networks", in preparation. Humphries D. L., J. A. Grogan, and E. A. Gaffney.

5 Stiffening in heterotypic fibre networks

In many cross-linked biopolymer networks, different filament types interact, granting these networks richer mechanical behaviours than their monotypic counterparts. In Chapter 4 we investigated how single stiff inclusions can lead to mechanical responses that are architecture dependent. This may be taken as representative of low density double-fibre networks, where one fibre type is present in far smaller densities than the other, thus preventing close-ranged mechanical interactions between the inclusions. Here we relax the low density assumption, and investigate composite filament assemblies across a range of base fibre stiffnesses and inclusion densities, and for two choices of base network architecture. 'Exceptional' stiffening and rapid transitions to stretch-dominated networks have previously been reported in synthetic fibre composites. However, the general mechanisms that produce this increase in stiffness remain poorly understood. Our objective is to identify a general explanation for the physical cause of this stiffening effect, and the parameters that characterize it.

5.1 Introduction

Systems formed from complex arrangements of filaments exist throughout biology, where they combine many desirable mechanical properties, including tunable stiffness [9], large failure strains [72, 76], alignment with strain directions [40, 200], and

the facilitation of stress transmission [108, 195]. While many of these diverse and interesting behaviours arise even within random networks formed from a single fibre type, as discussed in Chapters 2 and 3, an even greater range of attributes may be attained when multiple components combine to produce composite systems [230, 240]. The advantages of composite materials have been known for many years, with many synthetics fabricated from interwoven or cross-linked composites, including textiles and papers with targeted strengths and mechanics [241, 242]. Within biological systems, ECM contains stiff collagen fibres, more flexible elastin, alongside other components such as fixed charges and fluid phases [3, 228, 243]. Such a variety of components allows this matrix to adapt to dynamic stresses incurred by locally resident cells or tissues [22, 198], while the specialized architecture of cartilage or bone allows for the support of large stresses over many loading cycles [17, 231]. Within cells, the cytoskeletal mechanics involve dynamic interactions between stiff, bundled stress fibres, and the surrounding compliant actomyosin, allowing for cell polarization and the transmission of cell-derived forces into the microenvironment [60, 226]. Shared by all such systems is a complex assembly of fibres, whose discrete microstructure enables more varied and exotic mechanics [34, 187]. Throughout this thesis, we have discussed how the mechanics derives from an interplay of geometric properties, including fibre orientation, geometric persistence length and cross-link spacing [7, 18, 178], and mechanical properties, such as the fibre bending and stretching stiffnesses [51, 160]. The complexity involved, both from the detailed assembly of the composites as well as the various mechanical properties possessed by their constituents, has resulted in an incomplete understanding of their physics.

Recent experiments have begun to examine in greater detail the specific mechanical differences that arise in composite fibre networks. While strain stiffening in biopolymer systems is well known, and has been identified in for example actin, collagen and fibrin networks [13, 39, 175], a stronger stiffening response, and at lower critical strains, has been recently identified in semiflexible composites [240]. Here, rod-like carbon nanotubules were found to increase the nonlinear stiffness of semiflexible polymer systems drastically, even when present in small quantities.

This work also found that by varying relative densities of filaments, composites formed from two semiflexible fibre families could be tailored such that the nonlinear mechanics followed those of either of the two associated monotypic networks. The linear stiffness in this case was found to be provided by addition of the two single fibre networks in isolation. A different finding has been reported for the stiffness of microtubule-actin composites, where the network experiences a large increase in bulk stiffness beyond that given by the separate fibre types [103]. This 'synergistic stiffening' has been attributed to the suppression of nonaffine bending modes in the vicinity of the stiffer inclusions. Similar double-fibre experiments, where more compliant fibres form an assembly along with stiffer inclusions, found a likewise exceptional stiffening phenomenon, alongside a reduction in strain stiffening [244]. This agreed with the hypothesis that affine deformation modes are encouraged by the inclusions, whence the expected unfolding of nonaffine modes at high strains is less visible [175]. Heterotypic collagen networks have been observed to express stiffness differences upon varying the expression of collagen I and V [104]. Here, stiffer networks arose when collagen I was more heavily expressed in relation to collagen V, and the assemblies had increased strength. Notably, the architecture in these networks remained similar, independent of the collagen expression extents. Alterations to network failure strengths have also been observed in double-fibre hydrogel systems, alongside distinct nonlinear stiffening behaviour [245]. Similarly, investigations into fibre scaffolds from muscle nuclei suggested that composite biopolymer networks can combine both strength and resilience with stiffness, granting protection for the nucleus [229]. That this range of mechanical enhancements in composite fibre systems is broadly reported in the experimental literature suggests that their origins might be generic, shared by broad categories of fibre network systems. Theoretical investigations and computational modelling of composite filament assemblies are important steps towards elucidating the general mechanisms leading to the reported behaviours.

Extensive computational and theoretical investigations into the mechanics of biopolymer networks have been undertaken over the past decades [51, 163, 172].

As discussed and demonstrated in Chapter 3, a major focus in athermal DFN modelling has been the characterization of a bend-to-stretch transition, where the majority deformation modes in the fibre network moves from fibre deflections to extension and compression [170, 172, 173]. This is accompanied by a likewise move towards more affine displacements, where the microscale displacement field more closely follows that of the bulk. Indeed, this should be viewed as a generic quality of athermal fibre networks, where networks containing sufficiently compliant fibres with large mesh spacing will be bending dominated, and those formed from stiff fibres with short segment lengths will be stretching dominated. Research involving less idealized discrete fibre networks has included studies where the elastic moduli [181] and fibre lengths [178] follow a distribution, rather than a single shared value. This research can be viewed as a move towards composite, or heterotypic, networks, where fibres of varying diameters, interfibrillar cross-linking and stiffnesses coexist within the assembly. Given that real networks possess these complicating factors to varying extents, this progress in modelling efforts is an important step towards a better understanding of physical biopolymer network systems. Indeed, the aforementioned affine-nonaffine transition becomes nontrivial in real composite biopolymer systems, where different fibres possess a variety of distinct bending and stretching behaviours. Owing to the inherent complexity in dense composite systems, the majority of similar work has involved *in silico* simulations of composites based around different architectures and constitutive choices. In the research presented in Chapter 4 we investigated and characterized the deformations arising in low density composites with distinct network architectures. Inclusions were found to compete with nonaffine displacements within the compliant base network, giving rise to geometry-dependent bulk stiffening effects. Similar studies, investigating both single and many inclusion systems, identified pronounced increases in the network stiffness as the density of inclusions increased. By interpreting the cause of this as a percolation of 'interphases', that is stretch-dominated regions adjacent to the inclusion, the stiffening could be understood as a transition to stretch-dominated networks in many inclusion systems [219]. A different interpretation of this stiffening

effect was suggested by Bai et al. [166], in conjunction with consistent experimental evidence for stiffening in two-fibre systems [103]. Here, it was argued that the geometric nonaffinity present in the nonaffine, compliant matrix was suppressed by inclusions, whence it was translated instead to other regions of the fibre network. This work also identified a jump in the network stretch energy content in the presence of very few inclusions. While these investigations have primarily involved studies where fibres are taken to follow Mikado network architectures [163, 168], similar behaviours are observed in composites with different network geometries. Van Doorn et al. [194] formed model composites based upon a triangular lattice architecture, where edge dilution provided different densities of stiff elastic bonds, cross-linked to a base of flexible springs. Dependent on these densities, different mechanical regimes were identified. In particular, even below the percolation threshold of the stiffer fibres, many orders of magnitude stiffening could be observed. Disordered 3D composites, formed through Monte Carlo methods, also identified rich and interesting mechanical behaviour, with the onset of rapid strain stiffening occurring at far lower strains when stiff inclusions were present in the matrix [234]. Even within the linear regime, the effect of stiff inclusions was nontrivial, with a rapid increase in the shear modulus apparent as the density of inclusions increased.

As discussed above, various explanations have been provided, both within the experimental and theoretical literature, as to the origins of 'exceptional' stiffening in fibre network composites, that is a stiffness increase in composite networks beyond that predicted from the isolated monotypic fibre constituents. However, it is not clear how properties relating to the network architecture contribute to, or detract from, this phenomenon. Nor is it clear which of the competing explanations best captures the physics of the problem. Here, we investigate whether composite, double-fibre network stiffening is a generic property of fibre networks, or if it is dependent on the specifics of the fibre assembly, including fibre geometric persistence length and network geometry. To address this, we quantify the mechanics of composites formed from stiff inclusions cross-linked into Voronoi and Mikado networks. The stiffening effect is compared and contrasted between these two different network types, and

the energy partition, that is the ratio of bend to stretch energy, is quantified for varying elastic moduli and inclusion densities. The geometric origins of composite stiffening are investigated by considering both random and aligned stiff inclusions. We present a new interpretation for the stiffening effect reported here and elsewhere, and provide evidence for our interpretation over others within the literature by considering the spatial energy profile in the fibre networks, the energy probability density functions, and a percolation threshold that we quantify numerically.

5.2 Model

In this work, we shall consider fibre composites based upon Mikado [163, 168] and Voronoi [186, 187] architectures, similar to the study in Chapter 4. As discussed there, we consider a key differences between these network types to be that of fibre length; in Mikado networks a model fibre can persist through many cross-links, while no notion of filament length beyond the segments between cross-links is apparent in Voronoi architectures. Throughout this chapter we will use Voronoi and 'nonfibrous' interchangeably, likewise with Mikado and 'fibrous', consistent with the low density examples described in Chapter 4. Two-dimensional networks of these types are considered within square computational domains, with area W^2. These networks are termed 'base networks' in this work, while we refer to the rod-like fibres that are introduced into the networks as 'inclusions'.

Mikado networks are formed according to the same procedure presented in Chapter 1, while Voronoi networks are generated as in Chapter 4. To form the composite networks, inclusions of length L_i, are placed within the square domain in the same manner as Mikado fibres. Inclusion density is given by the (non-dimensional) quantity $\rho_i = N_i L_i^2/W^2$, where N_i denotes the number of inclusion fibres, and subscript i denotes quantities relating to inclusions. Inclusions are considered both for random orientation, as in the base Mikado case, and aligned, in which case they are placed at a given angle θ_i, taken as positive from the horizontal $x-$axis. Intersections between base and inclusion fibres are identified and considered as further network cross-links, and geometric periodicity is enforced

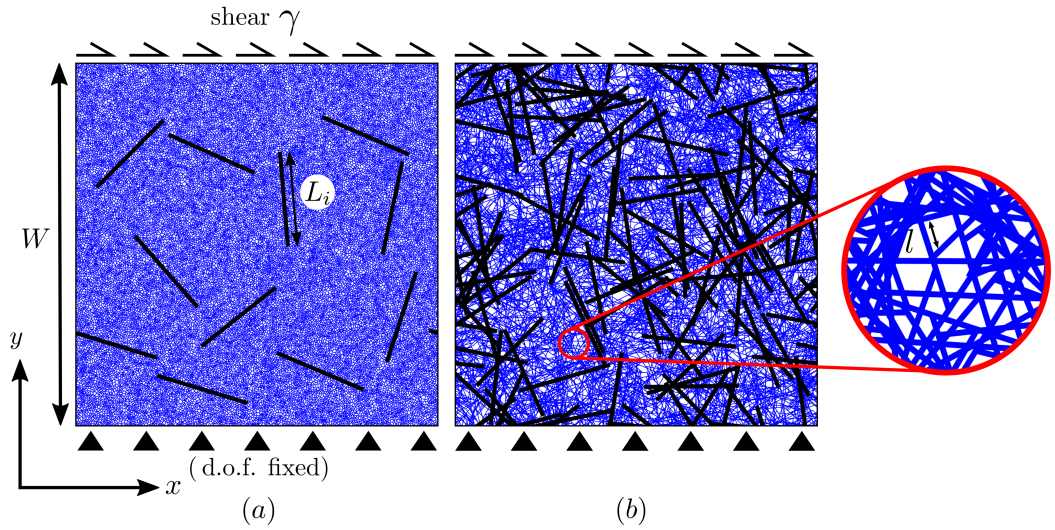

Figure 5.1: Examples of composite networks used in this work. Fibre networks are generated within square domains of area W^2. Nodes on the upper boundary are shifted to produce a bulk small shear strain γ, while nodes on the lower boundary are fixed in all degrees of freedom (d.o.f). Periodic boundary conditions apply on left and right boundaries. **(a)** A Voronoi base network to which a low density ρ_i of rigid inclusions, length L_i, have been added. **(b)** A Mikado composite with high inclusion density. The base network is comprised of Mikado fibres of length L, where $L_i/L = 2$. A closer look at the microstructure is shown, displaying segment length l; throughout $l_c := \langle l \rangle$. Where inclusions and base fibres intersect, a permanent cross-link is formed, but no direct connections between inclusions exists, that is inclusions are not cross-linked with each other.

for inclusions as for Mikado base fibres. In the model presented here, inclusions do not cross-link to other inclusions, such that all motions of inclusion fibres are mediated solely through the base matrix [166]. The behaviour of double-fibre networks where inclusion-inclusion cross-linking is permitted has been discussed elsewhere [219]. Inclusion dangling ends are removed, forming the final composite network of either fibrous (Mikado) or nonfibrous (Voronoi) type. Illustrations of composites formed from both architectures and with different inclusion densities ρ_i are shown in Fig. 4.1. The mechanical behaviour of both inclusion and base fibres is modelled in the same manner as in Chapters 3 - 4, and simulations are performed through the Abaqus platform, as presented in Chapter 3.

The relevant parameters specifying the composite fibre networks in this study are as follows. Inclusions of length L_i are formed from segments of mean length

l_c^i, while Mikado (fibrous) networks are formed from fibres of length L and mean segment length l_c. Inclusions of length $L_i/L = 2$ are used throughout this work except where otherwise stated, similar to other investigations [219], and we discuss the relevance of this choice towards the end of the chapter. Voronoi networks lack a natural definition of fibre length, such that the only similar geometric length is given by the mean cross-link spacing l_c. The density of Mikado networks is taken here as $L/l_c \approx 45$ unless otherwise stated, and we ensure that the mean segment length l_c is the same in both composite types. The domain length W is taken to be large enough that the size effects observed in DFN systems do not affect the results presented here [239]. The mechanical properties of base and inclusion fibres are defined as follows. The deformation of the base networks is governed by the bending length $l_b := (\kappa/\mu)^{1/2}$, in particular through the ratio to mean segment length l_c. Inclusions are taken to be stiff and rod-like, such that for $l_b^i := (\kappa_i/\mu_i)^{1/2}$, $l_b^i/l_c^i \approx 1$, and $\mu_i/\mu = 100$. The importance of these choices for inclusion length L_i and mechanical properties are again discussed later in this chapter. Whenever the network shear modulus $\mathcal{G}$ is discussed, this quantity is calculated from the total network energy as $\mathcal{G} = 2\mathcal{H}_{\text{total}}/\gamma^2 W^2$, for total internal strain energy $\mathcal{H}_{\text{total}}$ defined in Eq. 3.39, bulk shear strain γ, and square domain area W^2. To ensure fluctuation errors remain small, simulations are averaged over between 20 and 100 simulations.

5.3 Results

As discussed in the introduction, we wish to understand how the exceptional stiffening reported within the literature can be generalized for arbitrary network geometries. Towards this end, it is prudent to ask whether the stiffening within the fibre composite arises due to properties at the scale of the inclusion fibres, that is local micromechanical properties such as nonaffine fluctuations, cross-link spacing and fibre stiffness, or global, network-scale properties, such as bulk network affinity and stiffness. In particular, we expect to categorize the mechanics of a general double-fibre network according to either the local or global properties. It is not *a priori* clear which of these two possibilities will define the inclusion

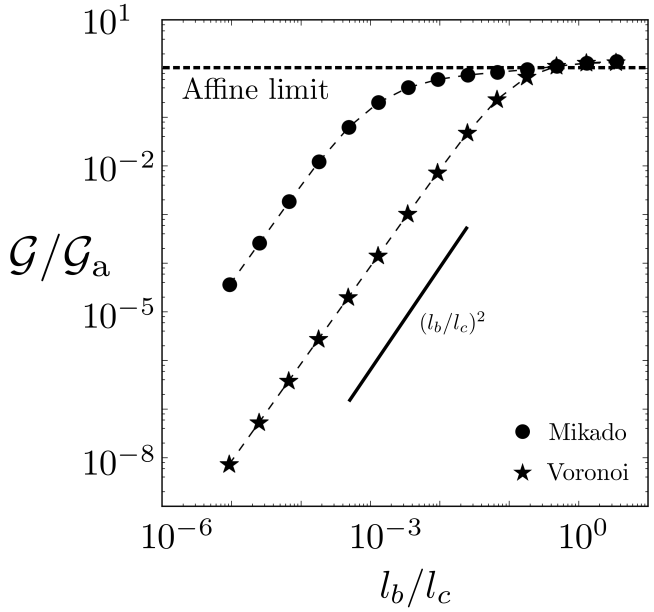

Figure 5.2: The scaling of the bulk shear modulus $\mathcal{G}$ with the ratio of bending length scale l_b and mean segment length l_c in Voronoi (star) and Mikado (circle) composite networks, normalized by the affine prediction $\mathcal{G}_a$ (indicated by dash line). While both network types undergo a bend-stretch transition, coinciding with a move towards more affine displacements, this transition occurs at smaller values of l_b/l_c in Mikado networks, due to the presence of the additional length scale L of the fibres. Within the nonaffine regime, both networks scale linearly with bending stiffness κ. The slight increase in shear modulus within the affine regime is due to fully welded, rather than rotating, cross-links being employed, whence exact affine deformations are precluded.

stiffening response, or whether some other, architecture-dependent property will determine the network behaviour. We note that local and bulk properties are not independent. However, in our previous composite work from Chapter 4, we identified the competition between nonaffine and affine displacements at different scales as the dominant cause of network stiffening in the presence of single stiff inclusions. The size of nonaffine fluctuations was not trivially related to the global, bulk, energetic definition of affinity. Stiffening due to local responses has been suggested by Shahsavari and Picu [219], where local regions of stretching dominated network arise adjacent to the fibre inclusions, the percolation of these regions leading to a stretch-dominated, stiffer bulk network. In contrast, the suppression of nonaffine deformations, and their relocation to regions of the network with low inclusion densities, has been suggested by other researchers [166].

To facilitate the investigation into whether local or global properties govern the stiffening behaviours of fibre composites, we first clarify how the affine-nonaffine transition differs for base networks of different architectures. In particular, we consider the affine prediction for the base network shear modulus, $\mathcal{G}_a$. If all cross-links are considered to be freely rotating, such that fibre rotations incur no energetic cost, and all constituent cross-links follow a precisely affine displacement, then each fibre or fibre segment, at orientation angle θ, experiences a strain equal to $\frac{\gamma}{2}\sin 2\theta$, leading to an increase in energy for this fibre segment of $\frac{\mu}{8}\gamma^2 l \sin^2 2\theta$. Averaging over all such segments, we can write the prediction for the affine shear modulus as:

$$\mathcal{G}_a = \frac{2\Sigma\mathcal{H}}{\gamma^2 W^2} = \frac{\mu N_s \langle l \sin^2\theta\rangle_{(l,\theta)}}{W^2} = \frac{1}{8}\hat{\rho}\mu \tag{5.1}$$

for the total number of fibre segments within the network N_s, the total network line density $\hat{\rho}$, and summation $\sum$ that extends over all polymer segment energies $\mathcal{H}$. While more specific forms of the above can be derived for Mikado networks [170], as discussed in Appendix A, the above expression suffices for the discussion of the two architectures considered here. We note that, given the constitutive choices for model cross-links, neither network type can deform precisely in this affine manner without additional energy contributions arising from bending modes. Nevertheless, the ratio of the observed network shear modulus to this affine 'limit' serves to identify the regime in which a network reside, with values of $\mathcal{G}/\mathcal{G}_a$ close to unity indicating affine networks. The affine-nonaffine transition for base networks considered in this work is shown in Fig. 5.2. The linear scaling of the networks with bending stiffness κ within the nonaffine regime is indicated (or equivalently in the networks considered here, $(l_b/l_c)^2$ for fixed l_c and μ). As is clear from the figure, one consequence of considering networks of different architectures with equivalent mean segment spacing l_c is that nonfibrous (Voronoi) fibre networks approach the affine transition at higher bending rigidities. Parameters are selected such that both network architectures possess affine and nonaffine regimes, in which the behaviours are dominated by either stretching or bending energetics. Within the affine regime, owing to the aforementioned cross-link modelling, there is a small dependence of the

shear modulus on the base fibre bending stiffness κ, such that the observed shear modulus slightly surpasses the analytical prediction indicated by the dashed line.

We expect that the local material stiffness, as experienced by the stiff inclusions, is governed by the base fibre bending rigidity and its ratio to the fibre segment lengths, so that we might expect similar behaviours between composites formed from different architectures under equivalent values of l_b/l_c. We investigate how the stiffness of the composites scales as stiff inclusions are introduced in Fig. 5.3, for many values of the ratio l_b/l_c. For l_b/l_c sufficiently large, all base networks become affine, whence little dependence on either inclusion density or constituent base fibre properties is observed. Here, a less than 10 fold increase in network shear modulus is measured as inclusion density ρ_i varies in the range 0 to 10. Similarly, varying the base fibre bending stiffness by many orders of magnitude within the affine regime leads only to small changes in network shear modulus, and the scaling behaviour is similar irrespective of network architecture or inclusion density. However, for small values of the ratio l_b/l_c in Fig. 5.3, we observe striking differences between the scaling behaviours of the shear moduli in the two different composite architectures. For high inclusion densities $\rho_i \approx 10$ in this regime, the shear modulus of Mikado composites varies only slightly, with a less than 3 times stiffness increase across 2 orders of magnitude in the bending length scale. The scaling behaviour for equivalent high inclusion density and bending length scales l_b in nonfibrous Voronoi composites (Fig. 5.3 **(Right)**) is markedly different, with the bulk shear modulus following a sigmoidal data curve, leading to a 100 times increase in the network shear modulus. Differences are also observed for small inclusion densities, as indicated by darker markers in Fig. 5.3. In Voronoi composites, the linear scaling of $\mathcal{G}$ with κ persists until large numbers of inclusions are present, while even for small densities $\rho_i \approx 1$, Mikado composites have greatly reduced sensitivity to the base fibre bending stiffness. These results suggest that the mechanics of general fibre composites within the nonaffine regime are not fully dictated by the flexibility of the base fibres, and that distinct scaling behaviours can be observed between composites possessing identical bending length scale l_b, cross-link spacing

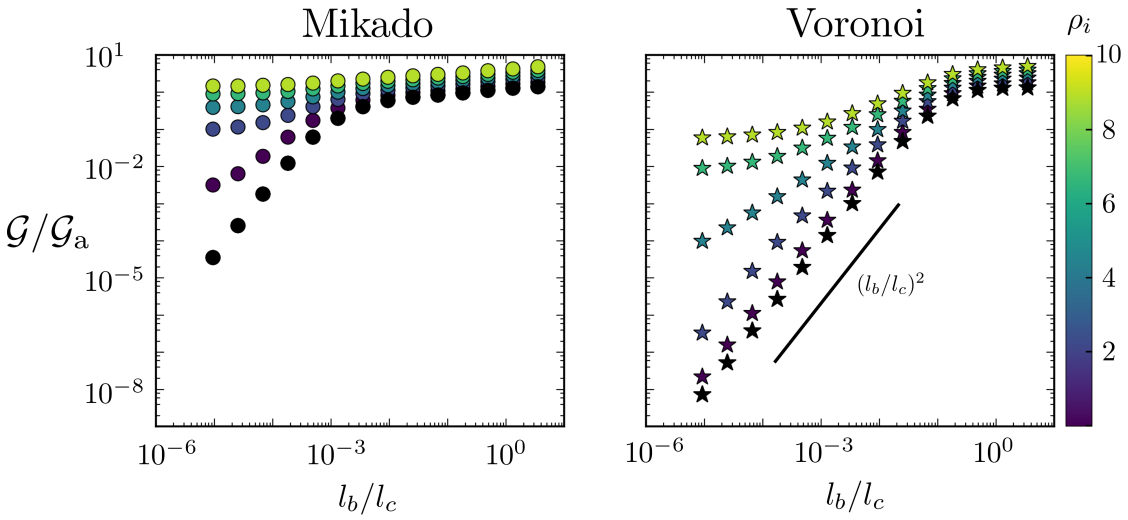

Figure 5.3: The scaling of the shear modulus of composite networks with the bending length scale l_b, normalized by mean segment length l_c, is plotted for composite networks of both types, as the density of stiff inclusions ρ_i is increased, normalized by the affine shear modulus of the base network. As inclusion density increases, Mikado architectures **(Left)** rapidly lose their linear dependence on κ, with even a small density of inclusions leading to a greatly reduced sensitivity to fibre bending rigidity. While networks without inclusions experience an increase in stiffness of approximately 5 orders of magnitude over the bending rigidities considered here, this is reduced to a below 100 fold increase for composites with inclusion density $\rho_i \approx 4$. In contrast, despite a jump in the stiffness of Voronoi composites **(Right)** as inclusions are introduced, a close to linear dependence on κ persists until the number of inclusions becomes far greater. Even for the highest inclusion densities considered, a greater than 100 fold increase in stiffness is observed in nonfibrous, Voronoi cases as the bending length scale l_b increases. These observed architectural differences disappear within the affine regime, with both composite types behaving similarly, as expected. These results suggest that outside of the affine regime, the bending length-scale of the base network is insufficient to determine the scaling behaviour of the shear modulus. Colour bar gives inclusion density ρ_i.

l_c, inclusion density ρ_i and inclusion geometry. In particular, knowledge of the polymer properties and inclusion density will not allow for detailed predictions of the bulk network stiffness for general polymer composites.

Given the different scaling behaviours of composites formed from distinct architectures under varying base fibre bending stiffness, we might expect that the mechanics of composite fibre networks is determined instead by the network nonaffinity, similar to the suggestion of Bai et al. [166]. Indeed, we noted in Fig. 5.2 that the affine-nonaffine transition occurs for different values of the bending length

l_b in each architecture, and that within the affine regime, composites formed from both architectures behaved similarly. It is therefore reasonable to ask whether the scaling behaviour of the composites is similar when considered for equivalently affine networks. To investigate this explanation, we overlay shear stiffness data from both composites in Fig. 5.4, for varying base network affinity as quantified by $\mathcal{G}_0/\mathcal{G}_a$. As expected, the scaling of network stiffness within the affine regime ($\mathcal{G}_0/\mathcal{G}_a \approx 1$) is similar for both architectures and for all inclusion densities. However, rather than observing similar behaviour for equivalent ρ_i and measure of affinity $\mathcal{G}_0/\mathcal{G}_a$, pronounced, architecture-dependent differences are still observed. While introducing small families of stiff inclusion fibres into Voronoi networks does not affect the stiffness scaling with network affinity, as evidenced by the same power law dependence in Voronoi networks with low values of $\rho_i < 4$, Mikado composites exhibit a lesser dependence on base network affinity, with a sublinear scaling for inclusion densities $\rho_i > 1$. When viewed in conjunction with Fig. 5.3, it is clear that neither the mechanical properties of the base polymer, the mean segment length nor network properties such as affinity, are sufficient to determine the shear modulus of the composite network. This is in contrast to what would be expected should the mechanics of general fibre composites be controlled by elliptic inclusion interphases (which depend on inclusion length), or the redistribution of similar nonaffine fluctuations to regions of low inclusion density.

To better understand the origins of the composite stiffness increase, we investigate the energy partition in composites formed from different architectures. Within the fibre network literature, considerable discussion has centred around the simultaneous transition from affine to nonaffine and stretching- to bending-dominated networks. To investigate how network deformation modes relate to the network affinity, we investigate the energy partition by quantifying the ratio of total bend to stretch energy contained within the composites discussed here. Fig. 5.5 displays the ratio of the two energy storage modes as the base network bending stiffness increases, for varying inclusion densities in both composite types. The data curves observed in both network types are nontrivial, and do not relate in an obvious manner to

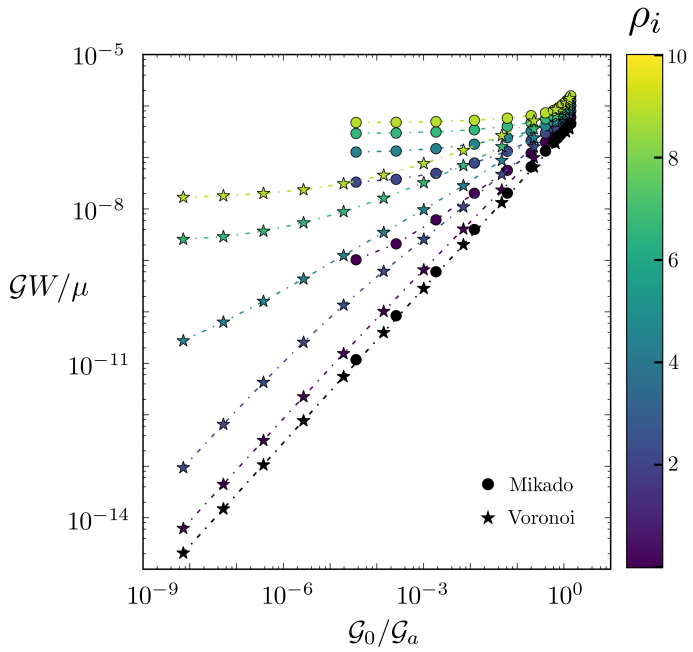

Figure 5.4: The scaling of the composite shear modulus $\mathcal{G}$ with base network affinity $\mathcal{G}_0/\mathcal{G}_a$ is plotted. Clear differences in the scaling behaviour of the shear modulus are observed for curves of equivalent inclusion density, and for equivalent affinity in the base networks. In combination with Fig. 5.3 this suggests that neither the mechanical properties of the constituent biopolymers, nor the bulk network affinity are sufficient to explain the mechanical differences observed between composites formed from different network architectures.

those from the base network (black markers). At low inclusion densities, $\rho_i \approx 3$, Mikado composites become stretching dominated for all values of the fibre bending ratio l_b/l_c. In contrast, even for the largest number of inclusions considered here, nonaffine Voronoi composites (low l_b/l_c) remained marginally bend-dominated. The undulations in Mikado data curves are consistent with the introduction of a large stretching energy contribution as inclusions are introduced that is independent from the base fibre bending stiffness. If the deformation leading to this increase in stretching energy is not affected by variations in fibre bending stiffness, we expect a decrease in the bend-stretch ratio as l_b increases, as the bending content within the network increases linearly with rigidity κ in this regime. As the base network becomes stretch-dominated, the ratio increases once again, as all fibres begin to stretch instead of bending, as in the monotypic case. To evidence the existence of sudden stretching deformations when inclusions are introduced to

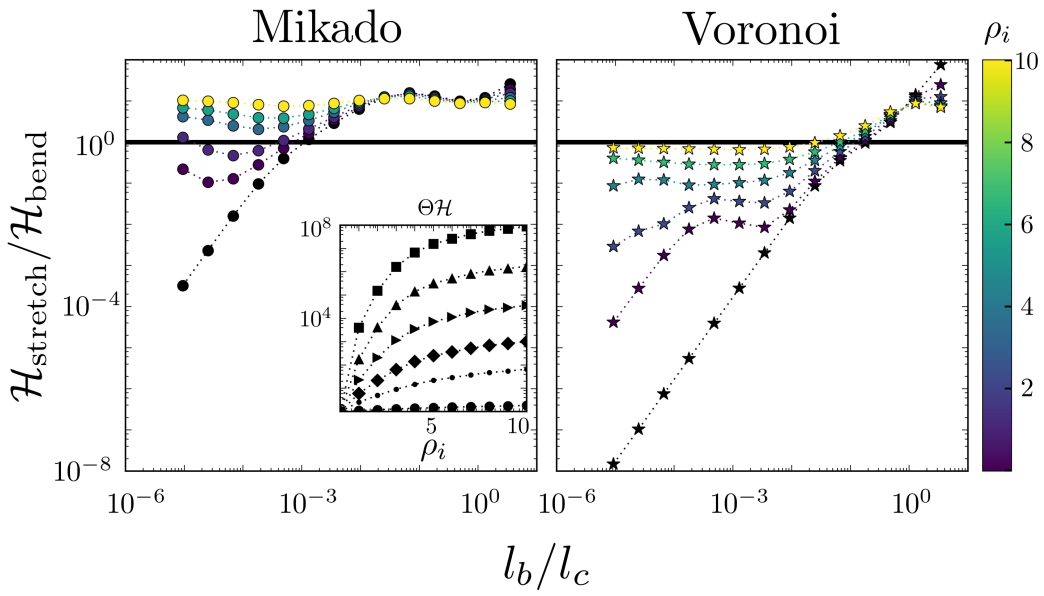

Figure 5.5: A visualisation of the ratio between total stretch and bending energy content in composite networks comprised of different inclusion densities, and for increasing l_b/l_c. Even at low inclusion densities, Mikado networks with nonaffinely deforming bases become stretch dominated. In contrast, Voronoi composites do not become stretch dominated, even at the highest inclusion densities considered, but remain marginally bend dominated until the base network enters the affine regime. Colour bar displayed inclusion density ρ_i. **(Inset)** The ratio of stretch energy in the composite base network to that in the zero density case, $\Theta\mathcal{H} := \mathcal{H}_{\text{stretch}}/\mathcal{H}^0_{\text{stretch}}$, showing many order of magnitude increases in the stretching contributions for nonaffine Mikado base networks. Parameters for square, triangle, side-triangle, diamond, dot and circular markers in the inset plot are for $l_b/l_c \approx 9.4 \times 10^{-6},\ 2.5 \times 10^{-5},\ 6.8 \times 10^{-5},\ 1.8 \times 10^{-4},\ 4.9 \times 10^{-4}$, and 9.4 respectively.

Mikado composites, we plot the ratio of stretching energy in the base network to that in the fibre composite in Fig. 5.5 **(Inset)**. That is, we plot $\Theta\mathcal{H} := \mathcal{H}_{\text{stretch}}/\mathcal{H}^0_{\text{stretch}}$, where 0 denotes the quantity in the zero inclusion case, and quantities refer only to fibres within the base network. As one moves up the graph vertically, the curves display this ratio for composites of decreasing base bending stiffness κ. For the most nonaffine Mikado composites, the stretch energy ratio increases by 8 orders of magnitude as inclusion density increases to the maximum value $\rho_i = 10$. This suggests an architecture-dependent source of stretching energy contributions that is independent of the constituent fibre properties, and of the network nonaffinity within the bending dominated regime.

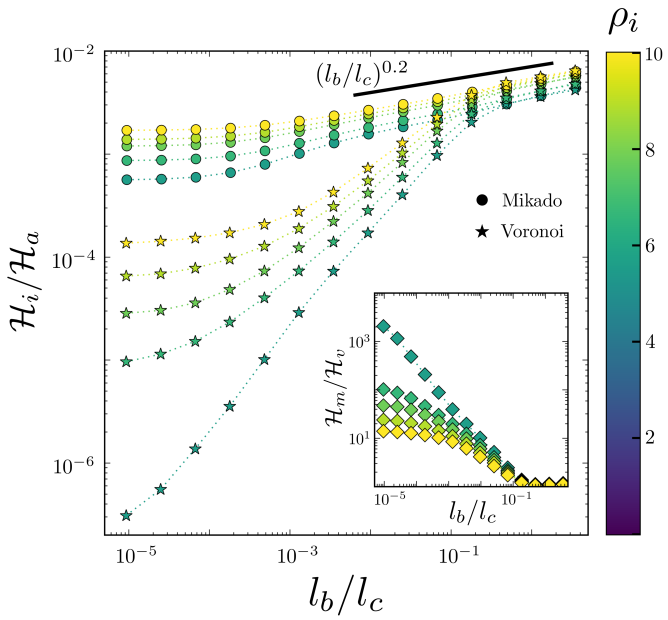

Figure 5.6: The total energy content of the stiff inclusions $\mathcal{H}_i$, normalised by the affine energy prediction for the whole network $\mathcal{H}_a$, is shown for increasing l_b/l_c, showing many order of magnitude differences between the two architectures. Inclusions within Mikado composites appear to contain significant energy, suggesting that the base Mikado network is able to deform the rod-like inclusions. In contrast, far less energy is stored in the stiff inclusions in nonfibrous cases, even at the highest inclusion densities ρ_i. **(Inset)** The ratio of inclusion energy in Mikado ($\mathcal{H}_m$) and Voronoi ($\mathcal{H}_v$) composites for equivalent ρ_i and l_b/l_c is shown, clarifying the marked differences between the energetics of the inclusions in the different architectures, despite identical inclusion geometry and constitutive choices being used.

Given the observed increase in stretching energy within the base network fibres when stiff inclusions are introduced into nonaffine base matrices, it is important to determine whether inclusions experience significant deformations as a consequence. In particular, the inclusions were modelled such that we expected the bending of base fibres to be favoured over inclusion deflections within the nonaffine regime, given the small base fibre bending length scale $l_b = \kappa/\mu$ for $\mu \gg \kappa$. If instead base fibres are stretched, the inclusions would experience far stiffer local networks, and the competition between base fibre stretching stiffness and inclusion bending rigidity could result in significant inclusion deflections. In Fig. 5.6 we compare the total energy content within the inclusion fibres as the base fibre bending stiffness increases. Within the nonaffine regime, far more energy is contained in inclusions within Mikado

composites than for the nonfibrous architectures investigated, for equivalent ρ_i. Interestingly, there was only a ten-fold increase in inclusion energy content as the bending length scale varied over 6 orders of magnitude, again suggesting that such composites are insensitive to the base fibre bending stiffness. In contrast, for Voronoi composites with inclusion density $\rho_i \approx 6$ the energy content increased by 4 orders of magnitude over the same range of base bending rigidity. Plotted in Fig. 5.6 **(Inset)** is the ratio of energy stored in stiff inclusions for the two different architectures, that is $\mathcal{H}_m/\mathcal{H}_v$, where here $m,\ v$ denote Mikado or Voronoi, and the energy refers only to the content in inclusion fibres. The magnitude of this ratio, showing a more than 3 order of magnitude increase in inclusion energy content, is particularly striking when considering that the inclusions possess identical mechanical properties, are placed within the domain with identical geometry, and within networks where the mean cross-link spacing l_c, bending and stretching stiffnesses are all equivalent.

The results presented so far suggest that there exists a source of stretching deformations that is dependent on architecture and inclusion density, yet independent of base fibre bending rigidity and bulk network affinity. To investigate the origins of these stretching deformations, and how they relate to the stiff inclusions, we visualise the spatial energy partition for a specific set of inclusions $\rho_i = 6$, in Fig. 5.7. Results are averaged over 30 realisations of nonaffine base networks, and both bend and stretch contributions within the base fibres are displayed for each network architecture, normalized relative to the total network energy. Voronoi composites remain dominated by bending deformations in the base fibres. In particular, energy storage is localized to the terminations of the inclusion fibres, similar to observations from single inclusion systems, as in Chapter 4. The networks stretching contributions remain small in comparison, and depend on the detailed geometry of the inclusions. In particular, where the crossings of several inclusions forms a polygonal region, a constant stretching energy appears to be shared by the fibres contained within. The mechanics in fibrous Mikado architectures is clearly different. Despite base networks that are deep within the nonaffine regime, and thus dominated by bending deformations in the absence of additional stiff fibres, the constraints imposed by the

inclusions leads to regions of far greater stretching contributions. We hypothesize that inclusions separated by distances below the base fibre length L become 'cross-linked' by base fibres coincident to multiple stiff inclusions. When these inclusions and coincident fibres percolate the whole domain, as is the case for the density of inclusions considered here, such base fibres appear to preferentially stretch, instead of bending, as evidenced by the large stretch energy content in Mikado composites. Where regions in the matrix exist in which the distance between inclusions is greater than L, and there is a local absence of inclusions, no increase in stretch energy is observed. The spatial profile for bending energy in Mikado composites appears similar to the Voronoi case, where bending deformations are most prominent in the vicinity of inclusion end-points, though these energy contributions are far smaller that those from filament stretching. According to the above hypothesis, the lack of fibres with long geometric persistence in Voronoi base networks would preclude these deformations occurring in nonfibrous composites, as the probability of a (short) fibre segment being coincident to several inclusions is low.

Given the hypothesized dependence of the composite shear modulus on the stretching of base fibres coincident to more than one inclusion, we expect the mechanics of double-fibre composites to be governed by a percolation phenomenon. In particular, we are interested in the percolation threshold for a network formed from two families of fibres, neither of which associate with their own type, but which can cross-link with the other. In nonfibrous architectures, the relevant length of the base fibre is the mean segment length l_c, as long, straight fibres do not persist through model cross-links. However, in fibrous networks, the length is L, where $L/l_c \gg 1$, and percolation is expected to occur more rapidly with increasing inclusion density. We note that previous work has postulated that the 'exceptional stiffening' observed in fibre networks occurs due to the percolation of stretching interphases, that is regions of higher stretching energy forming an elliptical domain around the inclusions [219]. However, investigations into this phenomenon in Chapter 4 did not find evidence for such an increase in stretching energy, but rather a pronounced decrease in the bending energy, as evidenced by Fig. 4.5. Furthermore, Shahsavari

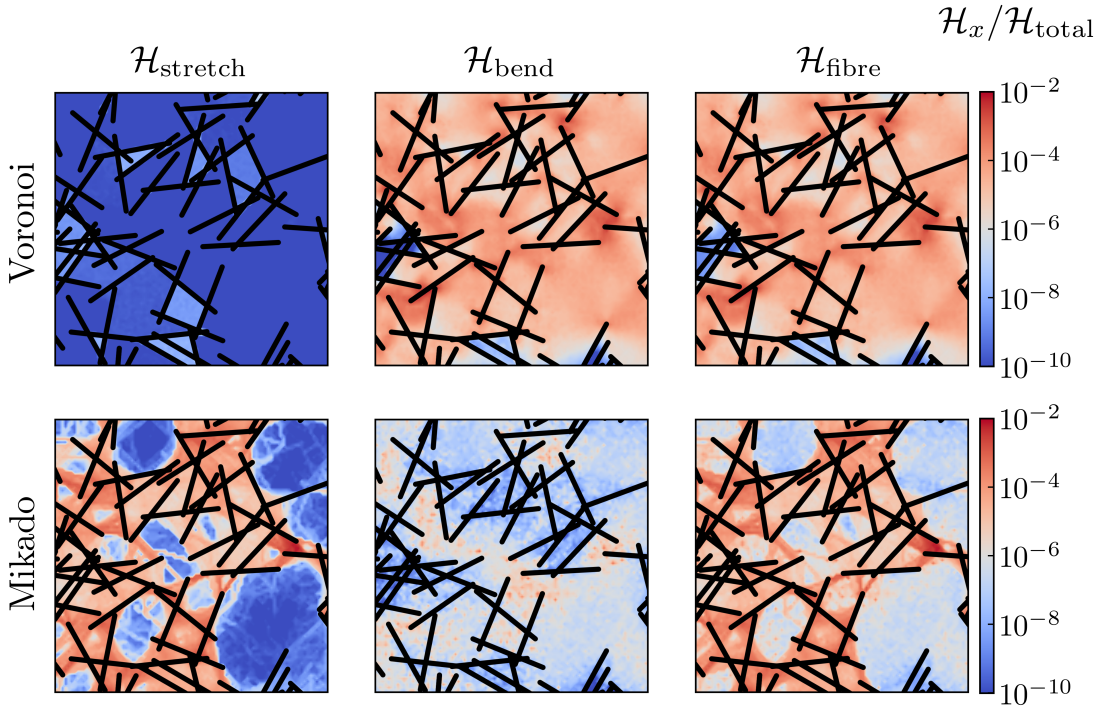

Figure 5.7: Visualisations of the spatial energy partitions in Voronoi and Mikado composite networks. Here $\mathcal{H}_{\text{bend}}$ and $\mathcal{H}_{\text{stretch}}$ are defined through Eq. 3.38, while $\mathcal{H}_{\text{fibre}}$ refers to the sum of all energetic contributions in a fibre, and $\mathcal{H}_{\text{total}}$ is defined through Eq. 3.39. The base networks in the absence of inclusions are nonaffine and bending-dominated. In Voronoi networks, bending remains the predominant mode of energy storage, with energy concentrated towards the ends of inclusions. In contrast, large regions of Mikado composites become stretch-dominated in the presence of the stiff inclusions. Regions displaying low inclusion density experience no such rise in stretch energy, while regions with adjacent inclusions experience the largest increases. We hypothesize that the geometric fibre persistence, that is the additional length scale L present in Mikado networks, allows for individual base fibres to 'cross-link' the stiff inclusions, explaining the rapid transition at low inclusion densities from bend- to stretch-dominated Mikado composites.

and Picu [219] argued that the interphase size depends on the stiff inclusion length, rather than the base fibre length or geometry, such that we should not expect to observe pronounced differences between composites with different architectures when inclusions of identical geometries and lengths are used, as in this work.

To investigate our hypothesis that the base polymers act as cross-links for the inclusions, we investigate the dependence of the shear modulus $\mathcal{G}$ on the stretching rigidity μ in Mikado composites. Indeed, within this 'percolated' regime, we expect that $\mathcal{G}$ is largely independent of base fibre bending stiffness κ, and that network

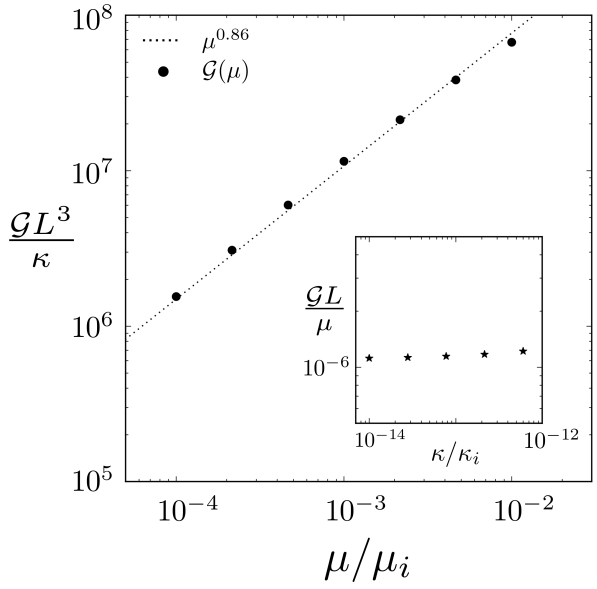

Figure 5.8: The dependence of the composite shear modulus $\mathcal{G}$ on the base stretching stiffness μ in Mikado composites of density $\rho_i \approx 6$ is investigated, for base networks within the nonaffine regime. The bulk stiffness is observed to scale as $\mu^{0.86}$. This is in contrast to the monotypic base cases, where no such dependence is expected. **(Inset)** The analogous scaling with bending rigidity κ is also investigated, displaying a striking insensitivity to this parameter.

stiffness increases with stretching rigidity μ. In Fig. 5.8 we plot the shear modulus $\mathcal{G}$ of composite Mikado networks in the nonaffine regime as a function of μ, while κ is held constant, for inclusion density $\rho_i \approx 6$, as in Fig. 5.7. We find that the modulus scales with μ with an exponent slightly less than unity, as $\mathcal{G}(\mu) \sim \mu_i^{0.86}$. Furthermore, we confirm that the dependence of the network shear modulus on κ is small, in Fig. 5.8 **(Inset)**. Here μ is held fixed, while the bending rigidity is varied for parameters that place the base network within the nonaffine regime.

Provided that the exceptional stiffening in fibre composites originates from a base-inclusion percolation, we should be able to predict the density of inclusions at which the stiffening is most pronounced, and how it depends on base fibre length. To produce such predictions, we generate double-fibre Mikado-type networks, where cross-links can only form at the crossings of different filament types; inclusions only cross-link to base fibres and vice versa. To relate to our earlier results, we fix inclusion length L_i and base fibre line density $\hat{\rho} = NL/W^2$, and vary base fibre

lengths L and inclusion density ρ_i. After fibres are placed within the domain and cross-links between fibres are identified, we classify composites as percolating if a continuous path of fibres exists between the lower and upper domain boundaries. If such a path exists, the total polymer length in all connected, percolated network components can be measured and we can investigate the rate at which the resulting network grows. In Fig. 5.9 we illustrate the results of averaging over 500 networks for four base polymer lengths L and many inclusion densities ρ_i. For larger ratios of inclusion to base fibre length L/L_i, the percolation transition is rapid, with the probability of percolation increasing from 0 to 1 across a small variation in inclusion density. Blue lines correspond to the Mikado parameters used for the results presented to this point. As the ratio of base to inclusion length decreases, the transition region, from nonpercolated to percolated becomes increasingly broad, such that knowing the inclusion density may be insufficient to determine whether a network will exhibit exceptional stiffening. We further quantify the total network size in Fig. 5.9 **(Right)**, where the percolating cluster initially increases in size rapidly, as fibres are recruited to the connected component, before a linear growth regime is reached. The gradient of this linear regime is again dependent on the ratio of the fibre lengths, with a more rapidly growing regime observed for long base fibres, in contrast with a slowly growing connected component in short base fibre composites. For sufficiently large inclusion densities, we expect that even Voronoi composites experience a similar stiffening effect, when the inclusion fibres would themselves independently percolate in the standard Mikado geometry. Here, even the short base fibre segments are likely to be coincident to multiple inclusions. However, as the size of the percolating cluster is expected to grow far less quickly, we predict that these networks will remain bending dominated until far higher inclusion densities are reached.

We test our predictions for the onset of exceptional network stiffening as inclusions are added in Fig. 5.10. The ratio of composite to initial stiffness $\mathcal{G}/\mathcal{G}_0$ is plotted against the inclusion density ρ_i for a range of base fibre bending stiffnesses l_b. In both composite architectures, we observe profound stiffening as the density of

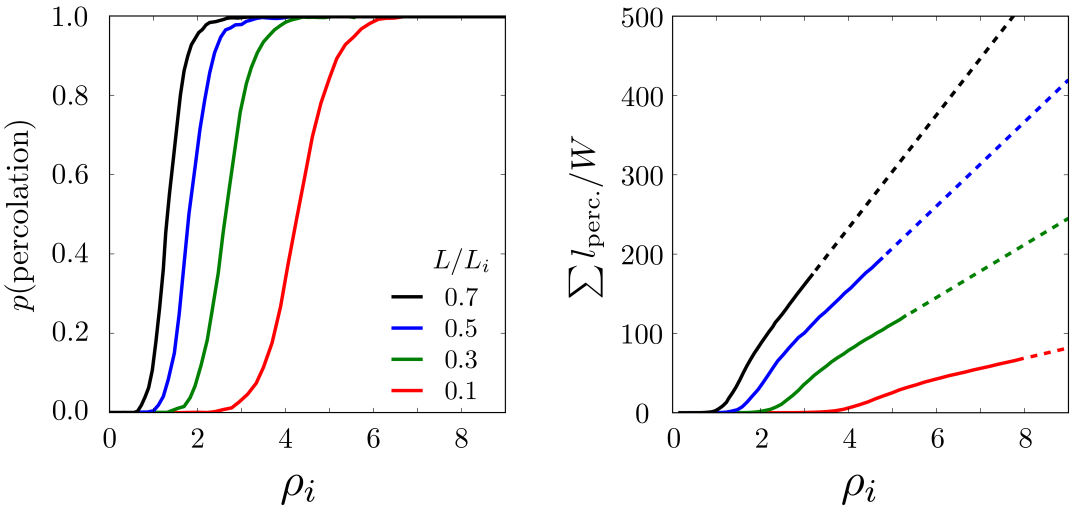

Figure 5.9: An investigation of the percolation threshold for double-fibre Mikado networks, where each fibre can only cross to those of the opposite type. **(Left)** The probability of observing a network which percolates across the domain from lower to upper boundaries is shown, calculated by averaging over 500 simulations for each inclusion density, and each base fibre length L. Base polymer density $\hat{\rho}$ is held constant. As base fibre length decreases, percolation occurs at higher inclusion densities. This is accompanied by a broadening in the transition region. **(Right)** The total length of the percolating cluster $\sum l_{\text{perc.}}$ is investigated for the same parameters as used for the left-hand plot, nondimensionalized by constant domain size W. In all cases we observed that the growth of the cluster becomes linear following an initially rapid increase. The cluster grows more slowly for shorter base fibres. Dotted lines display the extrapolated linear growth for inclusion densities beyond those simulated, assuming a constant linear growth.

inclusions increases to $\rho_i = 10$, with 5 and 7 order of magnitude stiffness increases in Mikado and Voronoi cases respectively. In Mikado networks, the greatest stiffening effect occurs between $\rho_i = 1 - 3$, which agrees well with the numerical results for the percolation threshold (Fig. 5.9, blue lines). Following the rapid stiffening in composites with larger inclusion densities, a steady increase in network shear modulus is observed, which can be understood through the linear growth of the connected components after the percolation threshold has been reached. As such, a small family of stiff fibres added to Mikado networks act to stiffen the networks 1000 fold. As expected from previous results, this effect is most pronounced in nonaffine networks, which are bending dominated in the absence of inclusions. In Voronoi composites, the onset of exceptional stiffening occurs at much higher inclusion densities, at values similar to the percolation threshold for the inclusion

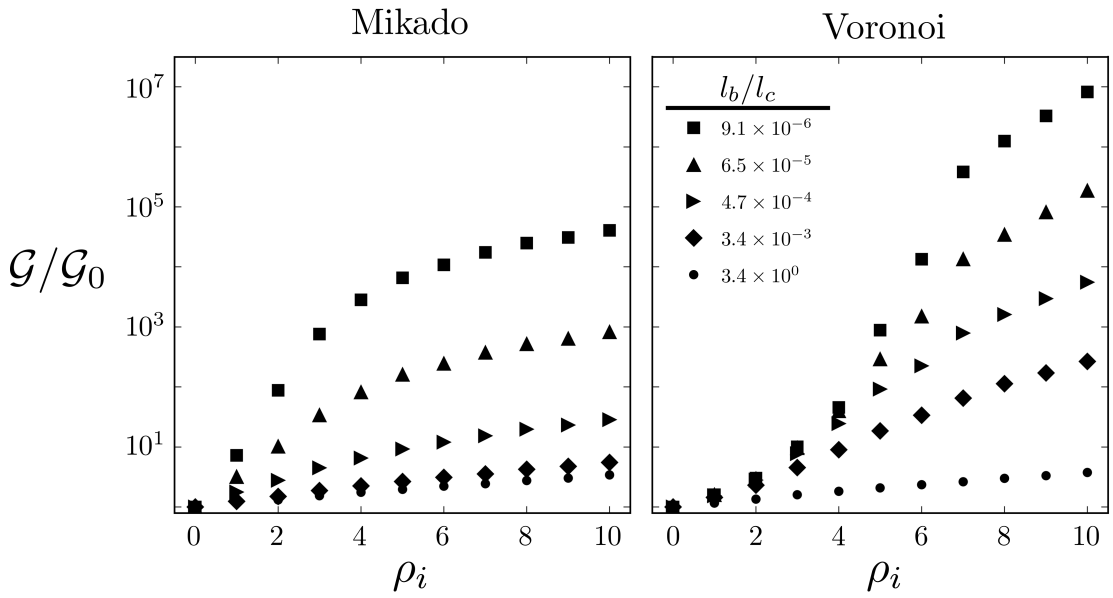

Figure 5.10: The ratio of composite to base network stiffness $\mathcal{G}/\mathcal{G}_0$ is shown with increasing inclusion density ρ_i. Results are shown for varying values of l_b/l_c, highlighting that exceptional stiffening is most pronounced in nonaffine cases. In both networks, the increase in network stiffness with inclusion density is large. The most rapid increase in stiffness occurs at different inclusion densities in each of the base architectures considered. In Mikado composites, this stiffening occurs at very low inclusion densities, while there is a pronounced increase in the shear modulus of Voronoi composites near to the percolation threshold of the inclusions. Taken alongside Fig. 5.9, the exceptional stiffening effect coincides with double-fibre network percolation. Within the affine regime (small circles), the stiffening effect is modest in both composite types, as expected for networks that are already stretch-dominated.

family of fibres in isolation. Again, the large increases in network stiffness are most pronounced for those composites formed from nonaffine base networks. Interestingly, the stiffening effect following the percolation threshold is larger in Voronoi cases than in Mikado networks, which we attribute to the lower energy for equivalent parameters in the relevant base networks (see Fig. 5.2).

The emergence of a cross-linked inclusion network as discussed above should induce significant changes in the energy probability density functions (pdfs) for the base network fibres. In particular, we should see clear evidence for a small family of high energy content fibres above the percolation threshold, where stretching leads to significantly more energy per fibre length. We plot the strain energy density pdf in Fig. 5.11 for composites based upon both architectures. Fibre segment strain energy

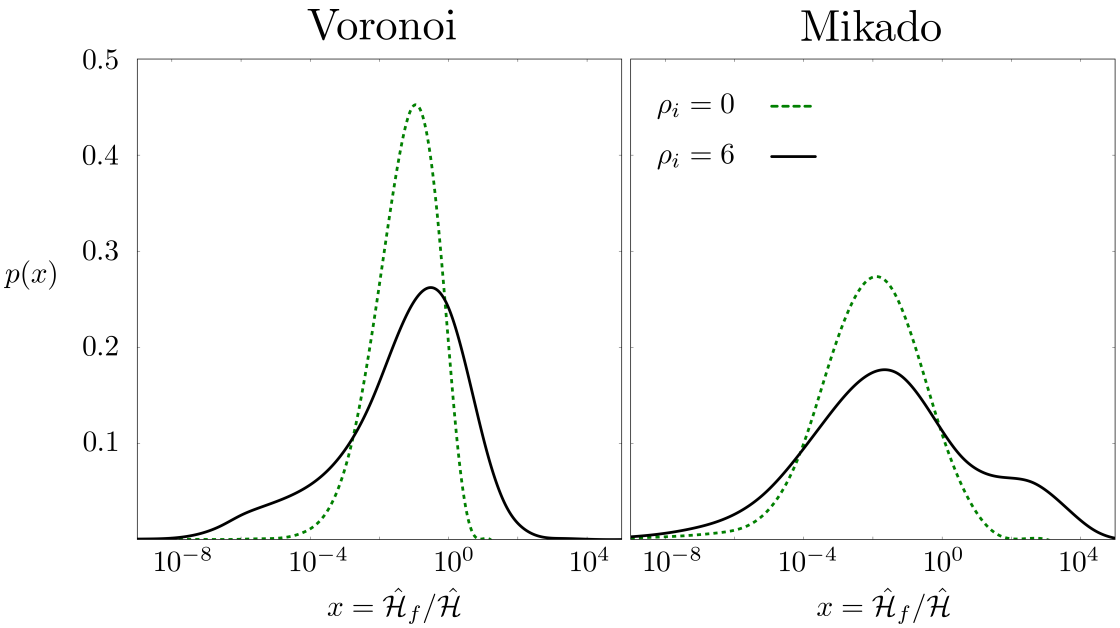

Figure 5.11: Probability density functions for the occurrence of fibre segments containing given energy densities in Voronoi and Mikado composites. Results are displayed both for the zero-inclusion base case $\rho_i = 0$, and higher density $\rho_i = 6$ as used for the spatial energy partition in Fig. 5.7. We observe a slight shift towards higher energy densities in Voronoi networks as inclusion density increases, along with a broadening of the energy density profile. A similar broadening in the energy density profile is noted in Mikado composites. However, an additional peak in higher energy densities arises, which we attribute to the sub-family of base fibres which stretch when 'cross-linked' to the inclusions.

density is denoted $\hat{\mathcal{H}}_f$, and is normalized by the strain energy density of the bulk network, that is $\hat{\mathcal{H}}$. Results are shown only for base fibres, both with ($\rho_i = 6$, black), and without ($\rho_i = 0$, green dash) inclusions. In nonfibrous, Voronoi composites, the inclusions act to generically increase the fibre bending energy content in the base network. This is accompanied by a broadening of the peak, such that, noting the log-scale axis, a smaller number of fibres contains the majority of network energy. Interestingly, there are also many more fibres containing drastically less energy. These fibres are likely to be those that follow rigid body rotations with the inclusions, as discussed for low density fibre composites in Chapter 4. In fibrous composites, a similar broadening in the peak is observed, albeit to a lesser extent, and the peak again moves slightly towards more energetic fibres. However, a pronounced difference is evident in the emergence of a second peak; here, a small family of fibre segments contains the large majority of fibre strain energy. Indeed, the peaks are separated

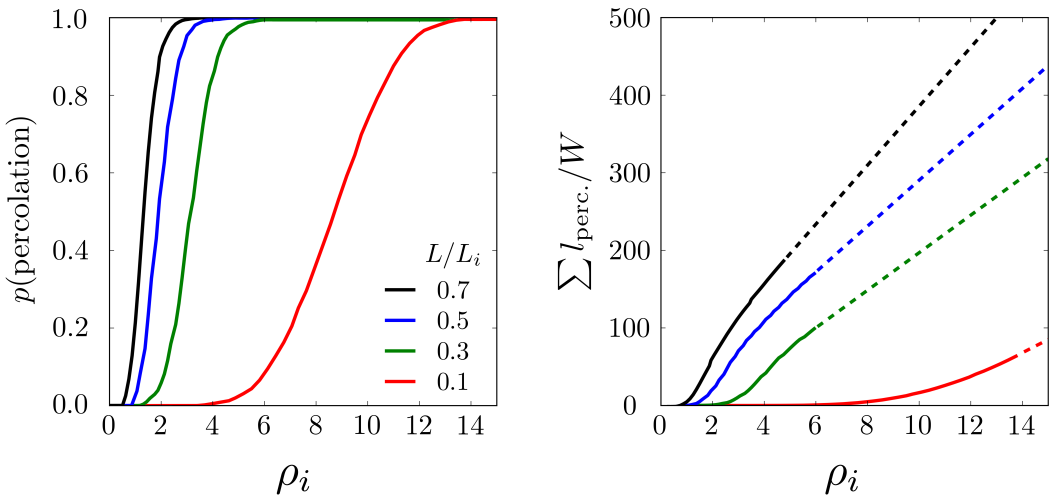

Figure 5.12: The percolation phenomenon is investigated for networks in which inclusions are placed at a constant orientation $\theta_i = \pi/4$. **(Left)** Longer fibres still exhibit relatively sharp transition regimes, moving from percolated to non-percolated over a small increase in inclusion density. However, for short fibres, the transition region becomes large, and knowledge of the fibre network parameters are insufficient to infer whether the network is percolating or not. **(Right)** The total polymer length in the connected spanning component is measured. In all cases the clusters grow more slowly than in the random cases, again approaching a linear regime for inclusion densities above the percolation threshold.

by 4 orders of magnitude in the fibre strain energy density. This large difference in the energy content of fibres could be potentially relevant to the failure behaviour of composite biopolymer networks, where damage incurred by a small subset of fibres (those that mechanically couple the inclusions), or the failure of the corresponding cross-links, would reduce the network stiffness by many orders of magnitude.

We have identified and provided evidence for the key architecture-dependent property that leads to exceptional stiffening in double-fibre composite systems similar to the ones studied here, that is the base fibre lengths. For randomly distributed inclusions, we predict that the profound stiffening response will always occur above a certain density of the inclusions, where the stiff fibres percolate independently and even the shortest base fibres can be coincident to 2 or more inclusions. However, in many biological networks, constituent fibres can become aligned [13, 40], while in cellularized networks, resident cells can align with the direction of strain, so as to maximise the stiffness they experience [150, 151]. In

the presence of these geometric differences, the percolation results presented in Fig. 5.9 no longer apply, and we expect that higher densities of aligned inclusions are required before the stiffening effect is expressed by the composite. We repeat the investigation into the percolation thresholds with networks containing aligned inclusions by altering the random orientation of the inclusion family of fibres to be uniformly equal, with $\theta_i = \pi/4$. Numerical results quantifying the percolation of double-fibre networks for aligned inclusions are displayed in Fig. 5.12. In all cases, the transition region is broader than in the random cases considered previously, noting that the $x-$axis is rescaled to encompass far larger inclusion densities ρ_i. However, the most significant differences are observed for shorter base fibres (red), where the transition region begins at $\rho_i \approx 4$, and terminates around $\rho_i \approx 14$. Similarly, the increase in cluster size with inclusion density is far slower, as seen in Fig. 5.12 **(Right)**. A similar connected component length is predicted for random networks at inclusion density $\rho_i = 8$ as for $\rho_i = 13$ in anisotropic cases, when $L/L_i = 0.7$ in both cases. Interestingly this suggests that, in contrast to classical or monotypic anisotropic materials where alignment with the strain direction can lead to a stiffer material response [177], a reduction in stiffness could be observed for aligned inclusions in nonaffine fibre networks.

Results for the ratio of the shear modulus of the composite network when inclusions are oriented at an angle $\theta_i = \pi/4$ to initial shear modulus $\mathcal{G}_0$ are presented in Fig. 5.13, for Voronoi composites and Mikado networks with equivalent base polymer density $\hat{\rho}$ but different base fibre lengths L. To account for the broader percolation transition, which we expect to result in bimodal simulation data, networks are first classified as percolating or nonpercolating. Simulations are then averaged over networks within the same classification. White markers relate to mean results for percolated networks, while solid black denotes nonpercolated composites. The background gradient illustrates the previously quantified percolation probability, taken from Fig. 5.12. The exceptional stiffening previously observed in Voronoi composites is entirely absent here. In fact, the stiffness ratio at inclusion density $\rho_i \approx 6$ is given approximately as $\mathcal{G}/\mathcal{G}_0 \approx 30$, compared with a 10^4 factor stiffness

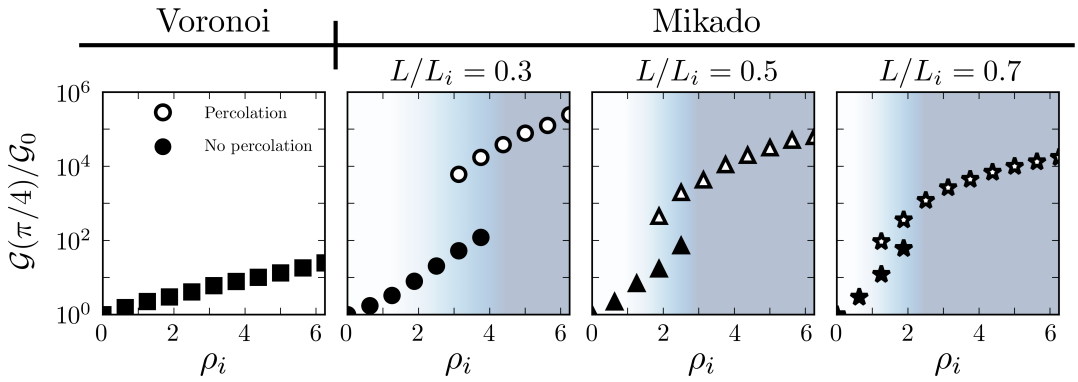

Figure 5.13: The stiffening effect with inclusion density is quantified for aligned inclusions $\theta_i = \pi/4$ in Voronoi and Mikado networks. Networks are categorized according to whether a percolating cluster of base-inclusion fibres spans the domain, with solid black markers representing nonpercolating networks, and white indicating percolating cases. In Voronoi networks, the exceptional stiffening observed for random inclusions is now absent, leading to a ≈ 30 fold increase in the shear modulus, in comparison to the far greater factor 10^4 increase previously observed in random Voronoi composites. In fibrous, Mikado composite examples, a jump in network stiffness is observed at the percolation threshold, leading to far greater stiffness increases for equivalent inclusion densities. Background gradient displays the probability of percolation, from Fig. 5.12.

increase in the case of random inclusions at a similar density. In Mikado composites, the jump in network stiffness occurs precisely at the percolation threshold, as evidenced by the background colour gradient; this confirms the base cross-linked hypothesis. This corresponded to a more-than-5 orders of magnitude stiffness increase for the shortest base fibres considered ($L/L_i = 0.3$), as inclusion density varies from $\rho_i = 0 - 6$. The smaller, yet still large, stiffness increase in networks with larger fibres can be understood by considering the reduction in affinity that one expects when L/l_c increases, according to energetic affinity measure $L/\lambda_1 = (L/l_c)(l_b/l_c)^{1/3}$ [163]. In particular, by maintaining a constant polymer density and varying L, we generate stiffer networks as L increases. As such, the stiffening effect appears less dramatic, due to the larger bending energy content in these networks.

5.4 Discussion

Cytoskeletal and extracellular matrices are just two broad examples of important biological composite filament assemblies, the understanding of which is key to better

characterize the micromechanics of biological systems. For the deformations of biopolymer network systems to be better understood from a theoretical standpoint, it is necessary to extend the scope of DFN models to include composite and heterotypic materials. With motivation from experimental studies [103, 244], recent theoretical work has made progress towards characterizing some of the behaviours observed in such double-fibre systems [166, 219]. However, in order to understand the general mechanisms that lead to the experimentally observed behaviours, it is important to question how the topology and geometry of the composite network influences the results.

The aim of this work was to investigate the general mechanism by which the exceptional stiffening observed both in experiment and numerical studies arises. Previous explanations for this phenomenon have been suggested in the literature. In particular, it has been argued that the increase in stretching energy adjacent to inclusions can lead to a percolation of interphases, leading to stretch-dominated composites that are far stiffer than their base networks. Other research has proposed that the nonaffinity present in the base network is locally suppressed by stiffer inclusions, translated instead to low inclusion density regions in the composite. If these explanations hold, we expected that for constant inclusion density and geometry, we should be able to explain the mechanical behaviours of general fibre composites either through the properties of the base network fibres or the network behaviour, in terms of nonaffinity. Instead, simulations revealed that distinct responses arose in composites of different architectures, which could not be explained purely by considering these features.

By considering network energy partitions, we found that the stiffness increase in both network architectures was accompanied by a large increase in base fibre stretching deformations, as well as an increase in inclusion energy. This motivated an investigation into the spatial energy profile of these composites. Here, Mikado composites were observed to exhibit regions of high stretching energy where inclusion fibres approached one another, and an absence of such energy in low inclusion density areas of the network. Despite the same inclusion geometry being used in nonfibrous

Voronoi composites, no such increase in stretching energy was measured, and these networks appeared strongly bend-dominated for the same inclusions. This suggests that the previous explanations offered in the literature are incomplete. We hypothesized that the stiffening response was controlled instead by a percolation phenomenon, defined by the formation of a network of two fibre types, each of which only cross-links to the other. By investigating the percolation threshold in such networks, we found that the location of the exceptional stiffening response coincided with percolation. Further evidence for this phenomenon leading to the stretch-dominated stiffening response was observed in the change in network strain energy density pdfs, where a small family of very high energy fibres emerged in fibrous composites, yet not in nonfibrous examples. Finally, recognising that such an interpretation has profound implications for composites in which inclusions are aligned, we generated anisotropic composites. We quantified the percolation threshold for such networks, and thus predicted the location of the 'exceptional' stiffness jump. By classifying networks according to their percolation condition, we showed that these predictions were accurate for three distinct base fibre lengths in Mikado networks, while the exceptional stiffening response was found to be entirely absent in Voronoi networks, where the lack of longer base fibre lengths precluded the percolation of the stiff inclusions by the base network.

While random Voronoi composites displayed a rapid stiffness increase with inclusion density around the independent percolation of those inclusions, which agrees with the proposed base cross-linked inclusion hypothesis, we did not see a likewise sudden move to stretch dominated networks. Instead, while there was a large increase in the stretching energy in these composites, they remained marginally bend dominated even at the highest inclusion densities considered, despite still exhibiting a 7 orders of magnitude increase in stiffness. We predict that this is due to the absence of stabilizing coincident base fibres in these networks. In particular, for long Mikado base fibres, stretching is likely to occur above percolation as bending deflections are suppressed by coincident base fibres, of which there are $L/l_c \gg 1$. We expect that for composites where base filaments are very compliant,

the stretch-dominated response should vanish. In the Voronoi composites considered in this work, there are no such constraining fibres. Further work is required to investigate the parameters for which a transition from stretch to bend dominated composites occurs for a given geometry.

The additional richness found in the mechanics of fibrous composites as discussed in this chapter might explain why they are so commonly found in Nature. We expect that the ability to regulate the network stiffness over many orders of magnitude through the inclusion of relatively few stiff fibres is likely to be of great utility both in intra- and extracellular matrices. Similarly, we expect that the ability to vary inclusion-base fibre cross-linking, and architectural variations within the base or inclusion networks, could also lead to similar mechanical changes. However, while the interesting mechanical behaviours we have investigated in this work arise from planar networks, many real world examples are of course three-dimensional. In these cases, the percolation phenomenon described here might not occur so naturally. Similar stiffening effects have been observed in computational studies for 3D filament networks [234]. Investigating whether the same physics as discussed here is responsible for this stiffening effect, and how our conclusions might change when considering 3D structures, would be important extensions of this work. Furthermore, while we observed a dramatic increase in the static shear modulus for composites in the small strain regime, the large deformation behaviours have not been characterized. As strain increases, initially floppy modes will be stretched out, and we expect that stress paths will form between the inclusions, such that even the nonfibrous networks considered here will experience considerable stiffening at low inclusion densities. We note that the reduction in strain-stiffening behaviour reported in certain experiments [245] could be explained by considering the percolation phenomenon, as the generic move from bending to stretching as strain increases has already partly occurred. For larger strains still, the failure properties of the composite will likely vary according to the architecture and the number of inclusions in the percolating double-fibre network. In particular, we expect that regions of high strain energy density will continue to exist in between

inclusion fibres, whence we expect network failure to occur either at base fibres coincident to multiple inclusions, or at the corresponding cross-links. These areas of study are highly relevant to real biopolymer networks, and could inform research into the generation of novel synthetic biopolymer networks with desirable properties.

5.5 Conclusions

In this work we have investigated the mechanics of composite fibre networks formed from two families of filaments, one of which was modelled to be stiff. In particular, we considered composites formed from two distinct architectures; nonfibrous Voronoi networks, in which there is no notion of geometric fibre persistence through cross-links, and fibrous Mikado networks, where each fibre has many coincident cross-links. Simulations confirmed that the exceptional stiffening observed in previous research occurs in both network architectures. However, this stiffening effect exhibited geometry-dependent differences that could not be explained by local fibre stiffness, nor bulk network affinity. The stiffening effect was found to be caused by a percolation phenomenon, where base fibres cross-link inclusions across the computational domain. As such, we identified the geometric persistence length of the base fibres, alongside the number and length of the inclusions, as the most important parameter for characterizing the network mechanics. Numerical results provided predictions for the location of this threshold for both random and aligned inclusions. These predictions were found to be accurate for three different base fibre lengths, and for both network architectures considered. This work provides an explanation for double-fibre network stiffening, as well as a means to predict which networks will exhibit such effects, and identifies the base fibre length as an important mediator of heterotypic fibre network stiffness.

6

Discussion and future directions

In this thesis we have investigated several of the many structural properties that affect the polymer networks frequently found in both synthetic and natural systems. The aim throughout has been to highlight the importance of the diverse structural properties exhibited by biopolymer systems, and how subtle changes to structure can have important consequences for the local and global behaviour of the assembly. The research presented here includes several extensions to the existing DFN literature, novel contributions to the theoretical understanding of their properties, and a basis for future directions into the ever-growing field of biopolymers and their networks. The computational equipment required to investigate a variety of network architectures, alongside tools to allow simulations of their deformations in commercial finite element software, has been developed, which will facilitate future extensions into many of the topics discussed here. Throughout, we have aimed to maintain a degree of generality, where we hope to demonstrate general physical principles, rather than producing quantitative studies relating to specific experiments on biopolymer networks. In this chapter, we synthesise the main findings of the research presented in this thesis, discuss their relation to the wider field, and suggest future investigations following this work. Proposed extensions to individual studies are discussed towards the end of the relevant research chapters, such that the future directions presented below relate to prospective research more generally.

6.1 Thesis contributions and conclusions

If one is to understand the complex mechanics that arises at the smallest length scales within and without cells, and how this relates to system-scale observations, it is necessary to investigate the relevant microstructures in finer detail. While high resolution models, such as polymer Brownian dynamics simulations, are useful for detailed studies into specific systems, they are extremely computationally expensive, and can lack in generality. As a compromise between the competing interests of generality and necessary detail, we have developed DFN models that explicitly incorporate the discrete microstructure observed in many biopolymer systems, while representing individual filaments through simple beam or spring models. This level of detail allowed us to question the importance of geometry and structure in biopolymer networks, and how these features might relate to biological function.

We began by developing the computational machinery to generate many different network geometries that have been used in existing studies into polymer assemblies. In particular, Voronoi, Mikado and growth networks were constructed, all of which fulfilled common criteria for the biopolymer network system, in that they were subisostatic, homogeneous in density at a bulk scale, and did not exhibit any global preferential directions (unlike, say, triangular, square or kagome lattice models). From these network architectures, further model geometries and systems could be developed in order to address specific structural questions regarding the network mechanics. In particular, we presented variations to Voronoi and growth networks that we termed 'dual' and 'perturbed' networks, and developed a new geometry, the phantom Mikado network. To accompany these architectures, we developed code that could interface with commercial finite element software, providing the advantages of well-tested development, robust solutions and computational efficiency, as well as bespoke code that allowed us to simulate finite strain deformations of spring networks.

In Chapter 2, we started our investigations into structure in biopolymer systems with motivation from mechanically active cells, such as fibroblasts or mesenchymal

stem cells. These cell types have been observed to mechanically sense one another, as well as distant boundaries and substrate depth, over long distances. While it was known that substrate alignment can allow for cell-derived strains to be propagated further into the matrix, it was not clear whether different isotropic geometries and architectures could improve, or inhibit, the range of these signals. The main findings of this work were that various fibre networks can support long-reaching displacement fields, and that certain (commonly used) networks can support mechanical signals over far longer distances than others. As such, we expect that network geometry is a key regulator of the mechanical behaviours of cellularized biopolymer systems, even when topology, cross-link density, fibre alignment and filament properties are controlled for.

We proceeded to investigate the mechanics of beam-fibre models in the small strain regime in Chapter 3. Here, we were motivated by recent experiments, where the extent of biopolymer network cross-linking could be varied for a given polymer density, with important consequences for cells seeded within. Given its influence in the literature, and its use in many important results within the DFN field, we focussed on the Mikado model in this chapter. We first validated our model and simulations against historic Mikado results from the literature, finding close agreement. We proceeded to develop a new model, which we termed the 'phantom' Mikado model, where cross-linking could be varied without disrupting network geometry or polymer density. The mechanics of the phantom Mikado model was discussed both within the nonaffine, bending-dominated regime, and the stretch-dominated, affine regime. Our main findings were that the network stiffness in the non-affine regime was highly sensitive to cross-link density, and that previously characterized length-scales for the affine-nonaffine transition are invalid in this more general model. We developed a new theoretical argument for the scaling of the shear modulus with a cross-link proportion parameter, which was absent in the existing literature. Furthermore, we presented an empirical, corrected length scale for the affine transition, which resulted in a data collapse within a given polymer density. These contributions serve to extend the generality and scope of

the Mikado model, the most commonly used random network within the DFN literature, and evidences the importance of network structure to bulk mechanics by quantifying the importance of cross-link density.

As most existing models consider DFNs formed from a single filament type, we continued by investigating the mechanics that arise in double-fibre networks. The added complexity that is introduced by the additional lengths and elastic moduli combines to make the characterization of these fibrous composites challenging. In Chapter 4 we investigated the mechanics of a single filament inclusion placed within networks of different architectures. In particular, we considered both 'fibrous' Mikado networks and 'nonfibrous' Voronoi architectures. The importance of the microstructural differences between different network geometries has been largely overlooked within the existing literature. The mechanics was discussed and quantified over a broad range of inclusion parameters, for base networks within the nonaffine regime. By considering floppy mode theory for the filament networks, we generated new theoretical predictions for the scaling of network stiffness, which were subsequently verified by simulations. We found that nonaffine displacement fluctuations lead to different responses, dependent on network architecture. Our main, and novel, contributions here were the thorough characterization of the system, both theoretically and numerically, as well as identifying a biologically relevant and testable difference between network types. Specifically, Voronoi double-fibre networks are largely insensitive to the bending stiffness of the inclusion, whereas large network energy variations arose in Mikado architectures, dependent on the inclusion bending rigidity.

In Chapter 5 we proceeded to study dense double-fibre systems, where a family of inclusions is introduced into the same two geometries. We aimed to find a generic explanation for the 'exceptional' stiffening observed in double-fibre networks, both in simulations and experiment. While similar systems have been investigated within the literature, they have focussed almost exclusively on Mikado composites, whence the general mechanics of double-fibre systems remain poorly understood. Initially, we expected that either the bulk network affinity or the properties of fibres close to

the inclusions would explain the jump in stiffness, as well as the dramatic increase in stretch energy, as suggested by other research groups. However, our main finding was that geometric fibre persistence governed the stiffening effect, for which we provided various forms of evidence. In particular, a percolation of base and inclusion fibres gave rise to the stretching of base fibres, whence the network became far stiffer, an explanation that we provide evidence for above others offered elsewhere in the literature. This interpretation allowed us to accurately predict the location of the stiffening phenomenon in different composite architectures, and explain recent experiments that observe this phenomenon *in vitro*.

6.2 Future directions

While we have discussed several different themes relevant to DFN modelling in this thesis, many interesting research areas have, by necessity, been omitted. However, there are many extensions to the work presented here that could become promising research projects in future months and years. Here, we discuss interesting directions in which we hope to continue this work, so as to broaden and extend our research findings

Finite strain mechanics

In three of the four research chapters in this thesis, we have considered the small-strain mechanics of the fibre networks. The extension of this work to large deformations is important, as it is not clear how the structural variations we introduced will affect biopolymer networks in this biologically relevant regime. For example, nonaffine Mikado networks (and indeed all bending-dominated subisostatic DFNs) will become stretching-dominated at some critical strain. How variations in the cross-link density impact this critical strain for a given Mikado network is unclear, and could be relevant when considering the failure of cross-links at large strains. Likewise, extending the double-fibre network model to the large strain regime could lead to further interesting micromechanics, as the nonaffine fluctuations and floppy modes responsible for the different network responses are pulled out. It is perhaps

not clear whether different composite mechanics will be observed between distinct network architectures in the large strain regime. Naturally, this applies to the dense fibre composites considered in Chapter 5, where we might expect that a secondary percolation phenomenon occurs, with stress paths forming between the inclusions, similar to those observed in Chapter 2, for example as in Fig. 2.7 for growth networks. In a similar manner, we might wish to consider changing the linear model used for the fibres, and investigate the impact of biopolymer nonlinearity on the material properties at large strains, similar to work presented by Hudson et al. [72].

Damage propagation and failure

It would be interesting to investigate the failure properties of the biopolymer networks considered in this thesis, and how they relate to the structural properties discussed throughout. As many biopolymer systems *in vivo* must undergo large strains, for example as seen in fibrin clots, their failure strength must often be large. Furthermore, it would be desirable to avoid catastrophic failure by accommodating damage through structural changes in the material. The models presented within this thesis are well-suited to address many of the damage problems of interest to the community. For example, consider the phantom Mikado model presented in Chapter 3; by including cross-link failure at certain strains, one could model the transition between a fully cross-linked Mikado network and the sparsely cross-linked phantom case. Fibre failure could be important to model at large strains within the double-fibre networks of Chapter 5. Here, we predict the formation of extremely energetic fibres between stiff inclusions. As strain progresses, these fibres are expected to be the first to fail, whence the percolation phenomenon is disrupted and the bulk stiffness would fall drastically. Further models could investigate failure in DFNs more generally, investigating crack formation and damage progression; whether certain geometries can accommodate damage in a more favourable way is an open question that fibre network modelling is well-placed to answer.

Three dimensional models and extended architecture

While this thesis has discussed some of the many interesting mechanical behaviours that arise in biopolymer networks, we have not attempted to explicitly model a *specific* biopolymer network, nor any of the particular structures that are observed within, instead focussing on general network representations that are isotropic and homogeneous. As discussed in Chapter 1, many functional biopolymer systems, such as articular cartilage or tendon, possess an intricate structure. The models we have developed in this thesis can readily be extended to incorporate representations of these structural aspects. Consider for example the peripheral matrix of contractile or passive cells. Different fibre alignments and densities are observed in a variety of systems, according to their physiological function. Models that involve cells contracting in matrices that are locally aligned with the cell, or where the proximal matrix has a lower or higher polymer density, could investigate the effects of this local structure. The results could then be compared with those of Chapter 2. Likewise, where cross-link density varies spatially, or where the fibre mechanical properties are zonal, the modelling efforts of Chapters 3 - 5 can be applied. These more specific models would be of particular in comparison with experimental data.

Extending the models presented in this thesis to 3D would help to frame the observed results in an even more general setting. Three-dimensional networks are likely to be less constrained than their planar counterparts, due to a reduced number of fibre crossings and additional bending modes becoming available. We therefore expect many of these biopolymer assemblies to be within the nonaffine regime, whence cross-link disruption as discussed in Chapter 3 could be particularly relevant. Furthermore, some of the phenomena discussed for double-fibre composites would not trivially apply in 3D. In particular, the percolation threshold responsible for exceptional stiffening becomes nontrivial. Investigating 3D heterotypic DFN models would allow us to quantify the extent to which exceptional stiffening arises here, and whether its origins are due to similar physics. For the research presented in this thesis, the extension to 3D is somewhat challenging, but important for highlighting the importance of structural properties in biopolymer networks more generally.

6.3 Closing remarks

The field of mechanics has grown to a remarkable extent over the past century, to encompass a vast and diverse range of subjects and applications. The investigations presented here contribute to one of the younger research areas, which has arisen from a need and desire to model and understand the complexity of microscale biological materials. Given recent improvements in electrospinning and 3D printing technologies, we hope that in the coming decades experimental platforms will be able to test and verify some of the hypotheses and predictions given within this thesis. As numerical, computational and theoretical techniques become ever more sophisticated, the research contributions offered in this thesis can be extended, forming the basis and motivation for future studies. Taken together, we advocate that this research provides further evidence for the functional role of structure and geometry in biopolymer networks, contributes understanding towards the complexity of their mechanics, and motivates further work into the fascinating and intricate world of micromechanics in biological and physical systems.

Appendices

A

Statistical properties of Mikado networks

In this section, we discuss the statistics of Mikado geometries, and clarify some of the results used in the main text, including the mean and distribution of segment lengths. Recall that Mikado networks are formed through the placement of N fibres, of identical length L within a square domain with sides of length W. The positions and orientations of the fibres are uniformly random. The probability that a fibre at angle θ with the x-axis crosses a given horizontal line is the given by the ratio of the fibre length to the total length of the line to which the segment belongs that falls within the domain. The total length of the line contained within the domain is given by $W/\sin\theta$, so that the probability of the segment intersecting the horizontal line is $L\sin\theta/W$. Now consider the ratio of fibre length to the length of the horizontal line within the domain, and we can see that the probability of two segments crossing is given by $L^2\sin\theta/W^2$. Averaging over uniformly random orientations θ, we arrive at the probability that two segments cross, as:

$$P(\text{int.}) = \frac{1}{\pi}\int_0^\pi \left(\frac{L}{W}\right)^2 \sin\theta \,\mathrm{d}\theta = \frac{2L^2}{\pi W^2} \ . \tag{A.1}$$

As Mikado fibres are placed randomly and uniformly within the planar domain, the expected number of intersections is just N times the probability for two fibres. That is, $\mathbb{E}(\text{int.}) = \frac{2NL^2}{\pi W^2} = \frac{2q}{\pi}$, for quantity $q := \frac{NL^2}{W^2}$. As fibre crossings are

independent, the distribution for the number n_f of crosslinks on a fibre is Poisson distributed, with mean $\lambda = \frac{2q}{\pi}$:

$$P(n_f) = \frac{\lambda^{n_f} e^{-\lambda}}{n_f!} \ . \tag{A.2}$$

We can see this by viewing the fibre crossings as a Poisson process, whence the segments lengths, with mean value l_c, are exponentially distributed, as:

$$P(l) \sim \frac{1}{l_c} e^{-l/l_c} \ . \tag{A.3}$$

Now, each fibre-fibre intersection increases the number of segments by 1. In particular, n_f crossings cut a fibre into $n_f + 1$ segments, such that the mean length of the segments l_c is $L/(\langle n_f \rangle + 1)$. However, dangling ends, that is the free ends of fibres, are removed during network generation. Instead, only $(n_f - 1)$ of the $(n_f + 1)$ segments are considered, such that to evaluate the average segment length l_c, we should average the quantity $L/(n_f + 1)$ over probabilities $P(n_f)$, and include a weighting of $(n_f - 1)$, followed by a normalization. Summation starts at $n_f = 2$, as a fibre with a single crossing contains only dangling ends. In particular:

$$l_c = \frac{\sum_{n_f=2}^{\infty} \frac{L(n_f-1)}{(n_f+1)} P(n_f)}{\sum_{n_f=2}^{\infty} (n_f - 1) P(n_f)} = \frac{e^{-\lambda} L \sum_{n_f=2}^{\infty} \frac{(n_f-1)}{(n_f+1)} \frac{\lambda_f^n}{n_f!}}{e^{-\lambda} \sum_{n_f=2}^{\infty} \frac{(n_f-1)}{n_f!} \lambda_f^n} \ . \tag{A.4}$$

For the denominator:

$$\sum_{n_f=2}^{\infty} \frac{(n_f - 1)}{n_f!} \lambda^n = \sum_{n_f=2}^{\infty} \left(\frac{1}{(n_f - 1)!} - \frac{1}{n_f!} \right) \lambda_f^n \ , \tag{A.5}$$

$$= \lambda \sum_{n_f=2}^{\infty} \frac{\lambda^{n_f - 1}}{(n_f - 1)!} - \sum_{n_f=2}^{\infty} \frac{\lambda_f^n}{n_f!} \ , \tag{A.6}$$

$$= \lambda e^{\lambda} - e^{\lambda} + 1 \ , \tag{A.7}$$

and for the numerator:

$$\sum_{n_f=2}^{\infty} \frac{(n_f - 1)}{(n_f + 1)} \frac{\lambda_f^n}{n_f!} = \sum_{n_f=2}^{\infty} \left(\frac{1}{n_f!} - \frac{2}{(n_f + 1)!} \right) \lambda_f^n \ , \tag{A.8}$$

$$= \sum_{n_f=2}^{\infty} \frac{\lambda^{n_f}}{n_f!} - \frac{2}{\lambda} \sum_{n_f=2}^{\infty} \frac{\lambda^{n_f+1}}{(n_f + 1)!} \ , \tag{A.9}$$

$$= e^{\lambda} - \lambda - 1 - \frac{2}{\lambda} \left(e^{\lambda} - \frac{\lambda^2}{2} - \lambda - 1 \right) \ , \tag{A.10}$$

$$= e^{\lambda} + 1 - \frac{2}{\lambda} (e^{\lambda} - 1) \ . \tag{A.11}$$

Finally, we can evaluate the quantity L/l_c to give:

$$\frac{L}{l_c} = \frac{\lambda + e^{-\lambda} - 1}{1 + e^{-\lambda} + \frac{2}{\lambda}(e^{-\lambda} - 1)} \ . \tag{A.12}$$

For large $q = \frac{NL^2}{W^2}$, we have $L/l_c \to \lambda = \frac{2NL^2}{\pi W^2}$. For line density $\hat{\rho} = \frac{NL}{W^2}$, this returns the Kallmes-Corte relationship, $l_c \sim \frac{\pi}{2\hat{\rho}}$. For low values, L/l_c approaches 3.

B

Affine deformations and discrete fibre network models

A common theme in the discussion of DFN models, both in this thesis and in the wider literature, is that of affinity. In particular, we are interested in the extent to which nonaffine fluctuations in the strain field, that is deviations from the displacements anticipated were every part of the sample deform according to an affine deformation. Here, we clarify in detail some of the results referred to in the text, for networks subjected to small simple shear strains.

Affine fibre strain

First, consider a reference fibre, defined by the vector $[X, Y]$, a current position for the same fibre after deformation, $[x, y]$, and a bulk affine shear, with small shear strain γ. If we assume that the current position follows from an affine deformation of the reference fibre, we have:

$$\begin{bmatrix} x \\ y \end{bmatrix} = \begin{bmatrix} 1 & \gamma \\ 0 & 1 \end{bmatrix} \begin{bmatrix} X \\ Y \end{bmatrix} = \begin{bmatrix} X + \gamma Y \\ Y \end{bmatrix} . \tag{B.1}$$

In particular, we can write down the change in fibre length under this affine shear. Let L be the reference fibre length, and L_γ denote the length following

the affine shear. Then,

$$L_\gamma^2 = x^2 + y^2 = (X + \gamma Y)^2 + Y^2 \ , \tag{B.2}$$

$$= (X^2 + Y^2) + 2XY\gamma + \gamma^2 Y^2 \ , \tag{B.3}$$

$$\approx L^2 + 2XY\gamma \ , \tag{B.4}$$

where we have only kept leading order terms in the small strain γ. Now, assume that the fibre is oriented at an angle θ with the horizontal x-axis, so that $X = L\cos\theta,\ Y = L\sin\theta$. Taking roots of both sides, and expanding for small γ gives:

$$L_\gamma \approx (L^2 + 2\gamma L^2 \sin\theta\cos\theta)^{\frac{1}{2}} \ , \tag{B.5}$$

$$= L(1 + \gamma\sin 2\theta)^{\frac{1}{2}} \ , \tag{B.6}$$

$$\approx L\left(1 + \frac{\gamma\sin 2\theta}{2}\right) \ . \tag{B.7}$$

As such, we can write the fibre axial strain ϵ as:

$$\epsilon = \frac{L_\gamma - L}{L} \approx \frac{\gamma\sin 2\theta}{2} \tag{B.8}$$

Affine fibre rotation

We can also use the affine assumption to produce a description of the fibre rotation under small shear strain, such that we will have descriptions of both the affine fibre strain and rotation, both of which are used within this thesis. Define the small angle between the fibre in reference and current configurations as ϕ, which we term the affine rotation angle. From Eq. B.1 and the cosine rule, we have:

$$\gamma^2 Y^2 = L^2 + L_\gamma^2 - 2LL_\gamma\cos\phi \ , \tag{B.9}$$

$$= 2L^2 + 2\gamma XY + \gamma^2 Y^2 - 2LL_\gamma\cos\phi \ . \tag{B.10}$$

Returning to the deformed length L_γ, we now retain higher order terms, such that after expanding:

$$L_\gamma = L(1 + 2\gamma\sin\theta\cos\theta + \gamma^2\sin^2\theta)^{\frac{1}{2}} \ , \tag{B.11}$$

$$= L\left(1 + \gamma\sin\theta\cos\theta + \frac{\gamma^2}{8}\left(4\sin^2\theta - 4\sin^2\theta\cos^2\theta\right)\right) + \mathcal{O}(\gamma^3) \ , \tag{B.12}$$

$$\approx L\left(1 + \gamma\sin\theta\cos\theta + \frac{\gamma^2\sin^4\theta}{2}\right) \ . \tag{B.13}$$

Substituting this expression into Eq. B.10 and expanding for small ϕ:

$$2L^2(1+\gamma\sin\theta\cos\theta) = 2LL_\gamma\cos\phi \ , \tag{B.14}$$

$$= 2L^2\left(1+\gamma\sin\theta\cos\theta+\frac{\gamma^2\sin^4\theta}{2}\right)\left(1-\frac{\phi^2}{2}\right) \ . \tag{B.15}$$

such that:

$$\frac{\phi^2}{2} = \frac{\gamma^2\sin^4\theta}{2} + \mathcal{O}(\gamma,\phi)^3 \ , \tag{B.16}$$

so that we arrive at the small angle and small strain result for the affine rotation angle:

$$\phi \approx \gamma\sin^2\theta \ . \tag{B.17}$$

Affine shear modulus

Having discussed the small strain results for rotation and stretching of DFN fibres under an affine assumption, we now wish to calculate the affine shear modulus from the properties of the constituent fibres. Note that, by the definition of an affine transformation, straight lines remain straight, such that a Mikado network with freely rotating crosslinks does not incur any bending costs for affine motions. In this case, as affine deformations are always available to the DFN, the affine shear modulus will act as a strict upper limit, while those networks with welded crosslinks will be prohibited from undergoing precisely affine motions by the fixed bond angles.

As discussed above, fibres rotate and stretch, such that each fibre undergoes an extension or compression. We wish to sum over the contributions of all constituent fibres. In particular, for fibre stretching modulus μ, we have the energy per fibre $\delta\mathcal{H}$ given by:

$$\delta\mathcal{H} = \frac{1}{2}\mu\epsilon^2 L = \frac{1}{8}\mu\gamma^2 L\sin^2 2\theta \ . \tag{B.18}$$

There are N such fibres within the network, at random orientations θ. Summing over the expected energy per fibre and averaging over the uniform orientations, we

have the expression for total network energy $\mathcal{H}_{\text{total}}$ given by:

$$\mathcal{H}_{\text{total}} = N\langle\delta\mathcal{H}\rangle = \frac{\gamma^2\mu NL}{8\pi}\int_0^\pi \sin^2 2\theta \,\mathrm{d}\theta \ , \tag{B.19}$$

$$= \frac{\gamma^2\mu NL}{16} \ . \tag{B.20}$$

Given this network energy is related to the affine bulk shear modulus $\mathcal{G}_{\text{affine}}$ as $\mathcal{H}_{\text{total}} = \frac{1}{2}\mathcal{G}_{\text{affine}}\gamma^2 W^2$, we can write our prediction for the affine shear modulus as:

$$\mathcal{G}_{\text{affine}} = \frac{2\mathcal{H}_{\text{total}}}{\gamma^2 W^2} = \frac{\mu}{8}\frac{NL}{W^2} = \frac{\hat{\rho}\mu}{8} \ , \tag{B.21}$$

where network density is given as $\hat{\rho} := \frac{NL}{W^2}$. By the results derived in Appendix A for the relationship between mean segment length l_c and line density $\hat{\rho}$, we can therefore approximate the Mikado affine shear modulus as:

$$\mathcal{G}_{\text{affine}} \approx \frac{\pi}{16}\frac{\mu}{l_c} \ . \tag{B.22}$$

References

[1] Robert Hooke. *Micrographia: or some physiological descriptions of minute bodies made by magnifying glasses, with observations and inquiries thereupon*. Courier Corporation, 2003.

[2] Jonathan Stricker, Tobias Falzone, and Margaret L Gardel. "Mechanics of the F-actin cytoskeleton". In: *Journal of biomechanics* 43.1 (2010), pp. 9–14.

[3] Peter Fratzl. *Collagen: structure and mechanics*. Springer Science & Business Media, 2008.

[4] O Kallmes and H Corte. "The structure of paper, I. The statistical geometry of an ideal two dimensional fiber network". In: *Tappi J.* 43.9 (1960), pp. 737–752.

[5] Candace K Chan et al. "Structural and electrochemical study of the reaction of lithium with silicon nanowires". In: *Journal of Power Sources* 189.1 (2009), pp. 34–39.

[6] Peter Fratzl and Richard Weinkamer. "Nature's hierarchical materials". In: *Progress in Materials Science* 52.8 (2007), pp. 1263–1334.

[7] F C MacKintosh, J Käs, and P A Janmey. "Elasticity of semiflexible biopolymer networks". In: *Physical Review Letters* 75.24 (1995), p. 4425.

[8] Fred T Bosman and Ivan Stamenkovic. "Functional structure and composition of the extracellular matrix". In: *The Journal of pathology* 200.4 (2003), pp. 423–428.

[9] Brendon M Baker et al. "Cell-mediated fibre recruitment drives extracellular matrix mechanosensing in engineered fibrillar microenvironments". In: *Nature Materials* (2015).

[10] Onur Bas et al. "Biofabricated soft network composites for cartilage tissue engineering". In: *Biofabrication* 9.2 (2017), p. 025014.

[11] Steven E Calvin and Michelle L Oyen. "Microstructure and mechanics of the chorioamnion membrane with an emphasis on fracture properties". In: *Annals of the New York Academy of Sciences* 1101.1 (2007), pp. 166–185.

[12] John M Gosline, M Edwin DeMont, and Mark W Denny. "The structure and properties of spider silk". In: *Endeavour* 10.1 (1986), pp. 37–43.

[13] Hyeran Kang et al. "Nonlinear elasticity of stiff filament networks: strain stiffening, negative normal stress, and filament alignment in fibrin gels". In: *The Journal of Physical Chemistry B* 113.12 (2009), pp. 3799–3805.

[14] Manuel Théry et al. "Cell distribution of stress fibres in response to the geometry of the adhesive environment". In: *Cytoskeleton* 63.6 (2006), pp. 341–355.

[15] Dennis E Discher, Paul Janmey, and Yu-li Wang. "Tissue cells feel and respond to the stiffness of their substrate". In: *Science* 310.5751 (2005), pp. 1139–1143.

[16] Lena R Bartell et al. “Measuring microscale strain fields in articular cartilage during rapid impact reveals thresholds for chondrocyte death and a protective role for the superficial layer”. In: *Journal of biomechanics* 48.12 (2015), pp. 3440–3446.

[17] Alice J Sophia Fox, Asheesh Bedi, and Scott A Rodeo. “The basic science of articular cartilage: structure, composition, and function”. In: *Sports Health* 1.6 (2009), pp. 461–468.

[18] Jan Wilhelm and Erwin Frey. “Elasticity of stiff polymer networks”. In: *Physical Review Letters* 91.10 (2003), p. 108103.

[19] Hailong Wang et al. “Long-range force transmission in fibrous matrices enabled by tension-driven alignment of fibers”. In: *Biophysical journal* 107.11 (2014), pp. 2592–2603.

[20] Farzan Beroz et al. “Physical limits to biomechanical sensing in disordered fibre networks”. In: *Nature Communications* 8 (2017), ncomms16096.

[21] Tatyana M Svitkina et al. “Analysis of the actin–myosin II system in fish epidermal keratocytes: mechanism of cell body translocation”. In: *The Journal of cell biology* 139.2 (1997), pp. 397–415.

[22] Leonard M Sander. “Alignment localization in nonlinear biological media”. In: *Journal of Biomechanical Engineering* 135.7 (2013), p. 071006.

[23] Cole D Chapman et al. “Onset of non-continuum effects in microrheology of entangled polymer solutions”. In: *Macromolecules* 47.3 (2014), pp. 1181–1186.

[24] Airidas Korolkovas, Philipp Gutfreund, and Jean-Louis Barrat. “Simulation of entangled polymer solutions”. In: *The Journal of chemical physics* 145.12 (2016), p. 124113.

[25] Aamir Shabbir et al. “Effect of hydrogen bonding on linear and nonlinear rheology of entangled polymer melts”. In: *Macromolecules* 48.16 (2015), pp. 5988–5996.

[26] Christoph F Schmidt et al. “Chain dynamics, mesh size, and diffusive transport in networks of polymerized actin: a quasielastic light scattering and microfluorescence study”. In: *Macromolecules* 22.9 (1989), pp. 3638–3649.

[27] Yiider Tseng et al. “The bimodal role of filamin in controlling the architecture and mechanics of F-actin networks”. In: *Journal of Biological Chemistry* 279.3 (2004), pp. 1819–1826.

[28] Silvia Jansen et al. “Mechanism of actin filament bundling by fascin”. In: *Journal of Biological Chemistry* 286.34 (2011), pp. 30087–30096.

[29] M Maier et al. “A single charge in the actin binding domain of fascin can independently tune the linear and non-linear response of an actin bundle network”. In: *The European Physical Journal E* 38.5 (2015), p. 50.

[30] Gary Laevsky and David A Knecht. “Cross-linking of actin filaments by myosin II is a major contributor to cortical integrity and cell motility in restrictive environments”. In: *Journal of cell science* 116.18 (2003), pp. 3761–3770.

[31] Hajer Ennomani et al. “Architecture and connectivity govern actin network contractility”. In: *Current Biology* 26.5 (2016), pp. 616–626.

[32] Jerôme Berger et al. “Structure and interactions in covalently and ionically crosslinked chitosan hydrogels for biomedical applications”. In: *European Journal of Pharmaceutics and Biopharmaceutics* 57.1 (2004), pp. 19–34.

[33] O Lieleg et al. “Transient binding and dissipation in cross-linked actin networks”. In: *Physical Review Letters* 101.10 (2008), p. 108101.

[34] Paul A Janmey et al. “Negative normal stress in semiflexible biopolymer gels”. In: *Nature Materials* 6.1 (2007), p. 48.

[35] Enrico Conti and Fred C MacKintosh. “Cross-linked networks of stiff filaments exhibit negative normal stress”. In: *Physical review letters* 102.8 (2009), p. 088102.

[36] L Angela Mihai and Alain Goriely. “Positive or negative Poynting effect? The role of adscititious inequalities in hyperelastic materials”. In: *Proc. R. Soc. A*. Vol. 467. 2136. The Royal Society. 2011, pp. 3633–3646.

[37] Stéphanie Motte and Laura J Kaufman. “Strain stiffening in collagen I networks”. In: *Biopolymers* 99.1 (2013), pp. 35–46.

[38] M L Gardel et al. “Elastic behavior of cross-linked and bundled actin networks”. In: *Science* 304.5675 (2004), pp. 1301–1305.

[39] Kendra A Erk, Kevin J Henderson, and Kenneth R Shull. “Strain stiffening in synthetic and biopolymer networks”. In: *Biomacromolecules* 11.5 (2010), pp. 1358–1363.

[40] David Vader et al. “Strain-induced alignment in collagen gels”. In: *PloS one* 4.6 (2009), e5902.

[41] Nicholas A Kurniawan et al. “Fibrin networks support recurring mechanical loads by adapting their structure across multiple scales”. In: *Biophysical journal* 111.5 (2016), pp. 1026–1034.

[42] Ovijit Chaudhuri, Sapun H Parekh, and Daniel A Fletcher. “Reversible stress softening of actin networks”. In: *Nature* 445.7125 (2007), p. 295.

[43] Oleg V Kim et al. “Structural basis for the nonlinear mechanics of fibrin networks under compression”. In: *Biomaterials* 35.25 (2014), pp. 6739–6749.

[44] Anne SG Van Oosten et al. “Uncoupling shear and uniaxial elastic moduli of semiflexible biopolymer networks: compression-softening and stretch-stiffening”. In: *Scientific reports* 6 (2016), p. 19270.

[45] Masao Doi and Samuel Frederick Edwards. *The theory of polymer dynamics*. Vol. 73. oxford university press, 1988.

[46] Frederick Gittes et al. “Flexural rigidity of microtubules and actin filaments measured from thermal fluctuations in shape.” In: *The Journal of cell biology* 120.4 (1993), pp. 923–934.

[47] Francesco Pampaloni et al. “Thermal fluctuations of grafted microtubules provide evidence of a length-dependent persistence length”. In: *Proceedings of the National Academy of Sciences* 103.27 (2006), pp. 10248–10253.

[48] Peter Fratzl et al. “Fibrillar structure and mechanical properties of collagen”. In: *Journal of structural biology* 122.1-2 (1998), pp. 119–122.

[49] Aleksander V Drozdetski, Ramu Anandakrishnan, and Alexey Onufriev. "Estimating Persistence Length of DNA from Molecular Dynamics Simulations". In: *Biophysical Journal* 108.2 (2015), 233a.

[50] Magnus Ullner and Clifford E Woodward. "Orientational correlation function and persistence lengths of flexible polyelectrolytes". In: *Macromolecules* 35.4 (2002), pp. 1437–1445.

[51] Chase P Broedersz and Fred C MacKintosh. "Modeling semiflexible polymer networks". In: *Reviews of Modern Physics* 86.3 (2014), p. 995.

[52] Ning Wang and Dimitrijie Stamenovic. "Mechanics of vimentin intermediate filaments". In: *Journal of muscle research and cell motility* 23.5 (2002), pp. 535–540.

[53] Linglei Ma et al. "Keratin filament suspensions show unique micromechanical properties". In: *Journal of Biological Chemistry* 274.27 (1999), pp. 19145–19151.

[54] Sarah Köster et al. "Intermediate filament mechanics in vitro and in the cell: from coiled coils to filaments, fibers and networks". In: *Current opinion in cell biology* 32 (2015), pp. 82–91.

[55] Albert James Licup et al. "Stress controls the mechanics of collagen networks". In: *Proceedings of the National Academy of Sciences* 112.31 (2015), pp. 9573–9578.

[56] Preethi L Chandran, Triantafyllos Stylianopoulos, and Victor H Barocas. "Microstructure-based, multiscale modeling for the mechanical behavior of hydrated fiber networks". In: *Multiscale Modeling & Simulation* 7.1 (2008), pp. 22–43.

[57] Thomas R Coleman and Mark S Mooseker. "Effects of actin filament cross-linking and filament length on actin-myosin interaction." In: *The Journal of cell biology* 101.5 (1985), pp. 1850–1857.

[58] Dan Strehle et al. "Transiently crosslinked F-actin bundles". In: *European Biophysics Journal* 40.1 (2011), pp. 93–101.

[59] ML Gardel et al. "Microrheology of entangled F-actin solutions". In: *Physical review letters* 91.15 (2003), p. 158302.

[60] Daisuke Mizuno et al. "Nonequilibrium mechanics of active cytoskeletal networks". In: *Science* 315.5810 (2007), pp. 370–373.

[61] Danijela Vignjevic and Guillaume Montagnac. "Reorganisation of the dendritic actin network during cancer cell migration and invasion". In: *Seminars in cancer biology*. Vol. 18. 1. Elsevier. 2008, pp. 12–22.

[62] Anne-Cécile Reymann et al. "Actin network architecture can determine myosin motor activity". In: *Science* 336.6086 (2012), pp. 1310–1314.

[63] Ben Harland, Sam Walcott, and Sean X Sun. "Adhesion dynamics and durotaxis in migrating cells". In: *Physical biology* 8.1 (2011), p. 015011.

[64] Pere Roca-Cusachs, Vito Conte, and Xavier Trepat. "Quantifying forces in cell biology". In: *Nature Cell Biology* 19.7 (2017), pp. 742–751.

[65] Ohad Medalia et al. "Organization of actin networks in intact filopodia". In: *Current biology* 17.1 (2007), pp. 79–84.

[66] Pieta K Mattila and Pekka Lappalainen. “Filopodia: molecular architecture and cellular functions”. In: *Nature reviews Molecular cell biology* 9.6 (2008), pp. 446–454.

[67] Timothy A Sanders, Esther Llagostera, and Maria Barna. “Specialized filopodia direct long-range transport of SHH during vertebrate tissue patterning”. In: *Nature* 497.7451 (2013), p. 628.

[68] Frank PL Lai et al. “Arp2/3 complex interactions and actin network turnover in lamellipodia”. In: *The EMBO journal* 27.7 (2008), pp. 982–992.

[69] Sébastien Schaub, Jean-Jacques Meister, and Alexander B Verkhovsky. “Analysis of actin filament network organization in lamellipodia by comparing experimental and simulated images”. In: *Journal of cell science* 120.8 (2007), pp. 1491–1500.

[70] Roy Hantgan et al. “Fibrin assembly: a comparison of electron microscopic and light scattering results.” In: *Thrombosis and haemostasis* 44.3 (1980), pp. 119–124.

[71] Alisa S Wolberg. “Thrombin generation and fibrin clot structure”. In: *Blood reviews* 21.3 (2007), pp. 131–142.

[72] Nathan E Hudson et al. “Stiffening of individual fibrin fibers equitably distributes strain and strengthens networks”. In: *Biophysical Journal* 98.8 (2010), pp. 1632–1640.

[73] Izabela K Piechocka et al. “Structural hierarchy governs fibrin gel mechanics”. In: *Biophysical Journal* 98.10 (2010), pp. 2281–2289.

[74] Johannes J Sidelmann et al. “Fibrin clot formation and lysis: basic mechanisms”. In: *Seminars in thrombosis and hemostasis*. Vol. 26. 06. Copyright© 2000 by Thieme Medical Publishers, Inc., 333 Seventh Avenue, New York, NY 10001, USA. Tel.:+ 1 (212) 584-4662. 2000, pp. 605–618.

[75] Russell F Doolittle. “Fibrinogen and fibrin”. In: *eLS* (2001).

[76] WJLM Liu et al. “Fibrin fibers have extraordinary extensibility and elasticity”. In: *Science* 313.5787 (2006), pp. 634–634.

[77] Martin Guthold et al. “A comparison of the mechanical and structural properties of fibrin fibers with other protein fibers”. In: *Cell biochemistry and biophysics* 49.3 (2007), pp. 165–181.

[78] M Andrew et al. “Fibrin clot lysis by thrombolytic agents is impaired in newborns due to a low plasminogen concentration.” In: *Thrombosis and haemostasis* 68.3 (1992), pp. 325–330.

[79] Anetta Undas and Robert AS Ariëns. “Fibrin Clot Structure and Function”. In: *Arteriosclerosis, thrombosis, and vascular biology* 31.12 (2011), e88–e99.

[80] PS Ciano et al. “Macrophage migration in fibrin gel matrices.” In: *Laboratory investigation; a journal of technical methods and pathology* 54.1 (1986), pp. 62–70.

[81] Lawrence F Brown et al. “Fibroblast migration in fibrin gel matrices.” In: *The American journal of pathology* 142.1 (1993), p. 273.

[82] Sudong Kim et al. “Engineering of functional, perfusable 3D microvascular networks on a chip”. In: *Lab on a Chip* 13.8 (2013), pp. 1489–1500.

[83] Karen L Christman et al. “Fibrin glue alone and skeletal myoblasts in a fibrin scaffold preserve cardiac function after myocardial infarction”. In: *Tissue engineering* 10.3-4 (2004), pp. 403–409.

[84] AJ Feinstein et al. “Fibrin glue eliminates the need for packing after complex liver injuries.” In: *The Yale journal of biology and medicine* 74.5 (2001), p. 315.

[85] André EX Brown et al. “Multiscale mechanics of fibrin polymer: gel stretching with protein unfolding and loss of water”. In: *science* 325.5941 (2009), pp. 741–744.

[86] Gloria A Di Lullo et al. “Mapping the ligand-binding sites and disease-associated mutations on the most abundant protein in the human, type I collagen”. In: *Journal of Biological Chemistry* 277.6 (2002), pp. 4223–4231.

[87] Irène Revenko et al. “Atomic force microscopy study of the collagen fibre structure”. In: *Biology of the Cell* 80.1 (1994), pp. 67–69.

[88] Christian Frantz, Kathleen M Stewart, and Valerie M Weaver. “The extracellular matrix at a glance”. In: *J Cell Sci* 123.24 (2010), pp. 4195–4200.

[89] Sharona Even-Ram and Kenneth M Yamada. “Cell migration in 3D matrix”. In: *Current opinion in cell biology* 17.5 (2005), pp. 524–532.

[90] Klod Kokini et al. “Tensile mechanical properties of three-dimensional type I collagen extracellular matrices with varied microstructure”. In: *J Biomech Eng* 124 (2002), pp. 214–22.

[91] T Christian Gasser et al. “Spatial orientation of collagen fibers in the abdominal aortic aneurysm’s wall and its relation to wall mechanics”. In: *Acta biomaterialia* 8.8 (2012), pp. 3091–3103.

[92] CG Bellows, AH Melcher, and JE Aubin. “Contraction and organization of collagen gels by cells cultured from periodontal ligament, gingiva and bone suggest functional differences between cell types”. In: *Journal of cell science* 50.1 (1981), pp. 299–314.

[93] Matthew S Hall et al. “Fibrous nonlinear elasticity enables positive mechanical feedback between cells and ECMs”. In: *Proceedings of the National Academy of Sciences* 113.49 (2016), pp. 14043–14048.

[94] RJ Minns and FS Steven. “The collagen fibril organization in human articular cartilage.” In: *Journal of anatomy* 123.Pt 2 (1977), p. 437.

[95] Vaclav Klika et al. “An overview of multiphase cartilage mechanical modelling and its role in understanding function and pathology”. In: *Journal of the mechanical behavior of biomedical materials* 62 (2016), pp. 139–157.

[96] Clifford Walters and David R Eyre. “Collagen crosslinks in human dentin: increasing content of hydroxypyridinium residues with age”. In: *Calcified tissue international* 35.1 (1983), pp. 401–405.

[97] Erin McNerny et al. “Bone Fracture Toughness and Strength Correlate With Collagen Cross-Link Maturity in a Dose-Controlled Lathyrism Mouse Model”. In: *Journal of Bone and Mineral Research* 30.3 (2015), pp. 455–464.

[98] AJR Palmer et al. “Non-invasive imaging of cartilage in early osteoarthritis”. In: *Bone Joint J* 95.6 (2013), pp. 738–746.

[99] Robert F Diegelmann, Melissa C Evans, et al. "Wound healing: an overview of acute, fibrotic and delayed healing". In: *Front Biosci* 9.1 (2004), pp. 283–289.

[100] Frank B Niessen et al. "On the nature of hypertrophic scars and keloids: a review." In: *Plastic and reconstructive surgery* 104.5 (1999), pp. 1435–1458.

[101] RZ Wang et al. "Deformation mechanisms in nacre". In: *Journal of Materials Research* 16.9 (2001), pp. 2485–2493.

[102] Yong Yang et al. "Toughness of spider silk at high and low temperatures". In: *Advanced Materials* 17.1 (2005), pp. 84–88.

[103] Yi-Chia Lin et al. "Control of non-linear elasticity in F-actin networks with microtubules". In: *Soft Matter* 7.3 (2011), pp. 902–906.

[104] Izabela K Piechocka et al. "Rheology of heterotypic collagen networks". In: *Biomacromolecules* 12.7 (2011), pp. 2797–2805.

[105] M Eastwood, DA McGrouther, and RA Brown. "Fibroblast responses to mechanical forces". In: *Proceedings of the Institution of Mechanical Engineers, Part H: Journal of Engineering in Medicine* 212.2 (1998), pp. 85–92.

[106] Thomas M Quinn et al. "Mechanical compression alters proteoglycan deposition and matrix deformation around individual cells in cartilage explants". In: *Journal of Cell Science* 111.5 (1998), pp. 573–583.

[107] Raimon Sunyer et al. "Collective cell durotaxis emerges from long-range intercellular force transmission". In: *Science* 353.6304 (2016), pp. 1157–1161.

[108] Jessamine P Winer, Shaina Oake, and Paul A Janmey. "Non-linear elasticity of extracellular matrices enables contractile cells to communicate local position and orientation". In: *PloS ONE* 4.7 (2009), e6382–e6382.

[109] Peter Friedl et al. "Migration of highly aggressive MV3 melanoma cells in 3-dimensional collagen lattices results in local matrix reorganization and shedding of $\alpha 2$ and $\beta 1$ integrins and CD44". In: *Cancer Research* 57.10 (1997), pp. 2061–2070.

[110] Michael Mak et al. "Single-cell migration in complex microenvironments: mechanics and signaling dynamics". In: *Journal of biomechanical engineering* 138.2 (2016), p. 021004.

[111] W Matthew Petroll, Lisha Ma, and James V Jester. "Direct correlation of collagen matrix deformation with focal adhesion dynamics in living corneal fibroblasts". In: *Journal of cell science* 116.8 (2003), pp. 1481–1491.

[112] Jennifer L West and Jeffrey A Hubbell. "Polymeric biomaterials with degradation sites for proteases involved in cell migration". In: *Macromolecules* 32.1 (1999), pp. 241–244.

[113] Stephanie I Fraley et al. "Three-dimensional matrix fiber alignment modulates cell migration and MT1-MMP utility by spatially and temporally directing protrusions". In: *Scientific reports* 5 (2015), p. 14580.

[114] Paolo P Provenzano et al. "Collagen reorganization at the tumor-stromal interface facilitates local invasion". In: *BMC Medicine* 4.1 (2006), p. 38.

[115] Daniela F Quail and Johanna A Joyce. "Microenvironmental regulation of tumor progression and metastasis". In: *Nature medicine* 19.11 (2013), pp. 1423–1437.

[116] Elias Barriga et al. “How mechanics orchestrate morphogenesis: Mesodermal stiffening triggers neural crest migration in vivo”. In: *Mechanisms of Development* 145 (2017), S46.

[117] András Szabó et al. “In vivo confinement promotes collective migration of neural crest cells”. In: *J Cell Biol* (2016), jcb–201602083.

[118] Peter Friedl and Darren Gilmour. “Collective cell migration in morphogenesis, regeneration and cancer”. In: *Nature reviews Molecular cell biology* 10.7 (2009), pp. 445–457.

[119] David Stopak and Albert K Harris. “Connective tissue morphogenesis by fibroblast traction: I. Tissue culture observations”. In: *Developmental Biology* 90.2 (1982), pp. 383–398.

[120] Chun-Min Lo et al. “Cell movement is guided by the rigidity of the substrate”. In: *Biophysical Journal* 79.1 (2000), pp. 144–152.

[121] Simon L Goodman, Gundula Risse, and Klaus von der Mark. “The E8 subfragment of laminin promotes locomotion of myoblasts over extracellular matrix.” In: *The Journal of Cell Biology* 109.2 (1989), pp. 799–809.

[122] Steven Munevar, Yu-li Wang, and Micah Dembo. “Traction force microscopy of migrating normal and H-ras transformed 3T3 fibroblasts”. In: *Biophysical journal* 80.4 (2001), pp. 1744–1757.

[123] Thomas E Angelini et al. “Cell migration driven by cooperative substrate deformation patterns”. In: *Physical review letters* 104.16 (2010), p. 168104.

[124] Han Bing Wang et al. “Varying the diameter of aligned electrospun fibers alters neurite outgrowth and Schwann cell migration”. In: *Acta biomaterialia* 6.8 (2010), pp. 2970–2978.

[125] Yonggang Pang et al. “The temporal and spatial dynamics of microscale collagen scaffold remodeling by smooth muscle cells”. In: *Biomaterials* 30.11 (2009), pp. 2023–2031.

[126] Yonggang Pang et al. “Dynamic quantitative visualization of single cell alignment and migration and matrix remodeling in 3-D collagen hydrogels under mechanical force”. In: *Biomaterials* 32.15 (2011), pp. 3776–3783.

[127] Matthew W Conklin et al. “Aligned collagen is a prognostic signature for survival in human breast carcinoma”. In: *The American journal of pathology* 178.3 (2011), pp. 1221–1232.

[128] Shawn P Carey et al. “Biophysical control of invasive tumor cell behavior by extracellular matrix microarchitecture”. In: *Biomaterials* 33.16 (2012), pp. 4157–4165.

[129] Kandice R Levental et al. “Matrix crosslinking forces tumor progression by enhancing integrin signaling”. In: *Cell* 139.5 (2009), pp. 891–906.

[130] Gregory T Christopherson, Hongjun Song, and Hai-Quan Mao. “The influence of fiber diameter of electrospun substrates on neural stem cell differentiation and proliferation”. In: *Biomaterials* 30.4 (2009), pp. 556–564.

[131] Urszula Stachewicz et al. “3D imaging of cell interactions with electrospun PLGA nanofiber membranes for bone regeneration”. In: *Acta biomaterialia* 27 (2015), pp. 88–100.

[132] Leonard M Sander. “Modeling contact guidance and invasion by cancer cells”. In: *Cancer research* 74.17 (2014), pp. 4588–4596.

[133] Ren Xu, Aaron Boudreau, and Mina J Bissell. “Tissue architecture and function: dynamic reciprocity via extra-and intra-cellular matrices”. In: *Cancer and metastasis reviews* 28.1-2 (2009), pp. 167–176.

[134] Hamid Mohammadi et al. “Inelastic behaviour of collagen networks in cell–matrix interactions and mechanosensation”. In: *Journal of The Royal Society Interface* 12.102 (2015), p. 20141074.

[135] Robert J Pelham and Yu-li Wang. “Cell locomotion and focal adhesions are regulated by substrate flexibility”. In: *Proceedings of the National Academy of Sciences* 94.25 (1997), pp. 13661–13665.

[136] TM Freyman et al. “Micromechanics of fibroblast contraction of a collagen–GAG matrix”. In: *Experimental cell research* 269.1 (2001), pp. 140–153.

[137] A S Abhilash et al. “Remodeling of Fibrous Extracellular Matrices by Contractile Cells: Predictions from Discrete Fiber Network Simulations”. In: *Biophysical Journal* 107.8 (2014), pp. 1829–1840.

[138] Nikolce Gjorevski and Celeste M Nelson. “Mapping of mechanical strains and stresses around quiescent engineered three-dimensional epithelial tissues”. In: *Biophysical journal* 103.1 (2012), pp. 152–162.

[139] Shamik Sen, Adam J Engler, and Dennis E Discher. “Matrix strains induced by cells: computing how far cells can feel”. In: *Cellular and molecular bioengineering* 2.1 (2009), pp. 39–48.

[140] Kelly M Schultz, Kyle A Kyburz, and Kristi S Anseth. “Measuring dynamic cell–material interactions and remodeling during 3D human mesenchymal stem cell migration in hydrogels”. In: *Proceedings of the National Academy of Sciences* 112.29 (2015), E3757–E3764.

[141] Julian Steinwachs et al. “Three-dimensional force microscopy of cells in biopolymer networks”. In: *Nature methods* 13.2 (2016), p. 171.

[142] Hamid Mohammadi, Paul A Janmey, and Christopher A McCulloch. “Lateral boundary mechanosensing by adherent cells in a collagen gel system”. In: *Biomaterials* 35.4 (2014), pp. 1138–1149.

[143] Amnon Buxboim et al. “How deeply cells feel: methods for thin gels”. In: *Journal of Physics: Condensed Matter* 22.19 (2010), p. 194116.

[144] Dan Ben-Yaakov et al. “Response of adherent cells to mechanical perturbations of the surrounding matrix”. In: *Soft matter* 11.7 (2015), pp. 1412–1424.

[145] Mathilda S Rudnicki et al. “Nonlinear strain stiffening is not sufficient to explain how far cells can feel on fibrous protein gels”. In: *Biophysical journal* 105.1 (2013), pp. 11–20.

[146] Xiaoyue Ma et al. “Fibers in the extracellular matrix enable long-range stress transmission between cells”. In: *Biophysical Journal* 104.7 (2013), pp. 1410–1418.

[147] Cynthia A Reinhart-King, Micah Dembo, and Daniel A Hammer. “Cell-cell mechanical communication through compliant substrates”. In: *Biophysical Journal* 95.12 (2008), pp. 6044–6051.

[148] René FM van Oers et al. “Mechanical cell-matrix feedback explains pairwise and collective endothelial cell behavior in vitro”. In: *PLoS computational biology* 10.8 (2014), e1003774.

[149] Nikolce Gjorevski et al. “Dynamic tensile forces drive collective cell migration through three-dimensional extracellular matrices”. In: *Scientific reports* 5 (2015), p. 11458.

[150] Benoit Ladoux, René-Marc Mège, and Xavier Trepat. “Front–rear polarization by mechanical cues: From single cells to tissues”. In: *Trends in cell biology* 26.6 (2016), pp. 420–433.

[151] Liel Sapir and Shelly Tzlil. “Talking Over the Extracellular Matrix: How do Cells Communicate Mechanically?” In: *Seminars in Cell & Developmental Biology*. Elsevier. 2017.

[152] Agustı Brugués et al. “Forces driving epithelial wound healing”. In: *Nature physics* 10.9 (2014), pp. 683–690.

[153] James W Reinhardt and Keith Gooch. “An Agent-Based Discrete Collagen Fiber Network Model of Dynamic Traction Force-Induced Remodeling”. In: *Journal of Biomechanical Engineering* (2017).

[154] Tony Yeung et al. “Effects of substrate stiffness on cell morphology, cytoskeletal structure, and adhesion”. In: *Cell Motility and the Cytoskeleton* 60.1 (2005), pp. 24–34.

[155] Stéphanie MC Bruekers et al. “Fibrin-fiber architecture influences cell spreading and differentiation”. In: *Cell adhesion & migration* 10.5 (2016), pp. 495–504.

[156] Yair Shokef and Samuel A Safran. “Scaling laws for the response of nonlinear elastic media with implications for cell mechanics”. In: *Physical Review Letters* 108.17 (2012), p. 178103.

[157] Xinpeng Xu and Samuel A Safran. “Nonlinearities of biopolymer gels increase the range of force transmission”. In: *Physical Review E* 92.3 (2015), p. 032728.

[158] Taeyoon Kim et al. “Computational analysis of viscoelastic properties of crosslinked actin networks”. In: *PLoS computational biology* 5.7 (2009), e1000439.

[159] EM Huisman, Cornelis Storm, and GT Barkema. “Frequency-dependent stiffening of semiflexible networks: a dynamical nonaffine to affine transition”. In: *Physical Review E* 82.6 (2010), p. 061902.

[160] T Van Dillen, PR Onck, and E Van der Giessen. “Models for stiffening in cross-linked biopolymer networks: A comparative study”. In: *Journal of the Mechanics and Physics of Solids* 56.6 (2008), pp. 2240–2264.

[161] Yi-Chia Lin et al. “Origins of elasticity in intermediate filament networks”. In: *Physical Review Letters* 104.5 (2010), p. 058101.

[162] Hubert M James and Eugene Guth. “Theory of the elastic properties of rubber”. In: *The Journal of Chemical Physics* 11.10 (1943), pp. 455–481.

[163] David A Head, Alex J Levine, and F C MacKintosh. “Deformation of cross-linked semiflexible polymer networks”. In: *Physical Review Letters* 91.10 (2003), p. 108102.

[164] Anindita Basu et al. “Nonaffine displacements in flexible polymer networks”. In: *Macromolecules* 44.6 (2011), pp. 1671–1679.

[165] Xiaoming Mao, Olaf Stenull, and Thomas C Lubensky. “Effective-medium theory of a filamentous triangular lattice”. In: *Physical Review E* 87.4 (2013), p. 042601.

[166] Mo Bai et al. “The mechanics and affine–nonaffine transition in polydisperse semiflexible networks”. In: *Soft Matter* 7.3 (2011), pp. 907–914.

[167] Preethi L Chandran and Victor H Barocas. “Affine versus non-affine fibril kinematics in collagen networks: theoretical studies of network behavior”. In: *Journal of Biomechanical Engineering* 128.2 (2006), pp. 259–270.

[168] M Latva-Kokko, J Mäkinen, and J Timonen. “Rigidity transition in two-dimensional random fiber networks”. In: *Physical Review E* 63.4 (2001), p. 046113.

[169] Shengmao Lin and Linxia Gu. “Influence of Crosslink Density and Stiffness on Mechanical Properties of Type I Collagen Gel”. In: *Materials* 8.2 (2015), pp. 551–560.

[170] D A Head, A J Levine, and F C MacKintosh. “Distinct regimes of elastic response and deformation modes of cross-linked cytoskeletal and semiflexible polymer networks”. In: *Physical Review E* 68.6 (2003), p. 061907.

[171] Alex J Levine, D A Head, and F C MacKintosh. “The deformation field in semiflexible networks”. In: *Journal of Physics: Condensed Matter* 16.22 (2004), S2079.

[172] R C Picu. “Mechanics of random fiber networks-a review”. In: *Soft Matter* 7.15 (2011), pp. 6768–6785.

[173] Claus Heussinger and Erwin Frey. “Floppy modes and nonaffine deformations in random fiber networks”. In: *Physical Review Letters* 97.10 (2006), p. 105501.

[174] DA Head, AJ Levine, and FC MacKintosh. “Mechanical response of semiflexible networks to localized perturbations”. In: *Physical Review E* 72.6 (2005), p. 061914.

[175] P R Onck et al. “Alternative explanation of stiffening in cross-linked semiflexible networks”. In: *Physical Review Letters* 95.17 (2005), p. 178102.

[176] Goran Žagar, Patrick R Onck, and Erik van der Giessen. “Two fundamental mechanisms govern the stiffening of cross-linked networks”. In: *Biophysical journal* 108.6 (2015), pp. 1470–1479.

[177] Andrew R Missel et al. “Affine-nonaffine transition in networks of nematically ordered semiflexible polymers”. In: *Physical Review E* 82.4 (2010), p. 041907.

[178] Mo Bai et al. “On the role of the filament length distribution in the mechanics of semiflexible networks”. In: *Acta Biomaterialia* 7.5 (2011), pp. 2109–2118.

[179] C T Koh and M L Oyen. “Branching toughens fibrous networks”. In: *Journal of the Mechanical Behavior of Biomedical Materials* 12 (2012), pp. 74–82.

[180] A S Shahsavari and R C Picu. “Elasticity of sparsely cross-linked random fibre networks”. In: *Philosophical Magazine Letters* 93.6 (2013), pp. 356–361.

[181] Ehsan Ban et al. “Softening in random networks of non-identical beams”. In: *Journal of the Mechanics and Physics of Solids* 87 (2016), pp. 38–50.

[182] Hamed Hatami-Marbini. "Scaling properties of three-dimensional random fibre networks". In: *Philosophical Magazine Letters* 96.5 (2016), pp. 165–174.

[183] Byoungkoo Lee et al. "A Three-Dimensional Computational Model of Collagen Network Mechanics". In: *PloS ONE* (2014).

[184] M Latva-Kokko and J Timonen. "Rigidity of random networks of stiff fibers in the low-density limit". In: *Physical Review E* 64.6 (2001), p. 066117.

[185] David A Head, F C MacKintosh, and Alex J Levine. "Nonuniversality of elastic exponents in random bond-bending networks". In: *Physical Review E* 68.2 (2003), p. 025101.

[186] Claus Heussinger and Erwin Frey. "Stiff polymers, foams, and fiber networks". In: *Physical Review Letters* 96.1 (2006), p. 017802.

[187] Claus Heussinger and Erwin Frey. "Role of architecture in the elastic response of semiflexible polymer and fiber networks". In: *Physical Review E* 75.1 (2007), p. 011917.

[188] L Zhang et al. "Cross-linked fiber network embedded in an elastic matrix". In: *Soft Matter* 9.28 (2013), pp. 6398–6405.

[189] Martin Ostoja-Starzewski. "Lattice models in micromechanics". In: *Applied Mechanics Reviews* 55.1 (2002), pp. 35–60.

[190] Christopher A R Jones et al. "Micromechanics of cellularized biopolymer networks". In: *Proceedings of the National Academy of Sciences* 112.37 (2015), E5117–E5122.

[191] M Sheinman, CP Broedersz, and FC MacKintosh. "Nonlinear effective-medium theory of disordered spring networks". In: *Physical Review E* 85.2 (2012), p. 021801.

[192] C P Broedersz, M Sheinman, and F C MacKintosh. "Filament-length-controlled elasticity in 3D fiber networks". In: *Physical Review Letters* 108.7 (2012), p. 078102.

[193] Xiaoming Mao, Olaf Stenull, and Thomas C Lubensky. "Elasticity of a filamentous kagome lattice". In: *Physical Review E* 87.4 (2013), p. 042602.

[194] Jan Maarten Van Doorn et al. "Criticality and mechanical enhancement in composite fiber networks". In: *Physical Review E* 95.4 (2017), p. 042503.

[195] Pierre Ronceray, Chase P Broedersz, and Martin Lenz. "Fiber networks amplify active stress". In: *Proceedings of the National Academy of Sciences* (2016), p. 201514208.

[196] Jacob Notbohm et al. "Microbuckling of fibrin provides a mechanism for cell mechanosensing". In: *Journal of The Royal Society Interface* 12.108 (2015), p. 20150320.

[197] J Clerk Maxwell. "On the calculation of the equilibrium and stiffness of frames". In: *The London, Edinburgh, and Dublin Philosophical Magazine and Journal of Science* 27.182 (1864), pp. 294–299.

[198] José Alvarado et al. "Molecular motors robustly drive active gels to a critically connected state". In: *arXiv preprint arXiv:1302.2798* (2013).

[199] A S Shahsavari and R C Picu. "Model selection for athermal cross-linked fiber networks". In: *Physical Review E* 86.1 (2012), p. 011923.

[200] Andrew M Stein et al. "The micromechanics of three-dimensional collagen-I gels". In: *Complexity* 16.4 (2011), pp. 22–28.

[201] MATLAB. *version 7.10.0 (R2015b)*. Natick, Massachusetts: The MathWorks Inc., 2015.

[202] Guido Rossum. "Python reference manual". In: (1995).

[203] Hibbett, Karlsson, and Sorensen. *ABAQUS/standard: User's Manual*. Vol. 1. Hibbitt, Karlsson & Sorensen, 1998.

[204] DL Humphries, JA Grogan, and EA Gaffney. "Mechanical Cell–Cell Communication in Fibrous Networks: The Importance of Network Geometry". In: *Bulletin of mathematical biology* 79.3 (2017), pp. 498–524.

[205] Adam J Engler et al. "Matrix elasticity directs stem cell lineage specification". In: *Cell* 126.4 (2006), pp. 677–689.

[206] Penney M Gilbert et al. "Substrate elasticity regulates skeletal muscle stem cell self-renewal in culture". In: *Science* 329.5995 (2010), pp. 1078–1081.

[207] Rebecca G Wells. "The role of matrix stiffness in hepatic stellate cell activation and liver fibrosis". In: *Journal of Clinical Gastroenterology* 39.4 (2005), S158–S161.

[208] Shelly R Peyton et al. "The emergence of ECM mechanics and cytoskeletal tension as important regulators of cell function". In: *Cell Biochemistry and Biophysics* 47.2 (2007), pp. 300–320.

[209] Thomas S Jacques et al. "Neural precursor cell chain migration and division are regulated through different beta1 integrins". In: *Development* 125.16 (1998), pp. 3167–3177.

[210] Sergey V Plotnikov et al. "Force fluctuations within focal adhesions mediate ECM-rigidity sensing to guide directed cell migration". In: *Cell* 151.7 (2012), pp. 1513–1527.

[211] Wen Shing Leong et al. "Thickness sensing of hMSCs on collagen gel directs stem cell fate". In: *Biochemical and Biophysical Research Communications* 401.2 (2010), pp. 287–292.

[212] Claus Heussinger, Boris Schaefer, and Erwin Frey. "Nonaffine rubber elasticity for stiff polymer networks". In: *Physical Review E* 76.3 (2007), p. 031906.

[213] Triantafyllos Stylianopoulos and Victor H Barocas. "Volume-averaging theory for the study of the mechanics of collagen networks". In: *Computer Methods in Applied Mechanics and Engineering* 196.31 (2007), pp. 2981–2990.

[214] Spencer P Lake et al. "Mechanics of a fiber network within a non-fibrillar matrix: model and comparison with collagen-agarose co-gels". In: *Annals of Biomedical Engineering* 40.10 (2012), pp. 2111–2121.

[215] Triantafyllos Stylianopoulos and Victor H Barocas. "Multiscale, structure-based modeling for the elastic mechanical behavior of arterial walls". In: *Journal of Biomechanical Engineering* 129.4 (2007), pp. 611–618.

[216] Bin Hu, V B Shenoy, and Yuan Lin. "Buckling and enforced stretching of bio-filaments". In: *Journal of the Mechanics and Physics of Solids* 60.11 (2012), pp. 1941–1951.

[217] Frank J Massey Jr. "The Kolmogorov-Smirnov test for goodness of fit". In: *Journal of the American Statistical Association* 46.253 (1951), pp. 68–78.

[218] Claus Heussinger and Erwin Frey. "Force distributions and force chains in random stiff fiber networks". In: *The European Physical Journal E* 24.1 (2007), pp. 47–53.

[219] AS Shahsavari and RC Picu. "Exceptional stiffening in composite fiber networks". In: *Physical Review E* 92.1 (2015), p. 012401.

[220] Fionn Dunne and Nik Petrinic. *Introduction to computational plasticity*. Oxford University Press on Demand, 2005.

[221] Ying-chun Chen et al. "Effect of crosslinking in cartilage-like collagen microstructures". In: *Journal of the Mechanical Behavior of Biomedical Materials* 66 (2017), pp. 138–143.

[222] O Lieleg et al. "Slow dynamics and internal stress relaxation in bundled cytoskeletal networks". In: *Nature Materials* 10.3 (2011), pp. 236–242.

[223] Qi Wen et al. "Non-affine deformations in polymer hydrogels". In: *Soft Matter* 8.31 (2012), pp. 8039–8049.

[224] Stefan B Lindström et al. "Biopolymer network geometries: characterization, regeneration, and elastic properties". In: *Physical Review E* 82.5 (2010), p. 051905.

[225] Albert James Licup, Abhinav Sharma, and Fred C MacKintosh. "Elastic regimes of subisostatic athermal fiber networks". In: *Physical Review E* 93.1 (2016), p. 012407.

[226] Priyamvada Chugh et al. "Actin cortex architecture regulates cell surface tension". In: *Nature Cell Biology* 19.6 (2017), pp. 689–697.

[227] Moumita Das, DA Quint, and JM Schwarz. "Redundancy and cooperativity in the mechanics of compositely crosslinked filamentous networks". In: *PloS ONE* 7.5 (2012), e35939.

[228] Jeffrey M Mattson, Raphaël Turcotte, and Yanhang Zhang. "Glycosaminoglycans contribute to extracellular matrix fiber recruitment and arterial wall mechanics". In: *Biomechanics and modeling in mechanobiology* 16.1 (2017), pp. 213–225.

[229] Shuoshuo Wang and Talila Volk. "Composite biopolymer scaffolds shape muscle nucleus: Insights and perspectives from Drosophila". In: *BioArchitecture* 5.3-4 (2015), pp. 35–43.

[230] Mikkel H Jensen et al. "Emergent properties of composite semiflexible biopolymer networks". In: *BioArchitecture* 4.4-5 (2014), pp. 138–143.

[231] Xin Pang et al. "Three dimensional microstructural network of elastin, collagen, and cells in Achilles tendons". In: *Journal of Orthopaedic Research* (2017).

[232] ME Cates and SF Edwards. "Linear theory of disordered fibre-reinforced composites". In: *Proceedings of the Royal Society of London A: Mathematical, Physical and Engineering Sciences* 395.1808 (1984), pp. 89–109.

[233] Moumita Das and FC MacKintosh. "Mechanics of soft composites of rods in elastic gels". In: *Physical Review E* 84.6 (2011), p. 061906.

[234] Elisabeth M Huisman et al. "Semiflexible filamentous composites". In: *Physical Review Letters* 105.11 (2010), p. 118101.

[235] Yifan Wang et al. "Affine and non-affine deformations quantified in cytoskeletal networks through three-dimensional form-finding model". In: *Journal of the Mechanical Behavior of Biomedical Materials* 72 (2017), pp. 52–65.

[236] H Hatami-Marbini and RC Picu. "Scaling of nonaffine deformation in random semiflexible fiber networks". In: *Physical Review E* 77.6 (2008), p. 062103.

[237] Qi Wen et al. "Local and global deformations in a strain-stiffening fibrin gel". In: *New Journal of Physics* 9.11 (2007), p. 428.

[238] C Bradford Barber, David P Dobkin, and Hannu Huhdanpaa. "The quickhull algorithm for convex hulls". In: *ACM Transactions on Mathematical Software (TOMS)* 22.4 (1996), pp. 469–483.

[239] AS Shahsavari and RC Picu. "Size effect on mechanical behavior of random fiber networks". In: *International Journal of Solids and Structures* 50.20 (2013), pp. 3332–3338.

[240] Maarten Jaspers et al. "Nonlinear mechanics of hybrid polymer networks that mimic the complex mechanical environment of cells". In: *Nature Communications* 8 (2017).

[241] Stepan Vladimirovitch Lomov et al. "Textile geometry preprocessor for meso-mechanical models of woven composites". In: *Composites Science and Technology* 60.11 (2000), pp. 2083–2095.

[242] Brian N Cox, Mahyar S Dadkhah, and WL Morris. "On the tensile failure of 3D woven composites". In: *Composites Part A: Applied Science and Manufacturing* 27.6 (1996), pp. 447–458.

[243] Stephen F Badylak, Donald O Freytes, and Thomas W Gilbert. "Extracellular matrix as a biological scaffold material: structure and function". In: *Acta biomaterialia* 5.1 (2009), pp. 1–13.

[244] Wolf H Rombouts et al. "Synergistic stiffening in double-fiber networks". In: *Biomacromolecules* 15.4 (2014), pp. 1233–1239.

[245] Wolf H Rombouts et al. "Enhanced rigidity and rupture strength of composite hydrogel networks of bio-inspired block copolymers". In: *Soft Matter* 9.29 (2013), pp. 6936–6942.